PERFORMANCE CHARACTERIZATION OF HIGH PERFORMANCE CONCRETES UNDER FIRE CONDITIONS

By

Wasim Khaliq

A DISSERTATION

Submitted to
Michigan State University
in partial fulfillment of the requirements
for the degree of

DOCTOR OF PHILOSOPHY

Civil Engineering

2012

ABSTRACT

PERFORMANCE CHARACTERIZATION OF HIGH PERFORMANCE CONCRETES UNDER FIRE CONDITIONS

By

Wasim Khaliq

In recent years, high performance concretes (HPC) are finding increasing applications in buildings and infrastructure due to numerous advantages, such as higher strength and durability, these HPC offer over conventional concretes. Structural members made of HPC, when used in buildings, have to satisfy the fire resistance requirements specified in building codes and standards. Although conventional concrete members have good fire resistance, same may not be true for HPC members due to faster degradation of strength with temperature and occurrence of fire induced spalling. Spalling in HPC columns can be overcome either through the addition of fibers in the concrete mix or through the provision of 135° bent ties. For evaluating the fire resistance of HPC columns, as well as to account for the beneficial effects of fibers and 135° tie configuration on spalling mitigation, high temperature properties of HPC and numerical models that can take in to account the effect of tie configuration is required. At present, there is lack of data on high temperature properties specific to different types of HPC (plain and with fibers). Also, there is no methodology to account for the effect of tie configuration on fire resistance of RC columns. To overcome these knowledge gaps, an experimental and numerical study is undertaken as part of this thesis.

Performance characterization of high performance concretes under fire conditions is carried out at both material and structural level (specifically columns). As part of material characterization,

thermal and mechanical property tests were carried out in 20-800°C temperature range on different HPC mixes (plain and with different combinations of fibers). Data from measured property tests was utilized to develop empirical relations for high temperature properties. As part of structural characterization, fire resistance tests were carried out on two fly ash concrete (FAC) and two high strength concrete (HSC) columns with different fiber combinations.

As part of numerical study, a macroscopic finite element (MFE) model, originally developed to evaluate fire resistance of RC columns, was extended to include the effect of tie configuration. The proposed tie sub-model is based on the approach used in seismic design and involves calculation of force acting on ties by evaluating stresses resulting from pore pressure, mechanical loading and thermal effects in RC columns under fire exposure. The force acting on ties is compared against temperature (time) dependent bond strength (tie-concrete interface) to evaluate the failure of ties. The model is validated by comparing response predictions against test data and the model was applied to carry out parametric studies to quantify the influence of HPC properties and tie configuration on fire response of HPC columns.

Results from high temperature material property tests show that HPC exhibit thermal properties similar to that in conventional concrete. However, mechanical properties of HPC degrade at faster rate (much severe) than that in conventional concretes. Results from fire resistance tests show that plain HPC columns exhibit lower fire resistance due to occurrence of fire induced spalling and faster degradation of strength. However, presence of different fiber combinations in HPC columns can significantly enhance the fire resistance of the columns. In addition, presence of 135° bent ties in HPC columns can significantly enhance the fire resistance of these columns through confinement action.

DEDICATION

To Amna, Fasih, and Khadija.

ACKNOWLEDGMENTS

I would like to express my greatest gratitude to my advisor, Prof. Venkatesh Kodur, Michigan State University, for his continued support, encouragement, and guidance during the course of my studies. I would like to convey my sincere thanks for his ideas and perseverance which made my graduate studies very rewarding.

I would also like to thank Prof. Parviz Soroushian, Prof. Neeraj Buch and Prof. K.N. Subramanian for joining my Ph.D. committee, and for their valuable advice throughout my course of research at MSU.

I would like to thank the lab manager, Mr. Siavosh Ravanbakhsh for his generous support and help during the experimental program in this research. And, I would also like to extend my sincere thanks to Laura Taylor, Mary Mroz, and Margaret Conner for all the help they provided.

I would like to thank Monther Dwaikat, Mahmud Dwaikat, Aqeel Ahmad, Rustin Fike, Nikhil Raut, Nikhil Chaudhary, Sonali Kand, Haihua Gu, Purushutham Pakala, Baolin Yu, Esam Aziz for their support, particularly in the experimental part of this study. My special thanks to Dr. Xiaoyong Mao whose continuous help made it possible for me to execute laborious experiments on HPC columns in this study.

Additionally, I would like to thank all the faculty members and students at the Civil and Environmental Engineering department at Michigan State University for their help and support during my doctoral studies.

TABLE OF CONTENTS

LIST OF TABLES

LIST OF FIGURES

CHAPTER 1

1 INTRODUCTION

1.1 General

Concrete is one of the most widely used construction material in buildings due to its excellent strength, durability, ease of fabrication, and fire resistance properties. Over the last three decades there has been significant research and development activities in concrete technology and this has led to improved concrete mixes often referred to as high performance concretes (HPC). HPC which include high strength concrete (HSC), self-consolidating concrete (SCC), fiber reinforced concrete (FRC), and high strength fly ash concrete (FAC), offer superior strength, durability and cost advantages, and thus finding wide range of applications in built infrastructure. In recent years the use of HPC, which was mainly used in bridges, off-shore structures, and infrastructure projects, has been extended to columns and beams in reinforced concrete (RC) buildings.

Fire represents one of the most severe hazard to which structures may be subjected during their life time and hence the provision of appropriate fire resistance measures is an important aspect of building design. This is to enhance safety of occupants, control the spread of fire, and minimize damage to property and environment in the event of a fire in the building. Fire safety design can be achieved through active and passive fire protection measures. Active systems generally get self-activated once the fire is triggered and they include fire detectors, smoke control systems, and sprinklers. Passive systems are built into the structure (buildings), and do not require specific operation to control the fire. The need for passive fire protection systems or what is commonly referred to as fire resistance, can be attributed to the fact that structural integrity is the last line of defense when other measures for containing the fire fail. Fire resistance is defined as the duration

during which a structural member (system) exhibits resistance with respect to structural integrity, stability, and temperature transmission when exposed to fire (Buchanan, 2002; Purkiss, 2007).

Conventional normal strength concrete (NSC) members generally exhibit good fire resistance properties. However, recent studies have shown that structural members made of high performance concrete (similar to HSC, SCC and FAC) have lower fire resistance properties (Bamonte and Gambarova, 2010; Kodur, 2000; Tang and Lo, 2009). This has been attributed to differences in thermo-mechanical properties of HPC and also to the occurrence of fire induced spalling (Castillo and Durrani, 1990; Fu et al., 2005; Kodur and Sultan, 1998; Tang and Lo, 2009). It has also been shown that the spalling in HPC members can be overcome through the addition of fibers (steel, propylene, and hybrid) in the concrete mix. Whilst most of the high temperature properties are available for NSC, no data is available for new types of HPC such as HSC, SCC, and FAC (plain and with different fiber combinations).

1.2 High Temperature Properties of Concrete

Evaluating fire resistance of a structural system requires knowledge of high temperature properties of constituent materials (Buchanan, 2002; SFPE, 2008). The properties of concrete that are needed for fire resistance analysis are thermal, mechanical, deformation, and special properties such as fire induced spalling. Thermal properties include thermal conductivity, specific heat, thermal diffusivity, thermal expansion, and mass loss. Deformation properties such as creep and mechanical properties such as strength, stress-strain curves, and elastic modulus significantly influence the fire response of a structural system. In addition, fire induced spalling which occurs in concrete under certain fire conditions can alter the response of a reinforced concrete structural system. All these properties vary with temperature and are influenced by the

mix proportions, type of aggregate, presence of fibers, and mineral and chemical admixtures (Bažant and Kaplan, 1996; Buchanan, 2002; Phan, 1996; SFPE, 2008).

HPC are typically made through addition of binders such as silica fume, fly ash, blast furnace slag, and other smaller amounts of mineral and chemical admixtures. These binders introduce specific properties to HPC such as flow ability and workability in fresh form and high strength and dense microstructure in the hardened form. Thus thermal and mechanical properties of HPC can be different from that of conventional concrete (Kodur and Sultan, 1998). When these HPC's are subjected to high temperatures, their performance is affected by changes in its thermal and mechanical behavior. Understanding the behavior of these HPC's at the material level and characterizing their high temperature properties is important for predicting the fire response of HPC structural members. However, at present there is very limited information on high temperature thermal and mechanical properties for these new types of HPC.

1.3 Response of HPC Columns under Fire Conditions

1.3.1 General Fire Behavior

One of the major applications for high performance concrete is in columns of high rise buildings since high compressive strength can effectively be utilized. The behavior of RC columns under fire is quite different from that at room temperature mainly due to the fact that under fire conditions, the strength and stiffness of the column deteriorate with temperature. Columns made of conventional NSC generally exhibit good fire resistance and can offer 3 to 4 hours of fire resistance rating without any additional measures. However, it has been shown through numerous experimental and numerical studies that HPC columns may not exhibit the same level fire resistance as that of NSC (Kodur, 2003; Kodur and Sultan, 1998). The effect of various parameters such as cross sectional size, cover thickness, reinforcement ratio, aggregate type,

load, and load eccentricity on fire resistance was investigated previously through series of fire experiments (Kodur and McGrath, 2003).

Data from reported fire tests can be used to illustrate the typical behavior of an RC column under fire. Figure 1.1shows the elevation and cross-section of a typical NSC and HSC column tested in the laboratory under ASTM E119 (ASTM Standard E119, 2007) standard fire (Figure 1.2), and Figure 1.3 shows the variation of axial deformation of a NSC and HSC column with fire exposure time (Kodur and Sultan, 1998; Lie and Woolerton, 1988). Concrete compressive strength for the HSC and NSC columns was 97 MPa and 36 MPa respectively. The HSC column was loaded with 2000 kN or 60% of the ultimate resistance whereas NSC column was subjected to a load of 1067 kN or 60% of its ultimate resistance. HSC column had four while NSC column had eight 20 mm longitudinal rebars as main reinforcement. The columns were provided with 135° bent ties. The NSC column had 8 mm at 305 mm spacing, whereas the HSC column had 10 mm ties at a spacing of 225 mm.

When a concrete column is exposed to fire, the cross-sectional temperatures increase with time as shown in Figure 1.2. At the beginning of fire exposure concrete and steel expand due to rising cross-sectional temperatures, as shown in Figure 1.3. The expansion in the initial stages of fire exposure is mainly due to the thermal expansion occurring in both concrete and steel. With the increase in temperature, concrete and steel rebars start to lose strength. Since the reinforcing rebars are in the outer core of the column, the temperature rises much faster in rebars than the inner core of concrete as shown in Figure 1.2. When the steel yields, as a result of rising temperatures, the concrete carries a progressively increasing portion of the load. The strength of the concrete also decreases with temperature due to deteriorating properties of concrete, and ultimately as it can no longer support the load, failure of the column occurs.

The difference between temperature progression in NSC and HSC can be seen in Figure 1.2. Since HSC has higher thermal conductivity, it displays higher temperature development at quarter depth and mid depth to that of NSC. Both NSC and HSC columns also display different deformation patterns, and these differences can be attributed to ductile behavior of NSC and differences in thermal expansion and elastic modulus properties of NSC and HSC (Kodur, 1999). The lower deformation (expansion and contraction) in HSC column can be attributed to the lower thermal expansion and high stiffness properties of HSC. The failure time for HSC column in the fire test was reported as 225 minutes as compared to 366 minutes for NSC column, indicating HSC columns has much lower fire resistance in comparison to NSC columns.

The above comparative illustration clearly indicates that NSC and HSC columns have significant difference in fire behavior. This difference in fire response of RC columns of two concrete types is attributed to difference in their high temperature thermal and mechanical properties. Although conventional NSC members have good fire resistance as illustrated above, same may not be true for HSC columns due to faster degradation of strength and occurrence of fire induced spalling. HPC columns having concrete properties identical to that of HSC members are also assumed to have lower fire performance. Therefore there is a need to characterize the high temperature properties specific to HPC. There is substantial amount data in literature on high temperature thermal and mechanical properties of NSC and to some extent for HSC as well. However, in the case of new types of HPC such as FAC, SCC (both plain and with fibers) this high temperature property data is very limited.

1.3.2 Fire induced Spalling

An RC column can be exposed to different fire scenarios (other than standard fire) during the life time of a structure as shown in Figure 1.4. Once exposed to some of these fire scenarios the

cross-section of RC columns can experience high thermal gradients which in turn can significantly influence the fire behavior of structural members. These thermal gradients can be moderate to severe, depending on thermal properties, cross-sectional size, and microstructure of concrete. The high thermal gradients resulting from rising temperatures in the cross-section lead to rapidly increasing pore pressure that cause fire induced spalling. Fire induced spalling that is caused by pore pressure buildup in concrete, is not a problem with NSC columns and is mostly associated to HSC columns due to low permeability (Ali, 2002; Ali and Nadjai, 2008; Kodur, 1999; Kodur, 2000).

Figure 1.5 shows a comparison of post fire status of NSC and HSC columns and extent of fire induced spalling in HSC. If the cross-sectional temperatures rise at faster rate, high pore pressure will build up due to moisture converting to vapors. This fire induced pore pressure in concrete increases with temperature while the tensile strength of concrete degrades with temperature. Since tensile strength of concrete is inherent resistance to spalling, when pore pressure exceeds the tensile strength of concrete spalling occurs. Spalling depends on a number of factors such as heating rate, permeability, moisture content, configuration of lateral (tie) reinforcement, and strength of concrete. Depending on all these factors the columns may undergo fire induced spalling thus hampering their strength and stiffness properties. HPC such as FAC, SCC which are characterized by dense microstructure similar to HSC are also prone to fire induced spalling.

1.3.3 Spalling Mitigation

To mitigate fire induced spalling in HSC, researchers have suggested addition of different fiber combinations, such as polypropylene fibers (Ali et al., 2004; Behnood and Ghandehari, 2009; Bilodeau et al., 2004), steel fibers (Kodur, 1999; Rossi, 1994) and hybrid fibers (Ali and Nadjai, 2008). Polypropylene fibers melt at relatively low temperatures (about 167-170°C) thus leaving

micro and macro channels randomly oriented inside the concrete that help diffusion of pore pressure (Bilodeau et al., 2004) resulting in spalling mitigation. Steel fibers enhance the tensile strength of concrete which provides resistance against pore pressure and thus helps mitigate spalling. Hybrid fibers take advantage of both types of fibers to mitigate spalling, by increase in porosity of concrete with melting of propylene fibers at higher temperatures and improvement in tensile strength with use of steel fibers.

Tests have also shown that modifying the tie configuration in HSC columns from conventional 90° to 135° is beneficial to reduce the effect of spalling (Kodur and McGrath, 2003). It was experimentally established that, (1) spalling occurs throughout the cross-section of columns when the ties are bent in a conventional pattern at 90° and (2) spalling only occurs in the outer layer of steel cage when ties are bent at 135° into the concrete core (Kodur and McGrath, 2006; Kodur et al., 2002). Figure 1.6 shows arrangements of conventional 90° and improved 135° ties and Figure 1.7 shows the failure modes of HSC columns with 90° and 135° ties respectively. It can be seen that extent of spalling has been reduced in column with improved tie configuration. For this reason, ACI 216.1 (2007) specifies that for fire design, cross ties in the column shall be anchored through 135° end hooks which turn around longitudinal bars and are embedded in the concrete core. Though based on experimental studies, the prescriptive approach has been adopted by ACI 216.1 to take into account the effect of tie configuration; however, there is lack of understanding of fundamental principles as to how it contributes in enhancement of fire resistance of RC columns.

1.4 Research Objectives

The difference in fire behavior of NSC and HSC columns results from different thermal and mechanical properties at high temperature. One of the major problems that affects the fire

behavior in HSC members is fire induced spalling. With the increased use of new types of HPC in RC columns, there is a need to characterize its' thermal and mechanical properties both at material and structural level. For evaluating the fire resistance of HPC columns, as well as to account for beneficial effects of fibers and 135° tie configuration on spalling mitigation, high temperature material properties of HPC (plain and with different fiber combinations) and including the effect of tie configuration is required. However, there is lack of data on high temperature properties specific to different HPC (plain and with fibers) as well as established mechanism with which fire resistance in RC columns is enhanced with provision of modified 135° tie configuration. To overcome the current knowledge gaps, this research is aimed at addressing the following objectives:

- Undertake a detailed state-of-the-art review on the high temperature properties of present day concrete mixes. The comprehensive review will compile the current state of experimental and numerical studies on HSC columns and code provisions on thermal, mechanical, deformation and special properties like fire induced spalling and technique to overcome problem of spalling in HSC.
- Undertake material property tests to generate database on high temperature thermal and mechanical properties of new types of HPC namely HSC, FAC, and SCC (plain and with different fiber combinations). Data from these tests will be utilized to develop empirical thermal and mechanical property relationships.
- Undertake fire resistance tests on two fly ash concrete (FAC) and two high strength concrete (HSC) columns with different fiber combinations as part of structural characterization of HPC structural members. Extensive data will be collected in the form of axial and lateral

deformations, cross-sectional temperatures and strains in steel rebars. Data from fire resistance tests was utilized to validate the numerical model for fire resistance predictions of HPC columns.

- Develop an approach for modeling the effect of tie configuration on fire resistance of HPC columns. This will include evaluation of the mechanics involved in opening and failing of ties by taking into account the forces acting on ties resulting from high temperature thermo-mechanical stresses and fire induced pore pressure. Effect of modification of tie configuration on spalling mitigation and enhancement of fire resistance of RC columns will be studied.
- Incorporate the high temperature properties of HPC and tie sub-model in to macroscopic finite element (MFE) model. Validate the extended MFE model for evaluating the fire response of HPC columns tested earlier by computing thermal and structural response predictions for HPC columns under different tie configurations.
- Carry out parametric studies to quantify the significant factors that influence the fire response of HPC columns with 90° and 135° bent ties.

1.5 Scope

The research proposed here involves experimental and numerical studies on characterization of fire performance of HPC both at material and structural levels. As part of experimental research, extensive high temperature experiments on small specimens were carried out for characterizing thermal and mechanical properties of FAC, SCC, and HSC (plain and with different fiber combinations) at material level. At structural level, four full scale RC columns made of FAC and HSC were fabricated and tested under design fire to evaluate the structural fire response of FAC columns with and without fibers to that with HSC columns. To develop a fundamental understanding on the effect of tie configuration on fire response of RC columns a numerical ‘tie

sub-model' was developed and incorporated into a macroscopic finite element model. The effect of tie configuration on fire resistance is modeled through mechanics based principles, similar to the approach used in seismic analysis of structures. Data from fire resistance tests is utilized to validate the fire resistance model. The validated MFE model was then applied to carry out parametric studies to quantify influence of various factors on fire response of HPC columns.

The thesis is organized into eight chapters:

- Chapter 1 provides background information on fire resistance of HPC and high temperature properties needed for fire resistance evaluation of HPC columns.
- Chapter 2 provides a review of the literature on the high temperature thermal and mechanical material properties of conventional NSC and HSC, the variability in existing data and also highlights limitations of available methods for fire resistance evaluation of HPC columns. A review of recent experimental and analytical studies on fire resistance evaluation of RC columns is also provided.
- Chapter 3 presents experimental studies on high temperature thermal properties of HSC, SCC, and FAC (plain and with different fiber combinations) and the development of empirical relationships for high temperature material properties.
- In Chapter 4 experimental studies on high temperature mechanical properties of HSC, SCC, and FAC (plain and with different fiber combinations) are presented. The chapter also provides empirical relationships developed for high temperature mechanical properties of HPC.
- In Chapter 5 details on fire resistance experiments on two FAC and two HSC columns (with different fiber combinations) under non-standard fire scenarios are presented. Results from

the fire tests are used to discuss the comparative response of FAC and HSC columns under fire conditions.

- In Chapter 6 covers the details on macroscopic finite element numerical model and analysis details for fire resistance predictions of RC columns. Development of subroutines based on high temperature material properties of HPC and tie configuration sub-model is also presented. Incorporation of these subroutines into macroscopic finite element (MFE) model and validation of the extended MFE model are covered in this chapter.
- Chapter 7 presents results from parametric studies showing influence of the significant factors such as high temperature thermal and mechanical properties and effect of different tie configurations on fire response of HPC columns.
- Chapter 8 summarizes the key findings, recommendations for future work and research impact based on this study.

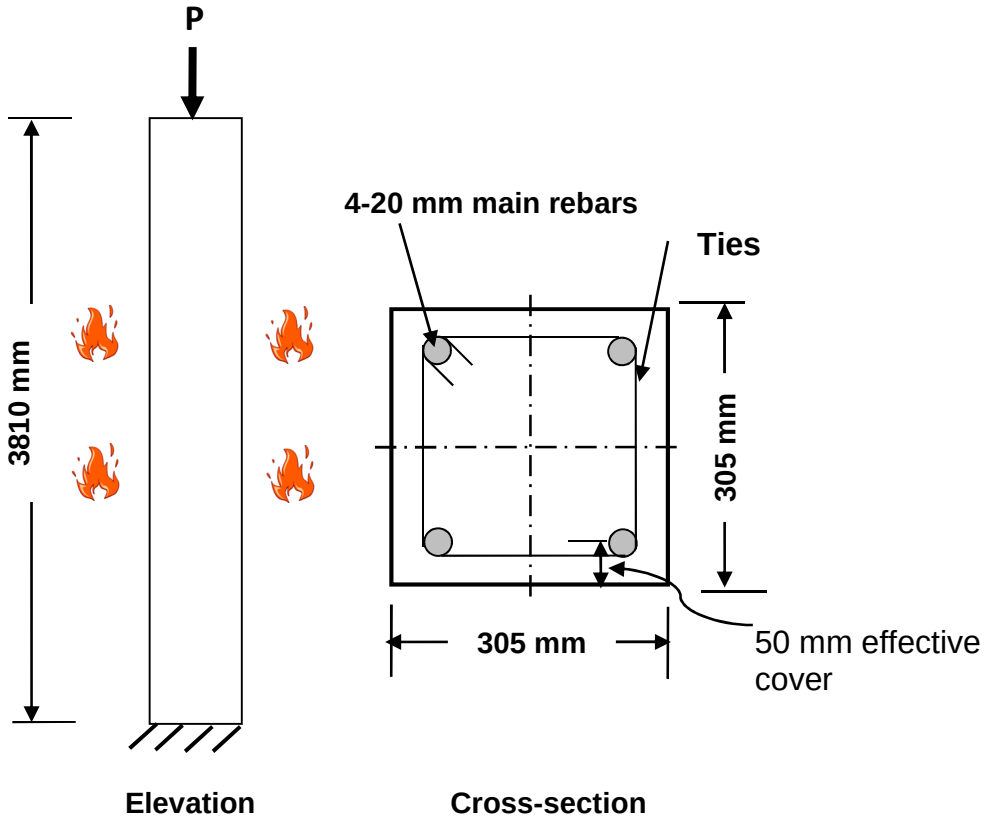

Figure 1.1 - Layout of columns used to show comparative response in NSC and HSC columns

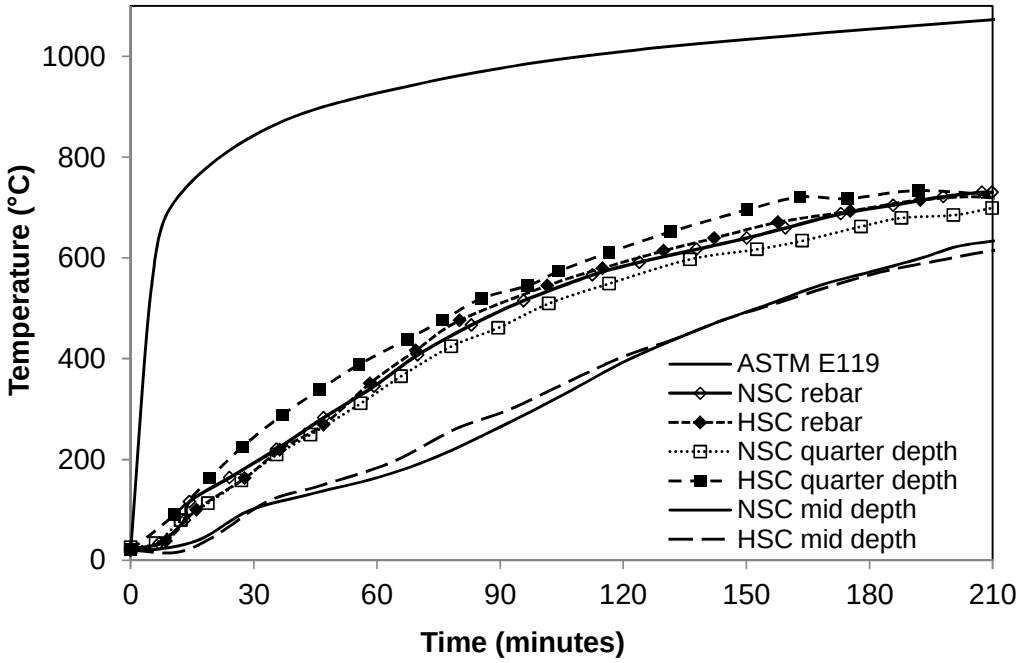

Figure 1.2 - Comparison of temperature distribution between NSC and HSC columns

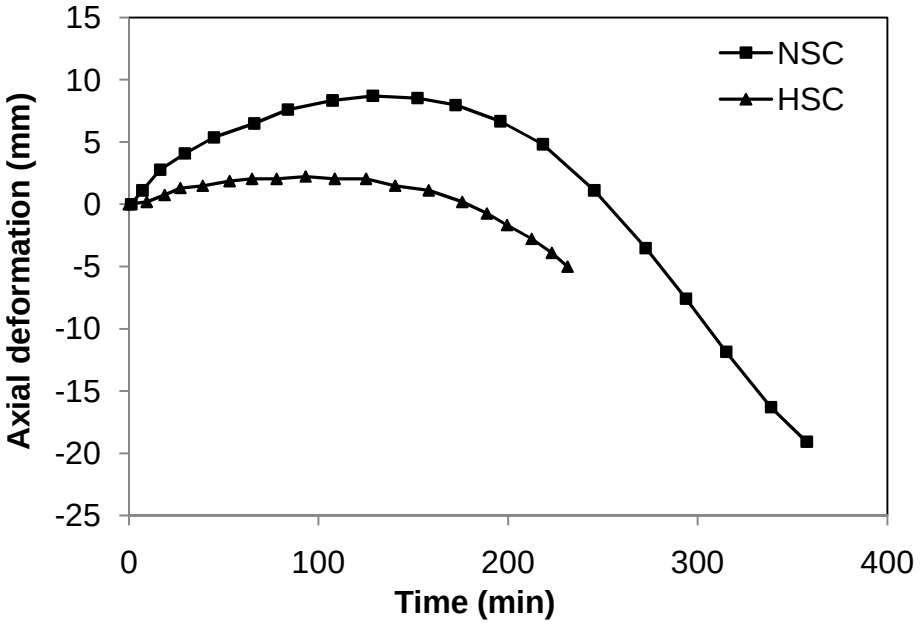

Figure 1.3 - Comparison of axial deformations between NSC and HSC columns

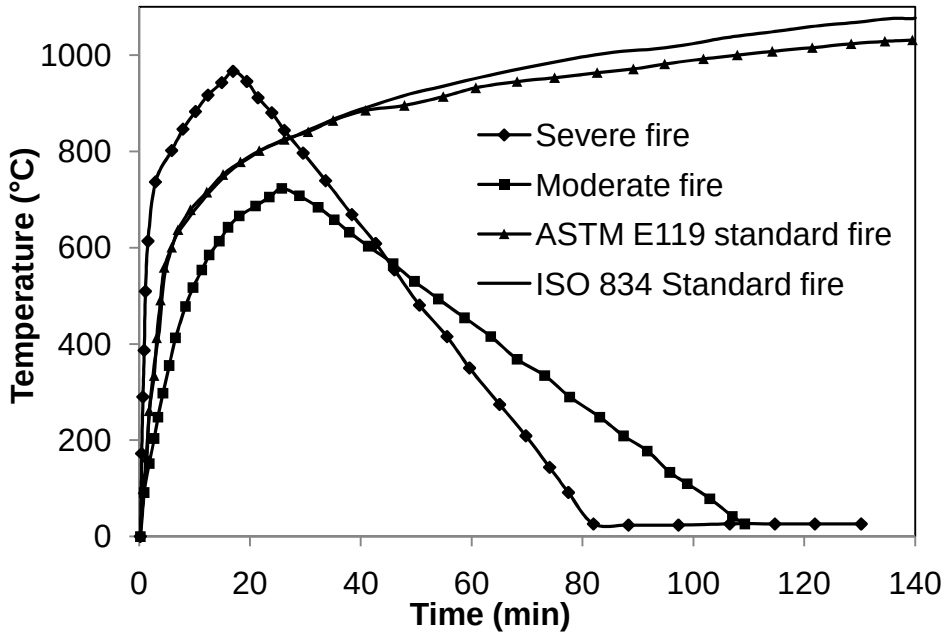

Figure 1.4 - Different fire scenarios encountered in practical fire situations

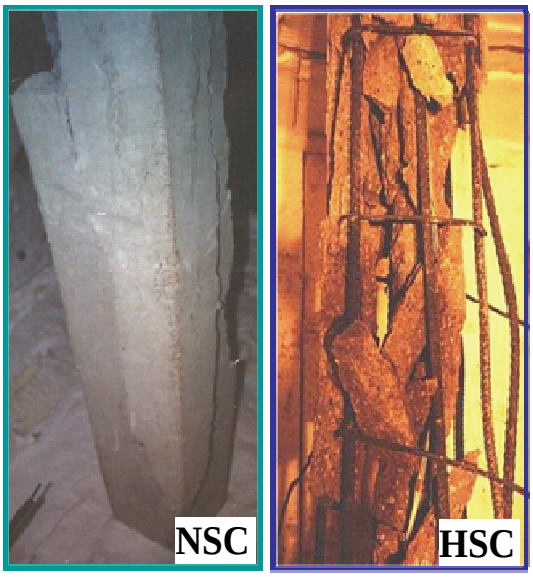

Figure 1.5 - Comparison of extent of fire induced spalling in NSC and HSC columns

(For interpretation of the references to color in this and all other figures, the reader is referred to the electronic version of this dissertation)

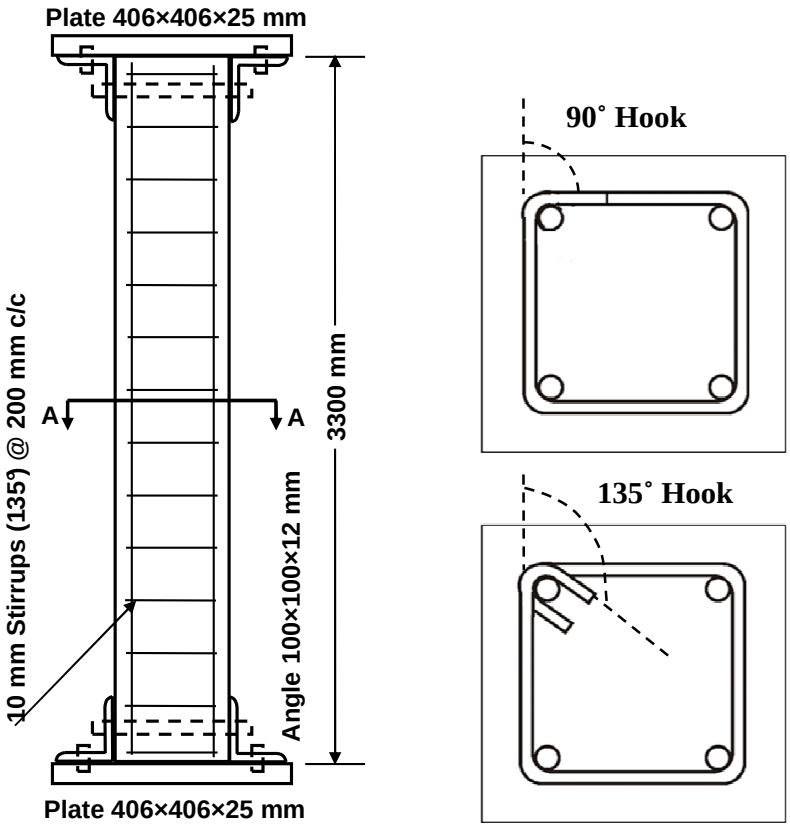

Figure 1.6 - Conventional and improved tie configuration in RC columns

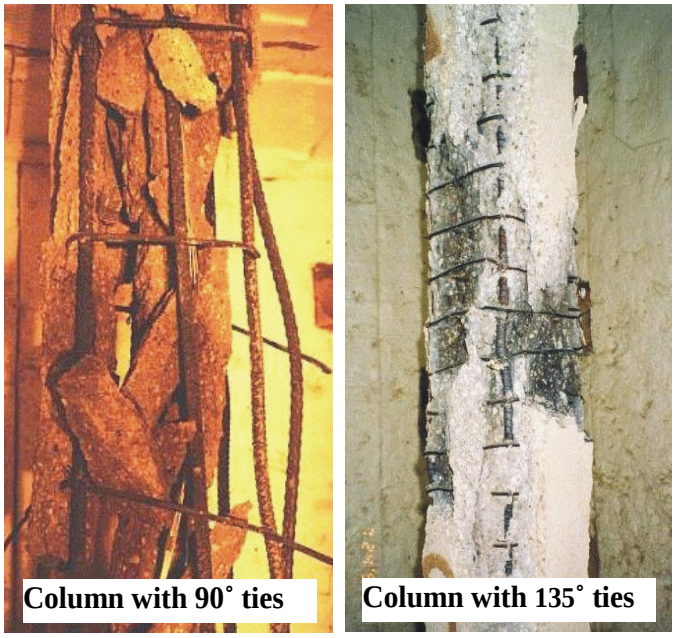

Figure 1.7 - Effect of ties on spalling in RC columns with 90° and 135° bent ties

CHAPTER 2

2 STATE-OF-THE-ART REVIEW

Part of this chapter is based on the following journal papers:

- Kodur, V., and Khaliq, W. (2011). "Effect of Temperature on Thermal Properties of Different Types of High Strength Concrete." Journal of Materials in Civil Engineering, ASCE, 23(6), 793-801.
- Khaliq, W., and Kodur, V. (2011). "High temperature properties of fiber reinforced high strength concrete." Innovations in Fire Design of Concrete Structures - ACI SP 279, 3-1-42.
- Khaliq, W., and Kodur, V. (2011). "Thermal and mechanical properties of fiber reinforced high performance self-consolidating concrete at elevated temperatures." Cement and Concrete Research, 41(11), 1112-1122.

2.1 General

Concrete generally exhibits good fire resistance properties and thus finds wide applications in buildings and other built infrastructure, where fire safety is one of the primary considerations. However, recent studies show that structural members made of new concrete types (HSC, SCC and FAC) known as HPC, may not have same level of fire resistance like conventional concrete (NSC) (Bamonte and Gambarova, 2010; Kodur, 2000; Tang and Lo, 2009). Typically, new types of HPC have lots of applications in columns of building because of the advantage of higher strength which is utilized to reduce size (cross-section) of columns. The fire resistance of concrete structural members is governed by high temperature thermal and mechanical properties

of constituent concrete. For predicting fire resistance of concrete structural members, knowledge of high temperature material properties is very critical which includes thermal, mechanical and deformation properties. In addition to that, fire induced spalling might significantly influence the fire resistance of HSC, therefore properties related to spalling are also important and should be known.

In this chapter previous studies related to the high temperature properties of concrete are reviewed. The phenomenon of fire induced spalling and methods for mitigating spalling are also presented. Moreover, previous experimental and numerical studies carried out to evaluate fire resistant of RC columns are also reviewed.

2.2 Thermal Properties of Concrete

2.2.1 General

For evaluating fire resistance of concrete structural members the temperature distribution within the member is to be established. This temperature distribution is dependent on high temperature thermal properties of concrete. The thermal properties that govern the temperature distribution are thermal conductivity and specific heat (or heat capacity). Other thermal properties that influence the fire behavior of RC structural members are thermal expansion and mass loss that have an effect on development of thermal stresses and specific heat respectively.

Thermal conductivity is defined as the ratio of rate of heat flow to temperature gradient, and represents the uniform flow of heat through concrete of unit thickness over a unit area subjected to a unit temperature difference between the two opposite faces. Concrete contains moisture in different forms and, type and amount of moisture has significant effect on thermal conductivity. Thermal conductivity is usually measured by means of 'steady state' or 'transient' test methods (Bažant and Kaplan, 1996). Transient methods are preferred to measure thermal conductivity of

moist concrete over steady-state methods (Shin et al., 2002), as physicochemical changes of concrete at higher temperatures cause intermittent direction of heat flow.

Specific heat is the amount of heat per unit mass, required to change the temperature of a material by one degree and is generally expressed in terms of thermal (heat) capacity which is the product of specific heat and density. Specific heat is highly influenced by moisture content, aggregate type, and density of concrete (Kodur and Sultan, 1998; Phan, 1996). Specific heat represents the energy absorbed by the concrete and accounts for sensible heat and latent heat involved during temperature change. Sensible heat ascribes to the heat involved in thermodynamic reaction during temperature change. Latent heat refers to the energy absorbed or released by the material during phase transition. The material absorbs considerable amount of energy during physiochemical changes and hence specific heat values are highly influenced by the phase transition in materials.

The coefficient of thermal expansion is defined as the percentage change in length of a specimen per degree temperature rise. Linear thermal expansion is the thermal strain resulting from increased temperature. Thermal expansion of concrete is generally influenced by cement type, water content, aggregate type, temperature and age (Lie, 1992). Thermal expansion of concrete is further complicated by other contributing factors such as additional volume changes caused by changes in moisture content, by chemical reactions (dehydration, change of composition), and by creep and micro-cracks resulting from non-uniform thermal stresses (Bažant and Kaplan, 1996). In some cases thermal shrinkage can also result from loss of water due to heating, along with thermal expansion, and this might lead to overall volume change to be negative, i.e. shrinkage rather than expansion.

Mass is a property that enables concrete to absorb and store significant amounts of heat. Mass loss can affect the enthalpy and amount of latent heat which directly affects all the thermal properties of concrete. Higher mass in concrete acts as heat sink, by absorbing and holding heat for longer time. This delays the heat transfer through material in an RC member, thus mass loss influences thermal properties of the concrete as well as strength and stiffness properties of RC members. Mass loss of conventional NSC and HSC has been investigated earlier with most of the information pertaining to NSC.

2.2.2 Test Methods for High Temperature Thermal Properties

There are many ways to measure the thermal conductivity of a given material and the results can vary depending on the test method used (Flynn, 1999). The general idea behind these testing techniques is to monitor the difference of temperature between two ends of the material specimen. Among various methods, hot wire method (ASTM C1113, 2009) and guarded heat flow meter method (ASTM E1530, 2011) are commonly used for measuring thermal conductivity of concrete. Hot wire method is used to measure the thermal conductivity of "refractories" such as insulating bricks, concrete and powder or fibrous materials. Because it is basically a transient radial flow technique, isotropic specimens are required. In guarded heat flow meter method a small sample of the material to be tested is held under a compressive load between two polished metal surfaces, each controlled at a different temperature. The lower surface is part of a calibrated heat flux transducer. As heat flows from the upper surface through the sample to the lower surface, an axial temperature gradient is established in the stack. By measuring the temperature difference across the sample along with the output from the heat flux transducer, thermal conductivity of the sample can be determined with known thickness. These

test methods for measuring thermal conductivity can also be applied for higher temperatures up to 850°C and above, but measuring at higher temperatures becomes cumbersome and costly.

Many techniques are available to measure the specific heat of concrete at room temperature; however, these methods can be used at elevated temperatures but they would become costly and time-consuming. Of these methods differential scanning calorimetry (DSC) is most common to measure specific heat of concrete (ASTM C1269, 2011). This technique is based on measuring the energy necessary to establish a nearly zero temperature difference between a substance and an inert reference material, as the two specimens are subjected to identical temperature regimes in an environment heated or cooled at a controlled rate. DSC hence can be used to establish the heat energy required to raise a certain amount of material to a certain temperature, which can lead to the determination of the specific heat of that material.

Among various techniques to measure linear thermal expansion, dilatometric technique and thermomechanical analysis technique (ASTM E831, 2006) are most common. Both these thermal expansion measurement techniques are similar where dimension change in specimens is measured as a function of temperature and percentage change is calculated. The mass loss with temperature is usually measured by means of thermogravimetric analyzer technique (ASTM E1868, 2010). A specimen of known mass is heated at a constant temperature while its mass is continuously measured as a function of time. At the end of a pre-determined time interval or temperature, the mass loss of the specimen is calculated as a percent of the original mass.

2.2.3 Previous Studies on Thermal Properties

There have been quite a few test programs for characterizing high temperature thermal properties of concrete. Harmathy (1970), Harmathy and Allen (1973), Lie and Kodur (1996), VanGeem et al. (1997), Shin et al. (2002) and Kodur and Sultan (2003) have evaluated the thermal properties

of NSC concrete. Based on the test data, empirical formulae for thermal properties of NSC have been developed (ASCE, 1992; Eurocode 2, 2004; Kodur and Sultan, 2003; Lie and Kodur, 1996). Some of the notable studies are reviewed here:

Harmathy and Allen (1973) studied the effect of temperature on thermal properties of NSC through thermogravimetry and dilatometry tests. In these tests the temperature of the specimen was raised form room temperature to 1000°C at a rate of 5°C/min and thermal properties namely, thermal conductivity, specific heat, thermal diffusivity, and mass loss were measured. It was concluded by the authors that heat flow in concrete at elevated temperatures cannot be accurately predicted unless latent heat effects associated with the process are properly considered. It was found that variation in apparent specific heat due to elevated temperatures was difficult to obtain and supplemental theoretical considerations were suggested. It was also concluded that the spalling of concrete in fire is not caused by the presence of quartz in the aggregate, but it is due to high moisture content in concrete.

Lie and Kodur (1996) measured high temperature thermal properties of steel fiber reinforced concrete in 0-1000°C range. These thermal properties comprised of thermal conductivity, specific heat, thermal expansion, and mass loss. They also proposed empirical relations for these properties as a function of temperature. It was concluded by the authors that thermal properties of steel fiber reinforced concrete are similar to conventional plain NSC. They proposed mathematical relations that can be used as input data in analytical models for fire resistance calculations of structural members.

Van Geem et al. (1997) experimentally investigated thermal properties of HSC at elevated temperatures. The HSC used in this study ranged from 69-138 MPa with water to cement ratio ranging from 0.26 to 0.32. Mineral admixtures such as silica fume and fly ash were also used in

the concrete mixes. They tested thermal conductivity, specific heat, thermal diffusivity and drying rates at 30, 150, and 370°C. They used different test methods to evaluate the thermal properties and found that these properties differed depending upon the test method used. Thermal conductivity using hot plate method, hot wire method and graduated hot plate apparatus was found to be similar and was within 1.7 to 2.6 W/m.K range. It was found that thermal conductivity of HSC decreases with increasing temperature. The specific heat values of HSC were also reported to be similar to those conventional NSC. Thermal diffusivity of HSC reduced with increasing temperature and was found to decrease significantly at 540°C and was attributed to increase rate of mass loss near this temperature. Mass loss of HSC was also found to be similar to that of NSC at elevated temperatures.

Shin el al. (2002) experimentally studied the thermal behavior of indigenous Korean concrete mixes (similar to US basaltic concrete) exposed to high temperature conditions. They tested density, thermal conductivity, thermal diffusivity and specific heat in 20-1100°C temperature range. It was found that most thermal properties except for specific heat decrease with increasing temperature. The thermal properties of concrete were found to be strongly temperature dependent. The density, thermal conductivity, and thermal diffusivity decrease with temperature, and particularly the conductivity and the diffusivity which have a 50% decrease at 900°C as compared to room temperature values. The specific heat was found to increase until 500°C, decrease in 700 to 900°C temperature range, and then increase again above 900°C. It was also concluded that the measurement beyond 1100°C is not accurate enough because the concrete decomposes to a liquid phase from a solid phase at that temperature.

Kodur and Sultan (2003) also carried out tests to measure thermal conductivity, specific heat, thermal expansion, and mass loss of plain HSC and steel fiber-reinforced HSC made of siliceous

and carbonate aggregate. Based on the measured property data, empirical relations were proposed for thermal properties as a function of temperature in the temperature range of 0 and 1000°C. It was concluded in this study that the type of aggregate has a significant influence on the thermal properties of HSC at elevated temperatures. The measured results showed that the presence of carbonate aggregate in HSC increases fire resistance. The authors also concluded that the thermal properties, at elevated temperatures, exhibited by steel fiber-reinforced HSC are similar to those of plain HSC.

Hu et al. (1993) investigated the thermal properties of construction materials commonly available in China. In this study mass loss was measured as a function of temperature up to 1000°C. It was found in this study that mass loss in carbonate aggregate concrete was only up to 97% for temperature up to 650°C, but mass loss was rapid in 650-900°C as it dropped to 75% in this range. It was reported that mass loss in siliceous aggregate concrete was not high and it dropped to only 97% at 1000°C.

Lie and Kodur (Lie and Kodur, 1996) investigated the mass loss of steel fiber reinforced conventional NSC made of siliceous and carbonate aggregates at elevated temperatures. Mass loss was measured using thermogravimetric analyzer in room temperature to 1000°C. It was found in this study that mass loss in concrete was small up to 600°C where only 3% mass was lost. However, mass was lost considerably up to about 30% of in 600-800°C in carbonate aggregate concrete, which was attributed to dissociation of dolomite in carbonate aggregate. However, in siliceous aggregate concrete on 3-4% of mass was lost in entire temperature range of 20-1000°C. It was also found that mass loss of concrete is not significantly affected by presence of steel fiber reinforcement in concrete in entire temperature range.

Kodur and Sultan (2003) measured the mass loss in plain and steel fiber reinforced HSC in temperature range of 0-1000°C. Mass loss was measured using thermogravimetric analyzer (TGA) up to 1000°C. The mass loss for both siliceous and carbonate concrete was very small until about 600°C, where it was about 3% of the original mass. Between 600 and 700°C, the mass of carbonate aggregate concrete dropped considerably with the temperature. Above 750°C, the mass loss again decreased slowly with temperature. The substantial mass loss and decrease in density for carbonate aggregate concrete was attributed to the dissociation of dolomite in the concrete.

2.2.4 Effect of Temperature on Thermal Properties of Concrete

The review of previous studies presented above is utilized to draw inferences on effect of temperature on thermal properties namely thermal conductivity, specific heat, thermal expansion and mass loss of concrete. The presented data shows that there is significant variation on test procedures, measurement techniques, range of measured temperatures and test results. Also it helped identify the drawbacks in state-of-the-art and availability of these properties for HPC.

2.2.4.1 Thermal Conductivity

Figure 2.1 illustrates variation of thermal conductivity of NSC as a function of temperature based on test data and empirical relations. The test data is compiled from different studies (Harada et al., 1972; Harmathy, 1970; Harmathy and Allen, 1973; Kodur and Sultan, 2003; Lie and Kodur, 1996; Shin et al., 2002) and standards (ASCE, 1992; Eurocode 2, 2004). It can be seen that there is large variation in available data in literature as shown by upper and lower bounds of the plotted. These variations in reported data can be attributed to different measurement techniques, test conditions, and environmental conditions adopted by various researchers (Bažant and Kaplan, 1996; Harada et al., 1972; Kodur et al., 2008; Phan, 1996). It should be noted that there

are very few standardized methods available for measuring thermal properties. On average, the thermal conductivity of conventional NSC, at room temperature, ranges between 1.4 and 3.6 W/m°C (Bažant and Kaplan, 1996). However, the thermal conductivity decreases graduallyS with temperature and this decrease is dependent on the concrete mix properties, specifically moisture content and permeability. It can be noted that as HPC are made of low w/c ratio and use of different binders, therefore thermal conductivity of FAC, SCC, and FRC will be different from that of NSC.

2.2.4.2 Specific Heat

Figure 2.2 illustrates the variation of specific heat for NSC with temperature as reported by test data and different standards. The data is compiled based on experimental data (Harmathy, 1970; Harmathy and Allen, 1973; Kodur and Sultan, 1998; Shin et al., 2002) and empirical relations given in different standards (ASCE, 1992; Eurocode 2, 2004). The variation in data is depicted by upper and lower bounds and this variation is mainly attributed to moisture content, type of aggregate, test conditions and measurement techniques used in experiments (Harmathy and Allen, 1973; Kodur and Sultan, 2003; Lie, 1992; Phan, 1996). The specific heat property is sensitive to various physical and chemical transformations that take place in concrete at elevated temperatures. This includes the vaporization of free water at about 100°C, the dissociation of $Ca(OH)_2$ into CaO and H_2O between 400-500°C and the quartz transformation of some aggregates above 600°C. Specific heat is therefore highly dependent to moisture content and considerably increases with higher w/c ratio.

2.2.4.3 Thermal Expansion

Figure 2.3 illustrates the variation of thermal expansion in conventional concrete with temperature (ASCE, 1992; Eurocode 2, 2004), where upper and lower bounds indicate the range of values reported by different researchers. The thermal expansion increases from zero at room temperature to about 1.3% at 700°C and then generally remains constant through 1000°C. Thermal expansion of concrete is complicated by other contributing factors such as additional volume changes caused by changes in moisture content, by chemical reactions (dehydration, change of composition), and by creep and micro-cracks resulting from non-uniform thermal stresses (Bazant and Kaplan 1996). In some cases thermal shrinkage can also result from loss of water due to heating, along with thermal expansion, and this might lead to overall volume change to be negative, i.e. shrinkage rather than expansion.

2.2.4.4 Mass Loss

Figure 2.4 illustrates the variation in mass of concrete as a function of temperature for concretes made with carbonate and siliceous aggregates. It can be seen that there is significant difference for mass loss in concretes made with two types of aggregates. In the case of siliceous aggregate concrete, the mass loss remained insignificant even above 600°C. The mass loss for steel fiber-reinforced HSC was found to be similar to plain HSC up to about 800°C. Above 800°C, in the case of the carbonate aggregate mix, the mass loss in steel fiber-reinforced HSC was slightly lower than that of plain HSC. Figure 2.5 shows variation in mass loss for conventional NSC and HSC at elevated temperatures. It is evident that significant variation exists between the mass loss of two types of concretes.

Mass loss of concrete at elevated temperatures is highly influenced with the type of aggregate (Kodur and Sultan, 1998; Lie and Kodur, 1996). The mass loss is minimal for both carbonate and

siliceous aggregate concretes up to about 600°C. However, in beyond 600°C, carbonate aggregate concrete experiences larger percentage of mass loss as compared to siliceous aggregate concrete. This higher percentage of mass loss in carbonate aggregate concrete is attributed to dissociation of dolomite in carbonate aggregate around 700°C (Kodur and Harmathy, 2008).

2.2.5 Summary

Thermal conductivity, specific heat, thermal expansion, and mass loss are important thermal properties which are desired for predicting the temperature profiles as well as spalling in concrete structures under fire exposure. As indicated by the review, there have been quite a few studies on NSC that show the influence of thermal properties on fire resistance of structural members. However, there is lack of data on these properties for new types of HPC (HSC, SCC and FAC). In order to predict the temperature rise in concrete members as well as fire induced forces, high temperature thermal properties specific to concrete type are to be determined which is one of the main objectives of this research.

2.3 Mechanical Properties

2.3.1 General

The mechanical properties that are of primary interest in fire resistance design are compressive strength, tensile strength, elastic modulus, and stress-strain response in compression. Mechanical properties of concrete at elevated temperatures have been studied extensively in literature in comparison to thermal properties. High temperature mechanical properties at small level are generally carried out on concrete specimens that are typically cylinders or cubes of different sizes. Unlike room temperature property measurements, where there are specified specimen sizes as per standards, the high temperature mechanical properties are usually carried out on a wide

range of specimen sizes due to lack of test standards for high temperature testing. The cylinder specimens of size 75x150, 100x200, and 150x300 mm whereas cube specimens of size 100x100, 150x150 and prism specimens of size 100x300 are usually used for high temperature.

The primary difference between HSC and NSC relates to the compressive strength that refers to the maximum resistance of a concrete sample to applied pressure. Although there is no precise point of separation between HSC and NSC, these days HSC is defined as concrete with a compressive strength greater than 70 MPa (Kodur et al., 2008).

Compressive strength of concrete depends upon water-cement ratio, aggregated-paste interface transition zone, curing conditions, aggregated type and size, admixture types and type of stress (Mehta and Monteiro, 2006). The tensile strength of concrete is much lower than compressive strength, due to ease with which cracks can propagate under tensile loads (Mindess et al., 2003). It is normal practice to neglect the tensile strength of concrete in strength calculations at room and elevated temperature. However, under fire conditions tensile strength of concrete can be crucial in cases where fire induced spalling occurs in a HSC structural member. Also tensile strength is an important property, because cracking in concrete is generally due to tensile stresses and the structural damage of the member in tension is often generated by progression in microcracking (Mindess et al., 2003).

Another property that influences fire resistance is the modulus of elasticity of concrete which decreases with temperature. At high temperature disintegration of hydrated cement products and breakage of bonds in microstructure of cement paste reduces elastic modulus and the extent of reduction depends on moisture loss, high temperature creep and type of aggregate.

The high temperature compressive stress-strain behavior of concrete is of significant importance in the fire resistance analysis of RC structural members. These high temperature stress-strain

curves are helpful to trace the structural response of RC structural members under fire conditions. The high temperature stress-strain response of concrete is dependent on factors such as aggregate-paste interface transition zone, curing conditions, aggregated type and size. The aggregate type has a significant effect on the ultimate strain attained in HSC exposed to elevated temperatures; carbonate aggregate HSC attains higher peak strains as compared to siliceous aggregate HSC (Cheng et al., 2004).

2.3.2 Testing Methods for High Temperature Mechanical Properties

Three steady-state test methods (conditions) are utilized to determine high temperature strength properties namely, stressed, unstressed and residual test methods (Fu et al., 2004; Phan, 1996). Figure 2.6 illustrates the general arrangements for heating and loading to measure high temperature mechanical properties. Figures 2.7, 2.8 and 2.9 graphically illustrate the main difference in three test methods to evaluate the high temperature mechanical properties of concrete. In the case of stressed test method, specimens are preloaded to a certain load usually 30-60% of room temperature ultimate compressive strength of concrete. Specimens are then exposed to the desired temperature and further loaded to failure.

In unstressed test method, specimens are heated to target temperature without and preload. Once equilibrium conditions are met, and the target temperature is reached, the specimens are subjected to loading (leading to failure). In the case of residual test method, test specimen is heated to a target temperature till reaching steady-state, and then allowed to cool down to room temperature. Specimen is then loaded to failure at ambient temperature to obtain the residual strength of concrete. Residual strength, representative of post fire exposure behavior of concrete, is less applicable for predicting high temperature mechanical properties of concrete.

2.3.3 Previous Studies

There have been significant test programs for characterizing high temperature mechanical properties of concrete. In the high temperature property tests, the response is measured while specimens are hot at a target temperature. Such high temperature tests (both stressed and unstressed) were carried out by limited researchers to measure the mechanical response (Castillo and Durrani, 1990; Khoury, 1992 ; Khoury, 2008; Khoury et al., 1985; Lie, 1992; Lie and Kodur, 1996). However, research on high temperature properties was mostly done through residual property tests after exposure to high temperatures (Chen and Liu, 2004; Felicetti and Gambarova, 1998; Felicetti et al., 1996; Fu et al., 2005; Fu et al., 2004; Li et al., 2004; Li and Guo, 1993; Xiao and König, 2004). Some of the notable studies on high temperature mechanical properties are presented in the following section.

2.3.3.1 Compressive Strength

Compressive strength of concrete is influenced by water-cement ratio, aggregate-paste interface transition zone, curing conditions, aggregate type and size, admixture types and type of stress (Mehta and Monteiro, 2006). Good amount of data is available on compressive strength of concrete at elevated temperatures for both NSC and HSC (Castillo and Durrani, 1990; Fu et al., 2005; Poon et al., 2001; Tang and Lo, 2009; Xu et al., 2001). Few of the notable studies presented here generate information on high temperature compressive strength of concrete.

Carette et al. (1982) did an important study on use of pozzolans in NSC at elevated temperatures. They reported that addition of fly ash and slag in NSC did not improve the residual compressive strength of concrete after exposure to high temperatures. Even change in water-cement ratio of NSC with these pozzolans did not show any effect on high temperature mechanical properties behavior of concrete.

Lie and Kodur (1996) investigated high temperature strength properties of NSC with and without steel fibers. They reported that compressive strength steel fiber reinforced concrete degrades at a much higher rate with temperature than similar concrete without steel fibers. They also concluded that effect of aggregate type on the compressive strength is not significant.

Chan et al. (1999) investigated the residual compressive strength of both NSC and HSC after exposure to high temperatures. He identified three distinct temperature ranges having an effect on loss of compressive strength of concrete namely, 20-400°C, 400-800°C, and 800-1200°C. He reported that only small part of strength was lost in 20-400°C (1-10% for HSC and 15% for NSC), however severe loss occurred in 400-800°C range. This severe loss in 400-800°C range was attributed to deterioration of calcium silicate hydrate (C-S-H) gel and cementing ability due to dehydration in concrete. They suggested the temperature range of 400-800°C be regarded as critical strength-loss range for concrete. Above 800°C the residual strength was reported as only a small part of original strength.

Li et al. (2004) experimentally studied the residual mechanical properties of NSC and HSC at elevated temperatures. They investigated the influence of temperature, water content, specimen size, strength grade and temperature profiles on mechanical properties. Authors reported that the compressive strength of HSC drops with temperature after 200°C. The strength loss in HSC was higher (36.8%) in 20-400°C as compared to NSC (28.8%), and this higher loss was attributed to dense microstructure and impermeability of HSC. It was also reported that water content had minimum effect on high temperature strength loss of concrete. As for specimen size, it was concluded that compressive strength loss of larger concrete specimens was lower than that in smaller size specimens.

Noumowé (2005) investigated the behavior of high temperature mechanical properties of plain HSC and polypropylene fiber reinforced HSC up to 200°C. He reported that the HSC containing polypropylene fibers has higher compressive strength loss as compared to plain HSC.

Sideris (2007) investigated the compressive strength characteristics of SCC exposed to elevated temperatures up to 700°C. For comparison, he also tested and compared the results with conventional concretes. Residual strength properties were tested after exposure to 100, 200, 500, and 700°C. He reported that the residual strength loss trend of both SCC and conventional concretes was similar in 20-700°C. Both SCC and HSC suffered explosive spalling at temperatures beyond 380°C.

Kim et al. (2009) recently investigated the compressive strength characteristics of HSC exposed to elevated temperatures up to 700°C through stressed test method. During heating, the specimens were subjected to a pre-load of 25% of the ultimate compressive strength at room temperature, and then loaded to failure at target temperature. It was concluded by the researchers that with increase in strength of concrete, the loss of strength due to high temperature exposure also increase. It was also concluded from this research that HSC loses minimum strength in 100-400°C temperature but the rate of strength loss is significant beyond 400°C.

The review of compressive strength properties above shows that good amount of research has taken place for high temperature behavior of both NSC and HSC. However, it can be observed that the strength trends for both NSC and HSC are not consistent and there are significant variations in strength loss, as reported by various authors. Moreover, there is very limited data in literature on high temperature strength properties of new types of concrete such as SCC, FAC and fiber reinforced HPC. Therefore data on strength properties of new types of concretes as a

function of temperature is needed for evaluating fire response of structural members made of HPC.

2.3.3.2 Tensile Strength

Tensile strength of concrete at ambient temperatures can be evaluated through three methods namely, flexural tensile, direct tension, and splitting tensile strength tests. Flexure tensile strength is obtained through subjecting a concrete beam to third-point flexural loading (ASTM C78, 2009). The direct tensile strength is measured by testing cylinder or prism specimens by applying axial tensile load in a suitable test machine until specimen breaks in direct tension (ASTM C1583, 2004). Direct tension test is less reliable as the specimen holding devices (grips) introduce secondary stresses leading to unreliable strength data. In splitting tensile test a compressive load is applied on the generatrices of the specimen which are diametrically opposite (ASTM C496, 2004). The load is increased until failure occurs by splitting of the specimen along the vertical diameter. At ambient temperature, splitting tensile strength is usually 50-70% greater than direct tension strength, where as it is 40-50% lower than flexure tensile strength (Popovics, 1998).

Tensile strength of concrete is dependent on compressive strength of concrete, water/cement ratio, aggregate-paste interface transition zone, presence of any flaws, and microstructure of concrete (Neville, 2004). A review of the literature indicates that there have been limited studies on high temperature tensile strength of concrete. It is also worth noting that all previous studies on high temperature tensile strength of concrete are based on residual strength tests that are applicable for concrete members cooled after fire exposure. This residual tensile strength property cannot represent the tensile strength behavior of hot concrete (during fire exposure)

which is required for predicting spalling. Some of the notable studies presented here generate information on high temperature tensile strength behavior of concrete.

Carette et al. (1982) investigated the temperature effect on the tensile strength of NSC. He tested concrete cylinders in 75-600°C temperature range through residual strength technique. He reported 65-70% reduction in splitting tensile strength at 600°C. He concluded that water cement ratio and type of aggregate has significant influence on the splitting tensile strength of NSC.

Felicetti et al. (1996) investigated the residual tensile strength of two types of HSC from room temperature to 600°C by testing through direct tension method. They noticed reduction in tensile strength to zero at about 600°C. It was also observed in this study that concrete softens at high temperature and that temperature has a marked effect on its tensile strength.

Recently, Bahnood and Ghandehari (2009) reported residual splitting tensile strength of plain and polypropylene fiber reinforced HSC up to 600°C. The authors inferred that the decrease in splitting tensile strength is due to decomposition of hydrated cement products and thermal incompatibility between aggregates and cement paste. They also observed that there was no noticeable difference in the splitting tensile strength of polypropylene fiber reinforced HSC up to 600°C in comparison to plain HSC.

Li et al. (2004) conducted tests for residual splitting tensile strength of HSC in 200-1000°C temperature range. HSC batch mix contained 27 per cent fly ash as cement replacement. 100 mm concrete cubes were used to measure splitting tensile for HSC at 200, 400, 800 and 1000°C temperatures. A retained splitting tensile strength of 51.9% at 800°C and 16.9% at 1000°C was reported which is significant at these temperatures. Appearance and propagation of cracks was observed to be more obvious in tensile strength as compared to compressive strength tests.

Reduction in splitting tensile strength with temperature was attributed to thermal stresses induced in dense microstructure of HSC that resulted in micro and macro cracks.

Chen and Liu (2004) experimentally studied the residual splitting tensile strength of HSC and hybrid fiber reinforced concrete at various temperatures in 20-800°C ranges. The authors found that higher residual splitting tensile strength was obtained by hybrid fiber reinforced HSC. Steel fibers in concrete were observed to provide restriction against initiation and expansion of cracking, while polypropylene fibers provided micro-channels resulting in reduction of thermal stresses.

Anagnostopoulos et al. (2009) investigated the residual splitting tensile strength properties of SCC with different fillers at 20, 300, and 600°C temperatures respectively. Sharp loss in tensile strength was observed and was attributed to micro and macro cracks produced in specimens due to thermal incompatibility. SCC with limestone filler was reported to have displayed better performance at high temperature by preserving splitting tensile strength. In this study, explosive spalling was also reported in high strength SCC at 600°C temperature.

Eurocode (2004) fire provisions recommend accounting for tensile strength properties of concrete in fire resistance calculations. It treats both NSC and HSC alike for temperature dependent tensile strength of concrete by provision of a simple relationship for representation of tensile strength of concrete with temperature. On the other hand ACI 216.1 (2007) does not provide any guideline or relationship for tensile strength of concretes.

2.3.3.3 Elastic Modulus

Another property that influences fire response of concrete structures is the elastic modulus of concrete which decreases with temperature. Elastic modulus of concrete degrades with

temperature and thus influences the fire resistance of structural members. At high temperature, disintegration of hydrated cement products and breakage of bonds in microstructure of cement paste reduces the elastic modulus and the extent of reduction depends on moisture loss, high temperature creep and type of aggregate (Bažant and Kaplan, 1996).

Some of the prominent studies undertaken on high temperature elastic modulus are discussed below:

Castillo and Durrani (1990) experimentally studied the effect of temperature on elastic modulus of both NSC and HSC in 20-800°C temperature range. Modulus was measured using closed-loop servo-controlled hydraulic testing machine integrated with an electric furnace. The authors reported that both NSC and HSC have similar loss of modulus under elevated temperature. Slight loss was recorded up to 400°C and faster loss was observed between 400-600°C. The higher loss above 400°C was attributed to progressive dehydration and loss of bond between materials.

Bamonte and Gambarova (2010) tested HSC and SCC cylinders up to 90 MPa for elastic modulus at 20, 200, 400, and 600°C. They reported that the elastic modulus is much lower in hot state than residual which was attributed to thermal affects. It was also concluded that there is no difference in the elastic modulus of HSC and SCC.

Perrson (2004) did extensive experimental investigation on the elastic modulus of SCC at elevated temperatures and as residual property. Tested temperatures consisted of 20, 200, 400, 600 and 800°C. He observed a lower elastic modulus for SCC, as compared to HSC, throughout the temperature range in both hot state and as residual property.

2.3.3.4 Stress-Strain Curves

Limited information is available on the compressive stress-strain curves of HSC exposed to elevated temperatures. The main reason for limited data is the complexity involved to generate

high temperature stress-strain curves through stressed or unstressed test methods. However, researchers have carried out investigation on stress-strain curves of concrete under all three test conditions (stressed, unstressed and residual) to study the effect of elevated temperatures on stress-strain behavior. Some of the previous studies are discussed here to generate information on high temperature stress-strain response of concrete:

Castillo and Durrani (1990) studied the effect of transient high temperature on stress-strain response of HSC and NSC under both stressed and unstressed test conditions in 23-800°C range. It was found in this study that effect of temperature on stress-strain curves is same for HSC and NSC in entire temperature range. For both NSC and HSC the strain at peak stress did not significantly vary in 100-200°C range. There was a slight increase in strain at peak stress in 300-400°C range. However, there was a significant increase in strain at peak stress in 500-800°C range. At 800°C the recorded strain was measured to be four times to the strain at room temperature.

Furumura et al. (1995) tested cylinders to generate stress-strain curves for NSC and HSC, during heating and after heating. The test data indicated that the stress-strain curves for HSC are quite different from NSC. For HSC stress-strain curves showed brittle response below 500°C. However the stress-strain curves above 500°C showed more ductile response, and it was attributed to internal microcracks developed due to thermal stresses caused by contraction of cement paste, expansion of aggregates and thermal gradients. For both NSC and HSC the strains at maximum strength during heating and after heating increased rapidly with increasing temperature above 300-400°C temperature. It was concluded in this study that concrete strength has only a little effect on the strain at maximum strength.

Felicetti et al. (Felicetti et al., 1996) studied residual mechanical properties, including stress-strain curves, for HSC after heating to 105, 250, 400 and 500°C temperatures. It was shown by stress-strain curves that there was significant decrease in the peak stress after exposure to high temperature. The peak stress decreased by 2.5% at 105°C, 25% at 250°C, 75% at 400°C, and 94% at 500°C. Above 500°C, residual strength was so small (10%) that HSC was considered to be unsuitable for bearing any loads.

2.3.4 Effect of Temperature on Mechanical Properties of Concrete

The review of previous studies presented above is utilized to draw inferences on effect of temperature on mechanical properties. The presented data shows that there is significant variation in reported mechanical properties which is attributed to test procedures and test techniques. Presented state-of-the-art also indicated that there is lack of high temperature propertied data on HPC.

2.3.4.1 Compressive Strength

Figure 2.10 and 2.11 illustrate the variation of compressive strength ratio of NSC and HSC concrete at elevated temperatures respectively with upper and lower bounds showing limit of variation in reported data.

In the case of NSC, the compressive strength of concrete is marginally affected by elevated temperatures up to 400°C. NSC is usually highly permeable and allows easy diffusion of pore pressure as a result of water vapors. This shows that NSC is most suited for concrete infrastructure exposed to fire hazards. On the other hand, use of different binders in HPC produce a superior and dense microstructure with less amount of calcium hydroxide which ensures a beneficial effect on compressive strength. Binders such as use of slag and silica fume gives best results to improve compressive strength which is attributed to dense microstructure.

However, as mentioned earlier, the compact microstructure is highly impermeable and under high temperature becomes detrimental as it does not allow moisture to escape resulting in buildup of pore pressure and rapid development of microcracks in HSC leading to its deterioration and spalling.

2.3.4.2 Tensile Strength

Figure 2.12 illustrates the variation of splitting tensile strength ratio of NSC and HSC as a function of temperature as reported in previous studies and recommended by Eurocode standard (Behnood and Ghandehari, 2009; Carette et al., 1982; Eurocode 2, 2004; Felicetti et al., 1996). The ratio of tensile strength at given temperature, to that at room temperature is plotted. The upper and lower bounds shown in Figure 2.12 shows range of variation in splitting tensile strength obtained by various researchers for NSC with conventional aggregates. The decrease in tensile strength of NSC with temperature can be attributed to weak microstructure of NSC allowing initial microcracks. At 300°C concrete loses about 20% of its initial tensile strength. Above 300°C temperature, the tensile strength in NSC drops at a faster rate. This is due to more pronounced thermal damage in the form of microcracks.

2.3.4.3 Elastic Modulus

Figure 2.13 illustrates variation of ratio of elastic modulus at target temperature (E_T) to that at room temperature (E_0) for HSC (Castillo and Durrani, 1990; Phan, 1996). It can be seen from the figure that the trend of loss of elastic modulus of both concretes with temperature is similar, but there is significant variation in the reported data. Figure 2.13 also illustrates the ratio of elastic modulus for SCC as reported in two studies (Bamonte and Gambarova, 2010; Persson, 2004). It can be observed that loss of elastic modulus in SCC is similar to HSC. This lower modulus in

both HSC and SCC can be attributed to the excessive thermal stresses and physical and chemical changes in concrete microstructure.

2.3.4.4 Stress-Strain Curves

Figure 2.14 and 2.15 illustrate the load-deformation response of NSC and HSC respectively (Castillo and Durrani, 1990). In general, it is established that HSC has steeper and more linear stress-strain curves in comparison to NSC in 20-800°C. High temperature has significant effect on the stress-strain response of both NSC and HSC, as with the rise in temperature, the strain at peak stress starts to increase, especially above 500°C this increase is significant and the strain at peak stress can reach four times to strain at room temperature. HSC specimens exhibit brittle response as indicated by post peak behavior of stress-strain curves shown in Figure 2.15.

2.3.5 Summary

Compressive strength, tensile strength, elastic modulus and stress-strain curves are central mechanical properties that are required for predicting fire performance of RC structural members. The above review illustrates that good amount of data exists for high temperature mechanical properties for NSC and also limited data exists on HSC. But this data is not available for HPC such as FAC and SCC with and without fibers. This data is desirable especially for high temperature tensile strength, elastic modulus and stress-strain curves for these HPC. Thus one of the major objectives of this research is to evaluate high temperature mechanical properties for these new types of concrete. The generated test data can be used to develop mathematical relations for various properties as a function of temperature.

2.4 Deformation Properties

2.4.1 General

Deformation properties of concrete include creep and transient strains and are mainly influenced by strength, aggregate type, sustained stress and chemical and physical reactions that take place in concrete under fire conditions (Schneider, 1988). Creep is defined as the time-dependent plastic strain under constant stress and temperature. At room temperature sustained external stress becomes the driving force for the movement of the physically absorbed water and water held in small capillaries (Mehta and Monteiro, 2006). Due to limited moisture movement in concrete at room temperature, creep deformations are slow to occur. However, at elevated temperatures, moisture movement is usually significant in concrete that leads to higher creep strains. High temperature creep strains are thus largely influenced by concrete temperature (Dwaikat, 2009). Because high temperature creep affects strains, deflections, and stress redistribution at elevated temperatures, it plays an important role on the fire resistance of structural members.

Transient strain on the other hand occurs during the first time heating of concrete, but it does not occur upon repeated heating (Khoury et al., 1985). Transient strain is independent of time and is essentially caused by the thermal incompatibilities between the aggregate and the cement paste (Purkiss, 2007). Exposure of concrete to high temperature induces complex changes in the moisture content and chemical composition of the cement paste. Moreover there exists a mismatch in thermal expansion between the cement paste and the aggregate. Therefore factors such as changes in chemical composition of concrete and mismatches in thermal expansion lead to internal stresses and micro-cracking in the concrete constituents (aggregate and cement paste) and results in transient strain in the concrete (Schneider, 1988).

2.4.2 Previous Studies

Literature review shows that there is very limited information on creep and transient strain of concrete at elevated temperature (Kodur et al., 2008). Anderberg and Thelandersson (1976) carried out tests to evaluate transient and creep strains under elevated temperatures. Figure 2.16 shows influence of initial moisture content on deformations under transient conditions. They found that pre-dried specimens at 45 and 67.5% of load level were less liable to deformation in 'positive direction' (expansion) under load. At 22.5% pre-load, specimen displayed no significant difference for strains. They also found that the influence of water saturation was not very significant except for free thermal expansion (0% preload), which was found to be smaller for water saturated specimens.

Khoury (1985) studied creep strain of initially moist concretes at four load levels measured during first heating at 1°C/min as shown in Figure 2.17. An important feature of these results was that considerable contraction under load was observed as compared to free (unloaded) thermal strains. This contraction is referred to as the 'load-induced thermal strain' and the actual thermal strain is considered to consist of total thermal strain minus the load-induced thermal strain.

Schneider (1988) also investigated the effect of transient and creep restraint on deformation of concrete. He concluded that the transient test for measuring total deformation or restraint of concrete have the strongest relation to building fires and are supposed to give most realistic data with direct relevance to fire. The important conclusions from the study were (1) w/c ratio and original strength are of little importance on creep deformations under transient conditions. (2) Aggregate cement ratio has a great influence on the strains and critical temperatures, the harder the aggregate the lower the thermal expansion therefore total deformation in transient state will

be lower. (3) Curing conditions are of great importance in 20-300°C range. Air cured and oven-dried specimens have lower transient and creep strains than water cured specimens.

Anderberg and Thelandersson (1976) developed constitutive models for creep and transient strain in concrete at elevated temperatures. These equations for creep and transient strain at elevated temperatures as suggested by Anderberg and Thelandersson are:

$$\varepsilon_{cr} = \beta_1 \frac{\sigma}{f_{c,T}} \sqrt{t}\, e^{d\left(T-293\right)} \tag{2.1}$$

$$\varepsilon_{tr} = k_2 \frac{\sigma}{f_{c,20}} \varepsilon_{th} \tag{2.2}$$

where: ε_{cr} = creep strain, ε_{tr} = transient strain, β_1 = 6.28×10^{-6} $s^{-0.5}$, d = 2.658×10^{-3} K^{-1}, T = concrete temperature (°K) at time t (s), $f_{c,T}$ = concrete strength at temperature T, and σ = stress in the concrete at the current temperature, k_2 = a constant ranges between 1.8 and 2.35, ε_{th} = thermal strain, and $f_{c,20}$ = concrete strength at room temperature.

2.4.3 Effect of Temperature on Deformation Properties

Time dependent deformations in concrete such as creep, get highly enhanced at elevated temperatures under compressive strains (Bažant and Kaplan, 1996). Creep in concrete under high temperatures increases due to moisture movement out of concrete matrix. This phenomenon is further intensified by moisture dispersion and loss of bond in cement gel (C-S-H). Therefore the process of creep is caused and accelerated mainly by two processes, (1) moisture movement and dehydration of concrete due to high temperatures and (2) acceleration of the process of bond breaking.

2.4.4 Summary

High temperature creep and transient strain of concrete are complex phenomenon and are influenced by factors such as temperature, strength, moisture content, loading, and mix proportions. The creep deformation generally increases with temperature, with low-modulus aggregates (Schneider, 1988) and also with increasing load levels at elevated temperatures. Transient strain is independent of time and does not recur as it is encountered only in first heating of concrete.

2.5 Fire Induced Spalling

Spalling occurs when concrete member is exposed to rapidly rising temperatures as encountered in a fire and is one of the major concerns with HSC. Low permeability and dense microstructure in HSC prevent easy dissipation of pore pressure that is generated due to moisture converting to vapors under elevated temperatures leading to buildup of high pore pressure. When this pore pressure exceeds the tensile strength of concrete, which also degrades temperature, spalling occurs. Previous studies have shown that spalling in HSC is affected by concrete strength, permeability, concrete density, moisture content, fire intensity, presence of fibers and specimen dimensions (Ali, 2002; Kodur and McGrath, 2003; Kodur and Sultan, 1998; Phan, 1996).

2.5.1 Causes of Spalling

A review of literature presents a conflicting data on the probability of occurrence of fire induced spalling and also on the exact mechanism for spalling. While some investigators reported explosive spalling in concrete structural members under fire conditions, few others reported little or no significant spalling at all. One explanation to this conflicting trend of observations is possibly the large number of factors and their inter-dependency that influence the fire induced

spalling in concrete. However, it has been established and agreed upon by most researchers that the major causes for fire induced spalling in concrete are low permeability of concrete and high moisture migration at elevated temperatures.

There are two general theories on which the spalling phenomenon can be explained (Kodur, 2003):

2.5.1.1 Pore pressure build-up

High strength concrete has low permeability as compared to NSC (Mindess et al., 2003) and therefore this low permeability is believed to be more detrimental in pore pressure built-up. The extremely high vapor pressure, generated during moisture converting to vapor under fire exposure, cannot escape due to the low permeability of HSC. This build-up of pore pressure is believed to be the major cause of spalling during heating. As the pore pressure builds up with temperature, tensile strength of concrete offers resistance against pore pressure which is degrading with temperature as shown in Figure 2.18. When the pore pressure exceeds the tensile strength of concrete, pieces/fragments of concrete break away from the structural member (Figure 2.18) and thus spalling occurs. This breaking off can often is explosive depending on the fire and concrete characteristics (Harmathy, 1993).

2.5.1.2 Brittle Fracture

Bažant (1997) presented a different hypotheses for fire induced spalling. According to him, high pore pressure develops at a certain distance inside heated surface of concrete and creates a crack as shown in Figure 2.19. However, as the crack starts to open up, the water vapor and liquid flow into the crack and increase in volume. Once no additional water is available to fill into the crack from surrounding concrete, the pore pressure drops while crack starts to open up and spalling

occurs. This shows that pore pressure plays a secondary role to trigger a crack but does not cause the explosion or cause the crack to open widely. Therefore, the spalling is assumed to be caused by another source of energy, which is basically present in the form of potential energy from thermal stresses. This hypothesis is consistent with high magnitude of pore pressure and spalling in wet concretes, and less spalling observation in pre-dried concrete specimens.

2.5.2 Previous Studies

A number of experimental studies have been performed to investigate fire induced spalling in high strength concrete specimens which include both large scale structural members and small scale laboratory specimens such as cubes and cylinders. Kalifa (2001), Hertz (2003), and Phan (2007) have conducted some noteworthy studies on small scale specimens. Kodur (2003), Kodur and McGrath (2003), and Bilodeau et al. (2004) have conducted studies on large scale specimens. It has been well established through all these experimental studies that HSC is more susceptible to fire induced spalling compared to NSC.

Kalifa et al. (2001) investigated 120-mm thick RC slabs by exposing them to rapid heating from one side (underneath) to study fire induced spalling in HSC concrete. Two types of HSC mix with and without polypropylene fibers were considered. A heating rate of 5°C/sec was used for the first two minutes and then the temperature was kept at 600°C. Within the depth of slab, pore pressure and temperatures were measured at different locations. It was concluded from the study that polypropylene fibers significantly facilitate the increase in permeability of HSC and thus decrease the pore pressure at elevated temperature. As a results fire induced spalling is mitigated due to lower pore pressure in concrete.

Hertz (2003) conducted tests on concrete prisms to investigate the influence of thermal stresses on fire induced spalling in dense concrete. Ten 600x600x20 mm prisms of dense concrete were

heated at a limited area of 200x200 mm at the center of one side of each specimen. These specimens were exposed to constant high temperature from a hole in an oven. He concluded that susceptibility of concrete to spall is less if it does not have pozzolans like silica fume and that if moisture content is below 3%. He also concluded that spalling mostly occurs at about 374°C which is the critical temperature of water when water becomes vapor. He also found that polypropylene fibers were effective in mitigating spalling in less permeable concrete.

Kodur (2003) investigated the fire resistance RC columns by conducting full-scale fire tests. The parameters that were investigated in this study were concrete strength, column dimensions, type of aggregate, tie configuration, use of fibers and their type, and load intensity. The columns were of 3810 mm long and were of square cross-section 305x305 mm. The compressive strength of NSC was 34 MPa and that of HSC was 110 MPa. It was concluded that HSC columns have lower fire endurance and are susceptible to spalling as compared to NSC columns. This study (Kodur, 2003) also showed that type of aggregate, concrete strength, concrete density, load intensity, fire intensity and tie configuration have an influence on the fire performance (both spalling and fire endurance) of HSC columns.

In another study, Kodur and McGrath (2003) experimentally investigated the fire endurance of HSC by testing six columns designated as HSC1 to HSC6. The main factors varied in the test included cross-sectional size, quantity of longitudinal reinforcement, tie configuration, and aggregate type. This study also established that HSC was more prone to fire induced spalling than NSC. It was also concluded that carbonate aggregate concrete experiences less fire induced spalling than siliceous aggregate HSC. HSC columns exhibited better fire endurance by closer tie spacing and better detailing. Once ties were bent 135° back into the core of the column and

amount of lateral reinforcement was increased, it also reduced the potential for fire induced spalling in HSC columns.

From these experimental studies it is clear that spalling of concrete is a very complex phenomenon that depends on many factors, namely strength, moisture content, density, heating rate, and specimen size. Strength of concrete is one of the primary causes as HSC is more susceptible to spalling, similarly higher moisture content in concrete also increases the potential of spalling. Concrete density is another factor that influences spalling as lightweight aggregate concrete is more susceptible to spalling. Heating rate also effects the fire induced spalling as higher heating rate increases the occurrence of fire induced spalling in concrete. An increase in specimen size also increases the risk of explosive. Type of aggregate can reduce the occurrence of spalling e.g. use of carbonate aggregate concrete is effective in minimizing the fire induced spalling in concrete than siliceous aggregate.

2.5.3 Spalling Mitigation

To minimize the occurrence of fire induced spalling in HSC, researchers have recommended addition of polypropylene fibers to concrete (Ali et al., 2004; Behnood and Ghandehari, 2009; Bilodeau et al., 2004; Kodur, 2000). Polypropylene fibers melt at relatively low temperatures (about 167-170°C) and create randomly oriented micro and macro channels inside concrete. These channels facilitate dispersion of high vapor pressure. Another approach to overcome the spalling is through enhancing tensile strength of concrete by addition of steel fibers (Kodur, 1999; Rossi, 1994). Ali and Nadjai (2008) recently carried out investigation on spalling mitigation through use of hybrid fibers (mix of polypropylene and steel fibers) in the concrete and found it very useful in minimizing the fire induced spalling in HSC columns.

Alongside use of fibers, bending of ties in columns similar to that in seismic region have been found to be useful and attractive to reduce the fire induced spalling and to enhance the fire resistance of columns (Kodur and McGrath 2003). In this technique, it was experimentally established that bending the ties at 135° as compared to conventional 90° bent ties, spalling can be minimized. These two tie configurations are shown in Figure 2.20. When ties are bent at 135° in to the core of concrete column, these provide additional confinement to concrete thus keeping the section intact in case of exposure to fire.

2.5.4 Summary

The moisture transformation and mass transport in concrete have a unique influence on its temperature profile and development of pore pressure. HPC due to impermeability and low porosity can experience significant pore pressure build-up and thus are more susceptible to fire induced spalling. Spalling in HPC is therefore a major concern that has to be overcome to enhance the fire resistance of structural members made of these concretes.

2.6 Fire Performance of Reinforced Concrete Columns

Concrete has generally good performance and it is well established that up to 6 hours of fire resistance rating can easily be obtained by provision of conventional NSC columns (Ali et al., 2004; Kodur, 2003; Lie and Woolerton, 1988). HSC due to high compressive strength are preferred in columns of high rise buildings. However, columns made of HSC have lower fire resistance due to deterioration of material properties and occurrence of fire induced spalling. There are a number of studies on high temperature performance of RC columns that are available in literature, only limited review on effect of tie configuration on fire response of RC columns is presented in this section.

2.6.1 Experimental Studies

A detailed review has recently been done by Kodur and Raut (2010) and Raut (2011) on fire performance of RC columns. In the state-of-the-art, experimental and analytical studies related to fire performance of RC columns is elaborated along with a review of fire resistance provisions in various codes and standards. It is evident from the review that there is lack of data on fire performance of RC columns made of new types of HPC. There are absolutely no studies on HPC columns made of FAC and SCC.

Since fire resistance of HSC columns is seriously hampered by fire induced spalling, fibers are often added to the mix to mitigate spalling. The fire performance of HSC columns with steel and with polypropylene fibers have been experimentally well studied before (Ali, 2002; Ali et al., 2004; Kodur, 2003). However, there is only one study done by Ali and Nadjai (2008) in which effect of hybrid fibers is investigated on fire response of HSC columns.

Alongside use of fibers, bending of ties in columns similar to that in seismic region have been found to be useful and attractive to reduce the fire induced spalling and to enhance the fire resistance of columns (Kodur and McGrath 2003). However, there is no fundamental understanding as to how the tie configuration helps improve the fire resistance. Further, the numerical models do not account for effect of tie configuration in fire resistance predictions of columns which is an important factor.

It can be inferred from the review that, the fire resistance of columns changes with type of concrete, mix design, use of different combination of fibers and tie configuration. Although, the tests have generated valuable data for understanding the behavior and for validation of computer models, the types of concrete investigated are only NSC and HSC.

2.6.2 Numerical Studies

A fair number of analytical studies have also been conducted to study the fire behavior of RC columns. The main objective in many of these studies is to trace the response and fire resistance of RC columns under fire conditions. Few of these studies were done on HSC columns and important factors such as high temperature material properties of specific concrete type, spalling, addition fibers and tie configuration were not fully incorporated in the analysis. A detailed review of studies for numerical modeling of fire response of columns is also done by Kodur and Raut (2010) and Raut (2011).

Review of numerical studies illustrates that numerical models used to predict the fire response of RC structural members simplify the calculations by making some ideal assumptions. These models do not incorporate the factors that are critical for accurate fire resistance calculations. Factors such as high temperature properties of new types of HPC, effect of different fibers and tie configuration have not been considered and need to be included in numerical models for realistic fire resistance predictions.

2.7 Codes and Standards

The specifications for fire resistant design are included in building codes and national standards of various countries. These provisions are usually prescriptive in nature, as the codes and standards provide tabulated values of fire resistance which are based on standard fire tests. These tabulated fire resistance values are mostly dependent on concrete cover thickness and minimum dimensions of structural members.

In the USA, concrete structures are designed in accordance with the American Concrete Institute (ACI-318) (2008) standard. While ACI-318 does not contain any fire provisions, it refers to ACI 216.1 (2007) standard which gives prescriptive based specifications for fire design of concrete

and masonry structures. ACI 216.1 standard specifies concrete cover thickness and minimum sectional dimensions required for achieving a desired fire resistance rating in RC columns. Similarly, Eurocode 2, Part 1–2 (2004) gives simplified approach for determining fire resistance of RC columns based on tables and advanced methods. For example, to reduce fire induced spalling; Eurocode suggests a reinforcement mesh with a nominal cover of 15 mm to HSC columns.

It can be seen that these provisions provide prescriptive approaches based on experimental studies. Tables, which are based on this approach, provide the faster and most direct method for determining the minimum dimensions and cover thickness in RC columns. The simplified equations may give more economical fire resistant designs, especially for small columns and/or high fire resistance periods. However, the important factors such as HPC, use of different combination of fibers and effect of tie configuration are not comprehensively taken into account by these standards.

2.8 Summary

Based on information presented in this chapter, it is evident that high temperature material properties are crucial for modeling the fire response of RC members. Good amount of data exists on high temperature thermal, mechanical and strength properties including elastic modulus of NSC and to some extent for HSC as well. However, there very limited property data on HPC (HSC, SCC, FAC) is available at elevated temperatures. It is also established that mostly the fire resistance tests were conducted on RC columns made of NSC and HSC, but these tests are not existent for HPC columns such as FAC and SCC. Moreover, limited data is available on effect of hybrid fibers on spalling mitigation in HPC columns. Further, the guidelines put forward by experimental studies have not been fully incorporated in numerical models. Important factors

such as high temperature material properties of HPC, use of hybrid fibers, and effect of tie configuration are not fully incorporated in numerical models.

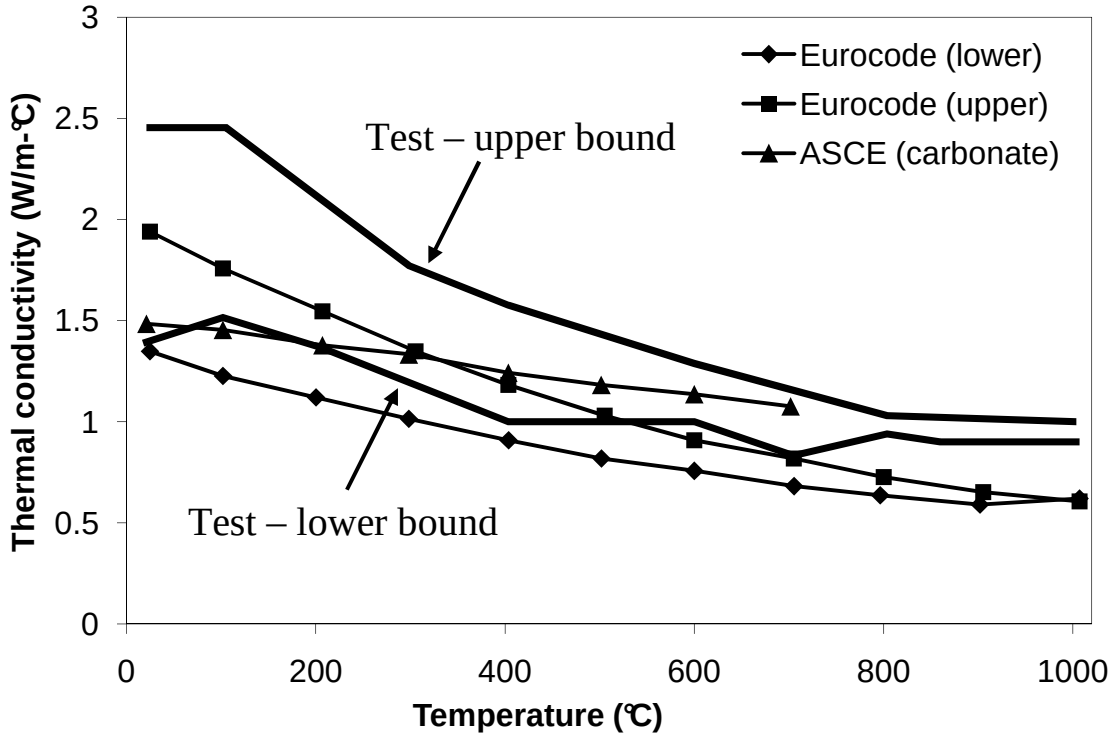

Figure 2.1 - Variation in thermal conductivity of NSC as a function of temperature

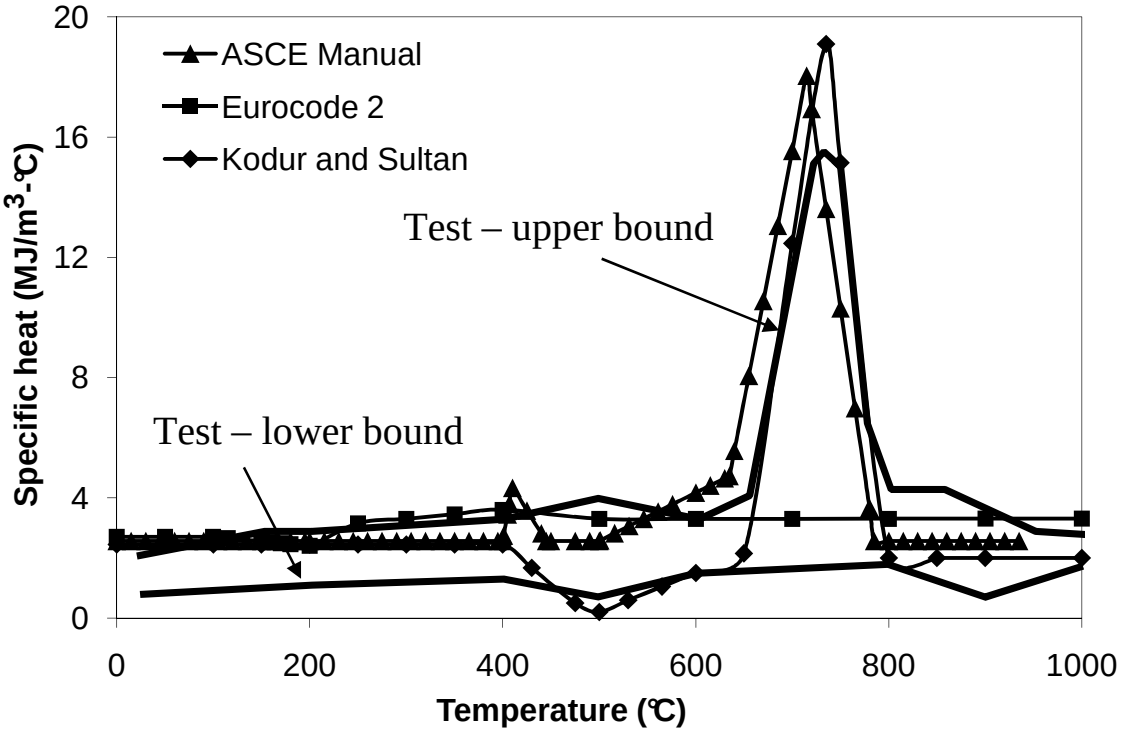

Figure 2.2 - Variation in specific heat of NSC as a function of temperature

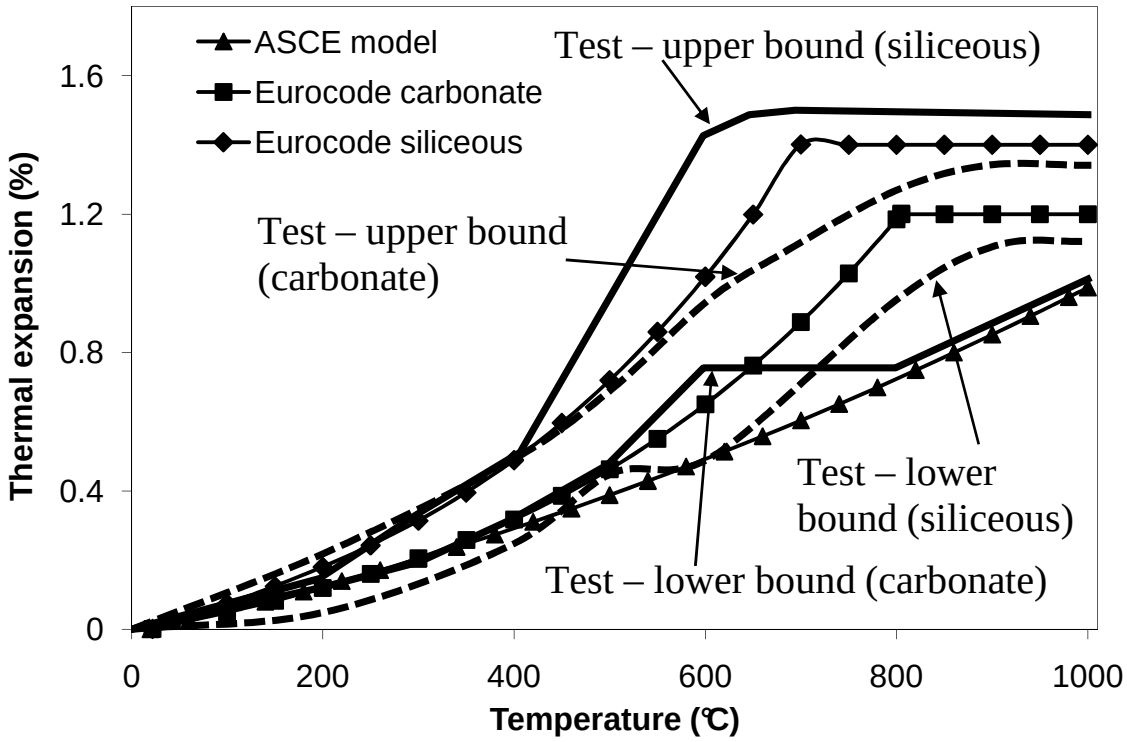

Figure 2.3 - Variation in linear thermal expansion of NSC as a function of temperature

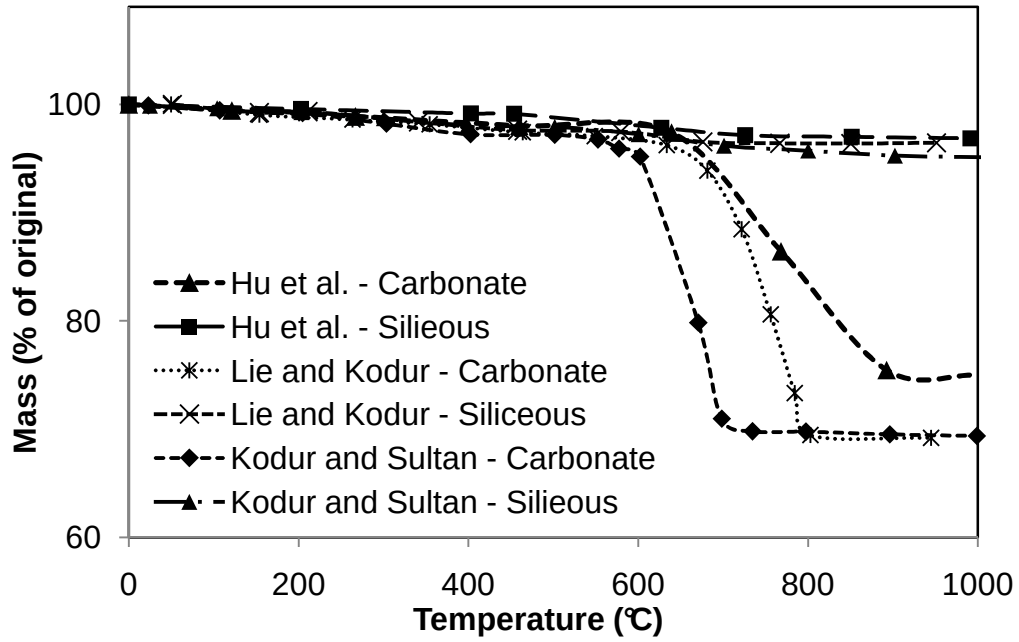

Figure 2.4 - Variation in mass of concrete with different aggregates as a function of temperature

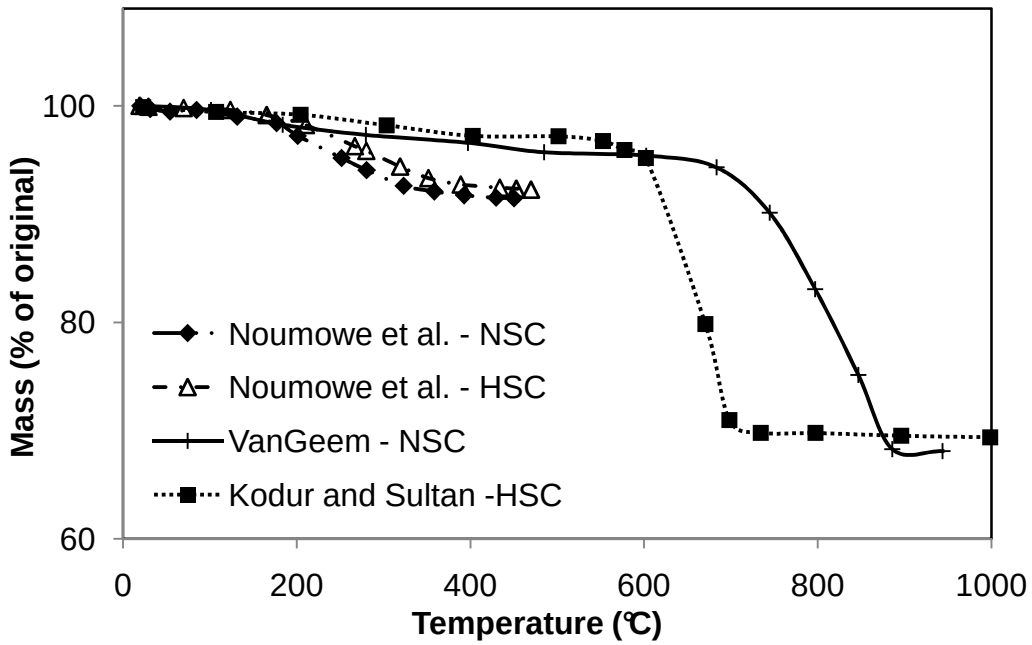

Figure 2.5 - Variation in mass of NSC and HSC as a function of temperature

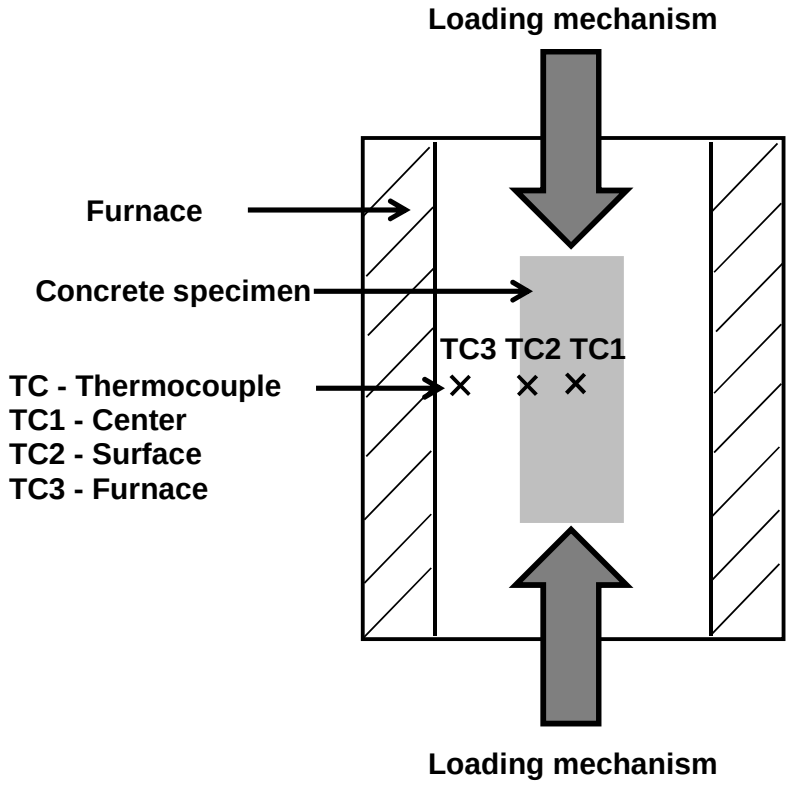

Figure 2.6 - General arrangement of concrete specimen under compressive loading inside furnace

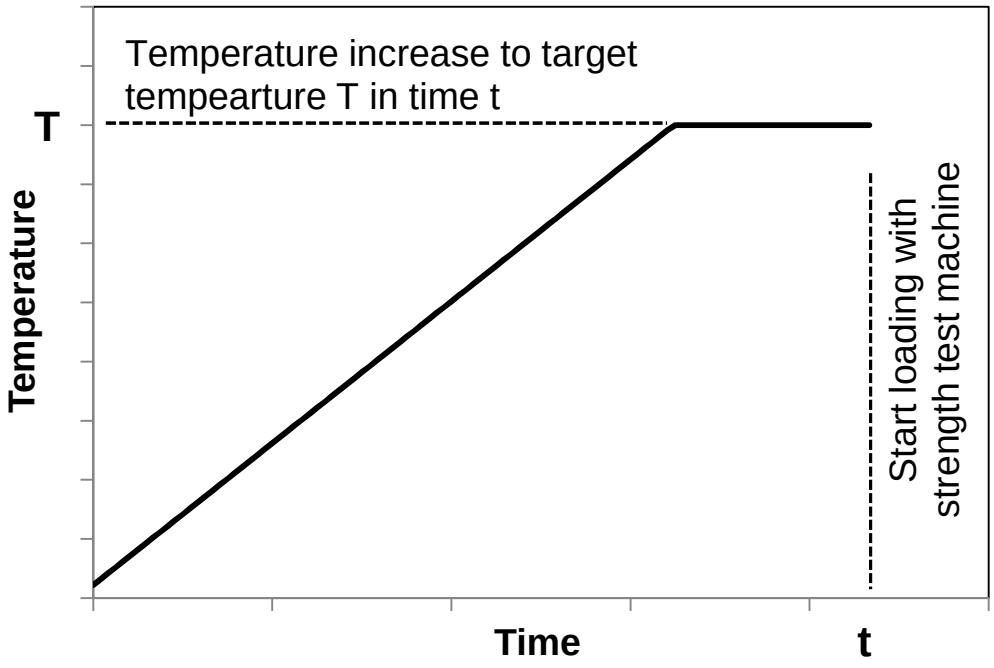

(a) Heating scheme

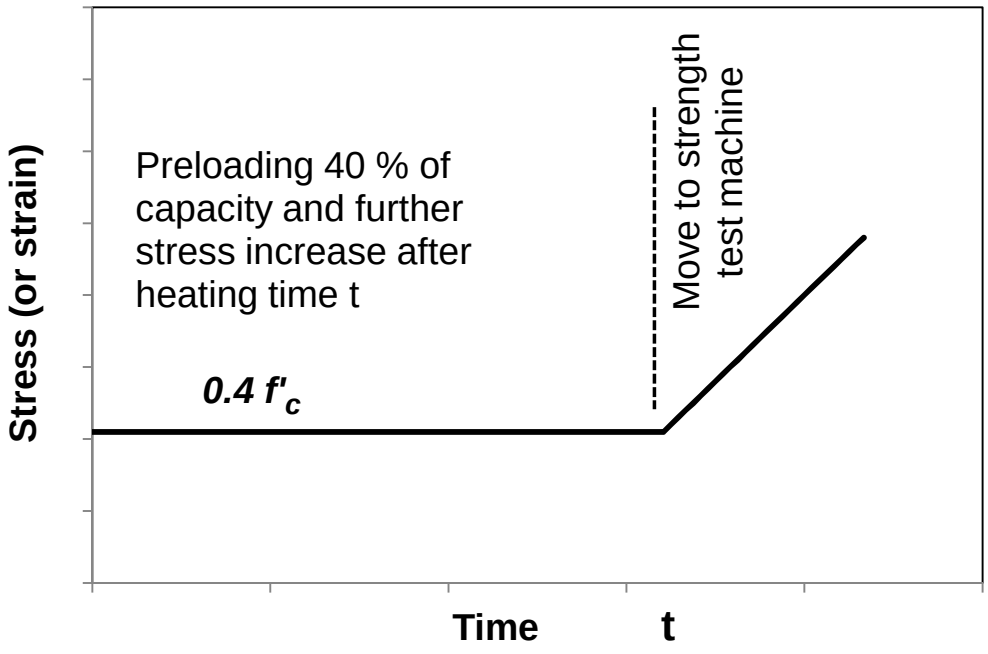

(b) Loading scheme

Figure 2.7 - Specimen heating and loading in stressed test method under preload

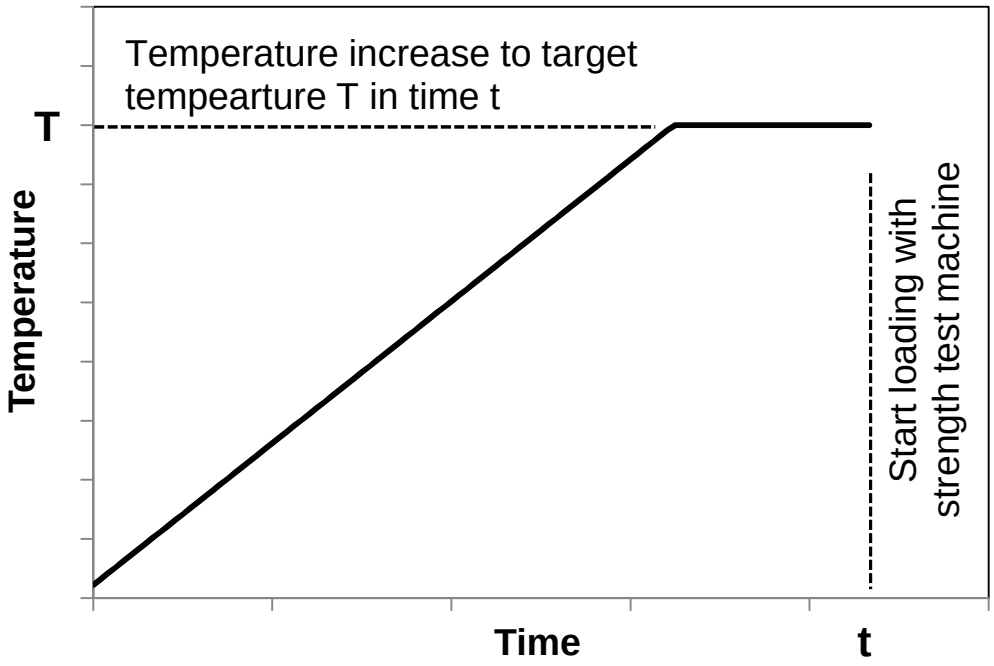

(a) Heating scheme

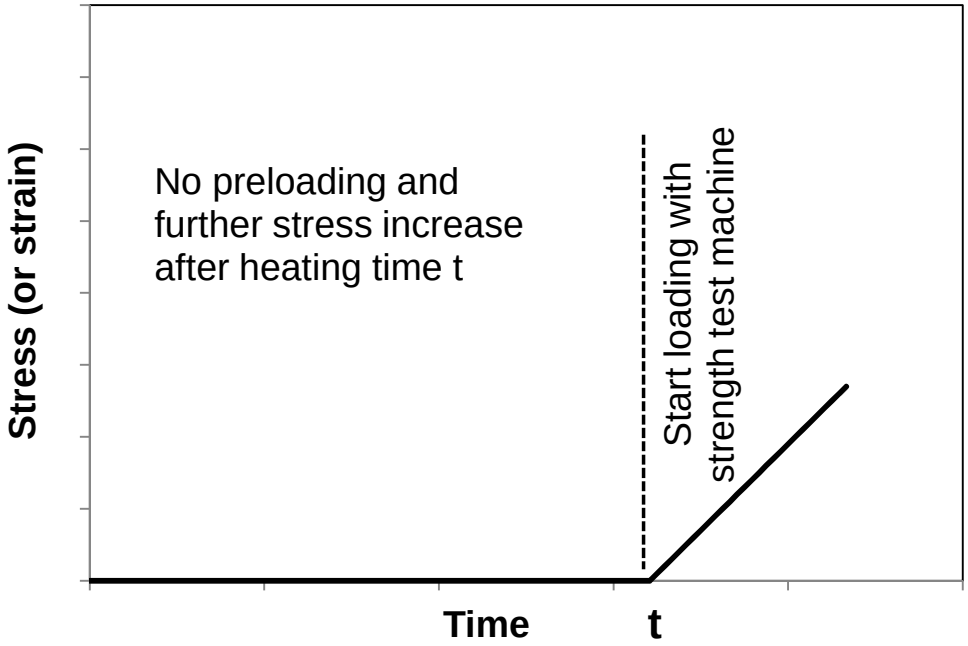

(b) Loading scheme

Figure 2.8 - Specimen heating and loading in unstressed test method without preload

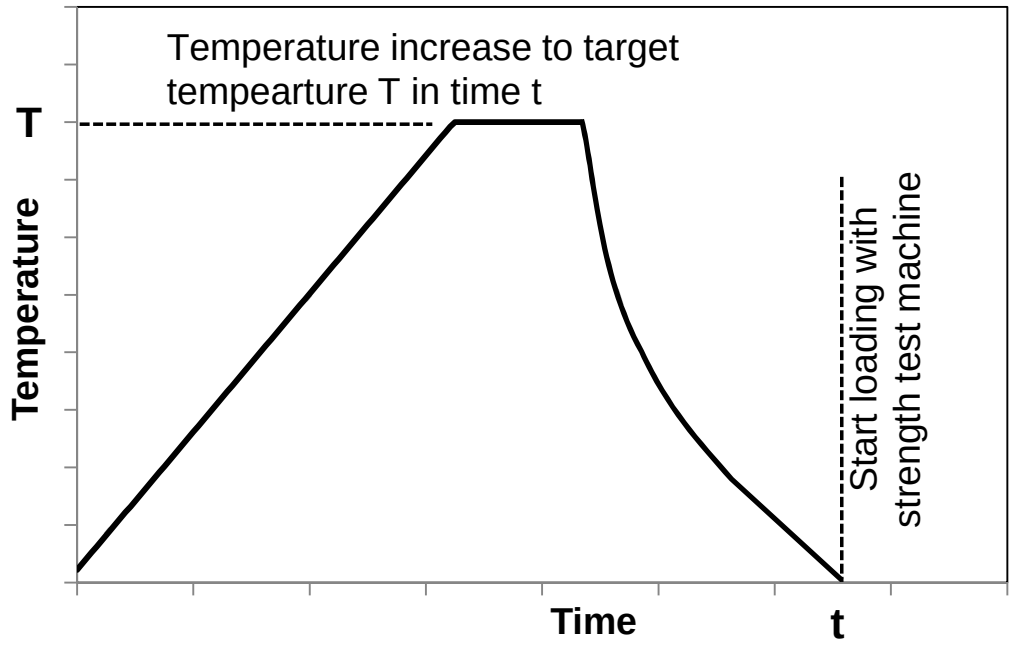

(a) Heating scheme

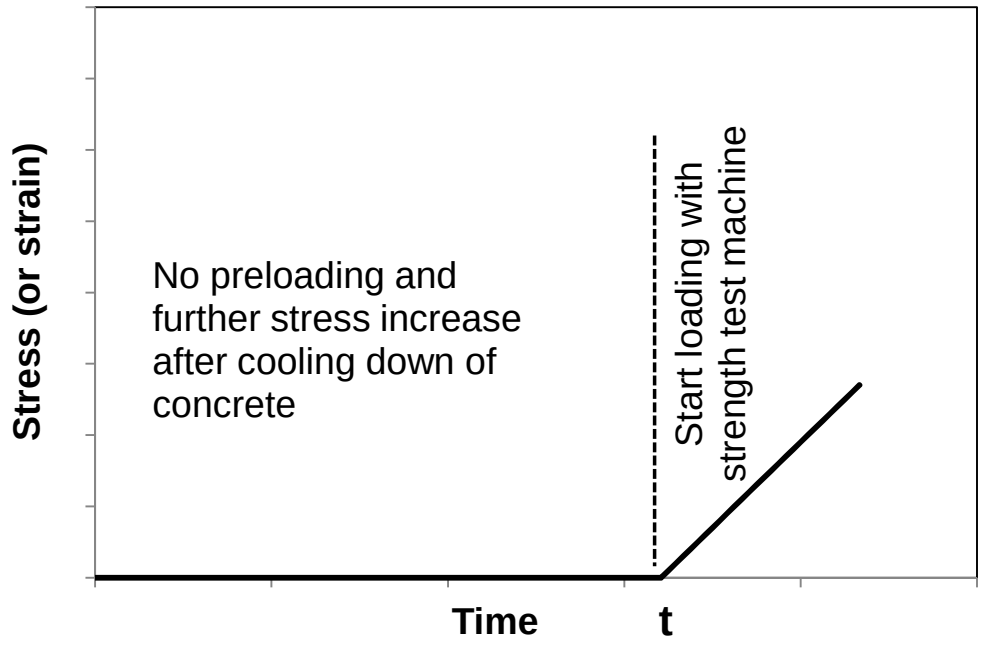

(b) Loading scheme

Figure 2.9 - Specimen heating and loading in residual strength measurements

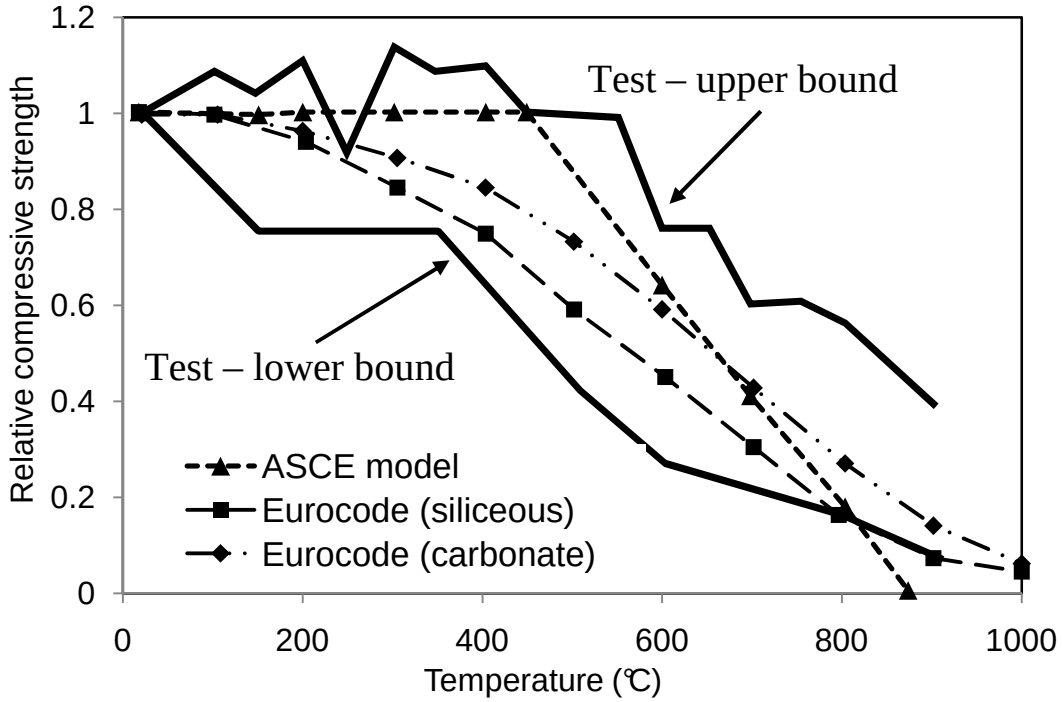

Figure 2.10 - Variation in relative compressive strength as function of temperature for NSC

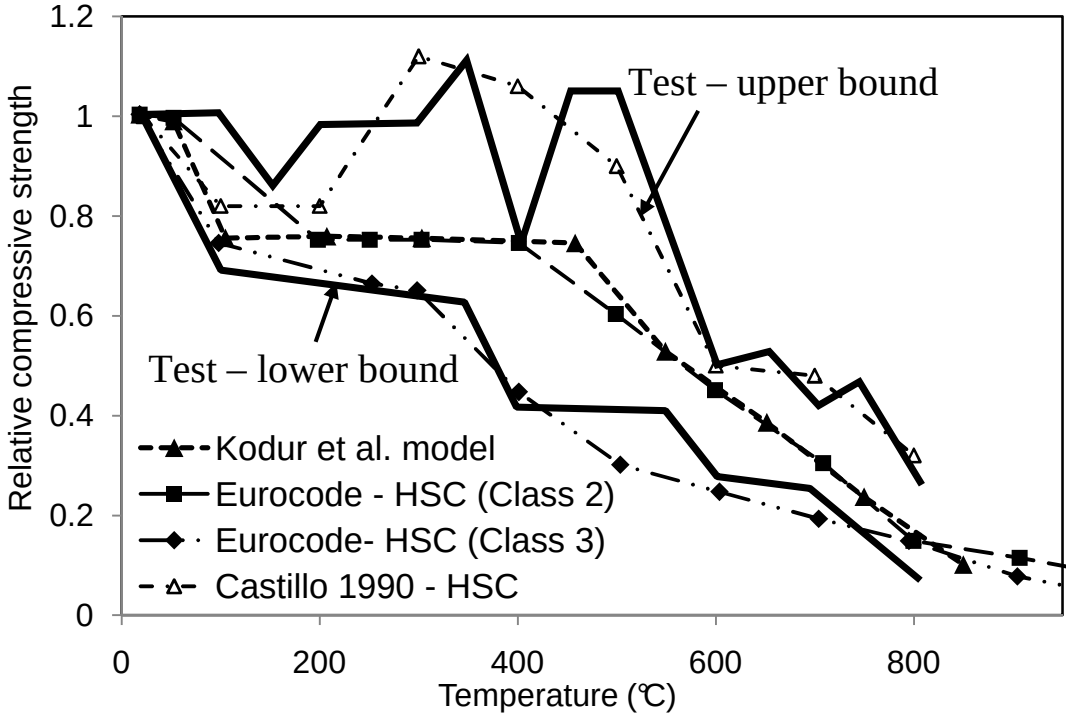

Figure 2.11 - Variation in relative compressive strength as function of temperature for HSC

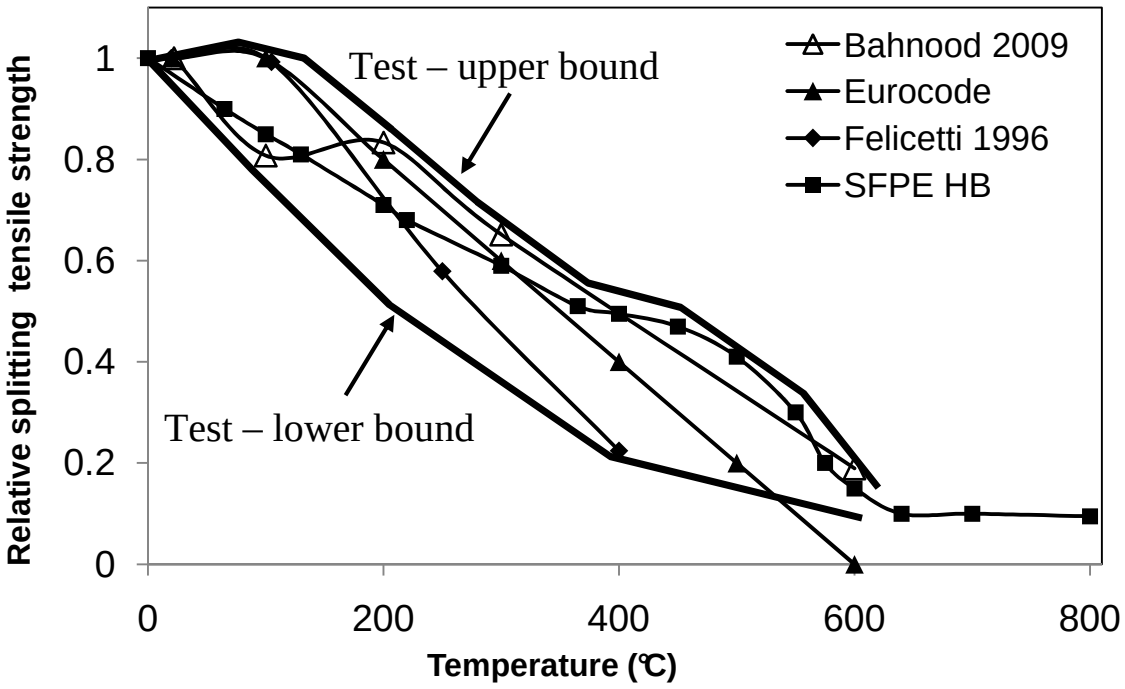

Figure 2.12 - Variation in relative splitting tensile strength as function of temperature

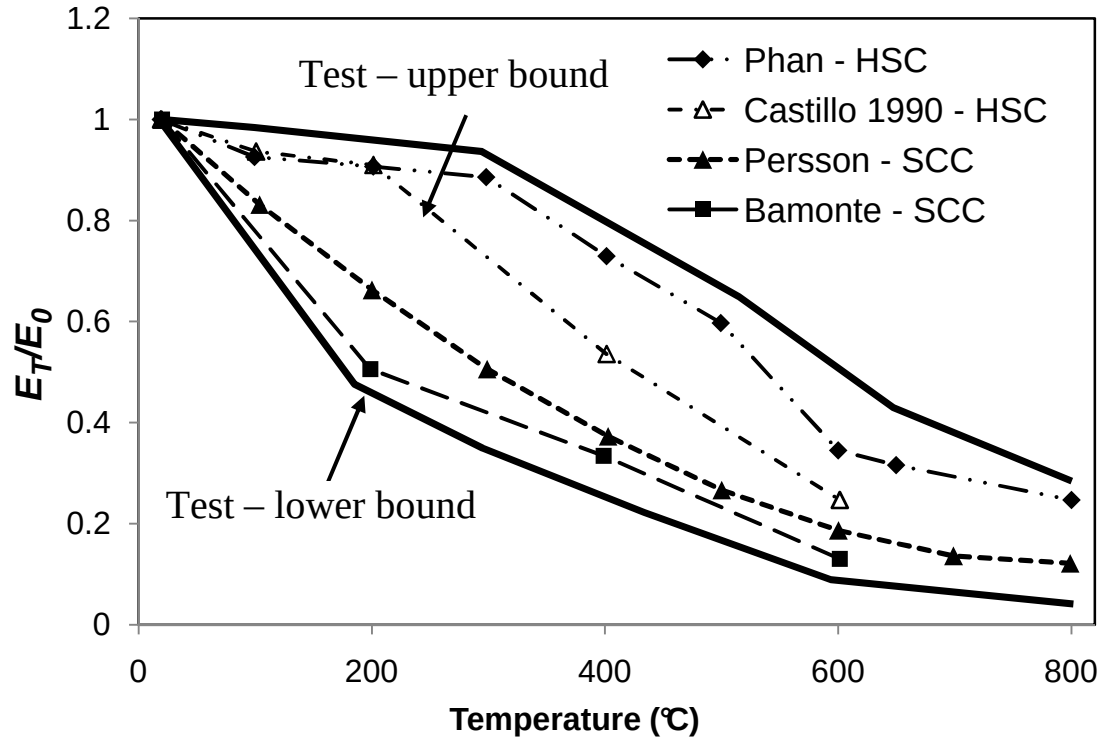

Figure 2.13 - Variation in elastic modulus as a function of temperature

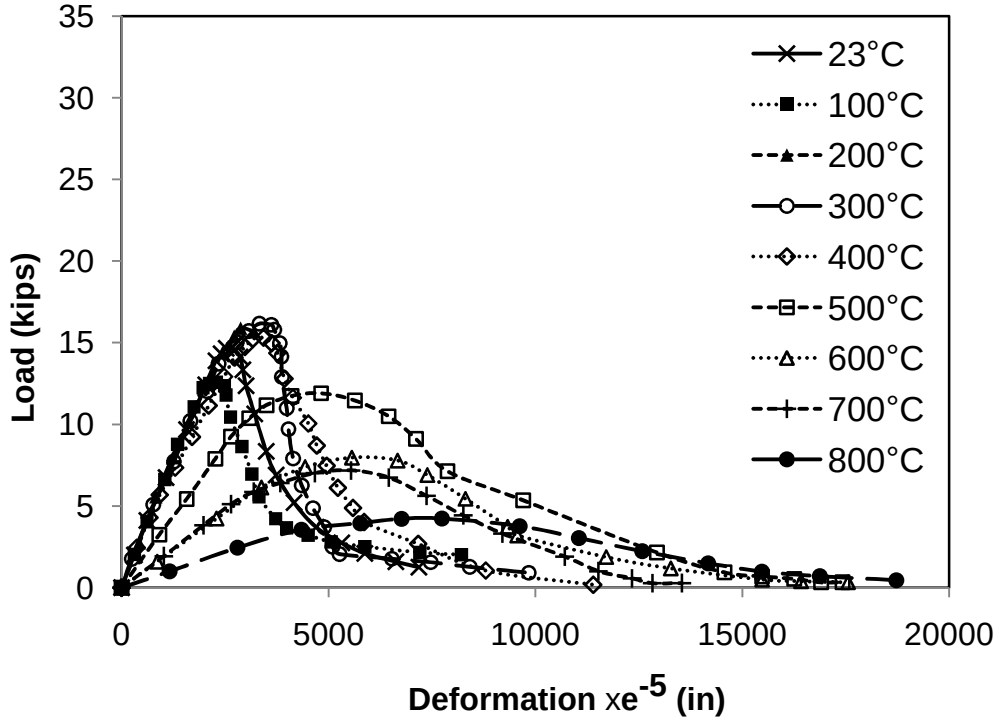

Figure 2.14 - Typical load deformation of NSC at various temperatures

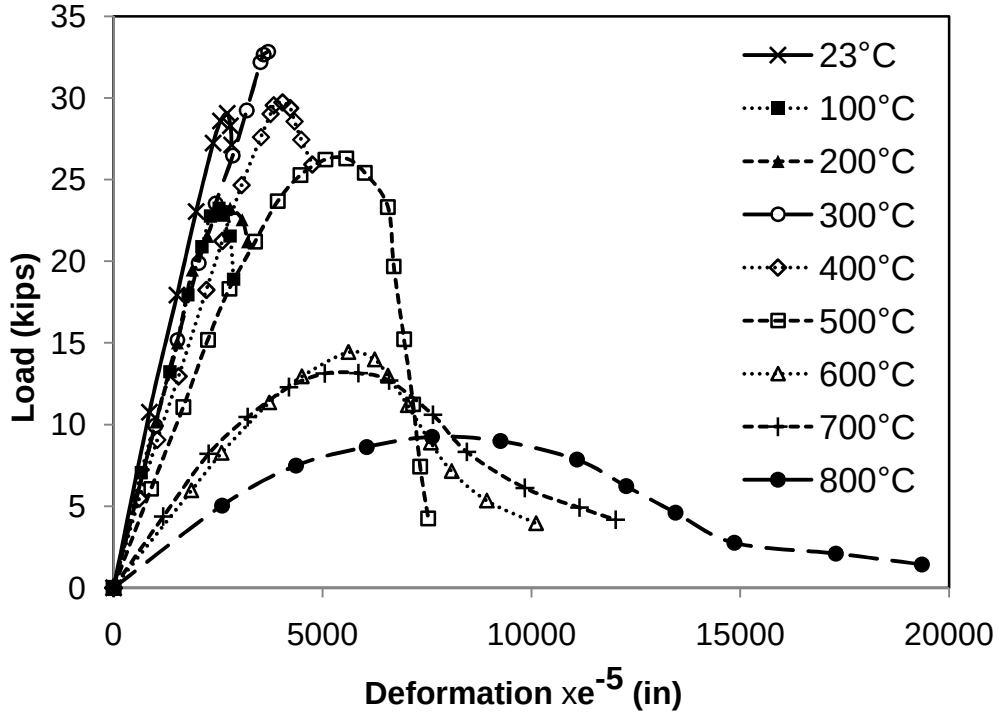

Figure 2.15 - Typical load deformation of HSC at various temperatures

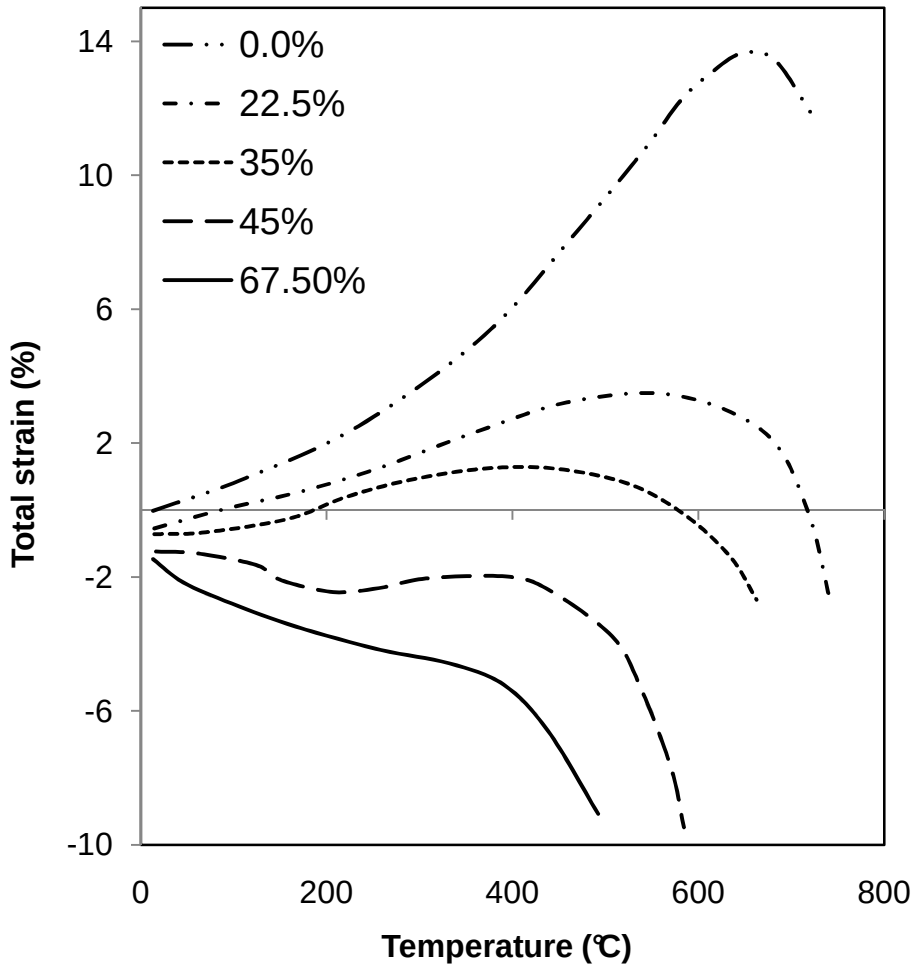

Figure 2.16 - Variation of total strain with temperature for concrete heated under differnet pre-loads (Anderberg and Thelandersson 1976)

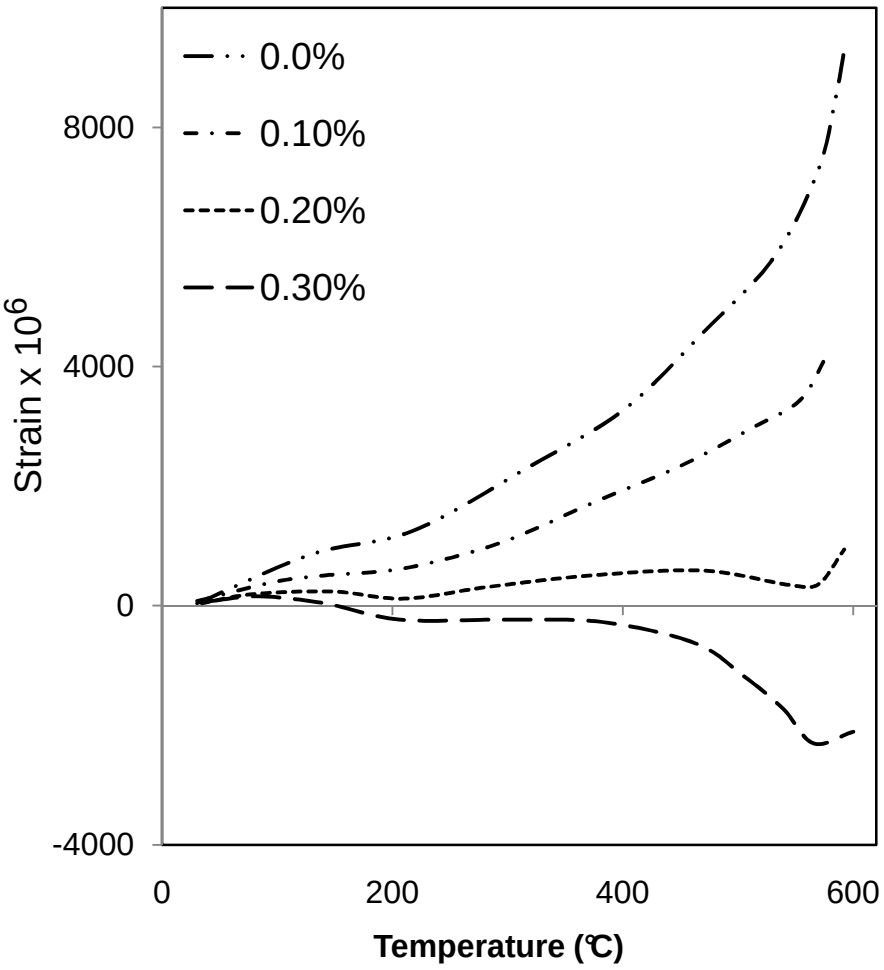

Figure 2.17 - Variation of thermal strain with temperature for limestone concrete heated under different pre-loads

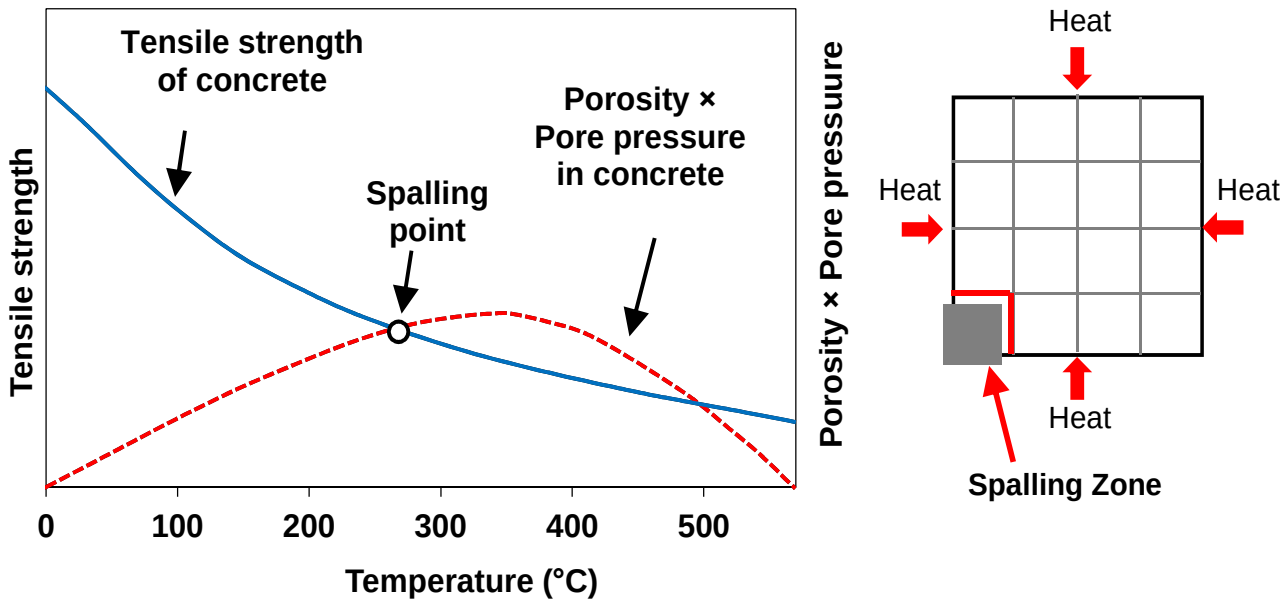

Figure 2.18 - Illustration of spalling process in concrete (Dwaikat, 2009)

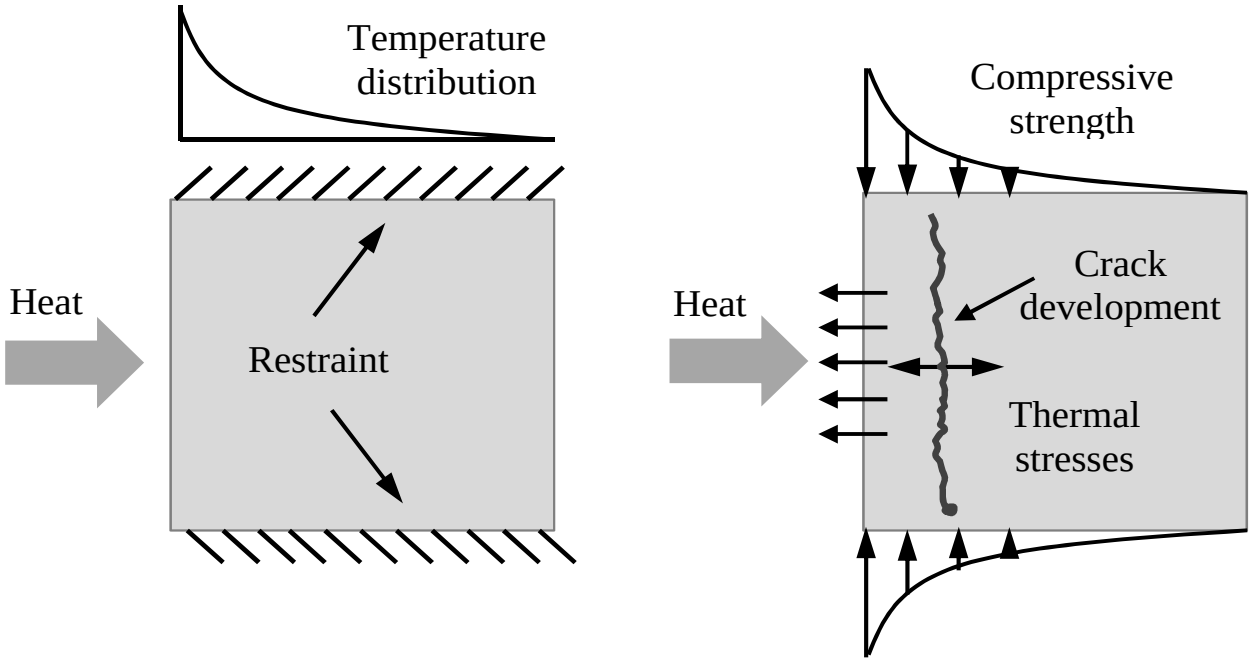

(a) Restrained concrete (b) Developed stresses

Figure 2.19 - Illustration of thermal dilation mechanism for fire induced spalling

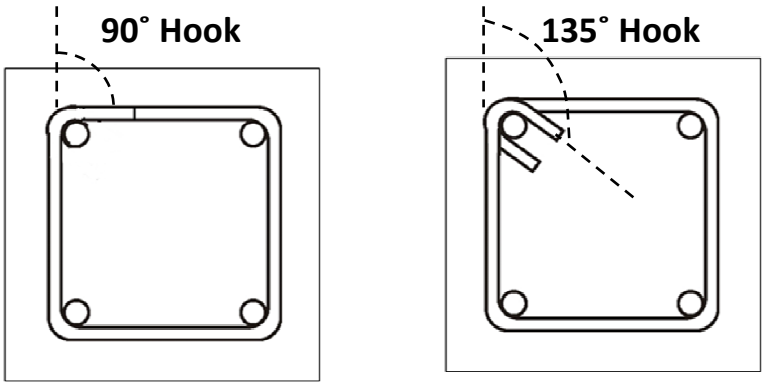

Figure 2.20 - Conventional 90° hook versus modified 135° hook configuration

CHAPTER 3

3 THERMAL PROPERTIES CHARACTERIZATION

This chapter is mainly based on the following journal papers:

- Kodur, V., and Khaliq, W. (2011). "Effect of Temperature on Thermal Properties of Different Types of High Strength Concrete." Journal of Materials in Civil Engineering, ASCE, 23(6), 793-801.
- Khaliq, W., and Kodur, V. (2011). "High temperature properties of fiber reinforced high strength concrete." Innovations in Fire Design of Concrete Structures - ACI SP 279, 3-1-42.
- Khaliq, W., and Kodur, V. (2011). "Thermal and mechanical properties of fiber reinforced high performance self-consolidating concrete at elevated temperatures." Cement and Concrete Research, 41(11), 1112-1122.
- Khaliq, W., and Kodur, V. K. R. (2011). "Effect of high temperature on tensile strength of different types of high-strength concrete." ACI Materials Journal, 108(4), 394-402.

3.1 General

Thermal properties of concrete are critical for evaluating temperature rise in concrete members, which are needed for determining strength and stiffness degradation and ultimately fire resistance of concrete structural members. These thermal properties vary with temperatures and thus accurate predictions of temperatures in concrete members require temperature dependent thermal property relations. As discussed in Chapter 2, there is lack of data specific to high temperature thermal properties of new types of high performance concrete. To develop such

information characterization of high temperature thermal properties of various HPC is undertaken and is presented in this Chapter.

The main thermal properties that influence the temperature rise and fire induced forces in concrete structural members are thermal conductivity, specific heat, thermal expansion and mass loss. At present, some codes and design standards provide thermal property relations as a function of temperature (ASCE, 1992; Eurocode 2, 2004). These relations are mainly derived from the experimental studies on conventional NSC and in some cases for conventional HSC. However, thermal properties of HPC, especially at high temperature, are influenced by factors such as presence of fibers, fly ash or silica fume, mix proportions, w/c ratio and permeability. To quantify influence of some of these factors, a series of thermal property tests were conducted on different type of HPC specimens and the effect of some of these factors on thermal properties of HPC is quantified. Based on the test data obtained from these thermal property tests, simple empirical relations for high temperature thermal properties are also presented. A detailed description of the tests and discussion of test results on thermal properties is presented here.

3.2 Design of Thermal Property Tests

A comprehensive test program was designed to undertake high temperature thermal property tests on four types of concrete namely HSC, SCC, and FAC and NSC. To quantify the effect of fibers on thermal properties three types of fibers namely steel, polypropylene and hybrid fibers were added to some of these mixes. This led to a total of eleven mix designs for measuring thermal properties. The effect of steel, polypropylene and hybrid fibers was studied in HSC and SCC, whereas to reduce the number of total tests (effort) only effect of polypropylene fibers was studied in FAC. Thermal properties namely specific heat, thermal conductivity, thermal expansion, and mass loss are measured for these concretes. Thermal conductivity and specific

heat measurements were made in the temperature range of 20-800°C (due to equipment limitations), while thermal expansion measurements were made in the temperature range of 20-1000°C. Mass loss measurements were done in the temperature range of 100-800°C at 100°C increments. The test matrix for evaluating thermal properties is given in Table 3.1.

Thermal conductivity and specific heat measurements were done using the state-of-the-art test equipment namely 'Hot Disk'. Hot Disk is relatively new equipment and it combines the measurement of three heat transfer properties (thermal conductivity, thermal diffusivity, and specific heat) in a single test unlike other existing test apparatus which require separate equipment for measuring thermal conductivity, thermal diffusivity, and specific heat. In the case of Hot Disk thermal conductivity and thermal diffusivity are measured directly and specific heat is internally calculated based on the measured thermal conductivity and thermal diffusivity. Description of the Hot Disk equipment together with the principles used in evaluating thermal properties is explained in Appendix A.

Thermal expansion is also measured using state-of-the-art test equipment namely thermomechanical analyzer (TMA). This equipment measures real time thermal expansion of the sample as a function of temperature through linear variable displacement transducer. Equipment details and the principles used in the measurement of thermal expansion are described in Appendix A.

Mass loss measurements were relatively simple in which the dimensions of a cylinder specimen was first accurately measured using a precise vernier caliper for volume calculations and a sensitive balance was used to calculate room temperature weight. The cylinder was exposed to a target high temperature in an electric furnace, and then weight of heated cylinder was recorded.

Mass loss was then evaluated using room temperature and high temperature weight measurements of cylinder.

3.3 Thermal Property Tests

Thermal property tests namely thermal conductivity, specific heat, thermal expansion and mass loss were carried out on HSC, SCC, FAC and NSC specimens as per design matrix given in Table 3.1. This section covers details on all thermal property tests.

3.3.1 Mix Proportions

Four concretes namely HSC, SCC, FAC, and NSC were used to fabricate the test specimens for measuring thermal properties. In addition, three types of fibers, namely steel, polypropylene and hybrid fibers were added to these mixes. The specimens are designated as HSC, HSC-S, HSC-P, and HSC-H for HSC, and SCC, SCC-S, SCC-P, and SCC-H for SCC, and FAC, and FAC-P for FAC where S, P and H designations indicate the presence of steel, polypropylene and hybrid (steel + polypropylene) fibers respectively. In addition to these HPC, a conventional NSC mix, designated as NSC was also included in the program for generating a bench mark data. These mixes had ordinary Portland cement (Type I), limestone (carbonate) based coarse aggregate of maximum size 10 mm, and natural source sand fine aggregate. In the FAC and FAC-P batch mixes, 25% fly ash (Type C) was used as replacement of cement. To achieve desired strength and workability properties, optimum amount of mineral admixtures, such as silica fume and slag (Grade 120), were added to batch mix. Silica fume, fly ash, and slag are the industrial by-products having cementitious properties used to produce HPC.

Silica fume is an industrial by-product of the induction arc furnaces in the silicon metal and ferrosilicon alloy industries (Mehta and Monteiro, 2006). Reduction of quartz to silicon at

temperatures up to 2000°C produces SiO vapors, which oxidize and condense in the low-temperature zone of the furnace to tiny spherical particles consisting of non-crystalline silica. The material removed by filtering the outgoing gases in bag filters possesses an average diameter on the order of 0.1 μm and surface areas in the range 15 to 25 m^2/g which is extremely fine as compared to normal portland cement. Silica fume is highly pozzolanic, but it is hard to handle and it increases the water requirement in concrete significantly unless water-reducing admixtures are used. Fly ash has cementitious and pozzolanic properties and is produced during the combustion of powdered coal in thermal power plants. As coal passes through high-temperature zone in the furnace the volatile matter and carbon are burned off. During combustion most of the fine particles fly out with the chimney gas stream and are called fly ash. This ash is subsequently removed from the gas by special filtration techniques. Blast furnace slag is produced in the production of cast iron when the slag is cooled slowly in air; the mineral components are usually present as crystalline melilites that do not react with water at ordinary temperature. When ground to very fine particles, we get blast furnace slag, a material which is cementitious and pozzolanic (Mehta and Monteiro, 2006).

For fiber reinforced HSC, SCC, and FAC mixes, commercially available fibers, NOVOCON XR type steel fibers and MONOFILAMENT (multi-plus) type polypropylene fibers were added. Figure 3.1 shows the steel and polypropylene fibers used in this study. Steel fibers were 38 mm in length and 1.14 mm equivalent diameter and had a specified tensile strength of 966 MPa. Polypropylene fibers are non-absorbent type with 20 mm length, 0.91 specific gravity and 162°C melting point. Steel fibers in HSC-S and SCC-S were 42 kg in a cubic meter of concrete representing 0.54% by volume. Polypropylene fibers in HSC-P, SCC-P, and FAC-P were 1 kg/m^3 representing 0.11% by volume. In the case of HSC-H and SCC-H the proportion of steel

and polypropylene fibers were 42 kg/m^3 steel, and 1 kg/m^3 polypropylene, representing 0.54% and 0.11% by volume respectively.

Details of the mix proportions, laboratory conditions at time of casting of plain HSC, SCC, FAC, and NSC are given in Table 3.2, and details of fiber reinforced HSC, SCC, and FAC are given in Table 3.3, 3.4, and 3.5 respectively. After casting, the test specimens were cured in curing room with controlled environment of 22°C temperature and 98% relative humidity. Specimens were pored with one mix at a time. The tests were completed over a period of 18 months with concretes casted first were tested first. Thermal property tests for a particular concrete were carried out over a period of 6 months to 10 months after casting of specimens. The 28 day compressive strength measured on specimens and for different concretes ranged from 16-81 MPa for plain HSC, SCC, FAC, and NSC as given in Table 3.6. The 28 days compressive strength of fiber reinforced HSC, SCC, and FAC ranged between 56-89 MPa as given in Table 3.7. Chemical admixtures such as superplasticizer, retarder, and water reducer were added to batch mixes to achieve desired concrete properties in HSC, SCC, FRC and FAC. For SCC, result for VSI was '1.0' and it was observed that mix was even with very less signs of segregation. Very little poppying of air was observed in slump patty in SCC. FAC displayed significantly high strength as compared to other types of concrete. HSC and SCC mixes were supplied by commercial concrete plants while FAC and FAC-P were mixed in laboratory under controlled conditions. This could be the main reason for FAC to achieve higher strength as compared to HSC and SCC.

3.3.2 Test Specimens

From each batch of concrete two 100×100×300 mm size prism specimens were fabricated. The specimens were demolded one day after casting and cured under controlled conditions of 90%

humidity and 20°C temperature. Test specimens of 60×60×25 mm size were machine cut from 100×100×300 mm prisms and prepared for determining thermal properties at elevated temperatures. Thermal property tests were carried out over 4 months period after 6 months of concrete pour.

Square specimens of size 60 mm on sides and 25 mm in height as shown in Figure 3.2(a) were used for carrying out thermal conductivity and specific heat tests. As the accuracy of test result greatly depends on the specimen-to-sensor contact, these specimens were ground smooth to ensure uniformity of the surface and enhance specimen-to-sensor contact. For thermal expansion tests, specimens of 10×10×18 mm size machine cut from same prisms described above. Sides of these specimens were smoothened carefully to have a balanced fit under thermal expansion probe as shown in Figure 3.2b. For mass loss measurements, 75×150 mm cylinders were used at different temperatures. The details and number of specimens for thermal properties are given in Table 3.8.

3.3.3 Test Apparatus

The thermal properties were measured using commercially available instruments. The specific heat, and thermal conductivity were measured using “Hot Disk TPS 2500S” thermal constant analyzer as shown in Figure 3.3a. This procedure follows ISO/DIS22007 (2008) test standards for measurement of thermal conductivity and specific heat properties. This equipment is connected to a furnace in which a specimen can be exposed to desired high temperature as shown in Figure 3.2(b). This state-of-the-art equipment utilizes transient plane source (TPS) technique to measure thermal properties of materials from room temperature to 800°C. A flat source sensor is placed between two halves of the specimens and it acts like a heater (constant effect generator) and as detector (resistance thermometer) at the same time (Adl-Zarrabi et al., 2006). This sensor

is either insulated with mica or kapton layers and accordingly called mica or kapton sensor as shown in Figure 3.4. Kapton sensor can be used for measurements up to 200°C, and mica sensor can be used for measurements in 100-800°C temperature range (Adl-Zarrabi et al., 2006). When a constant heat source is applied, the temperature in sensor rises and heat flow starts in the specimen being tested. The test specimen must have uniform temperature distribution throughout the specimen at the time of measurement.

For thermal expansion measurements, thermo-mechanical analysis (TMA) apparatus (Q-400 EM) was used as per ASTM E831-06 (2006) test procedure. TMA (Figure 3.5a) utilizes a movable-core linear variable differential transducer (LVDT), which generates an output signal directly proportional to specimen dimension change. TMA can be used for measuring dimensional changes in concrete specimens from room temperature to 1000°C. For thermal expansion tests, a flat-tipped standard expansion probe (Figure 3.5b) is placed on the concrete specimen with a small static force is applied to it so that probe stays steadily on the specimen. The specimen is subjected to temperature increase regimen according to user defined ramp and probe movement records the sample expansion or contraction. The TMA test is run through computer program while the input parameters such as heating rate, static load and maximum temperature are provided by the user.

The test equipment for mass loss calculations consisted of an electrical furnace and weight balance. The mass loss measurements, both at room and high temperatures, were carried out by utilizing a highly sensitive balance that has accuracy up to 0.001 gram. The concrete specimens were exposed to target temperatures of 100, 200, 400, 600, and 800°C in an electric furnace at a heating rate of 2°C/minute and were kept for two hours at the target temperature till steady state

conditions were attained. Heated specimens were then quickly taken out (without much heat loss) and weighed.

3.3.4 Test Procedure

3.1.1.1. Thermal Conductivity and Specific Heat

For thermal conductivity and specific heat measurements were carried out using Hot Disk (TPS 2500S) apparatus on 60×60×25 mm test specimens. The specimens were air dried and surfaces were ground smooth for ensuring good sensor contact. Thermal conductivity and specific heat of concrete were measured at thirteen temperature points namely 20, 100, 200, 300, 400, 450, 500, 550, 600, 650, 700, 750, and 800°C. The smaller increments towards higher temperatures were to capture effect of phase changes in concrete on thermal properties. The age of concrete at the time of thermal property measurements tests was 6 months or older.

Kapton sensor was used to undertake tests at room temperature (20°C). This Kapton sensor is sandwiched between two halves of concrete test specimens and is connected to Hot Disk. The specimen and sensor assembly rests on a platform of room temperature specimen holder (Figure. 3.6). A small pressure is applied to ensure good contact between the specimen and the sensor. The equipment sends and receives signal through the sensor connected to the TPS 2500S (Figure 3.3a), and is monitored with a computer program. The measurements at room temperature with kapton sensor are important to figure out the best test parameters as reasonable test results obtained at room temperature provide suitable parameters to be used for high temperature tests.

For high temperature tests, mica sensor was sandwiched between two specimens and the assembly was subjected to high temperatures in a furnace connected to the Hot Disk apparatus. Figure 3.7 illustrates mica sensor being placed between two specimens of concrete in the holder

assembly. This holder assembly is further placed inside the furnace (Figure 3.3b) for exposure to high temperature. The computer program controls the temperatures of specimen and furnace. The concrete specimens are exposed to high temperature in a furnace connected to Hot Disk apparatus as per defined test conditions. The test condition parameters namely, probing depth, sensor type, initial thermal coefficient of resistance (TCR), hold time at steady state, measurement power, and measurement times are to be programmed (as input) in to Hot Disk apparatus by user. For these tests, initial TCR of 0.004693 /K, probing depth of 20 mm, sensor measurement power of 0.9 W, hold time of 60 minutes and measurement time of 40 seconds was used. For high temperature measurements, a built-in value of TCR at each temperature as per sensor type was used. At each target temperature, once the thermal equilibrium is attained, thermal conductivity and specific heat are recorded. Then the temperature in the furnace is increased to next target temperature and this procedure is continued till 800°C. It took an average of 25 minutes to reach a target temperature with 100°C increments and an average of 17 minutes to attain a target temperature with 50°C increments. Average stabilizing time to obtain uniform temperature throughout the specimens was 300 minutes for 100°C increments and was 210 minutes for 50°C increments. This resulted in average time of running a complete test on each specimen to approximately 52 hours. Figure 3.8 illustrates time-temperature increments and stabilizing times at different target temperatures.

In order to verify reliability of measurements, thermal property tests were repeated on additional specimens from the same batch of concrete. For this, three SCC-P and two HSC samples were selected and Hot Disk tests were repeated in the entire temperature range. The variability in the thermal conductivity and specific heat was with in ±5% indicating good reliability of the

measurements. To keep the results consistent with other concretes, data from one batch of measurements is presented here.

For thermal expansion measurement, samples were prepared as per ASTM E 831-06 (2006). Since concrete is a heterogeneous material, the specimens were selected from concrete prisms in a manner that they contained aggregate and cement matrix in equal representative amount. After carefully placing the specimen on expansion probe (Figure 3.5c) a small load of 0.02 N was applied to the specimen through expansion probe to maintain static contact between the specimen and the probe. The test equipment was first calibrated and zeroed to make the TMA ready for new test. The initial length of the specimen and ambient temperatures were recorded by the TMA before start of test. Three TMA tests were performed for each type of concrete throughout the temperature range of 20-1000°C. The temperature increase for thermal expansion depends on the temperature ramp (heating rate) set by the user for that particular test. Once specimen is placed in position, inside TMA furnace, the test is run and controlled by software that records dimensional change with increasing temperature. For concrete specimens, the selected ramp was 5°C per minute. It took three hours and twenty minutes for each specimen to reach target temperature of 1000°C. Figure 3.9 illustrates the temperature ramp used in thermal expansion tests. To ensure repeatability of the test results, 3 tests were conducted for each type of concrete and average value was considered as final results.

Mass loss of all concretes was measured at various temperatures using 75 mm dia and 150 mm height concrete cylinders. Mass loss measurement procedure involved weighing the cylinder at room temperature before it was exposed to high temperatures. Cylinders were taken out form the curing room and then air dried at room temperature for one hour before taking measurements and testing. The dimensions of the cylinder were measured using a precise vernier caliper at three

places along length and diameter and average of the dimensions were used for volume calculations. Room temperature density and mass calculations were then based on weight of the cylinders measured at ambient temperature.

Following room temperature density and mass calculations, the cylinders were then exposed to higher temperatures in an electric furnace at a heating rate of 2°C/minute to target temperature. Specimens were then allowed to stabilize for two hours to reach steady state conditions throughout the specimen. Then the heated specimens were quickly transferred to a sensitive balance (with accuracy of 1000^{th} of a gram) and weighed to record change in weight at that target temperature. Mass loss was then evaluated at high temperature using both recorded room temperature and high temperature weights. This procedure was repeated for various target temperatures.

3.4 Results and Discussion

The measured thermal conductivity (k_t), specific heat (c_p), thermal expansion (ε_{th}) and mass loss properties for plain and fiber reinforced HSC, SCC, and FAC are presented in this section. Results of thermal property tests on NSC are utilized to compare the thermal properties of different concrete types. Data from these tests is also used to discuss the effect of various parameters on high temperature thermal properties.

3.4.1 Thermal Conductivity

The measured thermal conductivity of HSC, SCC, FAC, and NSC are plotted in Figure 3.10 as a function of temperature. Thermal conductivity of these three concrete types is between 2.4 and 3.3 W/m°K at room temperature range. For all three concretes, thermal conductivity initially decreases with temperature up to 400°C, then it remains almost constant between 400 and

500°C, and finally decreases again up to 800°C. This trend in thermal conductivity can be attributed to variation of moisture content with increase in temperature (Bažant and Kaplan, 1996). The initial steep slope of thermal conductivity up to 400°C can be attributed to moisture loss at a faster pace resulting from the evaporation of free and pore water in concrete with rise in temperature. The minor variation in thermal conductivity between 400°C and 500°C is due to dissociation of small amounts of physically bound water present in concrete as a result of phase change. Beyond 500°C, there is slow decrease in thermal conductivity due to liberation of small amount of strongly held moisture left within calcium silicate hydrate (CSH) layers.

Thermal conductivity for FAC follows quite similar trend and lie closer to that of HSC and NSC, therefore it is deduced that there is not much difference in thermal conductivity values of HSC, NSC and FAC. Thermal conductivity of NSC follows trend close to these concretes till 600°C, however, after the thermal conductivity of NSC seems to stay constant. The main reason for constant thermal conductivity of NSC beyond 600°C is that maximum dehydration of NSC has already taken place and there is not much physically or chemically bound water left to lose. This is not the case with other concretes, as high permeability allows retaining some chemically bound water till higher temperature range and therefore cause further thermal conductivity variation.

Thermal conductivity of SCC also follows a similar trend to HSC, except that it is slightly higher as compared to other concrete types within 600°C temperature range. This might be attributed to the fact that SCC is produced by excessive use of chemical admixtures, and thus it has increased amount dissolved chemical ions in mixed water. This higher concentration of chemical ions slightly increases thermal conductivity of SCC (Ganguli et al., 2008).

Figures 3.11 and 3.12 and 3.13 show the effect of fibers on the thermal conductivity of HSC, SCC, and FAC as a function of temperature respectively. For HSC, the trends indicate that addition of steel, polypropylene, and hybrid fibers to concrete does not significantly alter the thermal conductivity up to 600°C. However, beyond 600°C fibers have marginal influence on thermal conductivity of fiber reinforced HSC. This minor influence can be attributed to dehydration of the CSH, and also due to contribution of higher thermal conductivity of steel fibers present in the concrete mix.

For SCC the presence of fibers does have an effect as thermal conductivity is higher for SCC-S and SCC-H as compared to SCC-P. This modification might have been due to contribution from higher thermal conductivity of steel fibers as compared to polypropylene fibers. However, it can be observed form Figure 3.12 that reduction in thermal conductivity of SCC with three types of fibers follow similar trend throughout the temperature range tested.

In case of FAC, polypropylene fibers do not affect the thermal conductivity, as it is almost same for both FAC and FAC-P concretes. Thermal conductivity of FAC at room temperature was a little higher as compared to FAC-P, this can be attributed to the polypropylene fiber matrix that hinders flow of heat at room temperature, however, as the polypropylene fiber melt at about 169°C, the thermal conductivity of both concretes follow similar trend throughout the tested temperature.

3.4.2 Specific Heat

The variation of specific heat for HSC, SCC, FAC, and NSC with temperature is illustrated in Figure 3.14. The specific heat for all the concrete types remains almost constant up to 400°C, then increases up to about 650°C and then remains constant between 650-800°C range. SCC and FAC exhibit slightly higher values of specific heat throughout the temperature range. This could

be attributed to varying permeability characteristics of concrete. The permeability coefficients for different concrete types as reported in literature are tabulated in Table 3.9. It can be observed that SCC and FAC are less permeable than that of HSC and NSC. Since extra heat is absorbed for releasing bound water in less permeable concretes, SCC and FAC display higher specific heat values. Kodur and Sultan (2003) observed that the specific heat of HSC is affected by physiochemical processes that occur in the cement paste and aggregate above 600°C. This is generally true with FAC and SCC as well. Above 600°C enormous amount of heat is required to raise the temperature of the carbonate aggregate concrete. The substantial increase in specific heat of SCC and FAC between 600 and 700°C, as compared to HSC, can be attributed to presence of mineral and chemical admixtures in SCC and FAC. NSC has the specific heat closer to HSC between 600-800°C, porosity and dehydration resulting from loss of water at early temperatures is the cause of these decreasing values of NSC towards high temperature.

The effect of fibers on specific heat of HSC, SCC, and FAC as a function of temperature is illustrated in Figures 3.15, 3.16 and 3.17 respectively. Addition of steel, polypropylene, and hybrid fibers to HSC and SCC has marginal influence on the specific heat of concrete. Specific heat up to 400°C is constant for three types of fiber reinforced HSC and SCC, but beyond 400°C there is slight influence of fibers. Influence of steel and hybrid fibers on specific heat is similar as compared to polypropylene fibers concrete up to 600°C; however between 600 and 800°C, polypropylene fiber reinforced concrete experiences drop in specific heat. Steel fibers present in HSC-S and HSC-H help to control cracking and its propagation at higher temperatures and hence density of the concrete does not get reduced resulting in higher specific heat. However, in case of HSC-P, polypropylene fibers decompose (after burning) leading to increase in porosity of concrete. As a result HSC-P becomes more permeable with high crack density, which gives

lower specific heat for HSC-P in higher temperature range. Similar observations of crack control and preserved density (in the case of steel fibers) are noted for SCC-S and SCC-H concrete as compared to SCC-P and are illustrated in Figure 3.16.

In the case of FAC and FAC-P, the specific heat remains constant up to 400°C; however there is a marginal difference between the two concretes beyond 400°C. Higher specific heat in FAC can be attributed to the dense microstructure that does not allow easy evaporation of chemically bound water and thus requires extra heat. On the other hand easy evaporation and dehydration in the case of FAC-P is facilitated by enhanced porosity due to burning of polypropylene fibers. Over all there is significant difference in the specific heat of the FAC and FAC-P beyond 400°C.

3.4.3 Thermal Expansion

The variation of thermal expansion of HSC, SCC, FAC, and NSC is plotted as a function of temperature in Figure 3.18. Thermal expansion generally increases with temperature for all three concrete types. This increase is substantial in 20-600°C temperature range, and is mainly due to high thermal expansion resulting from constituent aggregates and cement paste in concrete. The expansion rate subsidizes between 600-800°C for all three concretes, as loss of chemically bound water in hydrates causes shrinkage. Thermal expansion again rises substantially after 800°C and this can be attributed to decarbonation of limestone based aggregates, when macro crack development is observed (Fu et al., 2004). Since calcium hydroxide, which is found in concrete matrix, dehydrates above 800°C, maximum thermal expansion occurs between 800 and 1000°C. At this point, the physically bound water held by limestone aggregate would also evaporate and lead to this higher thermal expansion in concrete. In case of NSC the expansion follows a trend similar to HSC and FAC, however expansion remains consistent till 800°C with significant

changes (contraction or degradation). It can be attributed to consistent properties associated with less damaged microstructure of NSC as compared to HSC or FAC.

It can be seen in Figure 3.18 that SCC has slightly higher thermal expansion as compared to other two concretes throughout the temperature range. This can be attributed to higher chemical and mineral admixtures present in SCC mix and also due to lower permeability of SCC. Thermal shrinkage, instead of expansion, is observed in FAC between 800 and 1000°C and this can be attributed to presence of fly ash (25%) in the mix. This has also been established by Shehata et al. (2000), who inferred that use of fly ash in concrete reduces the expansion of concrete and this reduction is dependent on the volume of fly ash in concrete mix.

The effect of fibers on thermal expansion of HSC, SCC, and FAC is illustrated in Figures 3.19, 3.20 and 3.21 respectively. The presence of fibers influences thermal expansion all three types of HPC. In case of HSC, the addition of fibers reduces thermal expansion. Generally this effect of fibers is much pronounced in 400-1000ºC temperature range. This can be attributed to differential thermal expansion of steel and also due to crack control effect facilitated by steel fibers. The addition of fibers shows an increased trend in thermal expansion in case of SCC. The addition of polypropylene fibers has the least expansion in HSC and SCC. Overall, SCC displayed 0.4% higher values of thermal expansion as compared to HSC over the entire temperature range.

In the case of FAC and FAC-P, the thermal expansion is higher in FAC; especially it is significant beyond 400°C. Higher thermal expansion in FAC can also be attributed to the impermeable and dense microstructure that does not allow easy dehydration and therefore causes extensive micro and macro cracks resulting from thermal stresses. Whereas this is not the case

with FAC-P, as the thermal expansion is quite gradual and smooth throughout 20-800°C temperature range.

3.4.4 Mass Loss

The variation in mass loss (ratio of mass at a specified temperature (M) to mass at room temperature (M_0)), as obtained from tests, is plotted in Figure 3.22 as a function of temperature for plain HSC, SCC, FAC, and NSC. It can be seen that no significant mass loss occurs till 600°C in all concrete types; however moderate mass loss that is about 10% of room temperature mass takes place in 600-800°C in the case of SCC and FAC. Higher mass loss takes place in HSC in 600-800°C (about 20% at 800°C), which can be attributed to the relatively easy dehydration in HSC which has comparatively less dense microstructure. The main reason for sudden higher mass loss beyond 600°C is the loss of the hidden moisture present in carbonate aggregate that vaporizes at temperatures above 600°C due to dissociation of dolomite. This is an endothermic reaction which absorbs lots of heat. All these concretes were made of carbonate aggregate; the mass loss in these concretes follows almost similar trends throughout 20-800°C. Compared to HPC, mass loss in conventional NSC is higher and this loss starts from the early stages of heating. This higher and early mass loss is attributed to easy loss of moister form NSC due to its permeable microstructure. However, ultimate mass loss in NSC at 800°C is quite similar to other types of concrete, therefore it can be deduced that earlier moisture retention in HPC is due to low permeability and therefore higher thermal properties as compared to NSC. This is the reason that conventional NSC behaves entirely different from HPC under elevated temperatures and suffers less from the detrimental effects of pore pressure that builds up in HPC.

The effect of fibers on mass loss of HSC, SCC, and FAC is illustrated in Figures 3.23, 3.24 and 3.25 respectively. It can be seen that there is no significant effect of fibers on mass loss of these HPC at elevated temperatures. This is explained by the plotted data (Figures 3.23, 3.24 and 3.25) which shows that fiber reinforced HSC, SCC, and FAC have almost similar trend of mass loss as compared to plain form of the concrete.

3.4.5 Repeatability of Thermal Property Tests

Thermal conductivity and specific heat measurements were carried out by testing one pair of specimens for each test. Since high temperature measurements were to be carried out at 12 temperatures (100, 200, 300, 400, 450, 500, 550, 600, 650, 700, 750, and 800°C) on each specimen type. Three measurements were carried out at target temperature in a single test with a time difference of 60 minutes at each temperature with Hot Disk equipment. However, the tests were not repeated for thermal conductivity and specific heat to save on time and resources. It should be noted that the sensors used for the high temperature thermal property measurements get destroyed after the test and these sensors are very expensive. Moreover, a single test on Hot Disk equipment took an average of 52 hours (about 3 work days). However, to ensure the repeatability of measurements and thermal conductivity and specific heat tests were repeated by conducting three tests for SCC-P and two tests for HSC specimens throughout the 20-800°C temperature range. The variability was with in ±5% and thus the authors are quite confident on the reliability of the measurements.

Thermal expansion measurements were carried out by testing three samples of each type of concrete throughout the temperature range. For statistical analysis, the y-error bars are shown on the TMA test on four types of concrete in Figure 3.26. These error bars shown in the line graph represent a description of confidence on mean representing the true expansion value as a function

of temperature. The more the original data values range above and below the mean, the wider the error bars and less confident you are in a particular value. The maximum standard deviation is depicted by HSC values that are within 10% of the measured range; values for all other concretes are much lower than 10%. Mass loss measurements were also done using one sample at each temperature. Like thermal conductivity and specific heat, mass loss is also time consuming test with each temperature test taking a day to complete. These tests were therefore only repeated to confirm results once mass loss property at a given temperature was a significant outlier.

3.4.6 Summary

Temperature has significant influence on thermal properties of HSC, FAC, and SCC. The thermal conductivity of all three concrete types generally decreases with temperature, while the thermal expansion increases with temperature up to 800°C. Conversely, specific heat of all three concrete types remains constant up to about 400°C, and then increases up to about 650°C before following a constant trend in 650-800°C range. Results show that SCC possesses higher thermal conductivity and thermal expansion as compared to HSC and FAC in the temperature range of 20-800°C. However, specific heat of SCC lie in-between that of HSC and FAC in 20-800°C temperature range. Compared to HSC and SCC, FAC has higher thermal expansion in 550-850°C, and it shrinks in 850-1000°C. No significant mass loss occurs in HSC, SCC, and FAC up to 600°C, and moderate mass loss occurs in 600-800°C.

The addition of steel, polypropylene, and hybrid fibers to HSC, SCC, and FAC does not significantly alter the thermal conductivity. However addition of fibers increases specific heat of SCC and HSC in 400-800°C, while in case of FAC the specific heat drops in 400-800°C temperature range. In the case of thermal expansion addition of fibers to SCC increases thermal expansion in 400-800°C, while in case of HSC and FAC the addition of fibers decreases the

thermal expansion in 20-800°C temperature range. Fibers do not have any effect on mass loss in HSC, SCC and FAC in the entire 20-800°C temperature range.

3.5 Relations for Thermal Properties

Data generated from the thermal property measurements is utilized to develop thermal property relations for plain and fiber reinforced HSC, SCC and FAC. These properties are expressed in the form of empirical relations over temperature range of 20-800°C for thermal conductivity, specific heat and mass loss, and in 20-1000°C for thermal expansion. These empirical relations were arrived at based on linear regression. For the regression analysis, measured thermal properties were used as response parameter with temperature as their predictor parameter. Three data points based on three measurements taken at a target temperature were used for regression analysis.

For regression analysis, linear regression was selected based on the fact that thermal properties are measured as a function of temperature and therefore linear relation of property verses temperature is simple and more suitable. The procedure for estimating the parameters of any linear model (linear fitting), the method of least squares can be used simply by fitting a straight line to a set of data points (Wackerly et al., 2008). The least-squares procedure is used for fitting a line through a set of 'n' data points where it is desired that the differences between the observed values and corresponding points on the fitted line to be minimum overall. A convenient way to accomplish this, and one that yields estimators with good properties, is to minimize the sum of squares of the standard deviations from the fitted line. These deviations in the response value (thermal property) given by the predicted value (temperature) is called the error and to reduce these deviations in response values, sum of squares of deviations/error is utilized. This quantity is referred to as sum of squares of error (SSE).

If the simple linear regression model fits the data well, the differences between the observed and predicted values are small, leading to a smaller for SSE. On the other hand if the regression model fits poorly, SSE will be large leading to a quantity known as coefficient of determination R^2 (Wackerly et al., 2008). This R^2 can be interpreted as the proportion of the total variation in the response that is explained by the variable prediction in a simple linear regression model. The accuracy of the statistical model is represented by coefficient of determination 'R^2', that represents proportion of the sum of squares of deviations of the response values about their predictor (Mendenhall and Sincich, 2007). The value of R^2 is always between 0 and 1, where 1 is the perfect fit of the equation to underlying data. For this study commercially available statistical software (Minitab) was used to find a linear fit through regression analysis. The R^2 value obtained for the proposed equations lies between 0.84-0.9 that represents a reasonably high confidence level in light of high variability in thermal properties. Since fibers do not significantly influence the thermal properties, the relations presented here are also applicable for fiber reinforced HSC, SCC and FAC unless stated otherwise. Selected fitted line plots for HSC, SCC and FAC obtained by regression analysis are illustrated in Figures 3.27 to 3.30 against their measured data for thermal conductivity, specific heat, thermal expansion, and mass loss respectively. In these figures, the fitted lines obtained by regression analysis show least deviation and thus provide a near perfect fit for the measured data. Due to property variations in different temperature ranges, the proposed equations give either linear or bi-linear and tri-linear relations.

3.5.1 Relations for Thermal Conductivity

The test data clearly indicate that thermal conductivity is influenced mainly by the type of high strength concrete, moisture retention in concrete and temperature range. To capture this trend

separate expressions are developed for thermal conductivity of HSC, SCC, and FAC. For each concrete type, thermal conductivity relations are presented in two temperature ranges i.e. between 20-400°C and 400-800°C. These relations are presented in Eqs 3.1 to 3.6.

HSC

$k_t = 2.5-0.0033T$ $20°C \leq T \leq 400°C$ (3.1)

$k_t = 2.3-0.002T$ $400°C \leq T \leq 800°C$ (3.2)

SCC

$k_t = 3.12-0.0045T$ $20°C \leq T \leq 400°C$ (3.3)

$k_t = 3-0.0028T$ $400°C \leq T \leq 800°C$ (3.4)

FAC

$k_t = 3-0.0045T$ $20°C \leq T \leq 400°C$ (3.5)

$k_t = 2.6-0.0025T$ $400°C \leq T \leq 800°C$ (3.6)

3.5.2 Relations for Specific Heat

The specific heat is mainly influenced by type of concrete mix (HSC, FAC, SCC) and temperature range. The effect of steel and hybrid fibers is minimal throughout the range of temperature specified. However, polypropylene fibers have some influence on specific heat of HSC and SCC in 650-800°C temperature range. To capture this trend separate equations are proposed for polypropylene fiber reinforced HSC and SCC in 400-800°C temperature range. These relations are presented in Eqs 3.7 to 3.21.

HSC

$c_p = 2.4+0.0002T$ $20°C \leq T \leq 400°C$ (3.7)

$c_p = 2.4+0.0006T$ $400°C \leq T \leq 800°C$ (3.8)

For HSC-P only:

$c_p = 2.4+0.0002T$ $20°C \leq T \leq 400°C$ (3.9)

$c_p = 1.0+0.0043T$ $400°C \leq T \leq 650°C$ (3.10)

$c_p = 9.1+0.009T$ $650°C \leq T \leq 800°C$ (3.11)

SCC

$c_p = 2.4+0.0001T$ $20°C \leq T \leq 400°C$ (3.12)

$c_p = 0.6+0.006T$ $400°C \leq T \leq 800°C$ (3.13)

For SCC-P only:

$c_p = 2.4+0.0001T$ $20°C \leq T \leq 400°C$ (3.14)

$c_p = 0.6+0.006T$ $400°C \leq T \leq 650°C$ (3.15)

$c_p = 10.6-0.01T$ $650°C \leq T \leq 800°C$ (3.16)

FAC

$c_p = 2.7+0.0004T$ $20°C \leq T \leq 400°C$ (3.17)

$c_p = 0.3+0.0065T$ $400°C \leq T \leq 600°C$ (3.18)

$c_p = 3.6+0.0014T$ $600°C \leq T \leq 800°C$ (3.19)

FAC-P

$c_p = 2.63+0.00074T$ $20°C \leq T \leq 400°C$ (3.20)

$c_p = 0.34+0.0021T$ $400°C \leq T \leq 800°C$ (3.21)

3.5.3 Relations for Thermal Expansion

The expression for thermal expansion of HSC, SCC and FAC are presented in Eqs 3.22-3.28. Since thermal expansion of HSC has a direct correlation with temperature, a single equation is developed over entire temperature range. However, as it is observed that low permeability and presence of mineral and chemical admixtures of SCC and FAC have different influence at different temperature range; three different thermal expansion relations are presented to capture the trend. As fibers have no pronounced effect on thermal expansion of HSC or SCC, same relations can be used for fiber reinforced HSC and SCC.

HSC

$\varepsilon_{th} = -0.5+0.001T$ $20°C \leq T \leq 1000°C$ (3.22)

SCC

$\varepsilon_{th} = -0.03+0.001T$ $20°C \leq T \leq 200°C$ (3.23)

$\varepsilon_{th} = -0.2+0.0017T$ $200°C \leq T \leq 700°C$ (3.24)

$\varepsilon_{th} = -0.5+0.002T$ $700°C \leq T \leq 1000°C$ (3.25)

FAC

ε_{th}= -0.03+0.001T 20°C ≤ T ≤ 200°C (3.26)

ε_{th}= -0.17+0.0013T 200°C ≤ T ≤ 600°C (3.27)

ε_{th}= -0.5+0.0005T 600°C ≤ T ≤ 1000°C (3.28)

3.5.4 Relations for Mass Loss

Mass of HSC, SCC and FAC are presented in Eqs 3.29-3.37. Since mass loss does not vary significantly throughout temperature range, a single equation is developed over entire temperature range for all these concretes. As fibers have no pronounced effect on mass loss of HSC, SCC and FAC, same relations can be used for fiber reinforced HSC, SCC, and FAC.

HSC

$M/M_0 = 1$ 20°C (3.29)

$M/M_0 = 1.01-0.0002T$ 20°C ≤ T ≤ 600°C (3.30)

$M/M_0 = 1.25-0.00055T$ 600°C ≤ T ≤ 800°C (3.31)

SCC

$M/M_0 = 1$ 20°C (3.32)

$M/M_0 = 1.01-.00014T$ 20°C ≤ T ≤ 600°C (3.33)

$M/M_0 = 1.01-.00016T$ 600°C ≤ T ≤ 800°C (3.34)

FAC

$M/M_0 = 1$	20°C	(3.35)
$M/M_0 = 1.004-.00016T$	$20°C \leq T \leq 600°C$	(3.36)
$M/M_0 = 1.004-.00019T$	$600°C < T \leq 800°C$	(3.37)

3.6 Summary

Tests were performed to measure high temperature thermal properties of different types of high performance concrete. For all three HPC (HSC, FAC and SCC), thermal conductivity was observed to have very little variation, however; specific heat had significant variation with temperature. Thermal expansion of three HPC increased with temperature and followed almost similar trend with slight variation for SCC. Similarly, the mass loss did not show any significant variation as a function of temperature. The presence of fibers in these HPC has an influence on the specific heat and thermal expansion, but has no effect on thermal conductivity and mass loss property. Data from tests is utilized to develop high temperature relations for thermal properties as a function of temperature. The proposed relations for the thermal properties can be used as input data in computer programs for validations and evaluating the response of HPC structures exposed to fire.

Table 3.1 - Test Matrix for evaluation of thermal properties

S/No	Property	Temperature range (and interval) (°C)	Test equipment	Concrete types (mixes) tested	Number of specimens tested	Total number of tests carried out
1	Thermal conductivity	20 to 400°C @100°C interval and 400 to 800°C @50°C interval	Hot Disk	HSC, HSC-S, HSC-P, HSC-H, SCC, SCC-S, SCC-P, SCC-H, FAC, FAC-P, NSC	28*	14 (11 + 3 repetitions)
2	Specific heat	20 to 400°C @100°C interval and 400 to 800°C @50°C interval	Hot Disk	HSC, HSC-S, HSC-P, HSC-H, SCC, SCC-S, SCC-P, SCC-H, FAC, FAC-P, NSC	28*	14 (11 + 3 repetitions)
3	Thermal expansion	20 to 1000°C @5° C per minute heating rate	TMA	HSC, HSC-S, HSC-P, HSC-H, SCC, SCC-S, SCC-P, SCC-H, FAC, FAC-P, NSC	33*	33
4	Mass loss	20, 100, 200, 300, 400, 500, 600, 700, 800°C	Sensitive balance, calipers and electric heating furnace	HSC, HSC-S, HSC-P, HSC-H, SCC, SCC-S, SCC-P, SCC-H, FAC, FAC-P, NSC	99*	99

* All types of concrete had 20% extra specimens prepared for testing

Table 3.2 - Mix proportions of plain HSC, SCC, FAC, and NSC batches

Components	HSC	SCC	FAC	NSC
Cement Type I ASTM C-150, kg/m^3	560	327	420	390
Fine aggregate ASTM C-33, kg/m^3	630	735	708	831
Course aggregate ASTM C-33 (max size 10 mm), kg/m^3	1090	904	1040	1038
Silica Fume, kg/m^3	42	-	42	-
Fly Ash (Class C) ASTM C-618 (25% replacement of cement), kg/m^3	-	-	140	-
Slag St Lawrence, kg/m^3	-	76	-	-
Water, kg/m^3	140	143	105	157
Water cement ratio (w/c)	0.25	0.44	0.25	0.4
Water to cementitious ratio (w/cm)	0.23	0.28	0.18	
Air entraining admixture ASTM C-260, kg/m^3	-	3	-	-
Superplastizer , kg/m^3	.24	-	.80	-
Retarding Admixture, kg/m^3	1.63	-	.45	-
High range water reducer ASTM C-494 (Type F), kg/m^3	-	81	-	-
Slump, mm	230	440	100	150
VSI index	-	1.0	-	-
Humidity, %	44	45	42	42
Ambient temperature, °C	23	23	24	22
Concrete mix temperature, °C	20	20	20	21

Table 3.3 - Mix proportions for fiber reinforced HSC

Components	HSC	HSC-S	HSC-P	HSC-H
Cement Type I ASTM C-150, kg/m^3	560	560	560	560
Fine aggregate ASTM C-33, kg/m^3	630	630	630	630
Course aggregate ASTM C-33 (max size 10 mm/0.4 inch), kg/m^3	1090	1090	1090	1090
Silica fume, kg/m^3	42	42	42	42
Polypropylene fibers, kg/m^3	-	-	1	1
Steel fibers, kg/m^3	-	42	-	42
Water, kg/m^3	140	140	140	140
Water cement ratio (w/c)	0.25	0.25	0.25	0.25
Retarding admixture, ASTM C494, mL/m^3	3403	3403	3403	3403
Slump, mm	230	200	100	50
Ambient humidity at casting (%)	44	45	44	44
Ambient temperature, °C	23	23	24	24
Concrete mix temperature at casting, °C	20	20	20	20

Table 3.4 - Mix proportions for fiber reinforced SCC

Components	SCC	SCC-S	SCC-P	SCC-H
Cement type-I ASTM C-150, kg/m^3	327	327	327	327
Fine aggregate ASTM C-33, kg/m^3	735	735	735	735
Course aggregate ASTM C-33 (maximum size 10 mm), kg/m^3	904	904	904	904
Slag St Lawrence ASTM C-989, (Grade 120), kg/m^3	76	76	76	76
water, kg/m^3	143	143	143	143
Water cement ratio (w/c)	0.44	0.44	0.44	0.44
Water to cementitious ratio (w/cm)	0.35	0. 35	0. 35	0. 35
Air entraining admixture, ASTM C-260, kg/m^3	3	3	3	3
High range water reducer & plasticizer, ASTM C-494 (Type F), kg/m^3	81	81	81	81
Slump flow/spread, mm	440	410	420	410
VSI index	1.0	1.0	1.0	1.0
Humidity at casting, %	45	45	45	45
Ambient temperature at casting, °C	23	23	23	23
Concrete mix temperature at casting, °C	20	20	20	20
Steel fibers, kg/m^3	-	42	-	42
Polypropylene fibers, kg/m^3	-	-	1	1

Table 3.5 - Mix proportions for FAC and FAC-P

Components	FAC	FAC-P
Cement (Type I), kg/m^3	420	420
Fine aggregate, kg/m^3	708	708
Course aggregate (max size 10mm), kg/m^3	1040	1040
Silica fume, kg/m^3	42	42
Fly ash - Class C (25% replacement of cement), kg/m^3	140	140
Slag - Grade 120), kg/m^3	76	76
Polypropylene fibers, kg/m^3	-	1
Water, kg/m^3	135	135
Water cement ratio (w/c)	0.32	0.32
Retarding admixture, mL/m^3	3403	3403
Superplasticizer - Type F, kg/m^3	27	27
Slump, mm	100	100
Ambient humidity at casting (%)	47	47
Ambient temperature at casting, °C	24	24
Concrete mix temperature at casting, °C	20	20

Table 3.6 - Compressive strength of plain HSC, SCC and FAC mixtures

Age of concrete (days)	Compressive strength (MPa)			
	HSC	SCC	FAC	NSC
7	71	46	53	20
28	81	61	72	41
90	90	72	86	50

Table 3.7 - Compressive strength of fiber reinforced HSC, SCC and FAC mixtures

Age of concrete (days)	**Compressive strength (MPa)**						
	HSC-S	HSC-P	HSC-H	SCC-S	SCC-P	SCC-H	FAC-P
7	80	72	74	48	45	46	50
28	89	71	67	57	56	57	68
90	90	82	86	70	68	72	74

Table 3.8 - Details of specimens for thermal properties for different batches of concrete.

S No	Type of concrete	Casted samples for thermal properties	Extracted samples thermal properties		Mass loss
			Thermal conductivity and specific heat	Thermal expansion	
		100×100×300 mm prisms	60×60×25 mm prisms	10×18 mm prisms	75×150 mm cylinders
1	HSC	2	4	4	12
2	HSC-P	2	4	4	12
3	HSC-S	2	4	4	12
4	HSC-H	2	4	4	12
5	SCC	2	4	4	12
6	SCC-P	2	4	4	12
7	SCC-S	2	4	4	12
8	SCC-H	2	4	4	12
9	FAC	2	4	4	12
10	FAC-P	2	4	4	12
11	NSC	2	4	4	12

Table 3.9 - Permeability coefficients for different types of concretes

S No	Concrete type	Permeability coefficient	Permeability measurement type
1	SCC	2.1×10^{-17} m^2	Gas permeability (Boel et al., 2008)
2	FAC	1.8×10^{-16} m^2	Gas permeability (Shi et al., 2008)
3	HSC	1.5×10^{-16} m^2	Gas permeability (Noumowé et al., 2009)
4	NSC	$2.4\text{-}6.8\times10^{-12}$ m/s	Liquid and gas permeability procedures (Mindess et al., 2003)

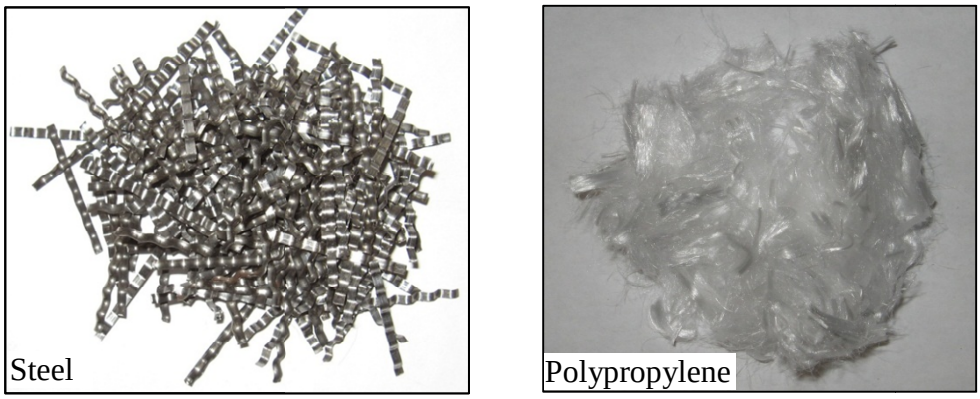

Figure 3.1 - Steel and polypropylene fibers used in the study

(a) (b)

Figure 3.2 - Typical test specimens for undertaking thermal conductivity and specific heat tests


(a) Hot Disk TPS 2500S thermal constants analyzer (b) Furnace

Figure 3.3 - Test setup and apparatus for room temperature and high temperature thermal conductivity and specific heat tests

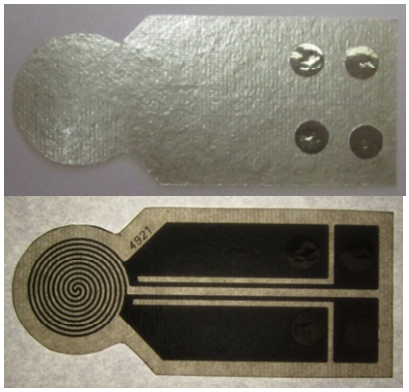
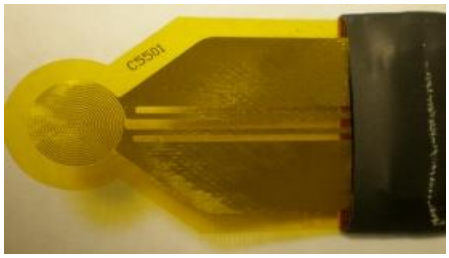

(a) Mica sensor (b) Kapton sensor

Figure 3.4 - Two types of sensors used with Hot Disk TPS 2500S thermal constants analyzer

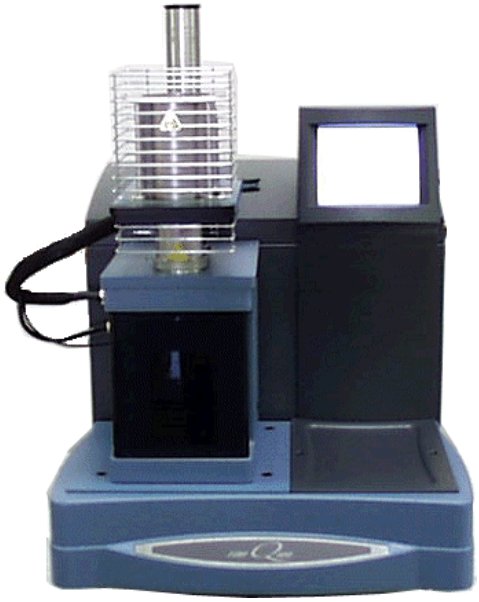

(a)

(b)

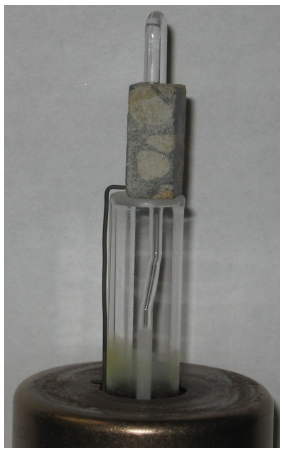

(c)

Figure 3.5 - TMA setup for measurement of thermal strain as a function of temperature

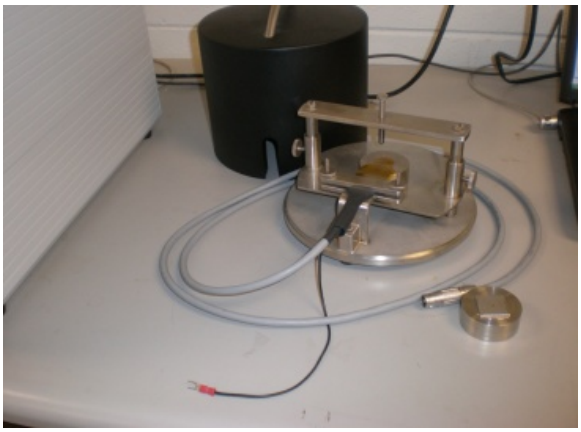

Figure 3.6 - Room temperature sample holder

(a) Hot disk sensor being placed between two concrete specimens

(b) Concrete specimens ready for thermal property tests with sensor placed inside

Figure 3.7 - Hot Disk (TPS) mica sensor being used between two specimens of concrete

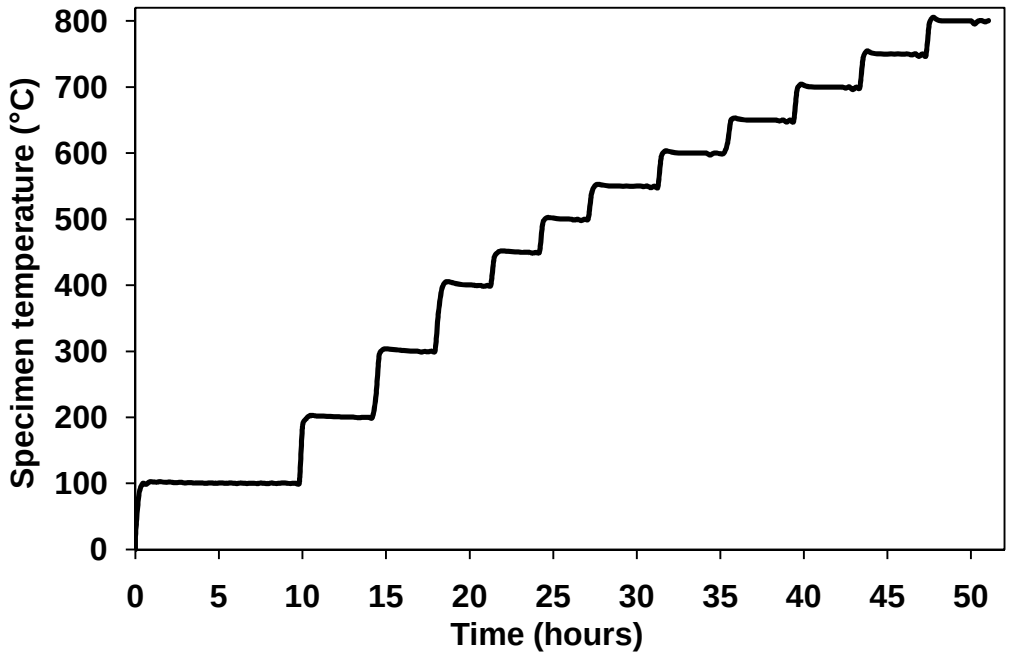

Figure 3.8 - Time-temperature graph showing heating rate and stabilizing time for Hot Disk tests

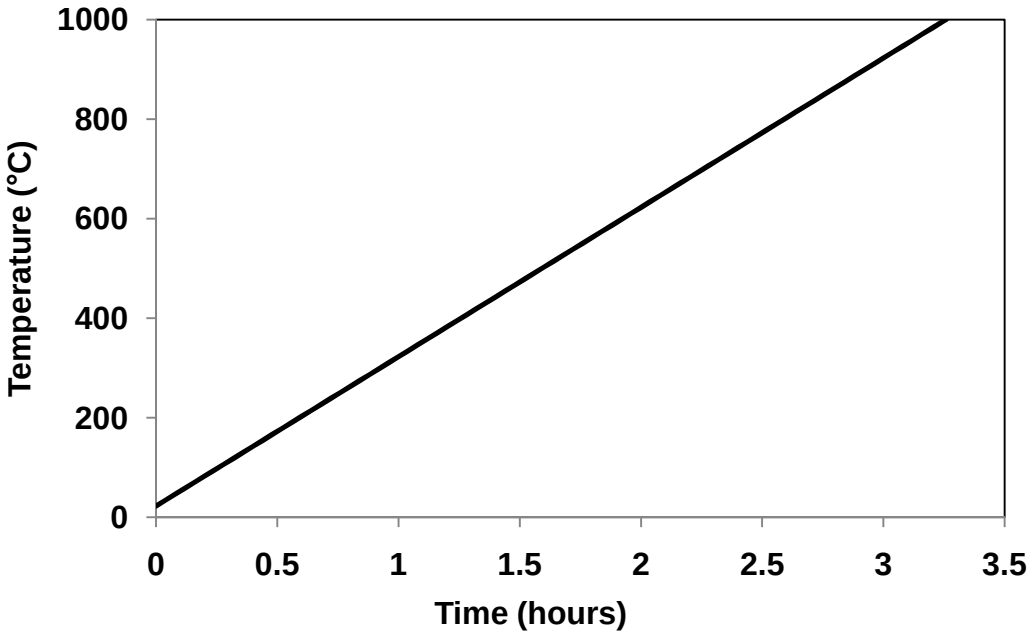

Figure 3.9 - Time-Temperature graph showing heating rate for thermal expansion tests

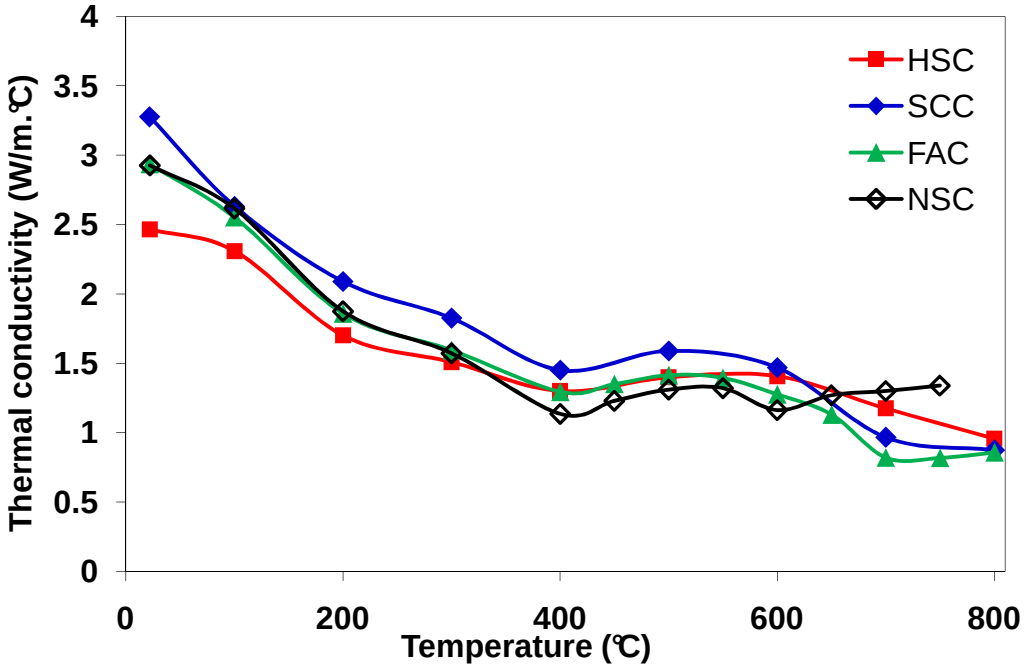

Figure 3.10 - Measured thermal conductivity as a function of temperature for HSC, SCC, FAC and NSC

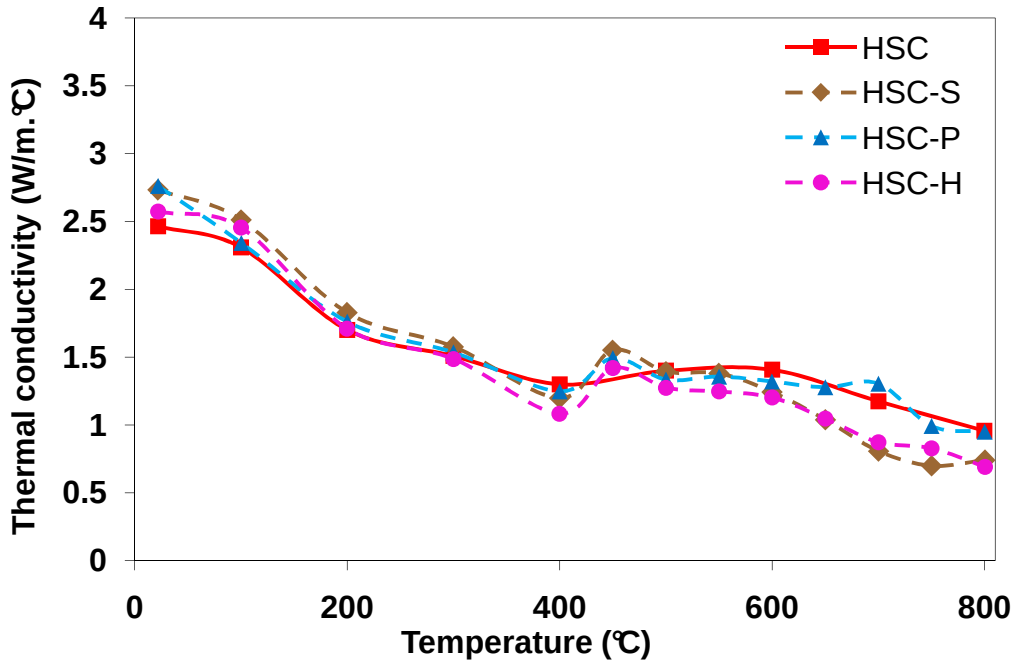

Figure 3.11 - Measured thermal conductivity as a function of temperature for plain and fiber reinforced HSC

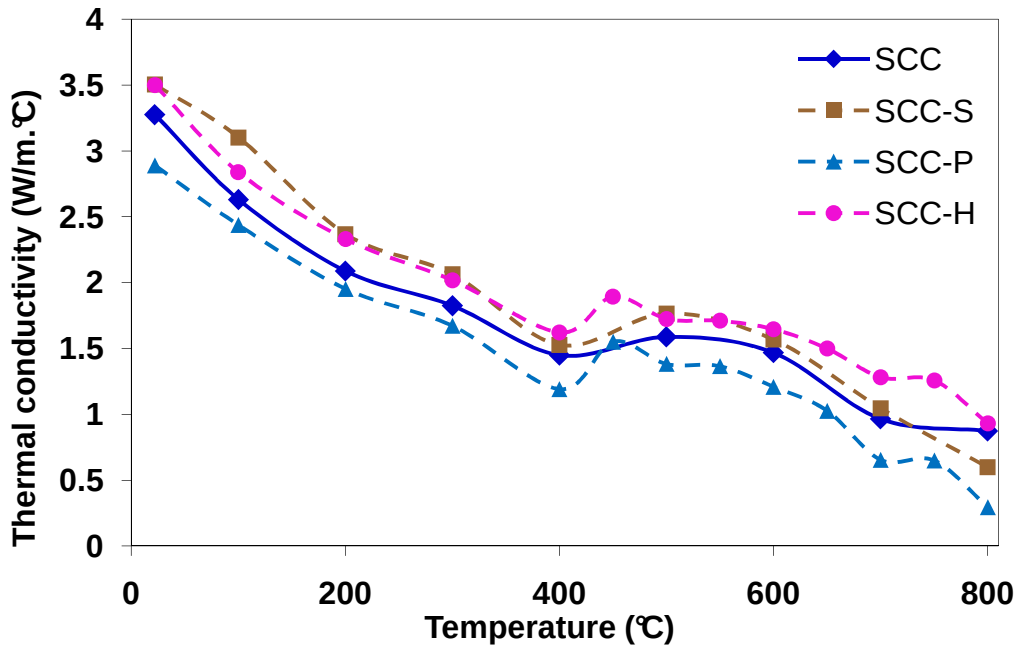

Figure 3.12 - Measured thermal conductivity as a function of temperature for plain and fiber reinforced SCC

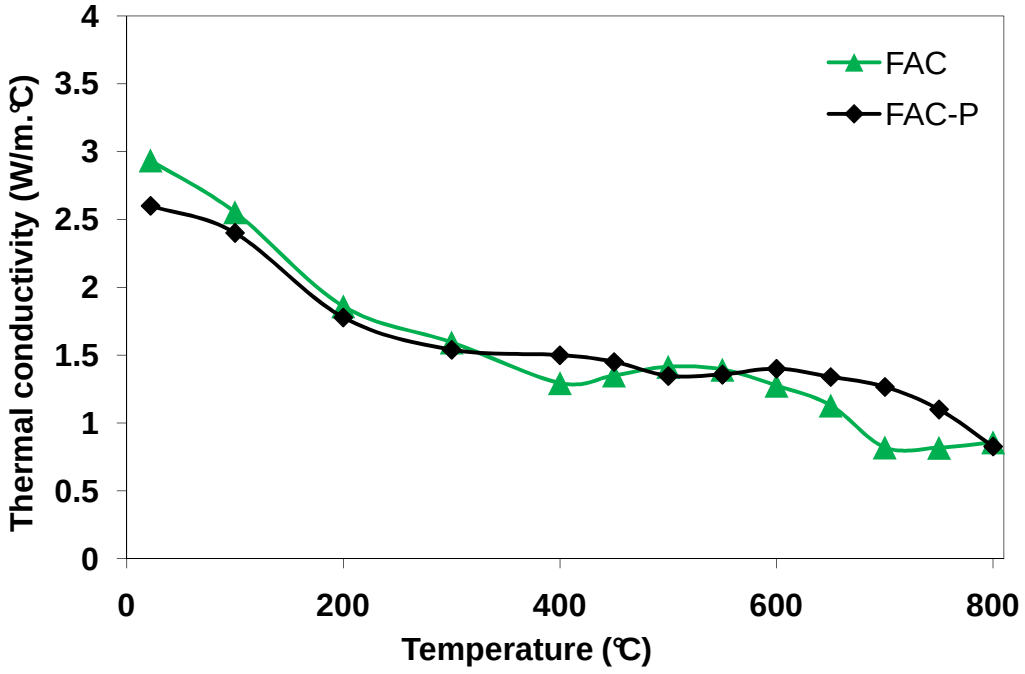

Figure 3.13 - Measured thermal conductivity as a function of temperature for FAC and FAC-P

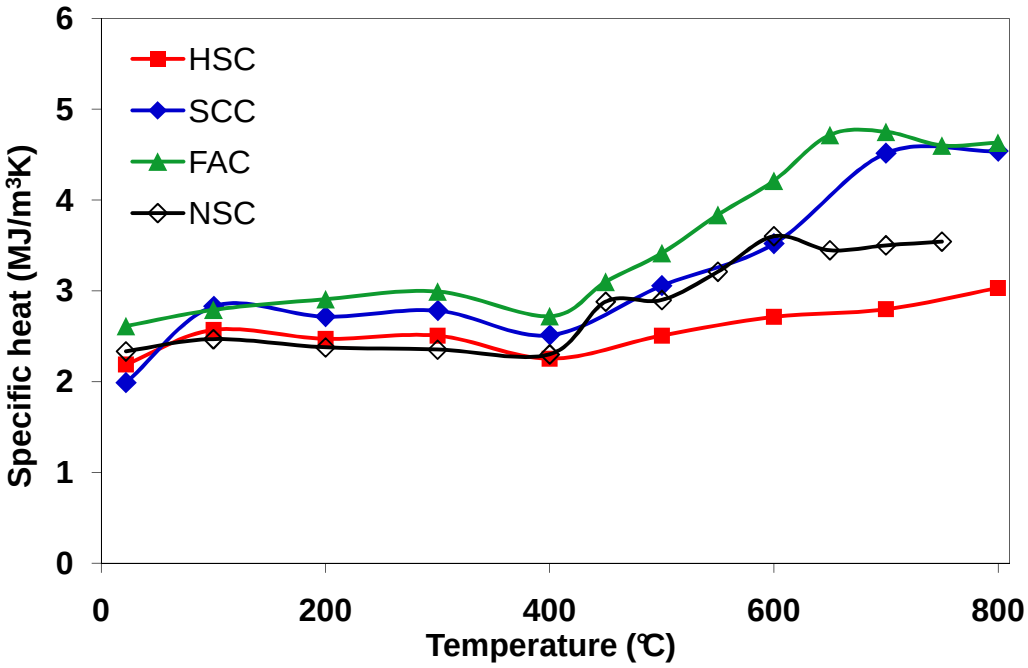

Figure 3.14 - Measured specific heat as a function of temperature for different HSC, SCC, FAC and NSC

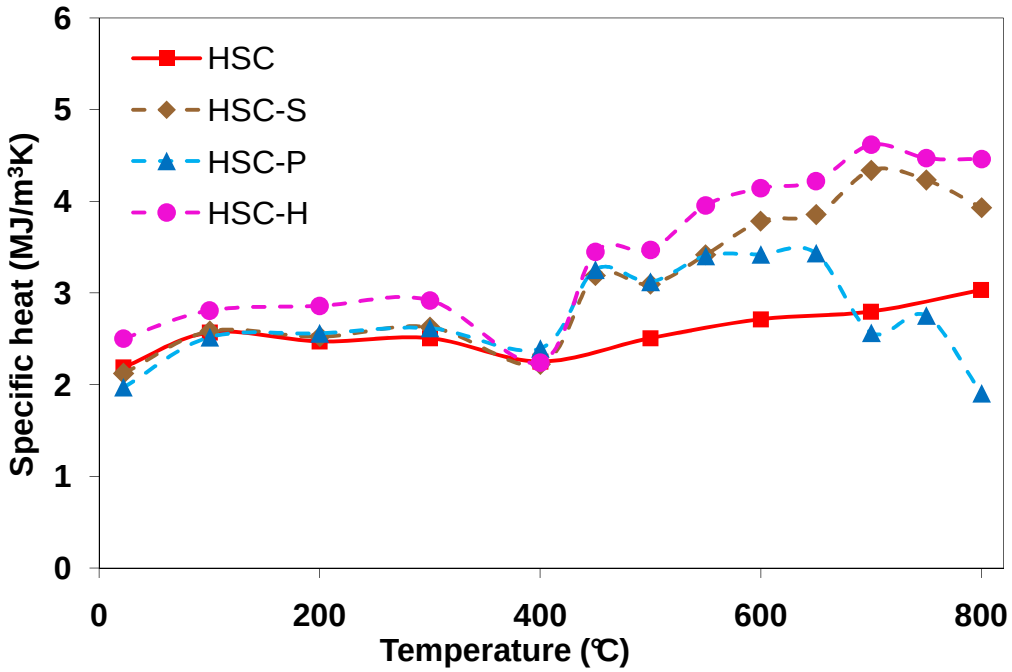

Figure 3.15 - Measured specific heat as a function of temperature for plain and fiber reinforced HSC

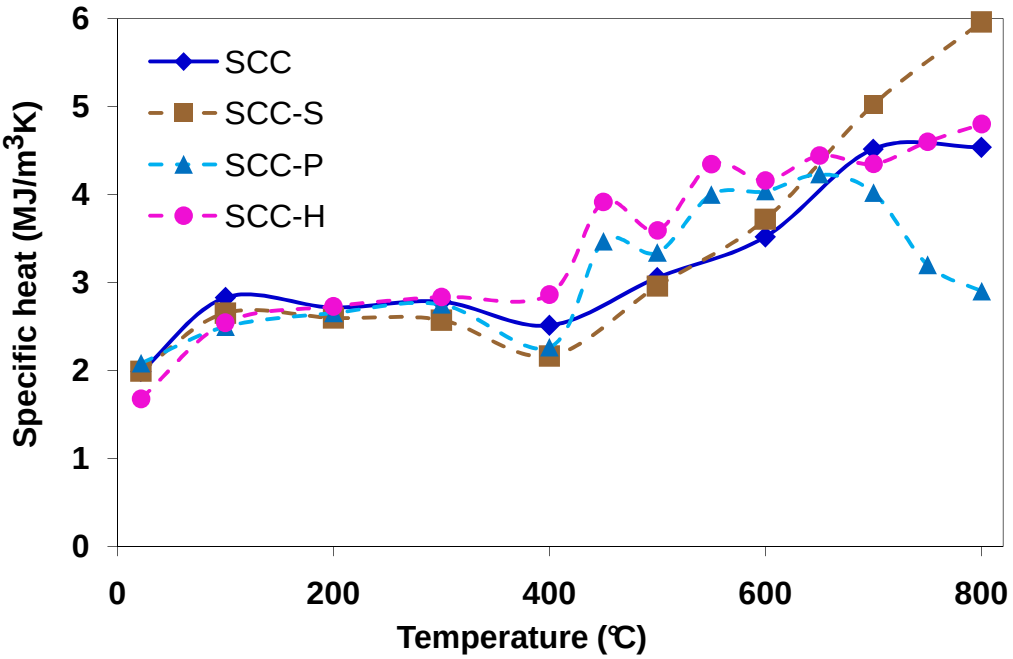

Figure 3.16 - Measured specific heat as a function of temperature for fiber reinforced SCC

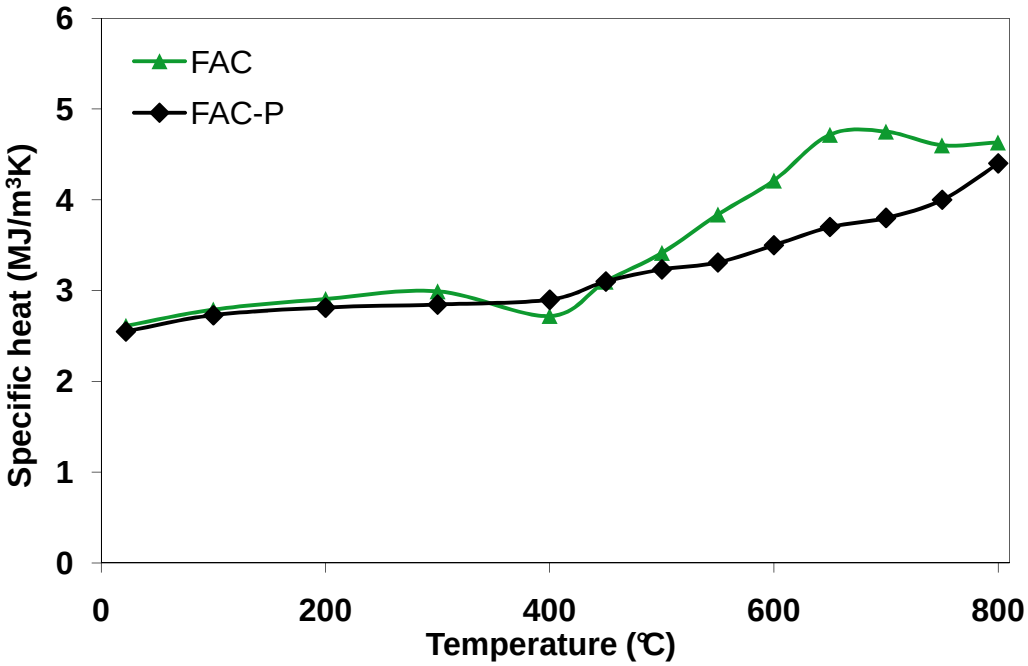

Figure 3.17 - Measured specific heat as a function of temperature for FAC and FAC-P

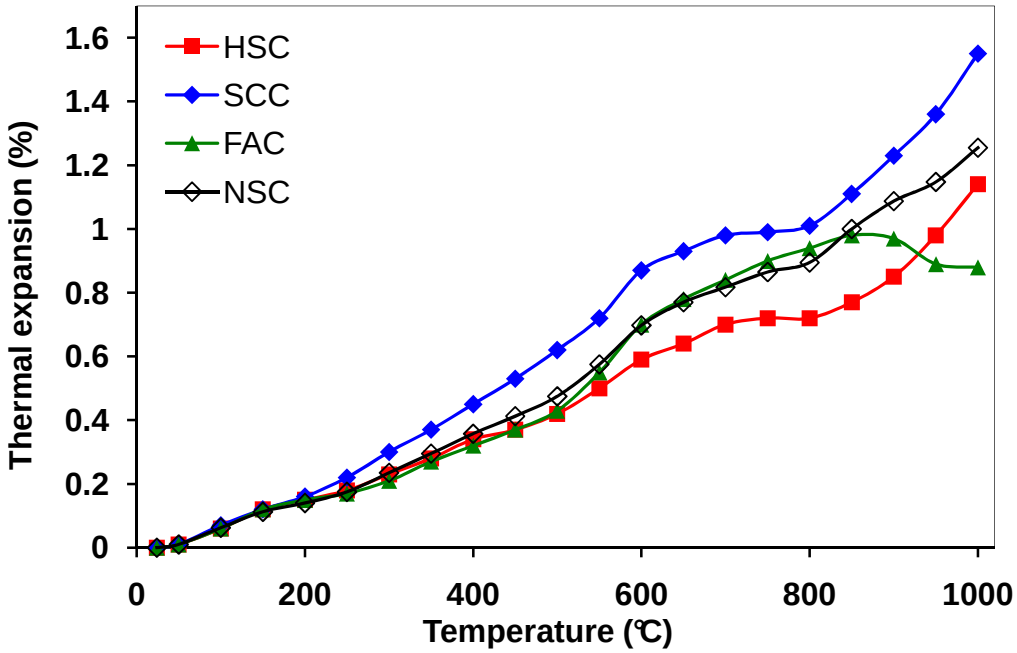

Figure 3.18 - Measured thermal expansion as a function of temperature for HSC, SCC, FAC and NSC

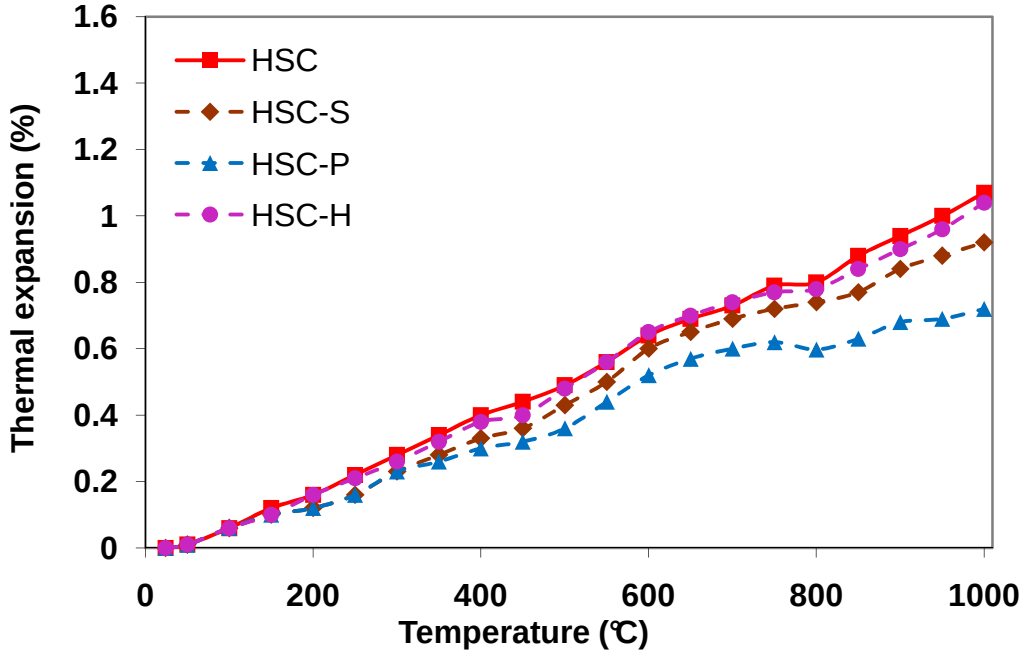

Figure 3.19 - Measured thermal expansion as a function of temperature for plain and fiber reinforced HSC

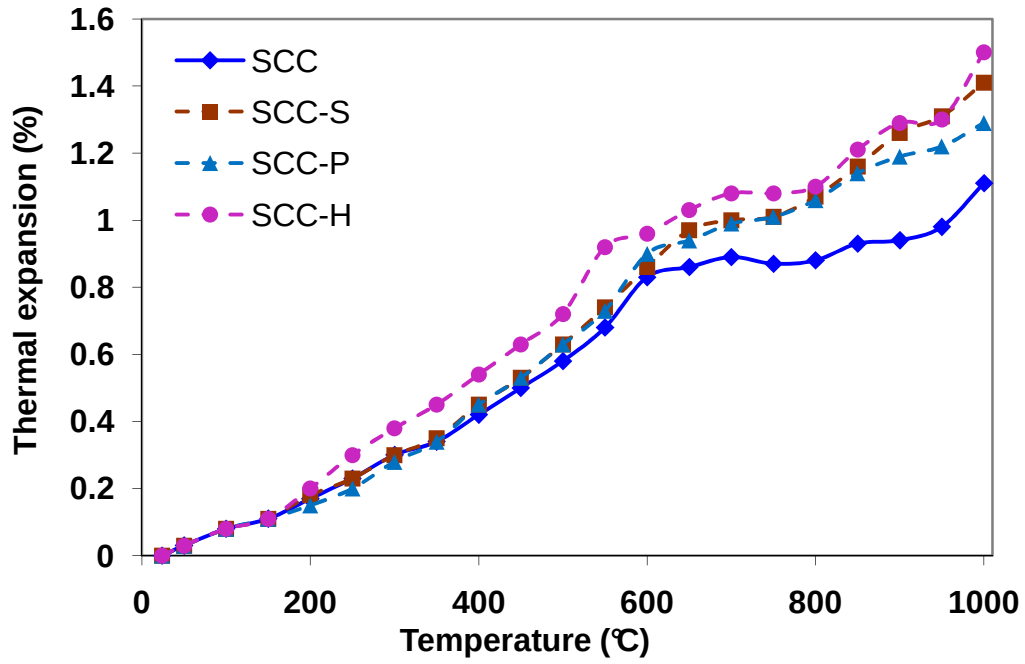

Figure 3.20 - Measured thermal expansion as a function of temperature for plain and fiber reinforced SCC

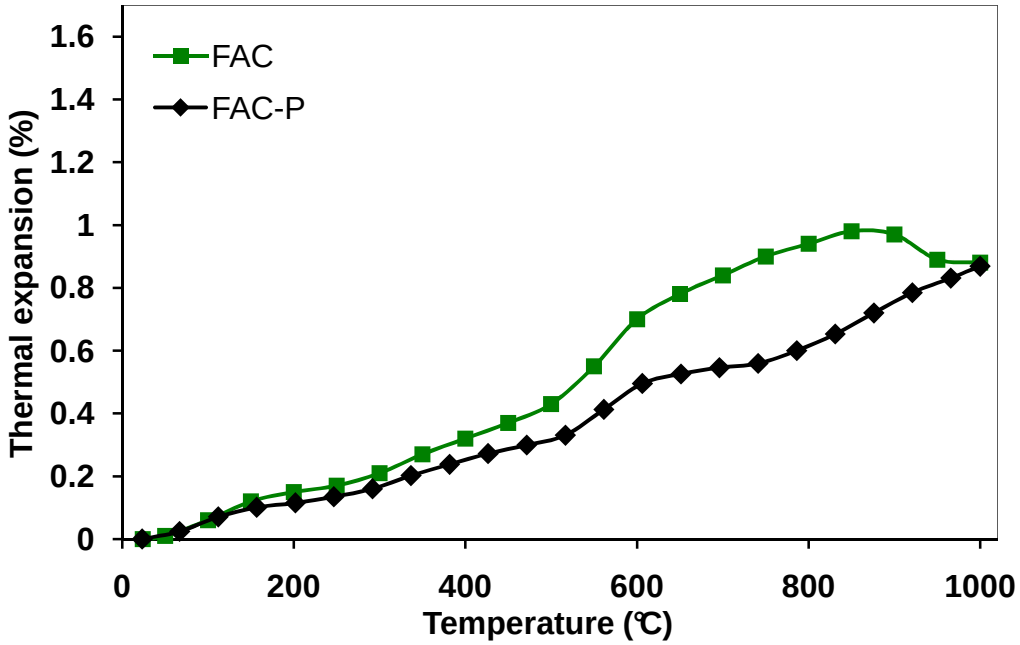

Figure 3.21 - Measured thermal expansion as a function of temperature for FAC and FAC-P

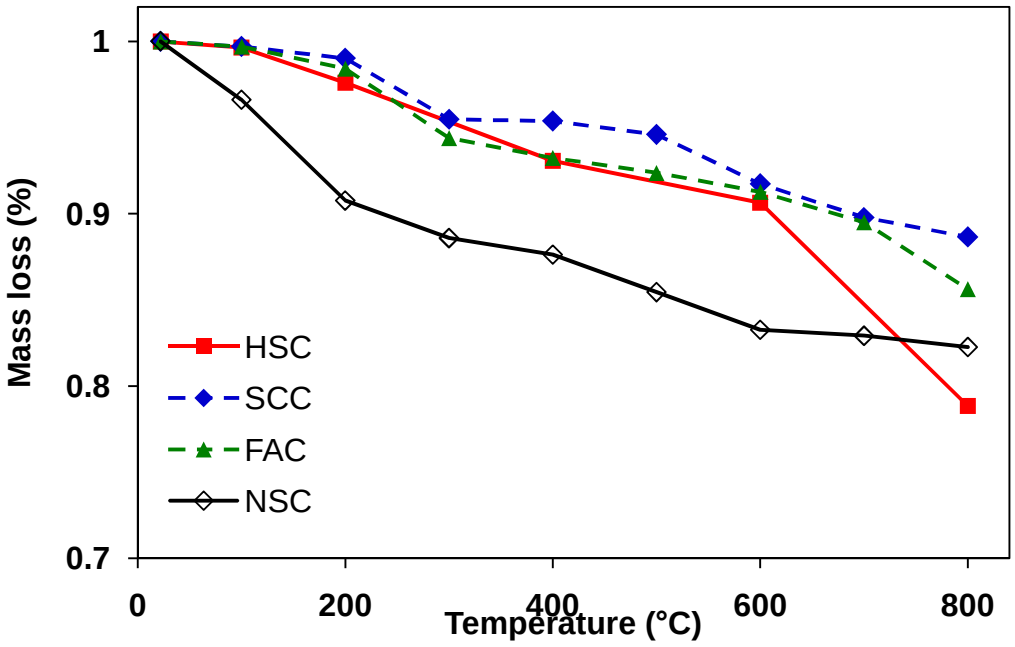

Figure 3.22 - Measured mass loss as a function of temperature for HSC, SCC, FAC and NSC

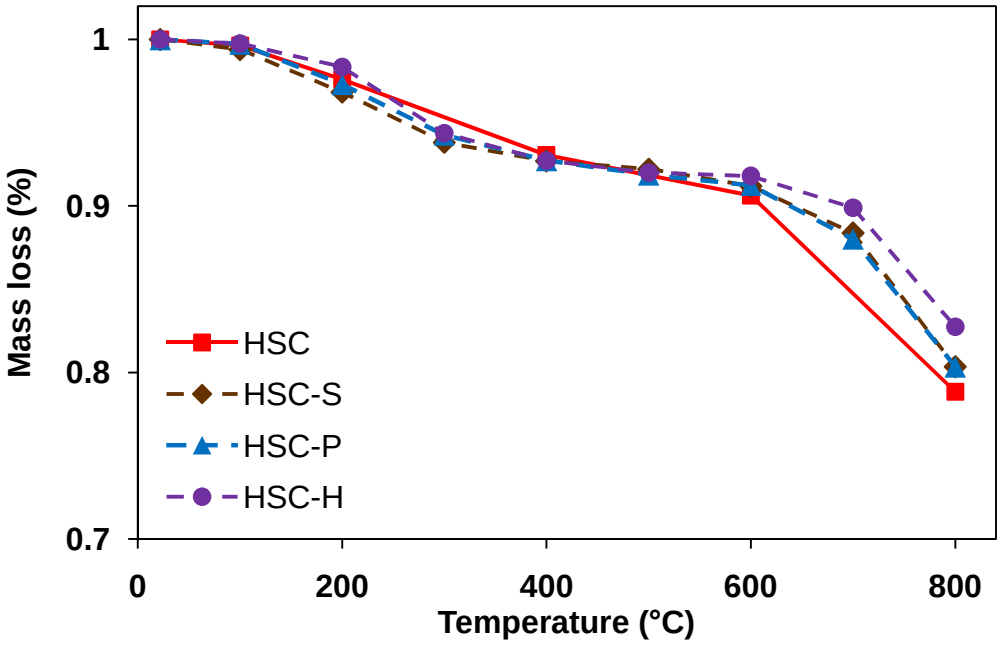

Figure 3.23 - Measured mass loss as a function of temperature for plain and fiber reinforced HSC

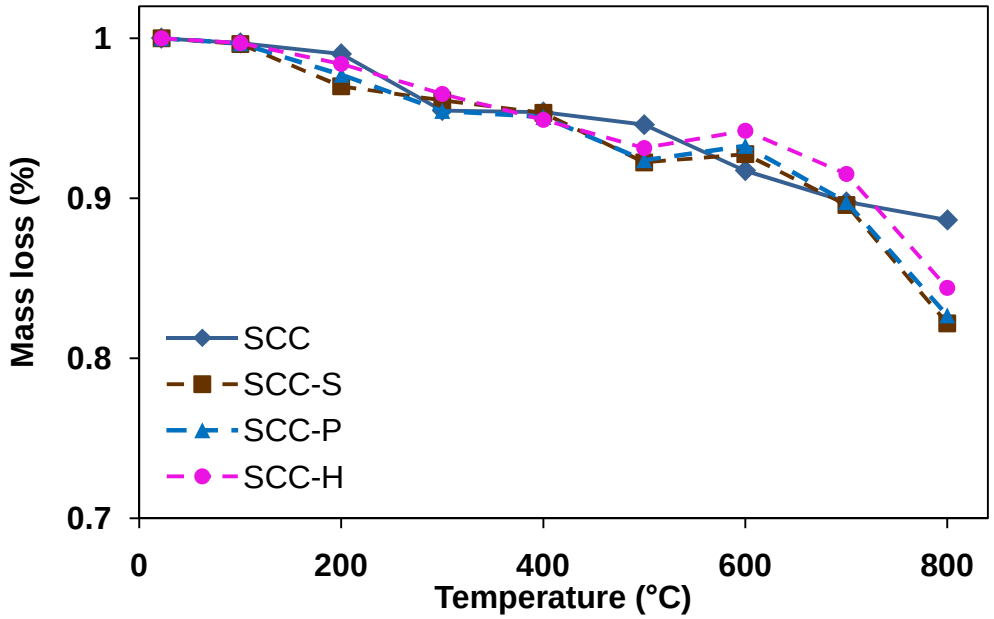

Figure 3.24 - Measured mass loss as a function of temperature for plain and fiber reinforced SCC

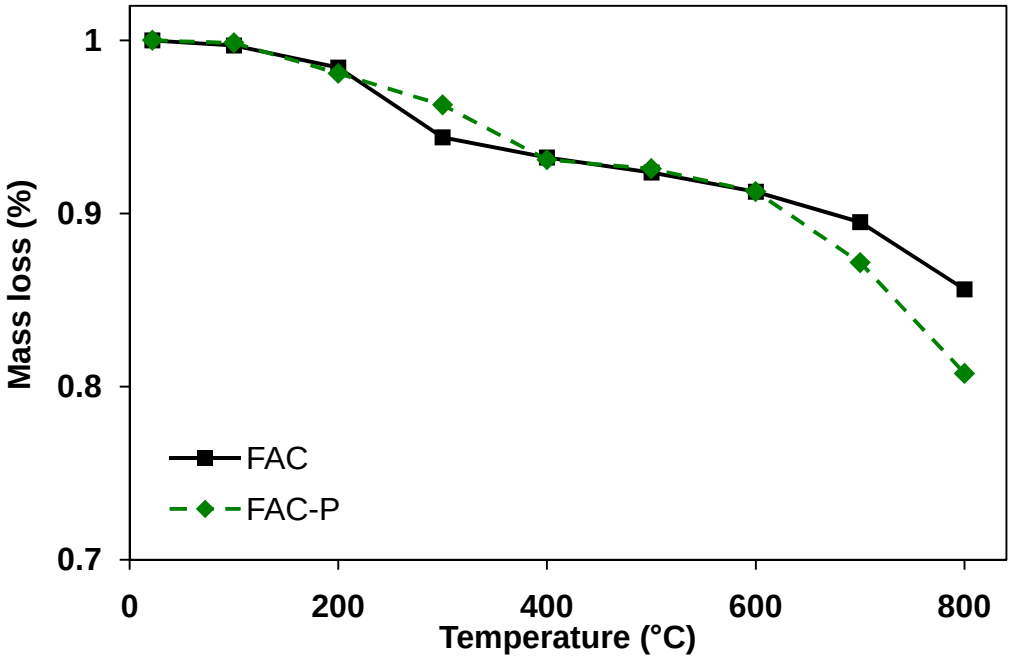

Figure 3.25 - Measured mass loss as a function of temperature for FAC and FAC-P

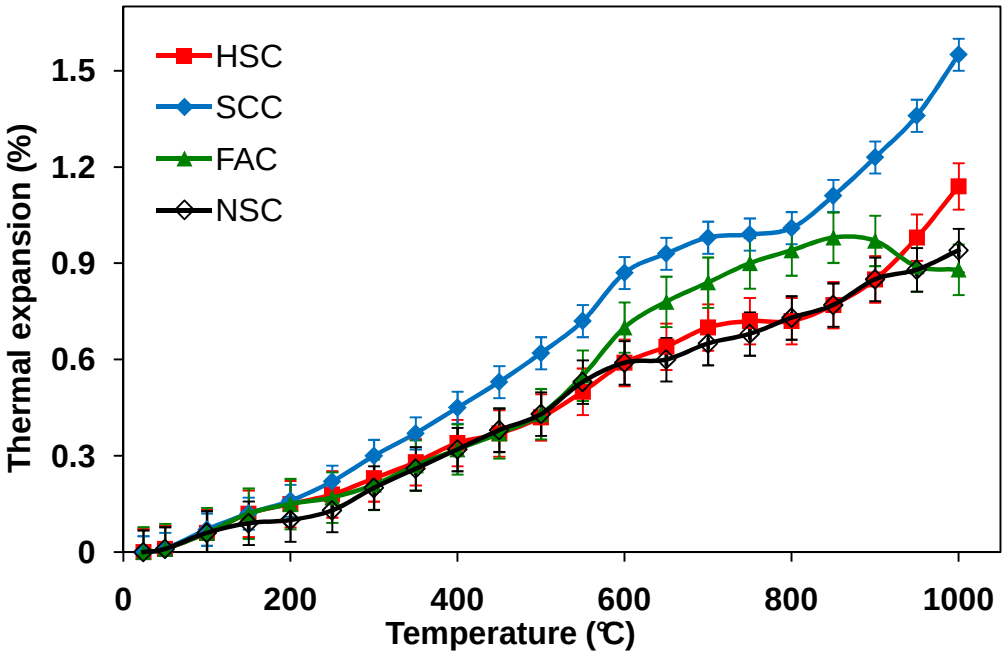

Figure 3.26 - Thermal expansion plot showing error bars for standard deviation for HSC, SCC, FAC, and NSC

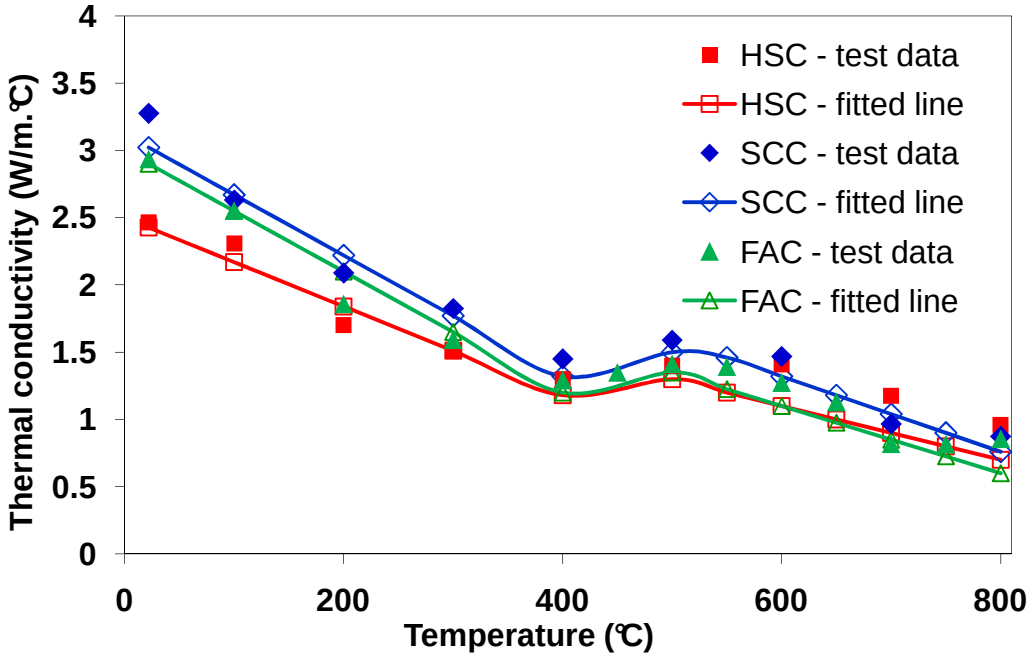

Figure 3.27 - Thermal conductivity data verses fitted lines for HSC, SCC, and FAC

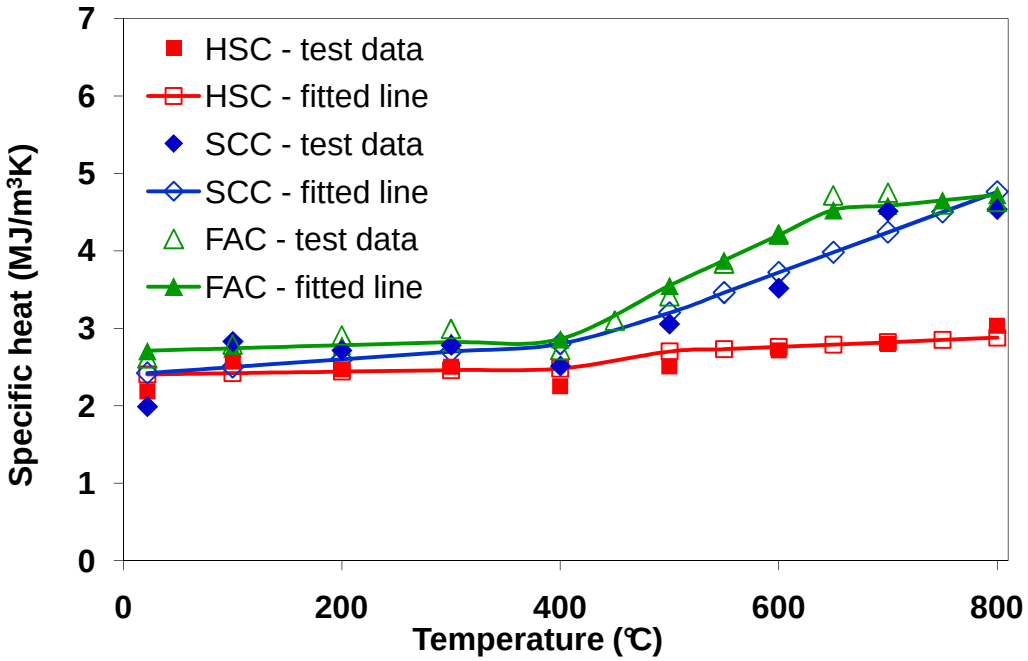

Figure 3.28 - Specific heat data verses fitted lines for HSC, SCC, and FAC

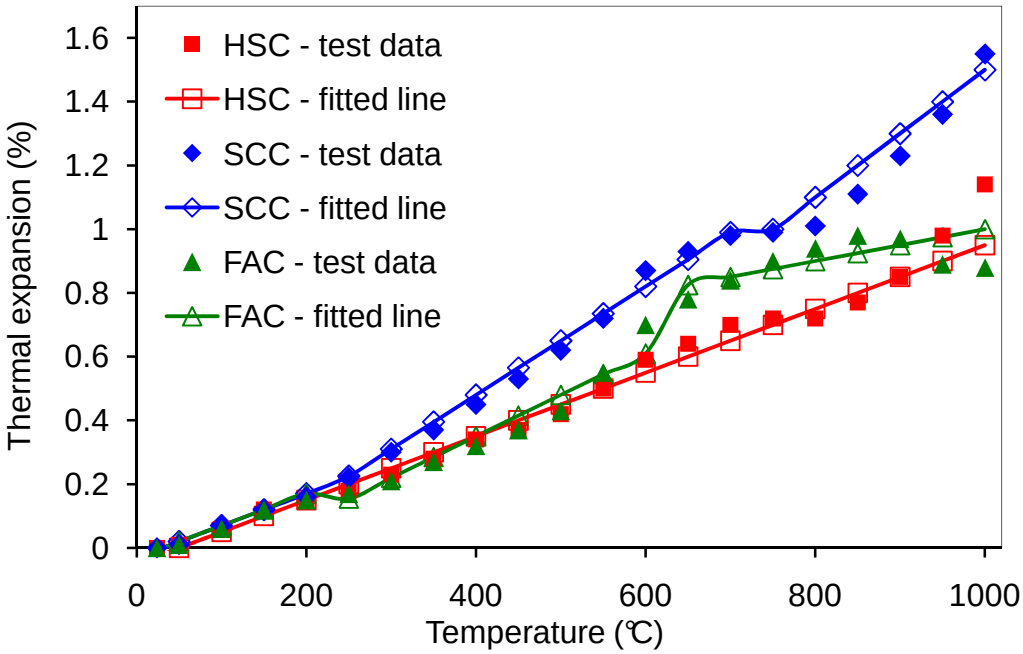

Figure 3.29 - Thermal expansion data verses fitted lines for HSC, SCC, and FAC

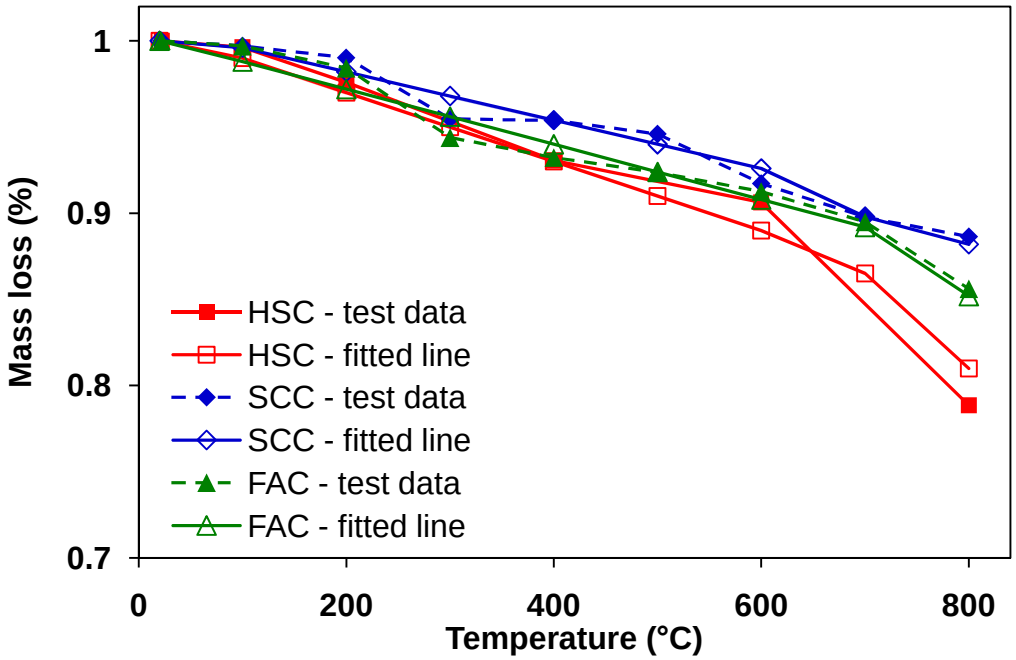

Figure 3.30 - Mass loss data verses fitted lines for HSC, SCC, and FAC

CHAPTER 4

4 MECHANICAL PROPERTIES CHARACTERIZATION

This chapter is mainly based on the following journal papers:

- Khaliq, W., and Kodur, V. K. R. (2010). "Effect of high temperature on tensile strength of different types of high-strength concrete." Conference Presentation, ACI Spring Convention, Chicago, IL.
- Khaliq, W., and Kodur, V. K. R. (2011). "Effect of high temperature on tensile strength of different types of high-strength concrete." ACI Mater Journal, 108(4), 394-402.
- Khaliq, W., and Kodur, V. (2011). "High temperature properties of fiber reinforced high strength concrete." Innovations in Fire Design of Concrete Structures - ACI SP 279, 3-1-42.
- Khaliq, W., and Kodur, V. (2011). "Thermal and mechanical properties of fiber reinforced high performance self-consolidating concrete at elevated temperatures." Cement and Concrete Research, 41(11), 1112-1122.
- Khaliq, W., and Kodur, V. K. R. (2012). "High temperature mechanical properties of high strength fly ash concrete with and without fibers." ACI Mater Journal, submitted and reviewed.

4.1 General

For evaluating fire response of concrete structural members, mechanical properties of high performance concretes (HPC) are required. These properties include strength, elastic modulus, stress-strain curves which vary with temperature. As discussed in the literature review Chapter, there is lack of data on high temperature mechanical properties of HPC. Availability of high

temperature mechanical property relations for HPC is critical for evaluating the strength degradation of structural members made of such concrete types.

In order to evaluate the effect of temperature on mechanical properties of HPC, high temperature property tests on compressive strength, tensile strength, elastic modulus and stress-strain behavior were carried out. The generated property data was utilized to develop relations for various mechanical properties as a function of temperature in 20-800°C. Details of experimental design, test equipment, test procedures and obtained results are discussed in this chapter.

4.2 Design of Mechanical Property Experiments

The test program was designed to undertake high temperature mechanical property tests on three types of high performance concrete mixes namely HSC, SCC, and FAC. To further study the effect of fibers on mechanical properties, three types of fibers namely steel, polypropylene and hybrid fibers were added to HSC, SCC, and FAC concrete mixes. For the tests, a number of cylinders were fabricated from each batch of concrete. These cylinder specimens were tested at various temperature points in 20-800°C temperature range to evaluate mechanical properties. For comparison purpose NSC specimens were also tested for compressive strength and splitting tensile strength behavior at elevated temperatures. As sufficient data is available for stress-strain curves and elastic modulus in literature on HSC and NSC mixes, therefore, these tests were not carried out for NSC, HSC and fiber reinforced HSC to reduce time and effort.

In the absence of standardized test methods for high temperature strength tests on concrete in ASTM standards, RILEM (2000; 1995) test procedures were mostly followed to evaluate the mechanical properties of concrete. Special handling techniques were developed as part of this study to transfer heated cylinders from furnace to strength test machine. For this purpose a thermal jacket was used to transfer the specimens for compressive strength and stress-strain tests

and insulated steel bracket frame was used to transfer specimens for splitting tensile strength tests. The strength test machine was also upgraded to accomplish high temperature tests on concrete (HPC) cylinders.

4.3 Mechanical Property Tests

Mechanical property tests, namely compressive strength, splitting tensile strength, elastic modulus and stress-strain curves were carried out on HSC, SCC, FAC and NSC as per test matrix given in Table 4.1. Details on specimen fabrication, test equipment, and test procedure are presented in this Section.

4.3.1 Mix Proportions

For mechanical property tests, cylinders were prepared from the same concrete batch mixes (HSC, SCC, FAC and NSC) as those used for thermal properties and the cylinders were cast at the same time under similar conditions. The details of the mix proportions, laboratory conditions at time of casting of these concretes are given in Chapter 3 in Tables 3.1 to 3.4. Room temperature compressive strength details of for plain and fiber reinforced HSC, SCC, FAC, and NSC at 7, 28, and 90 days are given in Chapter 3 in Tables 3.5 and 3.6 respectively. The 28 day compressive strength of different concretes ranged from 52-81 MPa for plain NSC, HSC, SCC, and FAC as given in Table 3.6. The 28 days compressive strength of fiber reinforced HSC, SCC, and FAC ranged between 56-89 MPa as given in Table 3.7.

4.3.2 Test Specimens

From each batch of HSC, SCC, FAC, and NSC, two sizes of cylinders were fabricated; 100×200 mm cylinders for room temperature compressive strength tests and 75×150 mm cylinders for high temperature compressive strength, stress-strain curves, and splitting tensile strength tests.

The use of smaller cylinders for high temperature properties was due to limitations on heating chamber of the electrical furnace. The heating chamber is of 150×200 mm size and specimen smaller than the furnace chamber can fit inside for exposure to high temperature. RILEM (2000; 1995) test standards do not impose a limitation on size of specimens for high temperature mechanical properties; therefore a specimen size of 75×150 mm cylinder was selected for this study.

The details on size and number of cylinders for high temperature mechanical properties are given in Table 4.2. In this table the difference in quantities of cylinders for high temperature strength tests is due to number of target temperatures tested for that particular concrete type. Two type K thermocouples (TCs) were embedded in cylinders one in the middle and one on the surface of the cylinder. Figure 4.1 illustrates these locations of thermocouples on a cylinder. For calibration purpose, 25% of test cylinders were instrumented with TCs to measure the temperature rise and stabilization times in the cylinder's cross-section during heating and also to measure the temperature drop during the testing process. The age of concrete at the time of mechanical property tests was 6 months or older.

4.3.3 Test Apparatus

The test setup for measuring mechanical properties consisted of an electric furnace (see Figure 4.2) to heat the concrete cylinders and Forney strength test machine to carry out compressive strength (including elastic modulus and stress-strain curve tests) and splitting tensile strength tests. In evaluating strength property at elevated temperatures, appropriate heating conditions have to be simulated. The electric furnace used to expose cylinders to heating was specially designed for simulating high temperature conditions and could produce a maximum temperature up to 927°C. It is equipped with internal heating electric elements, with a ramp and hold

temperature controller, capable of generating different heating rates. The furnace heating chamber, with 150×200 mm internal dimensions, is lined with steel jacket to withstand any possible spalling in concrete cylinders.

Forney strength test machine as shown in Figure 4.3, is a load controlled test machine which allows to manually control rate of loading during testing. This strength test machine that was utilized to undertake compressive and splitting tensile strength tests is an 1800 kN load controlled compressive test machine which is capable of loading cylinders up to 318 metric tons.

For stress stain response tests, modifications were done to the Forney strength test machine by introducing a 900 kN load cell and two linear variable displacement transducers (LVDTs). These instruments were connected to a state-of-the-art data acquisition system for recording load-displacement response. This data acquisition equipment is based on 'LabVIEW' measurement software, which helps in real-time data recording by automating several measurements from multiple instruments. Load-displacement measurements were recorded at a frequency of 100 readings/sec and were averaged out to 10 readings/sec as final results.

For handling (transporting) and loading the heated cylinders in compression and splitting tensile strength tests, special arrangements were made. A thermal jacket was used for moving the heated cylinders from the furnace to the Forney strength test machine for compressive strength tests (see Figure 4.4). This thermal jacket composed of 50 mm thick 'fiberfrax' high temperature insulation blanket sheet material (made of refractory ceramic fibers) and was designed to wrap tightly around heated cylinders. Use of thermal jacket allowed safe and easy transfer of cylinders for carrying out the compressive strength and stress-strain tests for temperatures up to 800°C. The thermal jacket also helped to minimize heat loss in the cylinders during testing and it was

noted through observations on instrumented cylinders that from start of the test to the end of the test an average temperature drop of only 10°C was recorded in cylinder's temperature.

Splitting tensile strength test is more complicated as it requires placing of cylinders in a precise manner under test machine to apply a diametral compressive force as per ASTM C 496 (2011). This gets further challenging under elevated temperatures when cylinder is heated (up to 800°C) and it becomes cumbersome to position (align) the cylinder precisely along its diametral lines. To overcome this problem, a specially designed and insulated steel bracket frame was used to transfer the heated cylinders from furnace to tensile strength test machine as shown in Figure 4.5. This frame had an opening of 45x172 mm at the bottom and was designed in such a manner that the cylinder could be placed on side extending out of this opening. Also two 38 mm wide and 19 mm deep rectangular notches were made on vertical sides of frame so that a steel loading strip of 38x25 mm cross-section would precisely run along and align on top of other diametral side of cylinder (opposite side of bottom opening in frame) as shown in Figure 4.5. To preserve the temperature in the cylinder, this frame was insulated with fiberfrax material. Alignment lines were marked on bracket, as well as on platens of strength test machine, to facilitate aligned placement. The frame thus helped carrying out splitting tensile strength tests at elevated temperatures with safe transfer and precise positioning of cylinders (see Figure 4.6).

4.3.4 Test Procedure

4.3.4.1 General Procedure

The mechanical property tests were carried out at various temperature points using unstressed test method as describe in Section 2.3.2. Figure 4.7 shows the two stages for this test; first the cylinders are heated without preload to the target temperature, and then moved to strength test machine for loading. The test parameters, such as age of concrete at testing, loading and heating

conditions, were followed as per RILEM (2000; 1995). A heating rate (ramp) of 2°C/minute was selected based on the cylinder size and type of tests as per RILEM test procedure (2000; 1995). The time-temperature graph shown in Figure 4.8 illustrates the heating ramp used to heat and hold times required to achieve steady state temperature in the cylinders at a given target temperature.

Figure 4.9 illustrates the temperature progression in the furnace, on the surface and at the center of 75×150 mm test cylinder for the case of 600°C target temperature. Three type K thermocouples (TC), two on the cylinder and one in the furnace (see Figure 4.9(a)) were used to record temperatures in the furnace, at the surface and mid-depth of the cylinder. As expected, the rise in temperature at the center of the cylinder was much slower than the surface and furnace temperature and this is due to low thermal conductivity of concrete (Figure 4.9(b)). It was observed that a hold time of two hours was required to reach the steady state (uniform temperature distribution) in the cylinder at all the target temperatures.

To further confirm effect of hold time required for reaching thermal equilibrium, additional calibration tests were repeated at 100°C with different hold times of 60, 90 and 120 mins. The effect of different hold times on moisture loss is plotted in Figure 4.10. It can be seen in Figure 4.10 that at 100°C, the core (mid-depth of cylinder) temperature was 68, 87, and 100°C at 60, 90 and 120 mins hold time respectively. The corresponding moisture loss with selected hold times was 0.65, 0.6, and 0.4% respectively. These results illustrate that a hold time of 120 mins (2 hours) ensures complete thermal equilibrium to be attained across the cross-section of the cylinder at a target temperature.

4.3.4.2 Compressive Strength

After achieving steady state condition, the heated cylinders were covered in thermal jacket and transferred to strength test machine to undertake compressive strength and stress-strain tests. The cylinders were then moved to strength test machine and gradually loaded at a loading rate of 0.5 MPa per second with a precision of ±1 % (as per RILEM test procedure) till failure occurred and the failure load was recorded. Figure 4.11(a) shows the cylinder prior to undertaking compression (and stress-strain) test and Figure 4.11(b) shows a failed cylinder after compression test. For high temperature compressive strength, one cylinder was tested at each target temperature. Test was repeated to confirm results at select temperatures where recorded result was unusual or lied outside the tolerance range. Compressive strength tests for NSC and HSC (plain and with fibers) were carried out at temperatures 20, 100, 200, 300, 400, 500, 600, and 800°C. For SCC (plain and with fibers) these tests were carried out 20, 100, 200, 400, 600, and 800°C. For FAC and FAC-P the compressive strength tests were done at 20, 200, 400, 600, and 800°C temperatures. The details on the tested temperatures and intervals for compressive strength are given in Table 4.1.

4.3.4.3 Tensile Strength

After heating, the cylinders were carried in steel bracket frame and transferred to strength test machine for undertaking splitting tensile strength tests. The cylinders were then gradually loaded at a loading rate of 0.25 MPa per second till failure occurred and the failure load was recorded. Figure 4.12(a) illustrates the cylinder prior to undertaking splitting tensile strength test, whereas Figure 4.12(b) shows a failed cylinder after failure. For high temperature splitting tensile strength tests, one cylinder was tested at each target temperature. Similar to compressive strength tests, some tests were repeated only at temperatures where recorded data were unusual or lied

outside the tolerance range. Splitting tensile strength tests for NSC and HSC (plain and with fibers) were carried out at temperatures 20, 100, 200, 300, 400, 500, 600, and 800°C. For SCC (plain and with fibers) these tests were carried out 20, 200, 300, 400, 600, and 800°C. For FAC and FAC-P the splitting tensile strength tests were done at 20, 200, 400, 600, and 800°C temperatures. The details on the tested temperatures and intervals for splitting tensile strength are also given in Table 4.1.

4.3.4.4 Stress-Strain Curves and Elastic Modulus

Stress-strain curve tests were carried out on SCC and FAC cylinders both with and without fibers. Figure 4.13 illustrates a cylinder prior to undertaking stress-strain curve test. Test procedure similar to one for compressive strength test was adopted for stress-strain curve tests. Load-deformation data was recorded with data acquisition system by loading the cylinders at a rate of 0.5 MPa per second till failure of the cylinders. While carrying out the tests for stress-strain curves, the failure load was also recorded through control panel of Forney test machine. This failure load was used to counter check the failure loads from compressive strength tests. Collected load-deformation data was used to evaluate stress-strain curves for tested concretes. Elastic modulus for SCC and FAC was calculated from the measured stress-strain curves. Elastic modulus at room temperature is generally evaluated as the slope of compressive stress-strain curve corresponding to 40% of stress (ASTM C39, 2009). This approach was extended to evaluate the modulus at high temperatures. For SCC (plain and with fibers), stress strain curves and elastic modulus was evaluated 20, 100, 200, 400, 600, and 800°C temperatures, whereas for FAC and FAC-P, these properties were evaluated at 20, 200, 400, 600, and 800°C temperatures. The details on the tested temperatures and intervals of these stress-strain tests are given in Table 4.1.

4.4 Results and Discussion

Results from above tests are utilized to discuss the effect of temperature on strength and modulus properties of plain and fiber reinforced HSC, SCC, and FAC in this section. To compare the strength loss with temperature, compressive and tensile strength results of conventional NSC are also discussed included with plain HSC. Effect of fibers on high temperature strength for particular type of concrete is also discussed in separate sub-sections.

4.4.1 Compressive Strength

The recorded applied load at which the heated cylinder failed in compression was used to compute compressive strength at each temperature and these values are plotted as a function of temperature for NSC, HSC, SCC and FAC in Figure 4.14. For all four concretes, compressive strength decreases with temperature which can be attributed to physical and chemical changes that occur in concrete at higher temperatures. This loss is significant in HSC and FAC as compared to NSC and SCC especially at temperatures beyond 300°C. SCC exhibits minimum strength loss throughout 20-800°C temperature range. The higher drop of compressive strength at 100°C in SCC can be attributed to excessive moisture loss at 100°C as SCC has the higher amount of initial moisture content (higher w/c ratio). Of different concretes, FAC exhibits maximum compressive strength loss especially in 20-400°C temperature range.

The relative compressive strength loss in NSC, HSC, SCC and FAC follows similar trend to its absolute strength as shown in Figure 4.15. NSC displays the least loss of compressive strength ratio as compared to HSC. It can be seen that both SCC and NSC exhibit better compressive strength ratio with about 35% of retention of compressive strength at 800°C as compared to HSC and FAC. Moisture content in concrete plays a significant role in retention of compressive

strength in high performance concretes. As in the case of HSC and FAC, low moisture content caused early desiccation leading to higher strength loss as compared to SCC and NSC.

4.4.1.1 High Strength Concrete

The compressive strength evaluated at each temperature is plotted as a function of temperature for HSC with and without fibers in Figure 4.16. In all types of concrete, physical and chemical changes that occur at elevated temperatures lead to significant reduction of compressive strength. HSC (plain and with fibers) gradually lose strength with temperature in 20-800°C range in a similar trend. This loss is slightly higher in 20-400°C and can be attributed to dense microstructure of HSC that undergoes more thermal stresses from evaporation of moisture up to 400°C and does not let water vapors to escape easily. This effect has been established by Castillo and Durrani (Castillo and Durrani, 1990) that moisture in concrete has detrimental effect on high temperature compressive strength of HSC. It can be seen that fibers do not have much effect on high temperature compressive strength of HSC. Beyond 400°C, all four HSCs exhibit similar trend of slower strength loss. This degradation in strength can be attributed to slow disintegration of microstructure due slower loss of chemically bound water in 400-800°C temperature range.

The ratio of recorded compressive strength $f'_{c,T}/f'_c$ for HSC with and without fibers is shown in Figure 4.17. The strength loss is higher in 20-400°C range and lowers in 400-800°C range. This can be attributed to higher loss of physically bound moisture in concrete up to 400°C as explained above. Fibers do not have much pronounced effect on the compressive strength of HSC both at room temperature and at higher temperature.

4.4.1.2 Self-Consolidating Concrete

Measured compressive strength of SCC and fiber reinforced SCC is plotted as a function of temperature in Figure 4.18. For SCC, there is an initial reduction in compressive strength at 100°C and then strength regain at 200°C. SCC is produced with higher water cement ratio; therefore the strength loss at 100°C can be attributed to initial moisture loss which is higher in case of SCC. The increase in strength in 100-200°C temperature range can be attributed to rehydration and moisture migration (Dias et al., 1990; Fares et al., 2010).

It has been established that moisture in concrete has significant effect on high temperature compressive strength of concrete (Castillo and Durrani, 1990). For initial moisture loss up to 100°C, due to evaporation of free water, the strength drops sharply; however, with excess loss of free water (SCC is produced with higher w/c ratio), compressive strength stabilizes at temperatures between 100 and 400°C. Beyond 400°C the strength loss becomes gradual with increase in temperature for SCC and fiber reinforced SCC. This gradual degradation of strength (without substantial drop) can be attributed to slow loss of chemically bound water due to dehydration and disintegration of C-S-H in concrete (FIB Bulletin 38, 2007). In the case of fiber reinforced SCC the loss of compressive strength with temperature is about same for SCC-S, SCC-P and SCC-H throughout temperature range. This can be deduced that the addition of fibers does not have much effect on the variation of compressive strength of SCC with temperature.

The ratio of recorded compressive strength at target temperature $f'_{c,T}$ to compressive strength at room temperature f'_c for SCC and fiber reinforced SCC is shown in Figure 4.19. The relative strength loss in all concretes follow similar trend to its absolute strength. The initial strength reduction at 100°C temperature is attributed to excess moisture lost as SCC (plain and with

fibers) is produced with higher w/c ratio. There is noticeable strength retention in SCC (with and without fibers) even at 800°C and this range from 30 to 44%. This level of strength retention is much higher than conventional HSC, which has less than 20% relative compressive strength at 800°C (Chen and Liu, 2004; Felicetti and Gambarova, 1998). This observation confirms that high strength SCC has superior microstructure and therefore displays better compressive strength even at higher temperatures.

4.4.1.3 Fly-ash Concrete

The compressive strength of FAC and FAC-P, which is plotted in Figure 4.20, decreases with temperature in 20-800°C. In the case of FAC, which has a compressive strength of 86 MPa at room temperature, there is high reduction in compressive strength at 200°C initially, followed by gradual loss in 200-600°C and then again rapid decrease in 600-800°C range. The initial strength loss up to 200°C can be attributed to damage caused by thermal stresses from pore pressure. After the moisture is driven out and pore pressure reduces, the strength loss becomes gradual in 200-600°C and this is mainly due to spreading of microcracks. The high degradation of compressive strength of FAC above 600°C can be attributed to both physical and chemical transformation of concrete that takes place between 600 and 800°C, resulting in decomposition, softening and loss of binder property in concrete (Khoury et al., 1985).

Unlike FAC, FAC-P experiences gradual loss in compressive strength throughout 20-800°C range. Despite lower initial compressive strength at room temperature (than FAC), FAC-P shows significant retention in tensile strength throughout 20-800°C. The moisture in concrete turns in to vapors above 100°C and induces pore pressure resulting in thermal stress on microstructure of concrete. This pore pressure gets alleviated due to increased porosity by melting of polypropylene fibers around 162°C temperature and reduces thermal stresses, which is a reason

for low degradation of compressive strength in FAC-P. In comparison to conventional HSC, FAC follows almost similar trend of strength loss in the entire temperature range. This shows that compressive strength variation of FAC is almost similar to that of conventional HSC.

The ratio of recorded compressive strength at target temperature ($f'_{c,T}$) to that at room temperature (f'_c) for FAC, FAC-P is shown in Figure 4.21. The relative strength loss in FAC and FAC-P follows similar trend to absolute strength variation, however, FAC-P shows much improvement in strength retention in 200-600°C range as compared FAC. This can be attributed to less damage to microstructure of FAC-P, facilitated through increased porosity resulting from melting of polypropylene fibers.

4.4.2 Splitting Tensile Strength

The recorded applied load at which the cylinders failed were used to compute splitting tensile strength (T) as per ASTM C496 (2004), using formula $T=2P/\pi ld$, where (P) is the failure load, (l) is the length and (d) is the diameter of the tested cylinder. Measured splitting tensile strength of NSC, HSC, SCC and FAC is plotted as a function of temperature in Figure 4.22. It can be seen that all concrete types experience loss in tensile strength with temperature. Loss in splitting tensile strength is dependent on the physical and chemical changes that occur at higher temperatures. Except SCC, other concrete types exhibit similar trend in loss of splitting tensile strength throughout 20-800°C temperature range; however in SCC tensile strength was degrade less in 20-400°C temperature range. FAC exhibited lower splitting tensile strength among tested HPC. Beyond 400°C all concretes significantly lose splitting tensile strength mainly because of excessive thermal stresses and thermal incompatibility within the concrete matrix. Moreover

development and spread of micro and macro cracks effect loss of tensile strength more as compared to compressive strength as these expedited the splitting of cylinder under compression.

The relative splitting tensile strength loss in NSC, HSC, SCC and FAC is illustrated in Figure 4.23. Loss of splitting tensile strength in HSC and FAC is similar to conventional NSC. In comparison, SCC exhibits higher tensile strength ratio, especially this ratio is significant and noteworthy in 20-400°C temperature range. This increase in tensile strength is of much advantage in mitigating the fire induced spalling in SCC and therefore can enhance the fire resistance rating of RC members made of SCC.

4.4.2.1 High Strength Concrete

Figure 4.24 illustrates the splitting tensile strength as a function of temperature for HSC with and without fibers. Splitting tensile strength reduces with temperature in all four concretes up to 800°C. In both HSC-S and HSC-H, significant retention in splitting tensile strength is observed up to 300°C which can be effective in minimizing fire induced spalling. This retention in tensile strength can be attributed to effectiveness of steel fibers in bridging cracks under tensile loading. Shah (1991) deduced that fibers substantially enhance room temperature tensile strength of concrete, as fibers suppress localization of microcracks into macrocracks and consequently tensile load capacity of concrete increases. In case of plain HSC and HSC-P the tensile strength loss is higher in 20-800°C temperature range compared to HSC-S and HSC-H.

The ratio of recorded splitting tensile strength $f'_{t,T/} f'_t$ for HSC and fiber reinforced HSC (HSC-S, HSC-P, and HSC-H) is shown in Figure 4.25. The ratio of tensile strength loss is higher for HSC and HSC-P in 20-400°C where as it is least for HSC-S and HSC-H. This can be attributed to effectiveness of steel fibers which arrest crack initiation and propagation. Test data indicates

that HSC and fiber reinforced HSC retain about 35% to 45% of original tensile strength at 600°C which is quite significant and can be effective to mitigate spalling.

4.4.2.2 Self-Consolidating Concrete

Figure 4.26 illustrates the degradation of splitting tensile strength in SCC and fiber reinforced SCC (SCC-S, SCC-P, and SCC-H) as a function of temperature. In the case of SCC which has a lower tensile strength of 4 MPa at room temperature, the reduction in tensile strength is gradual and almost linear in SCC up to 400°C and then there is sharp reduction in tensile strength to 800°C. This sharp reduction in splitting tensile strength beyond 400°C can be attributed to the development of excessive micro and macro cracks resulting from thermal stresses and thermal incompatibility within SCC. This is in line with the reported data by Sideris (2007), Chan (1999) and Khoury (1992).The slower degradation of strength (without substantial changes) at early stages in all SCC's can be attributed to its higher stiffness as compared to fiber reinforced SCC. Both SCC-S and SCC-H display higher ratio of splitting tensile strength in 300-800°C temperatures range which can be attributed to presence of steel fibers which help arrest the development and propagation of micro and macro crack under tensile loading. SCC-P has the lowest splitting tensile strength beyond 250°C which indicates that after melting of polypropylene fibers at about 180°C there is significant degradation in its microstructure resulting from increased porosity.

Figure 4.27 illustrates the ratio of recorded splitting tensile strength at a target temperature $f'_{t,T}$ to the splitting tensile strength at room temperature f'_t for SCC (plain and with different fiber combinations). The ratio plotted in these figures indicates that addition of polypropylene fibers to SCC caused more reduction in splitting tensile strength as can be observed for SCC-P and SCC-

H. Also the figure shows that SCC and fiber reinforced SCC retain about 40 -50% of its tensile strength at 600°C and this is quite significant as compared to plain HSC which has only 30% of its retained tensile strength at 600°C.

4.4.2.3 Fly-ash Concrete

Figure 4.28 shows the splitting tensile strength for FAC and FAC-P as a function of temperature. For FAC, which has a lower initial tensile strength of 4.2 MPa, the reduction in tensile strength is gradual and is almost linear in 20-800°C. This gradual degradation of strength (without substantial changes) can be attributed to enhanced microstructure that results from reaction of fly ash with calcium hydroxide formed during hydration of cement. In the case of FAC-P, the loss in tensile strength is similar to FAC up to 200°C. In both FAC and FAC-P, the early loss of tensile strength in 20-200°C can be attributed to the progression of microcracks resulting from the temperature induced pore pressure.

FAC-P retains significant tensile strength in 200-800°C range and this can be attributed to lesser microstructural damage in concrete facilitated through increased porosity resulting from melting of polypropylene fibers at about 162°C. This increased porosity helps in alleviation of pore pressure generated from moisture movement in FAC-P and reduces the extent of microstructure damage within the matrix and this helps in retention of higher tensile strength up to 600°C.

The ratio of recorded splitting tensile strength at target temperature ($f'_{t,T}$) to splitting tensile strength at room temperature (f'_t) for FAC and FAC-P is shown in Figure 4.29. Measured test data indicates that FAC and FAC-P have about 23, 48% of $f'_{t,T} / f'_t$ at 600°C respectively that is in the range of reported data for high strength concretes, by other authors (Behnood and

Ghandehari, 2009; Li et al., 2004). The improved tensile strength of FAC-P in entire temperature range, as compared to other two concrete types, is mainly due to the beneficial effect of polypropylene fibers that minimizes cracking in concrete as shown in Figure 4.29.

4.4.3 Elastic Modulus

The elastic modulus of concrete is dependent on moisture content and microstructure of hydrated cements products in paste (Bažant and Kaplan, 1996). As physical and chemical changes occur in concrete due to increase in temperature, elastic modulus degrades with temperature. Data generated from compressive stress-strain curves was used to obtain elastic modulus of different concretes at various temperatures.

4.4.3.1 Self-Consolidating Concrete

Figure 4.30 illustrates the relative elastic modulus ($E_{c,T}/E_c$) for SCC (plain and fiber reinforced) as a function of temperature. The elastic modulus for all four concretes decrease in 20-800°C temperature range. SCC exhibits lower elastic modulus which can be attributed to thermal damage to dense microstructure of SCC as compared to SCC-S, SCC-P and SCC-H. Use of fibers in SCC mix helped reduce (slow down) the degradation in modulus. This is achieved through melting of polypropylene fibers as they help alleviate pore pressure (thermal stresses), steel fibers help reduce propagation of micro and macro cracks and hybrid fibers help reduce both of these affects combined. SCC-H therefore exhibits the least deterioration in elastic modulus as compared to other types. The reduction in elastic modulus in SCC is similar to that reported by Persson (2004) and Bamonte and Gambarova (2010). However, the ratio of reduction for elastic modulus of fiber reinforced SCC is much less compared to SCC which is

attributed to presence of different fibers to SCC mix that enhances its elastic modulus at higher temperatures.

Modulus for SCC-S and SCC-H initially remains constant up to 100°C and then sharply reduces up to 200°C before gradual decay in the temperature range of 200-800°C. The higher modulus observed in SCC-S and SCC-H can be attributed to increased ductility due to the presence of steel fibers which act as crack arresters as these provide necessary bond against development of cracks. The addition of polypropylene fibers in SCC-P show higher degradation of elastic modulus in 20-200°C temperature range, in comparison to SCC-S and SCC-H. This higher loss in elastic modulus is higher in 20-200°C, but this degradation reduces above 200°C, after melting of polypropylene fibers.

4.4.3.2 Fly-ash Concrete

Measured elastic modulus for FAC and FAC-P at various temperatures is shown in Figure 4.31. For both FAC and FAC-P, the modulus of elasticity remains almost constant up to 200°C, decreases at a faster rate up to 600°C, and then finally stabilizes in 600-800°C reaching to about 7-8% at 800°C. This loss in elastic modulus with temperature is attributed to physical and chemical changes and thermal incompatibility of constituents. The loss of moisture due to high temperature and degradation of microstructure concrete results development of and propagation of micro and macro cracks that lead to degradation of elastic modulus.

In 200-600°C, FAC-P retains higher elastic modulus as compared to FAC and this can be attributed to relatively lower damage that occurs in FAC-P facilitated by melting of polypropylene fibers that reduces crack propagation under thermal stresses. Also, FAC has lower elastic modulus than that of conventional HSC in 200-600°C range and this is primarily due to

higher temperature induced damage in FAC resulting from dense microstructure and reduced permeability because of secondary hydration of fly ash in the mix (Nasser and Marzouk, 1979).

4.4.4 Stress-Strain Curves

The recorded load-deformation data in compressive stress-strain response was utilized to generate stress-strain curves at various temperatures for different HPC. The stress-strain response was obtained by measuring load-deformation through load controlled technique; as a result the descending branch of most of the curves could not be captured in totality. However, in some cases (such as SCC-S and SCC-H) where steel fiber was used in the mix, short descending branch of nonlinear portion of the curves could be captured due to their ductile response. As high temperature stress-strain response of HSC is available in literature, the stress-strain curves for SCC and FAC (with and without fibers) are presented in this section.

4.4.4.1 Self-Consolidating Concrete

Stress-strain curves for SCC, SCC-S, SCC-P, and SCC-H are plotted in Figures 4.32 to 4.35 respectively. At room temperature, both SCC and SCC-S, show linear-elastic response up to about 80% of peak stress. It can also be observed that room temperature peak stress decreases and peak strain increases in SCC-S and SCC-H as compared to SCC and SCC-S. It can be inferred that polypropylene fibers in SCC-P and SCC-H do not contribute much to the ductility of concrete. However, presence of steel fibers in both SCC-S and SCC-H has significantly enhanced the ductility of these concretes as shown in Figures 4.33 and 4.35.

For SCC and fiber reinforced SCC, the gradient (slope) of stress-strain curves decrease with temperature showing a drop in peak stress, and increase in peak strain. The plotted total strain is mainly composed of mechanical stain due to loading and thermal strain due to temperature. As

the tested were done by unstressed test method (heating without applied load), therefore the creep and transient strains are not significant in the measured (total) strain. In all these concrete, development of micro and macro cracks due to high temperatures lead to rapid increase in peak strains. Figures 4.32 to 4.35 illustrate that SCC-S and SCC-H attains higher peak strains as compared to SCC and SCC-P with increasing temperature. The attainment of higher strains in SCC-S and SCC-H can be attributed to two factors, namely stress-induced thermal strain and arresting of crack development due to presence of steel fibers. It is reported by Bažant and Chern (1987) that the stress-induced thermal strain in concrete is due to micro diffusion of pore water between capillary pores and gel pores. Therefore, higher peak strain in SCC-S and SCC-H can be attributed to additional thermal strain caused by easy diffusion of pore water facilitated due to increased ductility resulting from steel fibers.

4.4.4.2 Fly-ash Concrete

Figures 4.36 and 4.37 illustrate the stress-strain curves for FAC and FAC-P respectively at various temperatures. At room temperature, both FAC and FAC-P, show linear-elastic response up to about 80% of peak stress similar to high strength SCC and SCC-P. For FAC-P, short descending branch of nonlinear portion of the curves could be captured due to ductile response of FAC-P. It can also be observed that room temperature peak stress decreases and peak strain increases in FAC-P as compared to FAC. It can be seen that presence of polypropylene fibers has some contribution on its improved ductility.

For both FAC and FAC-P, the gradient of stress-strain curves decrease with temperature showing a drop in peak stress, and increase in peak strain. The plotted total strain is mainly composed of mechanical stain due to loading and thermal strain due to temperature due to similar reasons that the tested cylinders were not loaded during heating. Therefore the creep and transient strains are

not significant in the measured (total) strain for FAC and FAC-P too. In both FAC and FAC-P cylinders, larger macrocracks develop at temperatures above 400°C and these cracks further widen around 600°C leading to rapid increase in strains above 400°C. Figures 4.37 illustrates that FAC-P attains higher peak strains as compared to FAC at higher temperature. The attainment of higher strains in FAC-P can also be attributed the phenomenon explained for higher strains in SCC-S and SCC-H. Therefore, higher peak strain in FAC-P can be attributed to additional thermal strain caused by easy diffusion of pore water facilitated due to increased porosity resulting from burning of polypropylene fibers and increase in macrocracks due to elevated temperature.

4.4.5 Temperature Induced Spalling

While carrying out the high temperature material property tests on HSC, SCC, and FAC (plain and with different fiber combinations), no spalling was observed during heating or testing at elevated temperatures. It should be noted that the heating ramp selected for tests was 2°C per minute as per RILEM test standards for high temperature mechanical property tests (RILEM TC 129-MHT, 2000; RILEM TC 129-MHT, 1995). Fire induced spalling is generally associated with faster heating rates, therefore a heating rate of 2°C per minute is considered to be quite low to cause any spalling in HPC. It is envisaged that a higher heating rate has an effect on the spalling behavior of concrete; however, the increased splitting tensile strength and porosity in case of fiber reinforced concrete will help to minimize the spalling associated with fire. A fiber dosage of 0.1 – 0.5% by volume has been suggested (Ali et al., 2004; Bentz, 2000; Kodur, 2000) to mitigate spalling in HPC, however, the present dosage of 0.11% of polypropylene fibers and 0.54% of steel fibers by volume could not verify it due to the lower heating rate.

4.4.6 Summary

The mechanical properties of HPC namely, compressive strength, splitting tensile strength, elastic modulus and stress-strain response deteriorates with temperature. Addition of steel, polypropylene, and hybrid fibers do not have much effect on high temperature compressive strength of HPC. However, addition of polypropylene fibers slows down degradation of compressive strength in FAC with temperature. Steel fibers significantly reduce the degradation of tensile strength, elastic modulus and stress-strain response in HSC and SCC. The low degradation on tensile strength up to 400°C in HSC and SCC can be beneficial to reduce fire induced spalling. Polypropylene fibers do not have much effect on stress-strain curves of SCC-P, however strain at peak stress was increased in FAC-P. Elastic modulus of FAC and FAC-P does not degrade significantly up to 200°C, however rapid deterioration of elastic modulus occurs in 200-600°C. Comparatively FAC experiences higher degradation of elastic modulus as compared to FAC-P in entire 20-800°C range.

4.5 Relations for Mechanical Properties

4.5.1 General

Data generated from the mechanical property measurements is utilized to develop mechanical property relations for HSC, SCC, and FAC (plain and with different fibers). These properties are expressed in the form of empirical relations over temperature range of 20-800°C for compressive strength, splitting tensile strength and elastic modulus. The empirical relations were arrived at based on linear regression. For the regression analysis, measured mechanical properties were used as response parameter with temperature as their predictor parameter.

The procedure used for linear regression analysis for mechanical properties is similar to that adopted in developing for thermal property relations as discussed in Chapter 3, Section 3.4. The procedure for estimating the parameters of any linear model (linear fitting), the method of least squares can be used by fitting a straight line to a set of data points (Wackerly et al., 2008). The least-squares procedure is used for fitting a line through a set of 'n' data points where it is desired that the differences between the observed values and corresponding points on the fitted line should be minimum. A convenient way to accomplish this, and one that yields estimators with good properties, is to minimize the sum of squares of the standard deviations from the fitted line. In the case of mechanical properties, these deviations in the response value (mechanical property) given by the predicted value (temperature) is called the error and to reduce these deviations in response values, sum of squares of deviations/error called sum of squares of error (SSE) is utilized.

Commercially available statistical software (Minitab) was also used to carry out the regression analysis of the mechanical property experimental results similar to thermal properties. For regression analysis, coefficient of determination R^2 (Wackerly et al., 2008) defines the accuracy of the best fit equations. This, R^2 can be interpreted as the proportion of the total variation in the response that is explained by the variable prediction in a simple linear regression model. The accuracy of the statistical model is represented by coefficient of determination 'R^2', that represents proportion of the sum of squares of deviations of the response values about their predictor (Mendenhall and Sincich, 2007). The values of coefficient of determination 'R^2' obtained for the proposed mechanical property equations lies between 0.8-0.95 that represents a reasonably high confidence level in light of high variability in mechanical properties.

Figures 4.38 and 4.39 illustrate the measured compressive strength of SCC and FAC with and without fibers along with typical fitted line by regression analysis for similar concretes. It can be seen in these figures that the plots predicted by the empirical relations are in good agreement with the test data.

The variation of compressive strength ($f'_{c,T}$), tensile strength ($f'_{t,T}$) and elastic modulus (E_T) with temperature can be related through a coefficient β_T representing ratio of respective strength at target temperature to that at room temperature (f'_c, f'_t, and E_0) given by Eqns 4.1 to 4.3. Due to least variation in compressive strength of HSC and SCC (with and without fibers); single representative relation is presented for compressive strength. However, because of significant variation in tensile strength relations are presented separately for HSC and SCC (with and without fibers). Also separate relations are presented for SCC (with and without fibers) due to significant variation of high temperature elastic modulus. Due to property variations in different temperature ranges, the proposed equations give either linear or bi-linear and tri-linear relations. These empirical relations can be used for HPC up to a compressive strength of 100 MPa and tensile strength of 7 MPa. The strength reduction coefficient ratio (β_T) for compressive strength, splitting tensile strength and elastic modulus is given as:

$$\beta_{T,compressive} = f'_{c,T} / f'_c \quad (4.1)$$

$$\beta_{T,tensile} = f'_{t,T} / f'_t \quad (4.2)$$

$$\beta_{T,modulus} = E_T / E_0 \quad (4.3)$$

The value of β_T for respective mechanical property at different temperatures can be obtained from Eqns 4.4 to 4.42 for plain and fiber reinforced HSC, SCC and FAC. In lieu of equations, Table 4.3 and 4.4 give reduction factor β_T for compressive and splitting tensile strength of HSC and fiber reinforced HSC. Similarly, Table 4.5 and 4.6 give reduction factors β_T for compressive, splitting tensile strength and elastic modulus of plain and fiber reinforced SCC and FAC respectively**.** This reduction factor β_T at different temperatures can be used for evaluating compressive strength, splitting tensile strength and elastic modulus for these concretes. Using these values of reduction factors β_T for compressive, splitting tensile strength, and elastic modulus of plain and fiber reinforced HSC, SCC, and FAC the constitutive curves are obtained as shown in Figures 4.40 to 4.47. These figures show the constitutive plots based on the empirical relations derived from the experimental data in this study.

4.5.2 Relations for Compressive Strength

HSC, HSC-S, HSC-P and HSC-H

$\beta_{T,compressive} = 1.0$ 20°C (4.4)

$\beta_{T,compressive} = 1.0 - 0.0016T$ 100°C ≤ T ≤ 400°C (4.5)

$\beta_{T,compressive} = 0.74 - 0.0008T$ 400°C ≤ T ≤ 800°C (4.6)

SCC, SCC-S, SCC-P, and SCC-H:

$\beta_{T,compressive} = 1.0$ 20°C (4.7)

$\beta_{T,compressive} = 0.99 - 0.002T$ $100°C \leq T \leq 200°C$ (4.8)

$\beta_{T,compressive} = 0.73 - 0.0005T$ $200°C \leq T \leq 800°C$ (4.9)

FAC

$\beta_{T,compressive} = 1.0$ $20°C$ (4.10)

$\beta_{T,compressive} = 0.78 - 0.0009T$ $200°C \leq T \leq 800°C$ (4.11)

FAC-P

$\beta_{T,compressive} = 1.0$ $20°C$ (4.12)

$\beta_{T,compressive} = 1.09 - 0.0012T$ $200°C \leq T \leq 800°C$ (4.13)

4.5.3 Relations for Splitting Tensile Strength

HSC

$\beta_{T,tensile} = 1.0$ $20°C$ (4.14)

$\beta_{T,tensile} = 0.97 - 0.0011T$ $100°C \leq T \leq 800°C$ (4.15)

HSC-S

$\beta_{T,tensile} = 1.0$ $20°C$ (4.16)

$\beta_{T,tensile} = 0.9$ $100°C$ (4.17)

$\beta_{T,tensile} = 1.42 - 0.0018T$ $300°C \leq T \leq 800°C$ (4.18)

HSC-P

$\beta_{T,tensile} = 1\text{-}0.002T$ $20°C \leq T < 200°C$ (4.19)

$\beta_{T,tensile} = 0.82\text{-}0.001T$ $200°C \leq T \leq 800°C$ (4.20)

HSC-H

$\beta_{T,tensile} = 1.0$ $20°C$ (4.21)

$\beta_{T,tensile} = 0.78$ $100°C \leq T < 300°C$ (4.22)

$\beta_{T,tensile} = 1.\ 28\text{-}0.0016T$ $400°C \leq T \leq 800°C$ (4.23)

For SCC and SCC-P:

$\beta_{T,tensile} = 1.0$ $20°C$ (4.24)

$\beta_{T,tensile} = 0.98\text{-}0.001T$ $100°C \leq T < 800°C$ (4.25)

For SCC-S and SCC-H:

$\beta_{T,tensile} = 1.0$ $20°C$ (4.26)

$\beta_{T,tensile} = 1.1\text{-}0.001T$ $100°C \leq T < 800°C$ (4.27)

FAC

$\beta_{T,tensile} = 1.0$ $20°C$ (4.28)

$\beta_{T,tensile} = 1.05\text{-}0.0013T$ $200°C \leq T < 800°C$ (4.29)

FAC-P

$\beta_{T,tensile} = 1.0$ $20°C$ (4.30)

$\beta_{T,tensile} = 1.0$ 20°C (4.30)

$\beta_{T,tensile} = 0.98\text{-}.0006T$ $200°C \leq T < 400°C$ (4.31)

$\beta_{T,tensile} = 1.\ 44\text{-}0.0017T$ $400°C < T \leq 800°C$ (4.32)

4.5.4 Relations for Elastic Modulus

For SCC and SCC-P:

$\beta_{T,modulus} = 1.0$ 20°C (4.33)

$\beta_{T,modulus} = 0.84\text{-}0.001T$ $100°C \leq T \leq 800°C$ (4.34)

For SCC-S and SCC-H:

$\beta_{T,modulus} = 1.0$ 20°C (4.35)

$\beta_{T,modulus} = 1.1\text{-}0.002T$ $100°C \leq T < 200°C$ (4.36)

$\beta_{T,modulus} = 0.88\text{-}0.008T$ $200°C \leq T \leq 800°C$ (4.37)

FAC

$\beta_{T,modulus} = 1.0$ 20°C (4.38)

$\beta_{T,modulus} = 0.97$ 200°C (4.39)

$\beta_{T,modulus} = 0.74\text{-}0.0009T$ $400°C \leq T \leq 800°C$ (4.40)

FAC-P

$\beta_{T,modulus} = 1.0$ 20°C (4.41)

$\beta_{T,modulus} = 1.24\text{-}0.0015T$ $200°C \leq T \leq 800°C$ (4.42)

4.6 Summary

Tests were performed to characterize high temperature compressive strength, splitting tensile strength, elastic modulus and stress-strain curves for HPC. For all tested HPC, these high temperature properties deteriorate with temperature. Addition of steel, polypropylene and hybrid fibers do not influence the high temperature compressive strength, however it does have an effect on splitting tensile strength and elastic modulus as fibers (steel, polypropylene, and hybrid) help reduce deterioration in these properties due to rising temperatures. Data from the tests is utilized to develop high temperature relations for compressive strength, splitting tensile strength, and elastic modulus of HPC. The proposed relations can be used as input data in computer programs for evaluating the fire response of HPC structures exposed to fire.

Table 4.1 - Test matrix for evaluation of high temperature mechanical properties

S/No	Property	Temperature range (and interval) (°C)	Test equipment	Concrete types (mixes) tested	Number of cylinders tested (75x150 mm)
1	Compressive strength	20-800°C @100 and 200°C interval**	Elect furnace, thermal jacket, Forney strength test machine	NSC, HSC, HSC-S, HSC-P, HSC-H, SCC, SCC-S, SCC-P, SCC-H, FAC, FAC-P, NSC	222*
2	Tensile strength	20-800°C @100 and 200°C interval**	Elect furnace, steel bracket frame, Forney strength test machine	NSC, HSC, HSC-S, HSC-P, HSC-H, SCC, SCC-S, SCC-P, SCC-H, FAC, FAC-P, NSC	222*
3	Elastic modulus	20-800°C @100 and 200°C interval**	Elect furnace, thermal jacket, Forney strength test machine	SCC, SCC-S, SCC-P, SCC-H, FAC, FAC-P, NSC	108*
4	Stress-strain curves	20-800°C @100 and 200°C interval**	Elect furnace, thermal jacket, Forney strength test machine	SCC, SCC-S, SCC-P, SCC-H, FAC, FAC-P, NSC	108*

* All types of concrete had 20% extra cylinders prepared for testing
** Temperature intervals varied for different concretes

Table 4.2 - Details of cylinders for different batches of concrete.

S No	Type of concrete	Room temperature compressive strength	High temperature compressive strength	High temperature tensile strength
		Cylinder sizes		
		100×200 mm **cylinders**	75×150 mm **cylinders**	75×150 mm **cylinders**
1	HSC	18	24	24
2	HSC-P	18	24	24
3	HSC-S	18	24	24
4	HSC-H	18	24	24
5	SCC	15	18	18
6	SCC-P	15	18	18
7	SCC-S	15	18	18
8	SCC-H	15	18	18
9	FAC	15	18	18
10	FAC-P	15	18	18
11	NSC	12	18	18

Table 4.3 - Compressive strength reduction factor β_T at different temperatures for HSC and fiber reinforced HSC.

Temperature -°C	**Compressive strength reduction factor (β_T)**			
	HSC	**HSC-P**	**HSC-S**	**HSC-H**
20	1	1	1	1
100	0.9	0.9	0.8	0.78
200	0.8	0.9	0.6	0.78
300	0.7	0.9	0.52	0.78
400	0.52	0.7	0.45	0.66
600	0.35	0.5	0.38	0.52
800	0.2	0.34	0.3	0.36

Table 4.4 - Splitting tensile strength reduction factor β_T at different temperatures for HSC and fiber reinforced HSC.

Temperature -°C	**Splitting tensile strength reduction factor (β_T)**			
	HSC	**HSC-P**	**HSC-S**	**HSC-H**
20	1	1	1	1
100	0.86	0.90	0.82	0.78
200	0.75	0.90	0.60	0.78
300	0.64	0.90	0.52	0.78
400	0.53	0.70	0.42	0.64
600	0.42	0.52	0.32	0.48
800	0.31	0.34	0.22	0.32

Table 4.5 - Compressive strength, tensile strength and elastic modulus reduction factor β_T at different temperatures for SCC and fiber reinforced SCC.

Temperature -°C	Reduction factor (β_T)				
	Compressive strength	Tensile strength		Elastic Modulus	
	SCC and SCC with fibers	SCC-P	SCC, SCC-S, SCC-H	SCC and SCC-P	SCC-S and SCC-H
20	1	1	1	1	1
100	0.79	0.89	0.95	0.74	0.9
200	0.59	0.79	0.9	0.64	0.72
300	0.56	0.69	0.8	0.54	0.64
400	0.53	0.59	0.7	0.44	0.56
600	0.43	0.39	0.5	0.34	0.4
800	0.33	0.19	0.3	0.04	0.24

Table 4.6 - Compressive strength and elastic modulus reduction factor β_T at different temperatures for FAC and FAC-P

Temperature (°C)	Reduction factor (β_T)					
	Compressive strength		Splitting tensile strength		Elastic Modulus	
	FAC	FAC-P	FAC	FAC-P	FAC	FAC-P
20	1	1	1	1	1	1
200	0.6	0.85	0.79	0.86	0.97	0.94
400	0.42	0.61	0.53	0.76	0.38	0.64
600	0.24	0.37	0.27	0.42	0.2	0.34
800	0.06	0.13	0	0.08	0.02	0.04

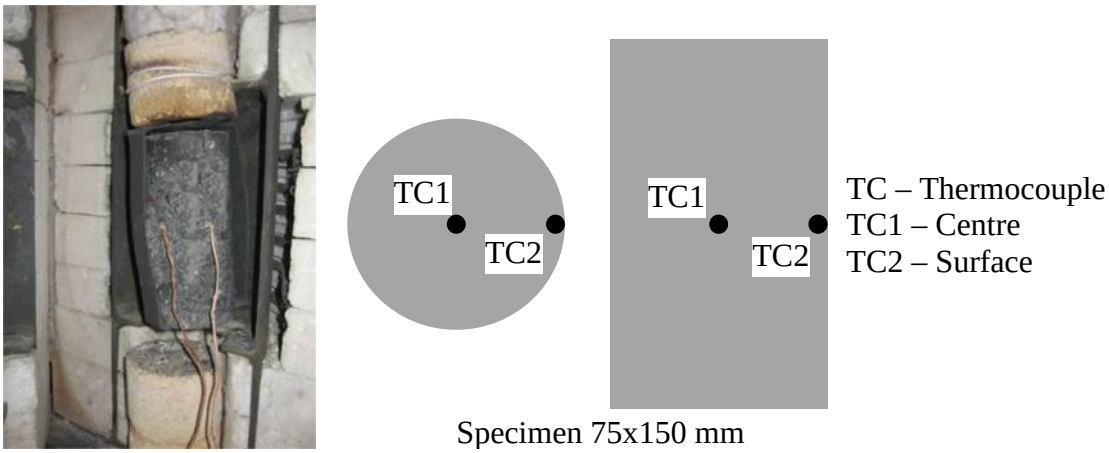

(a) Cylinder inside furnace (b) Thermocouples position in cylinder

Figure 4.1 - Arrangement of thermocouples on an instrumented cylinder

Figure 4.2 - Electrical furnace used to heat the small cylinders

Figure 4.3 - Forney strength test machine used for mechanical properties

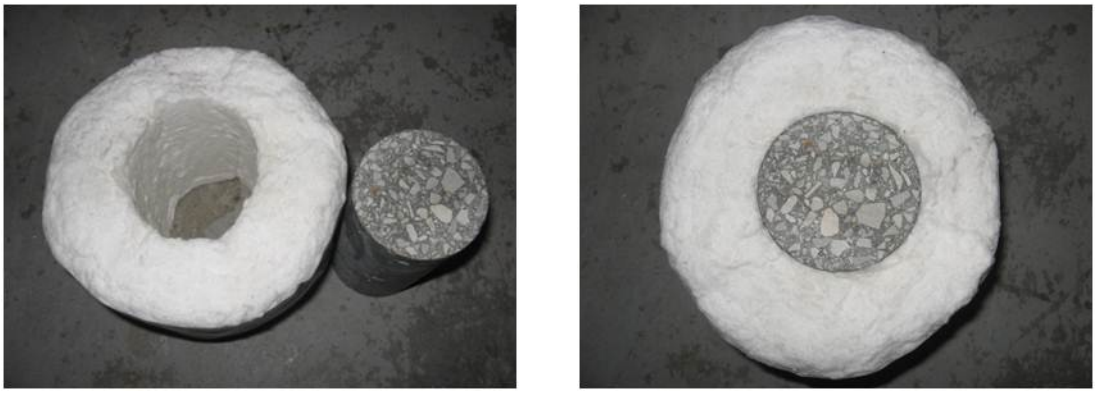

Figure 4.4 - Thermal jacket for handling heated cylinders and to preserve heat in cylinders during compressive strength tests

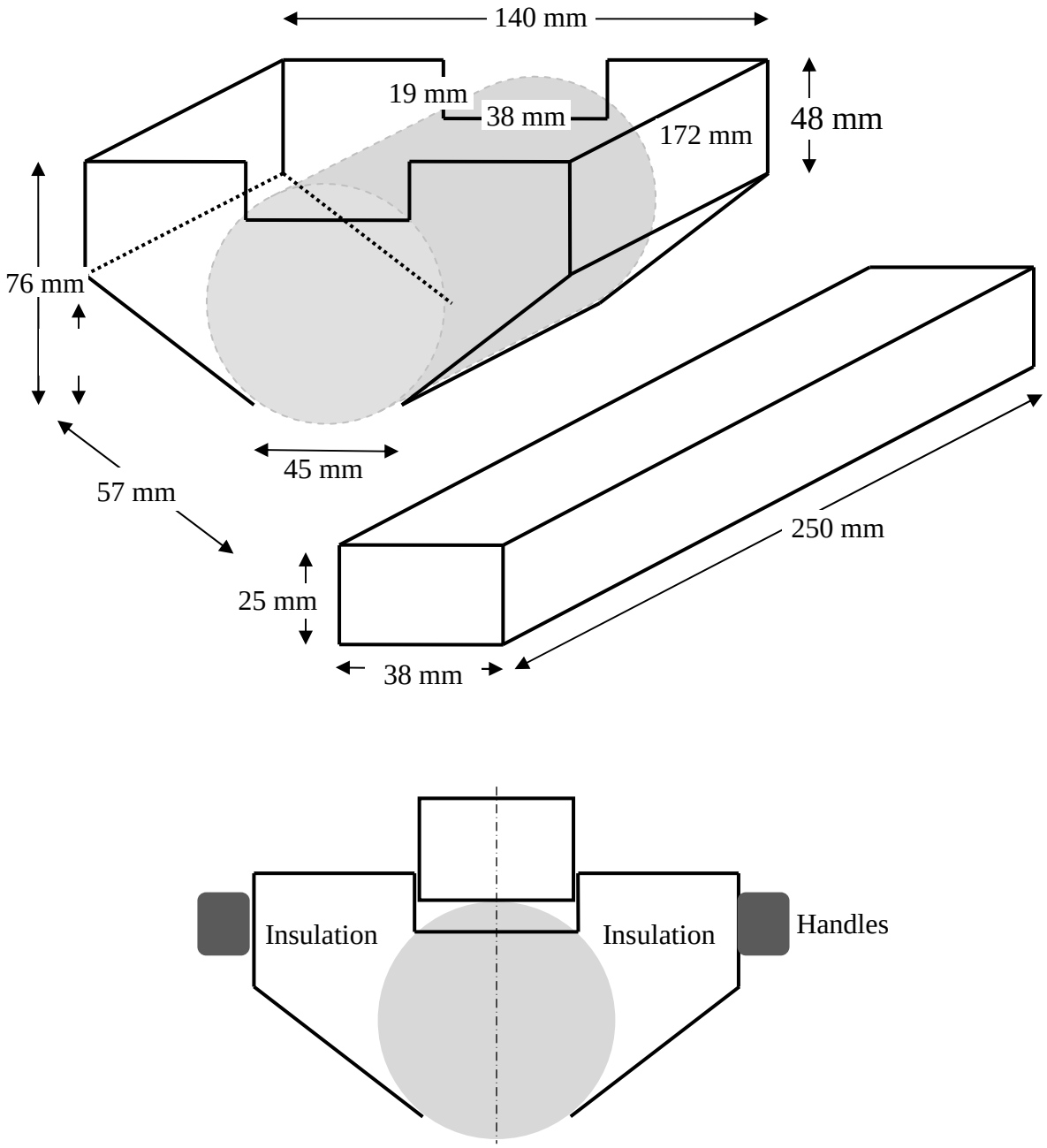

Figure 4.5 - Design details of steel bracket frame

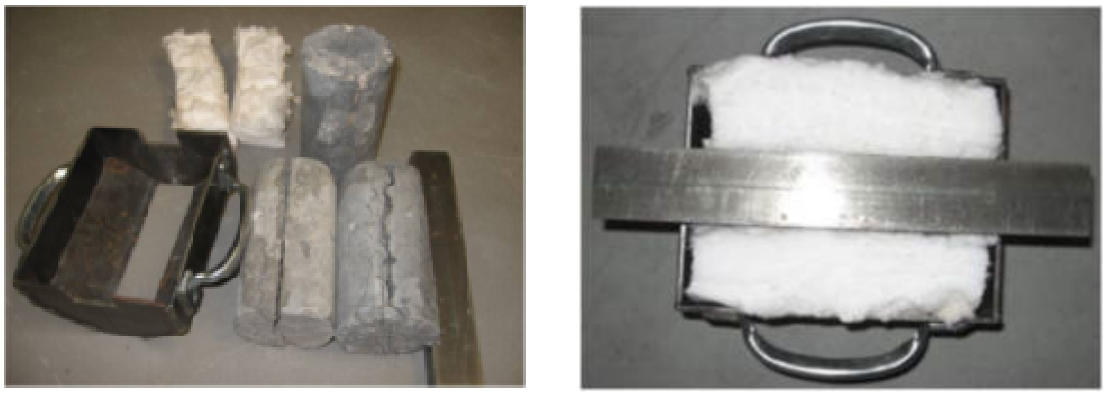

Figure 4.6 - Insulated steel bracket frame for handling heated cylinders and to preserve heat in cylinders during splitting tensile strength tests

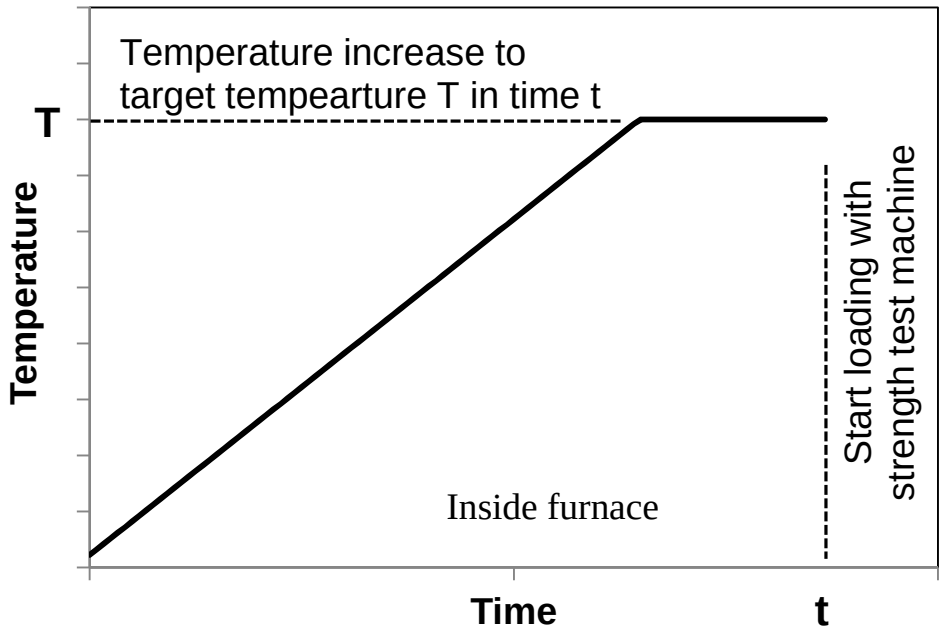

(a) Heating scheme

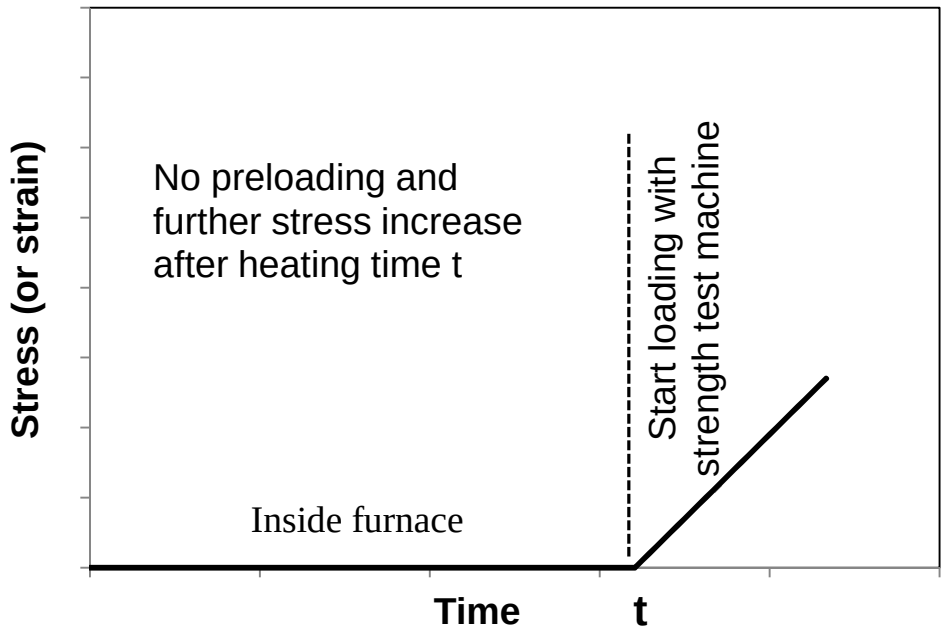

(b) Loading scheme

Figure 4.7 - Schematic of temperature and stress increments during heating and loading of test cylinders

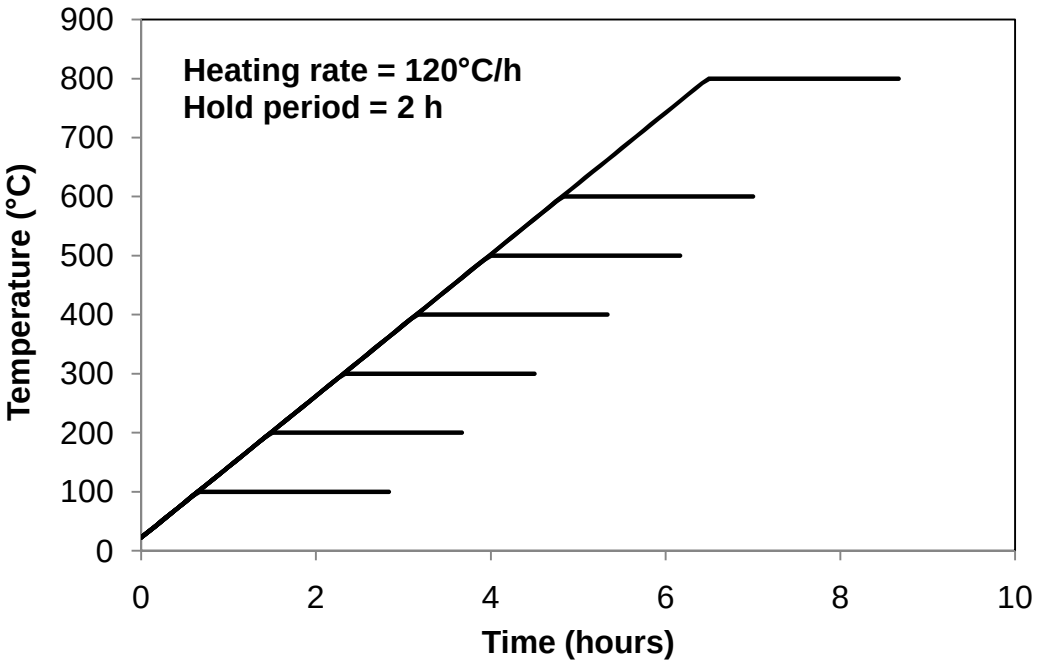

Figure 4.8 - Time-temperature graph showing ramp and hold times at each target temperature

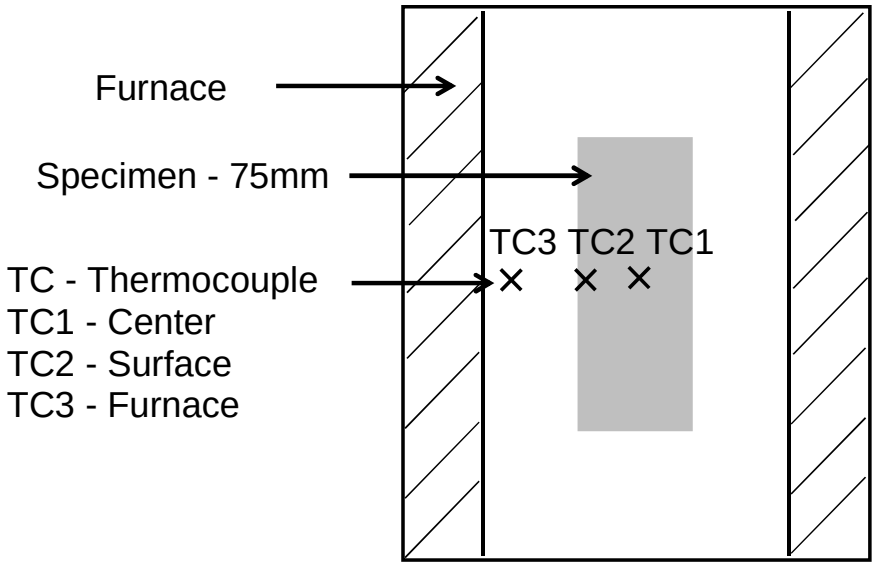

(a) Location of thermocouples on cylinder specimen and in furnace

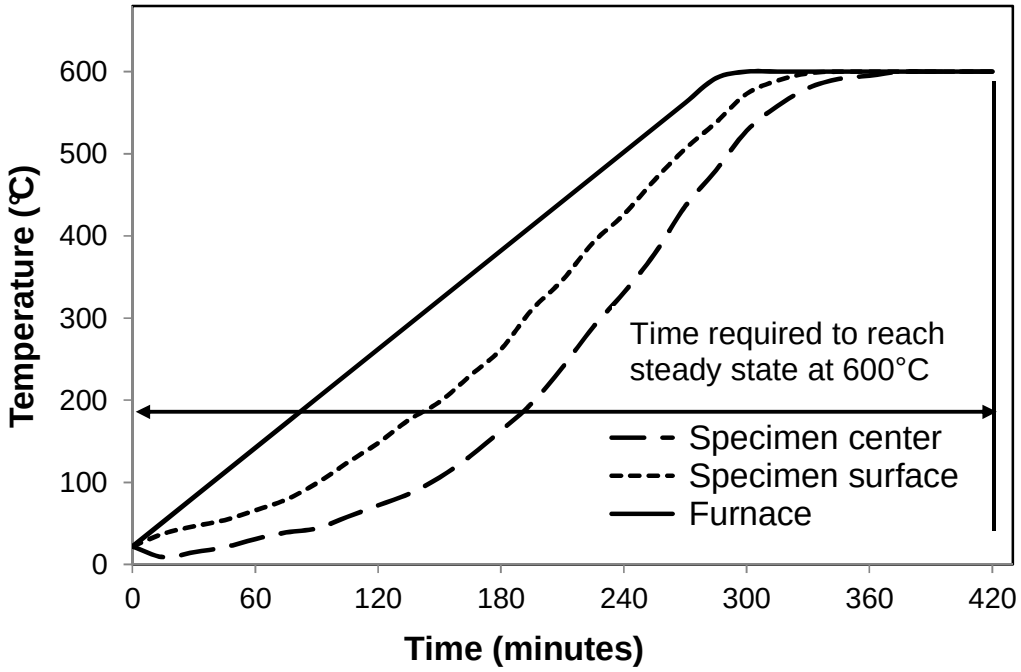

(b) Temperature rise recorded by thermocouples at different locations

Figure 4.9 - Heating characteristics of test cylinder at 600°C

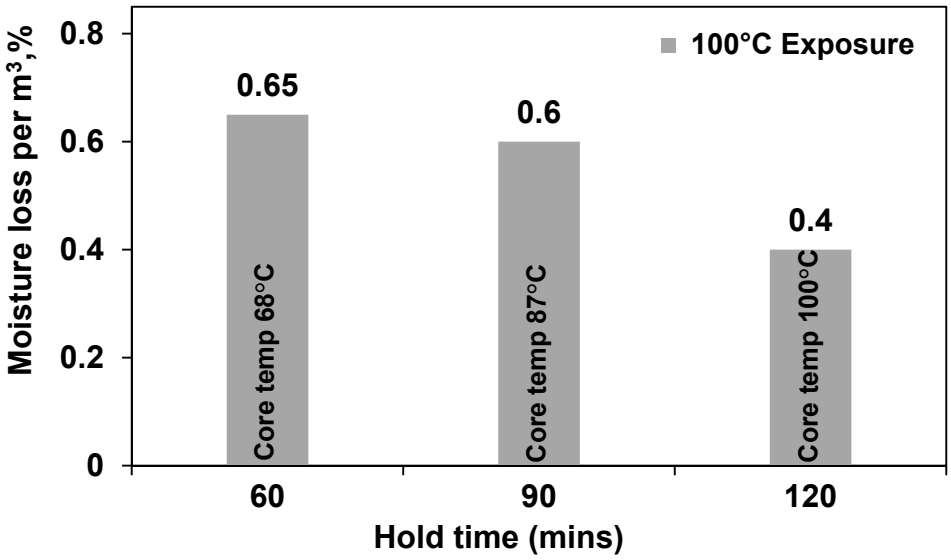

Figure 4.10 - Temperature progression at mid-depth of concrete cylinders at various hold times

(a) (b)

Figure 4.11 - Arrangement for high temperature compressive strength tests and tested cylinder

(a) (b)

Figure 4.12 - Arrangement for high temperature splitting tensile strength tests and tested cylinder

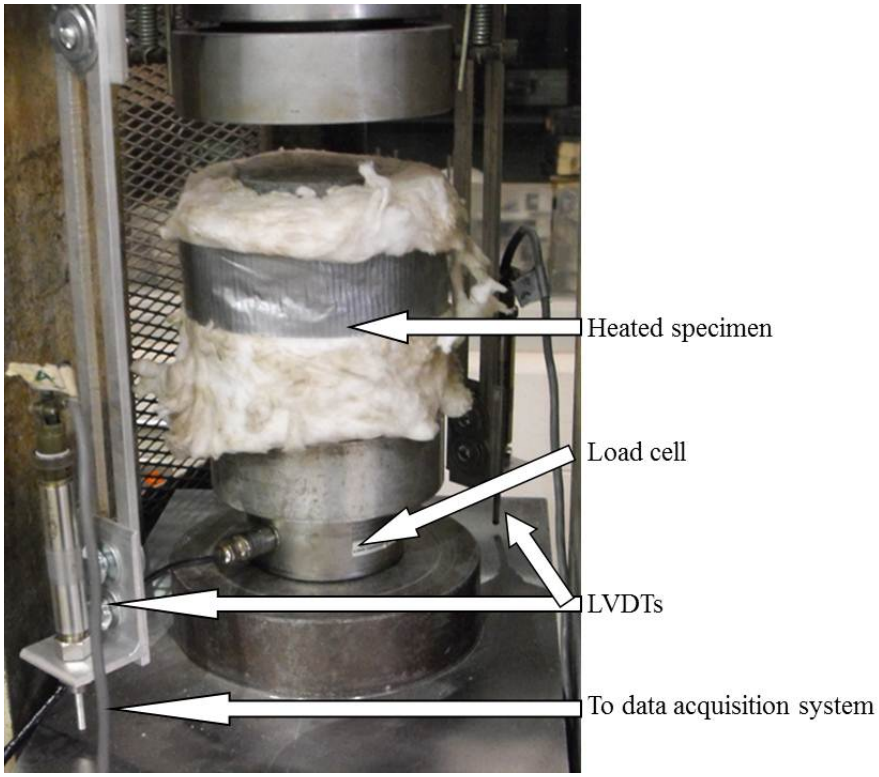

Figure 4.13 - LVDTs and load cell addition to Forney strength test machine for stress-strain measurements

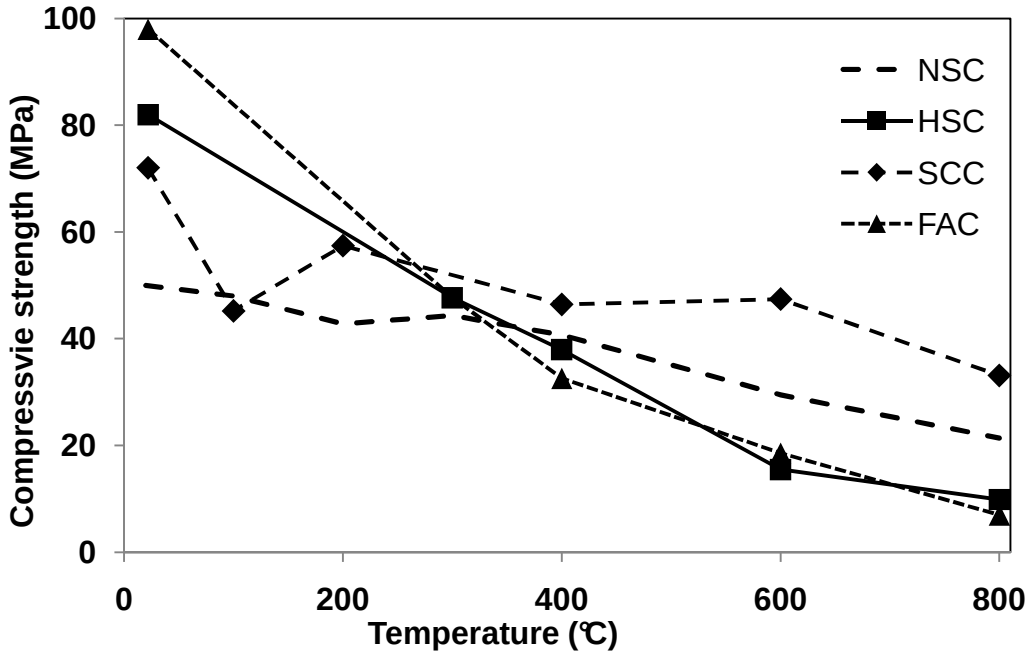

Figure 4.14 - Measured compressive strength of NSC, HSC, SCC, and FAC

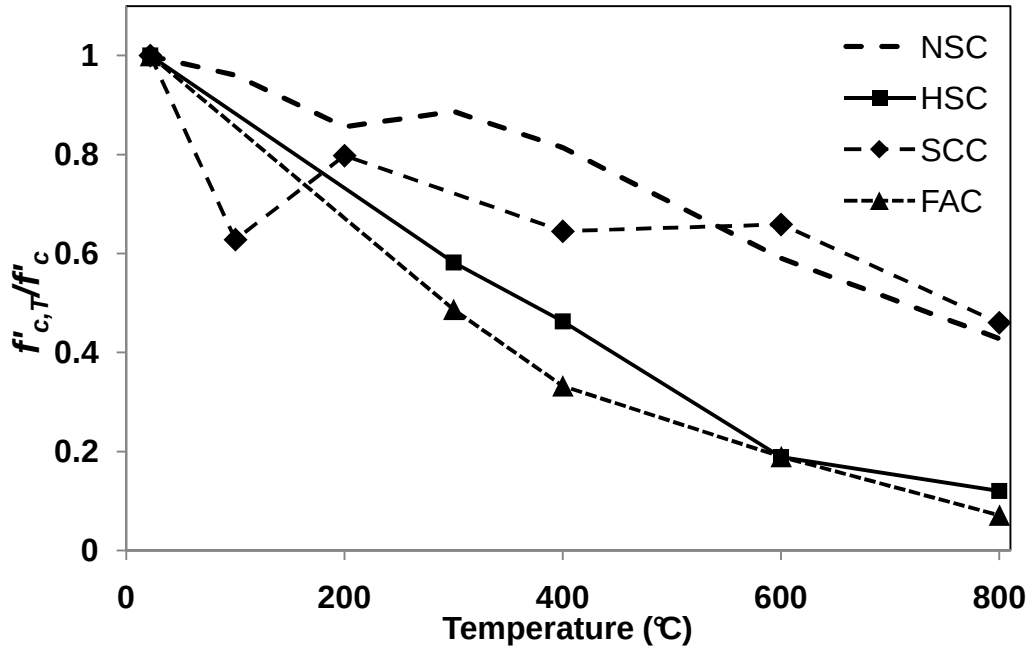

Figure 4.15 - Relative compressive strength of NSC, HSC, SCC, and FAC

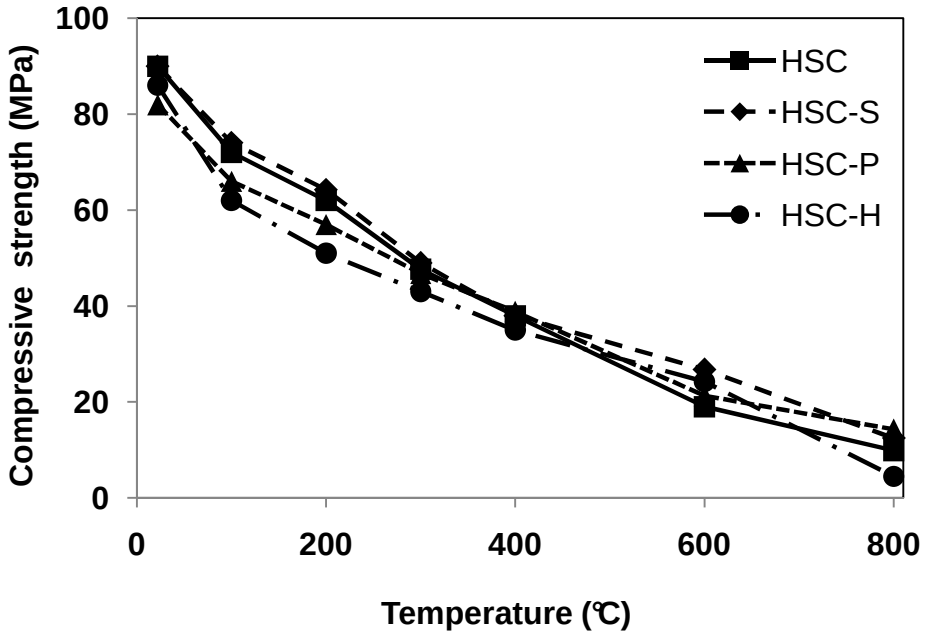

Figure 4.16 - Measured compressive strength of HSC and fiber reinforced HSC as function of temperature

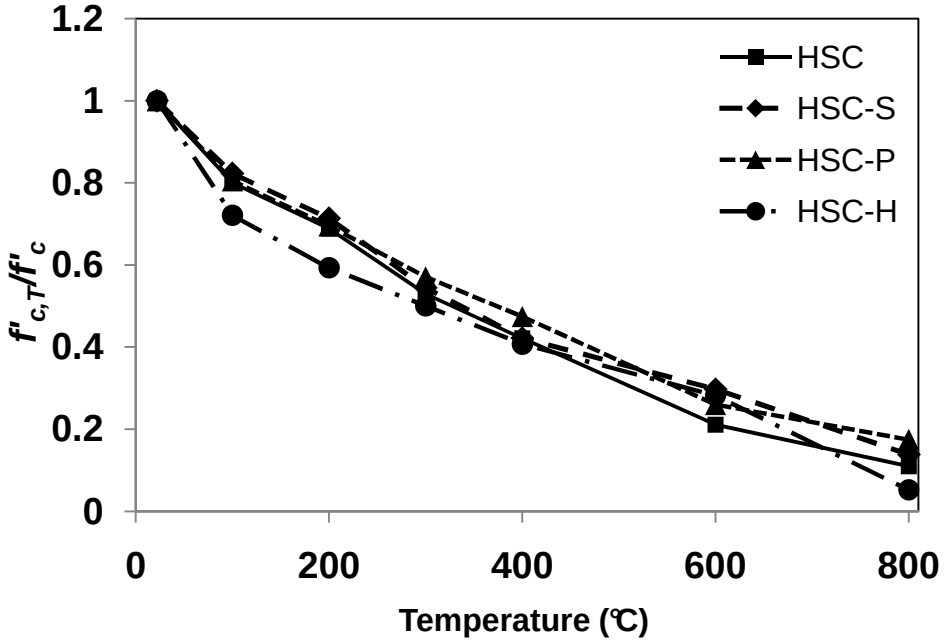

Figure 4.17 - Measured relative compressive strength of HSC and fiber reinforced HSC as function of temperature

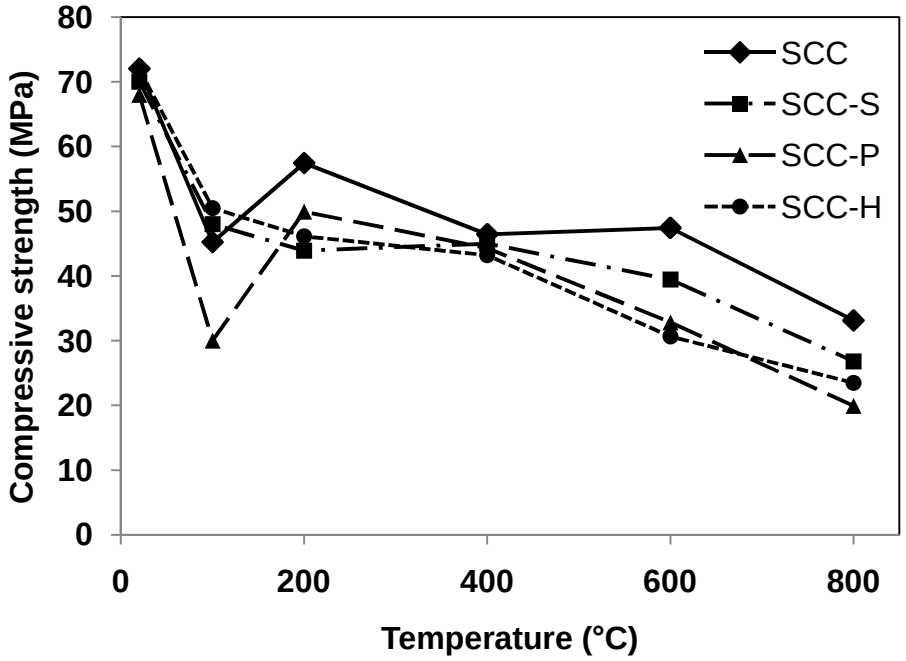

Figure 4.18 - Measured compressive strength of SCC and fiber reinforced SCC as function of temperature.

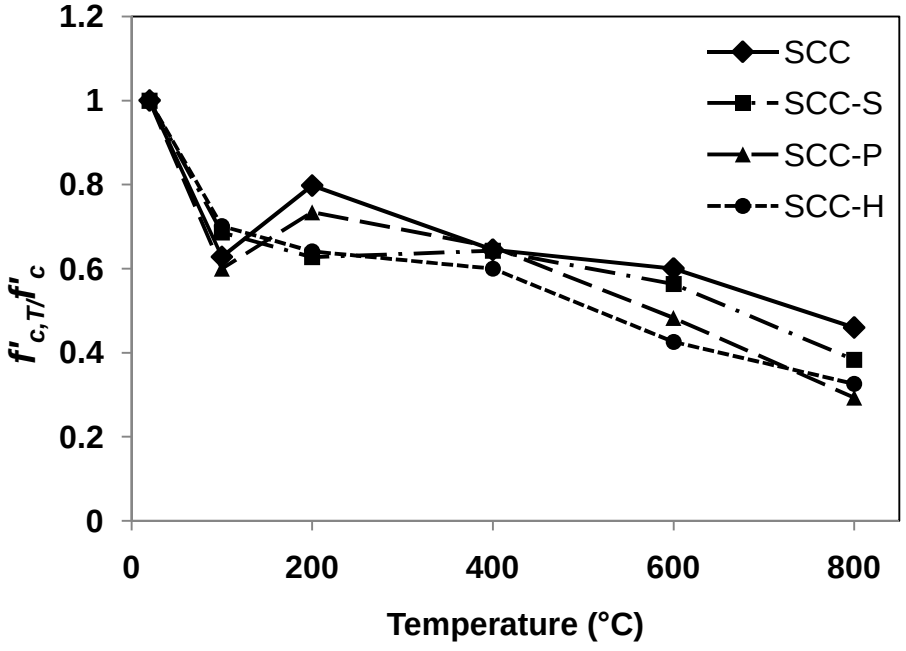

Figure 4.19 - Measured relative compressive strength of SCC and fiber reinforced SCC as function of temperature.

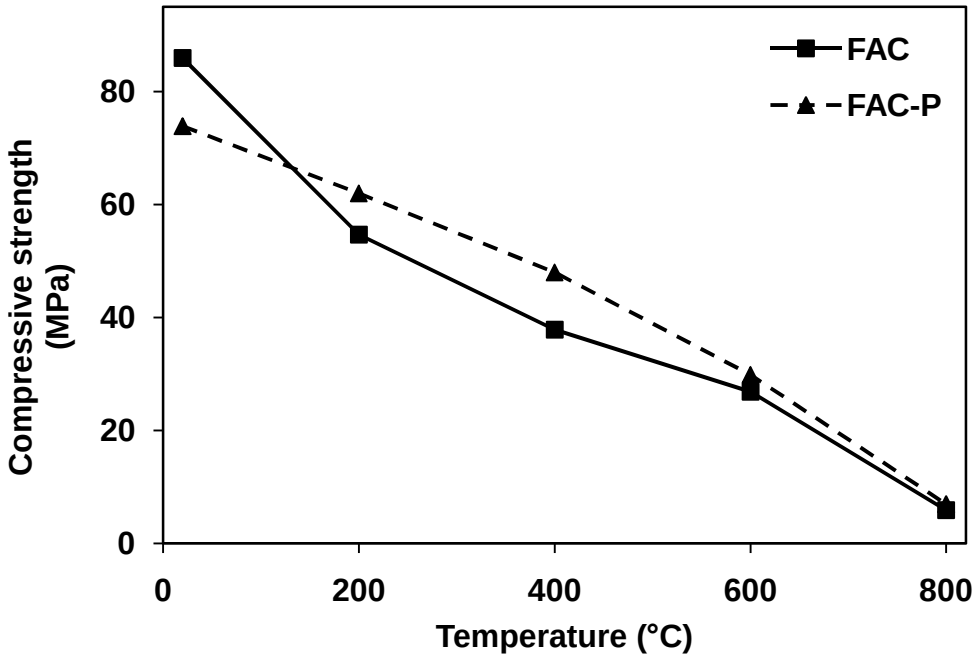

Figure 4.20 - Measured compressive strength of FAC and FAC-P as function of temperature.

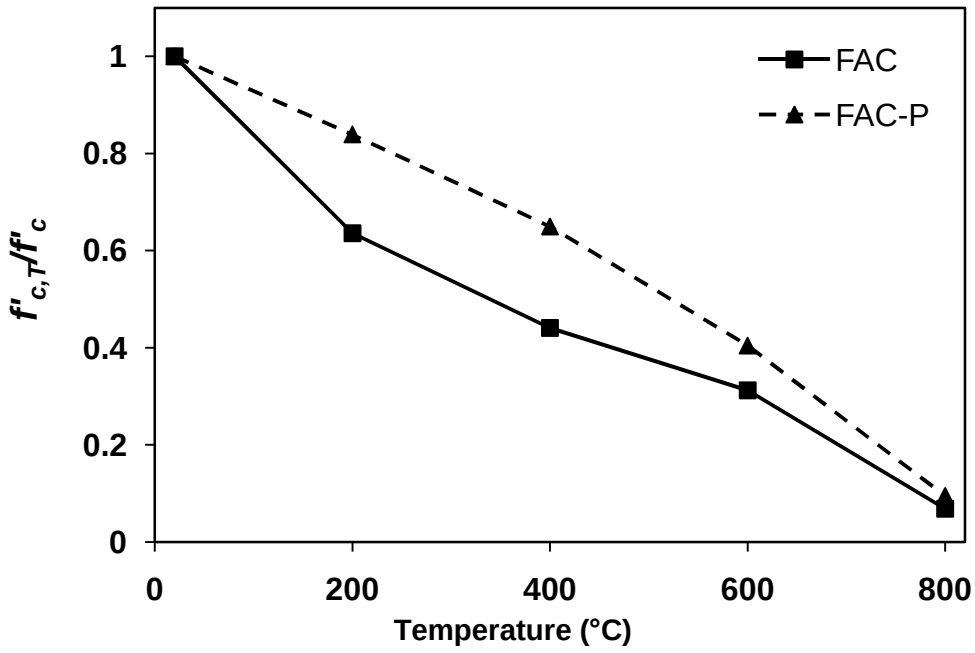

Figure 4.21 - Measured relative compressive strength of FAC and FAC-P as function of temperature

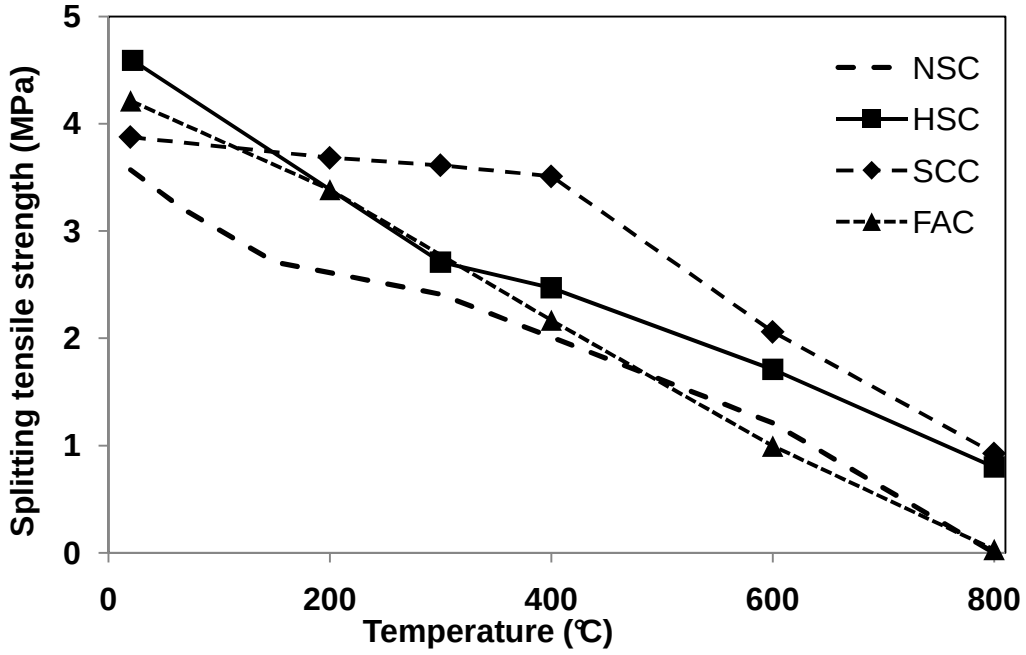

Figure 4.22 - Measured splitting tensile strength of NSC, HSC, SCC, and FAC

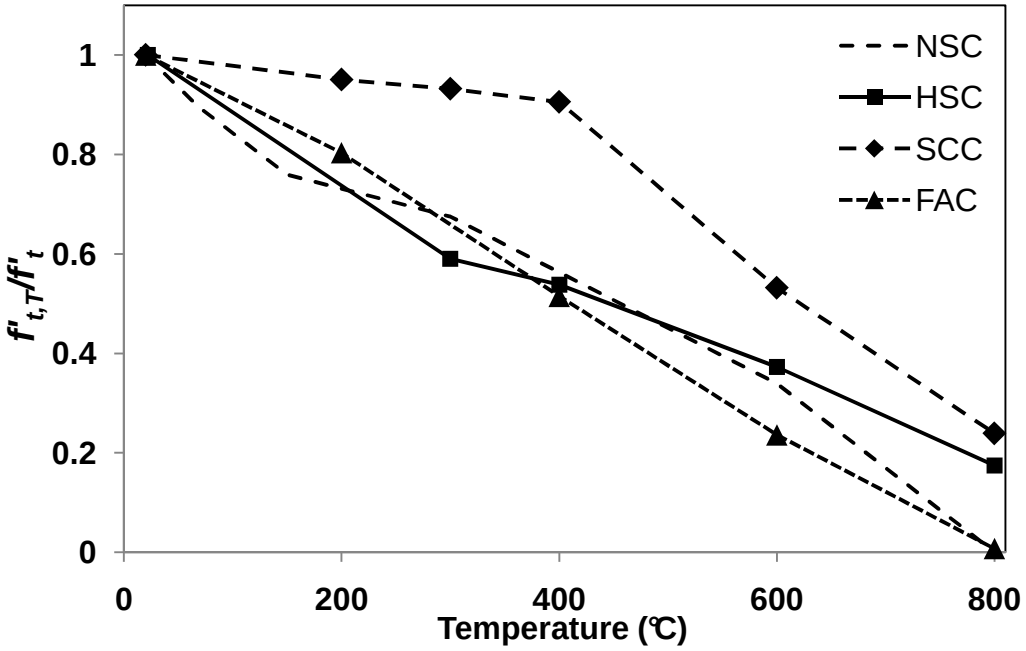

Figure 4.23 - Relative splitting tensile strength of NSC, HSC, SCC, and FAC

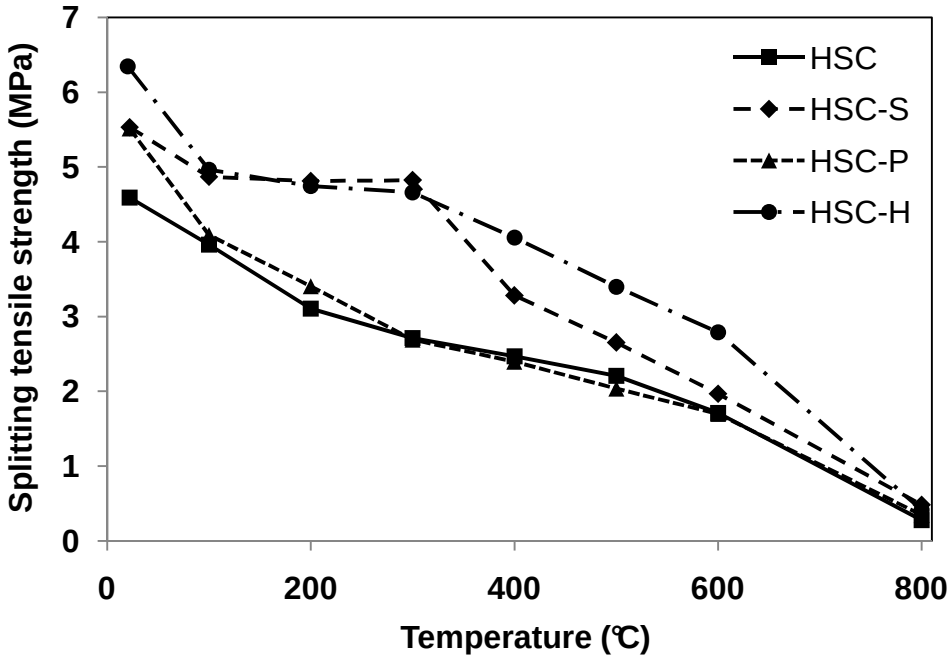

Figure 4.24 - Measured splitting tensile strength of HSC and fiber reinforced HSC as function of temperature

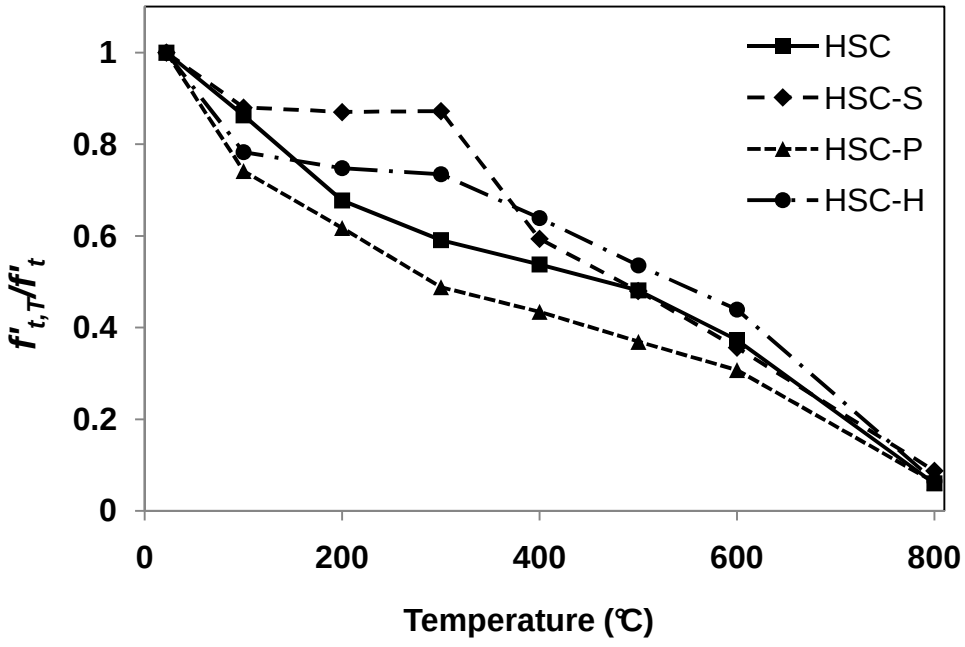

Figure 4.25 - Measured relative splitting tensile strength of HSC and fiber reinforced HSC as function of temperature

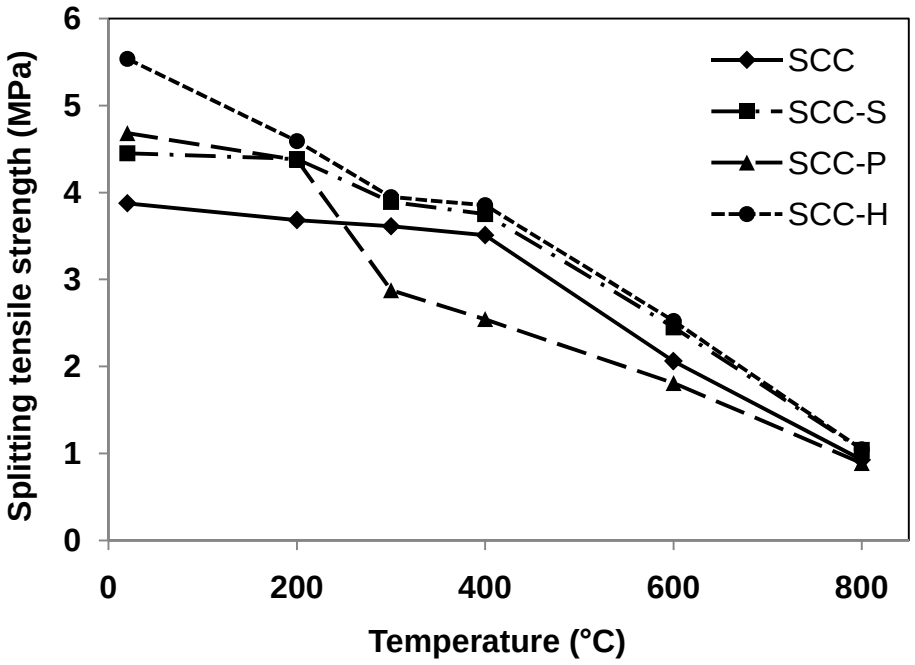

Figure 4.26 - Measured splitting tensile strength of SCC and fiber reinforced SCC as function of temperature

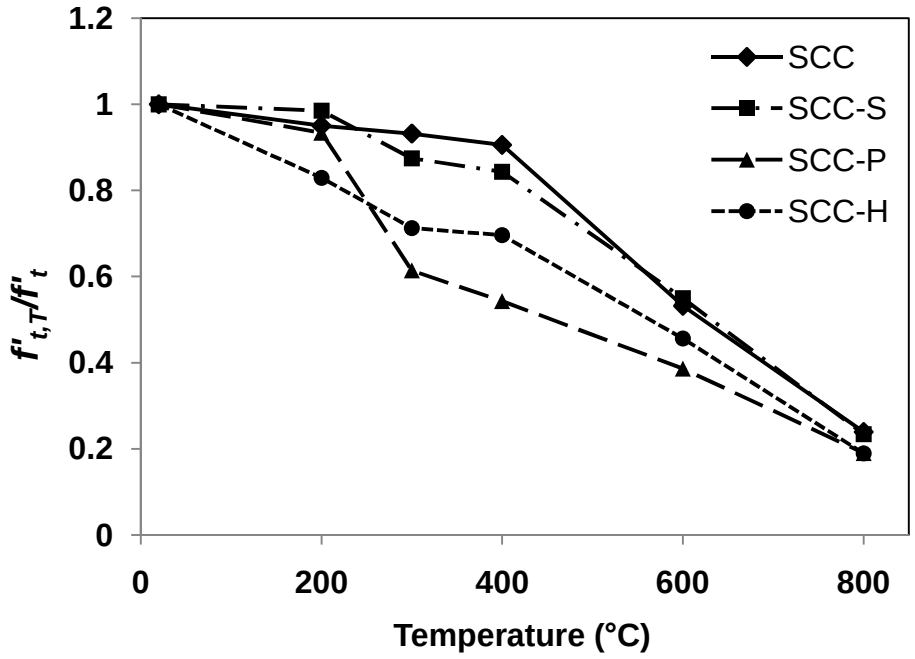

Figure 4.27 - Measured relative splitting tensile strength of SCC and fiber reinforced SCC as function of temperature

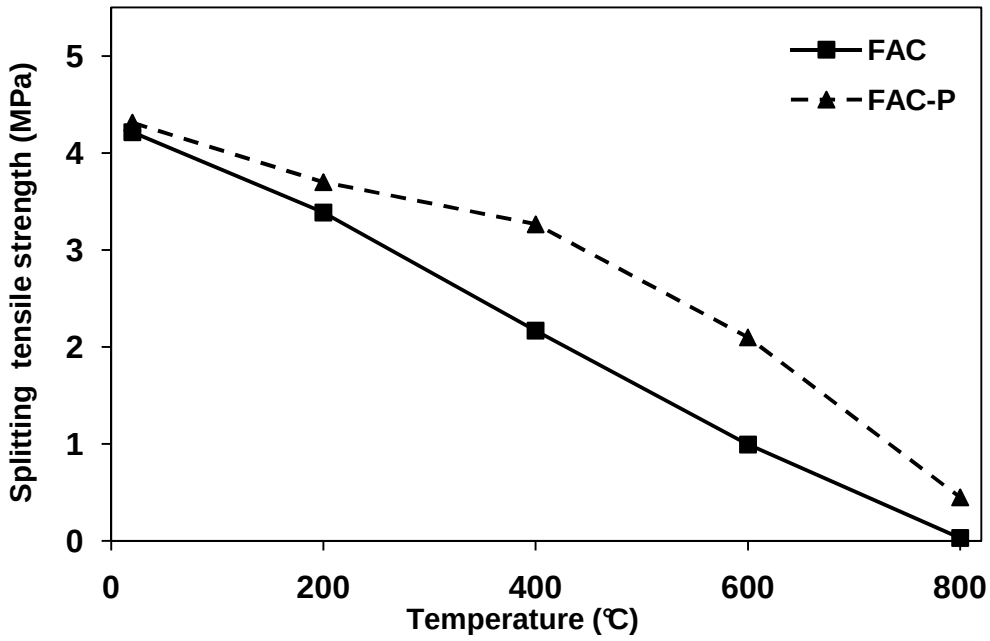

Figure 4.28 - Measured splitting tensile strength of FAC and FAC-P as function of temperature

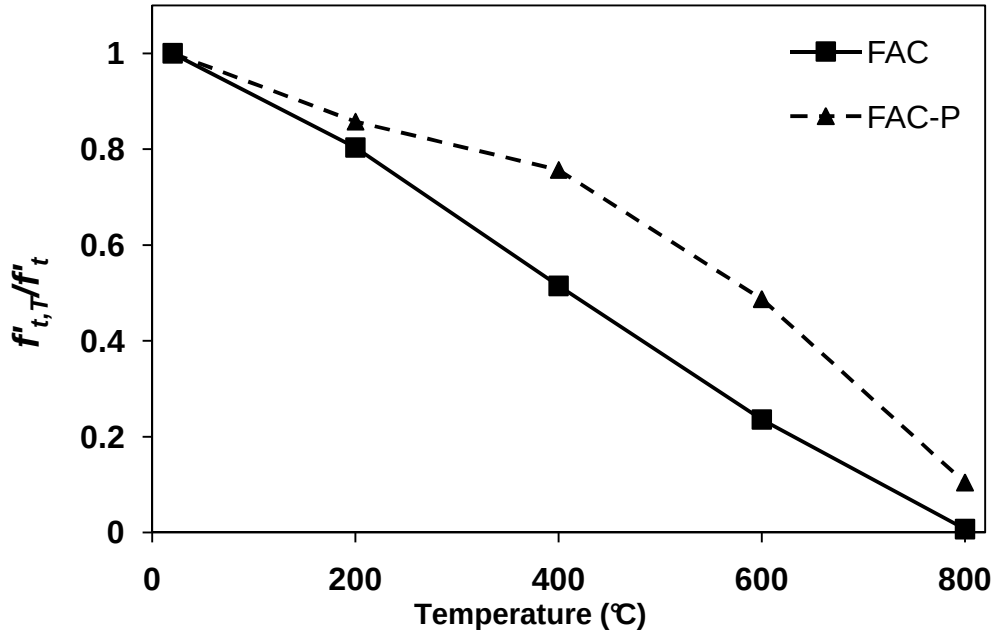

Figure 4.29 - Measured relative splitting tensile strength of FAC and FAC-P as function of temperature

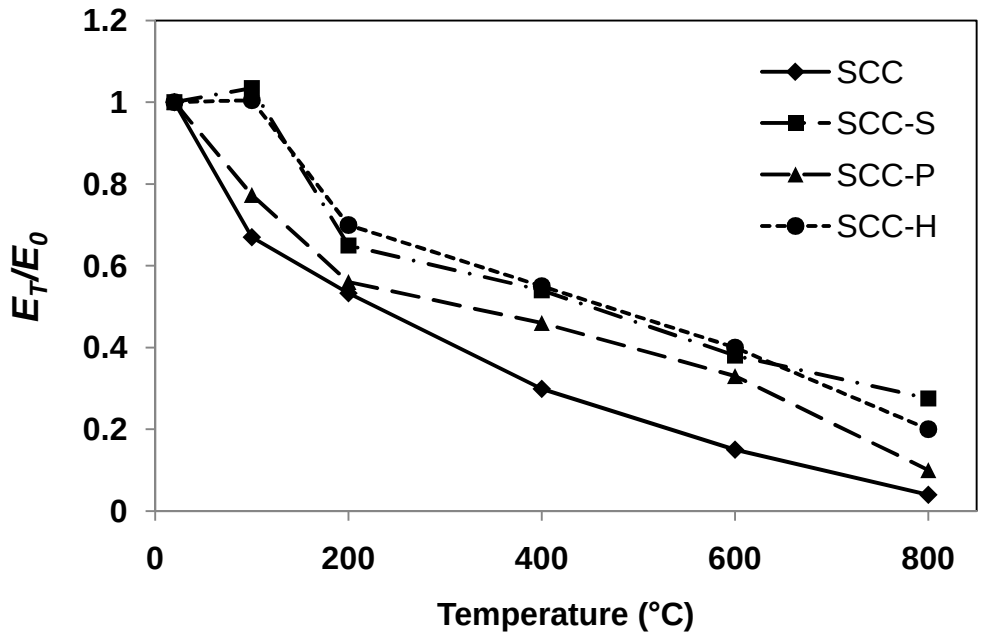

Figure 4.30 - Measured elastic modulus for plain SCC and fiber reinforced SCC

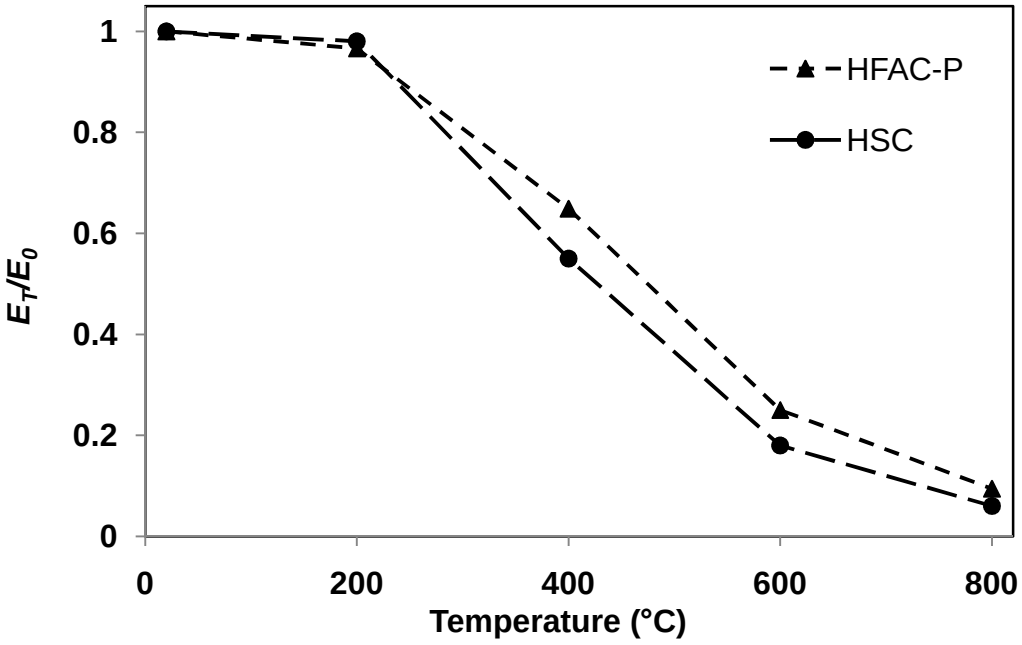

Figure 4.31 - Measured elastic modulus for plain FAC and FAC-P

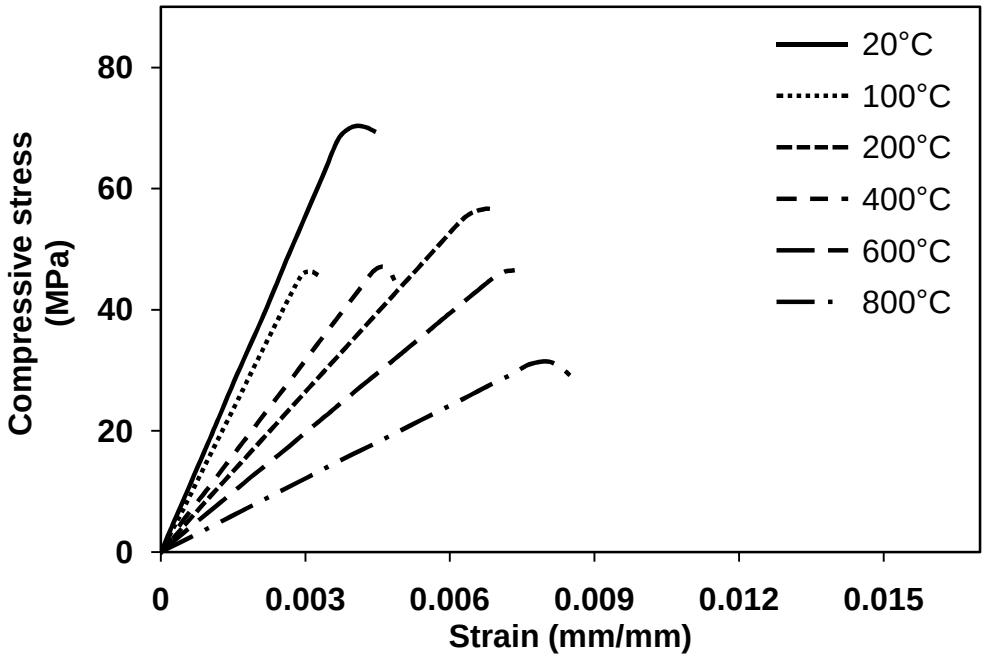

Figure 4.32 - High temperature stress-strain curves for SCC

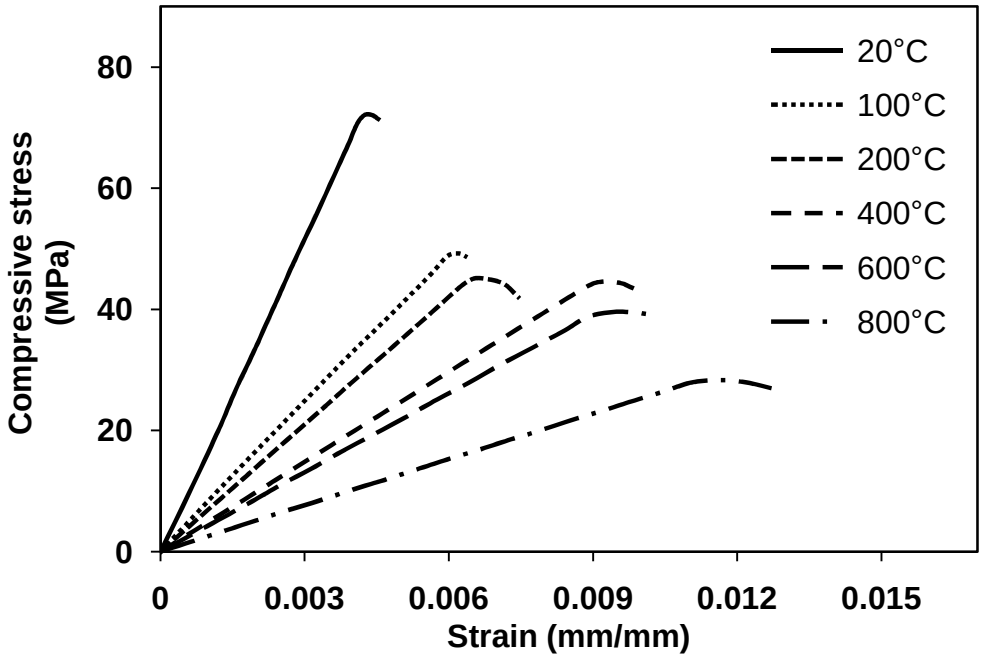

Figure 4.33 - High temperature stress-strain curves for SCC-S

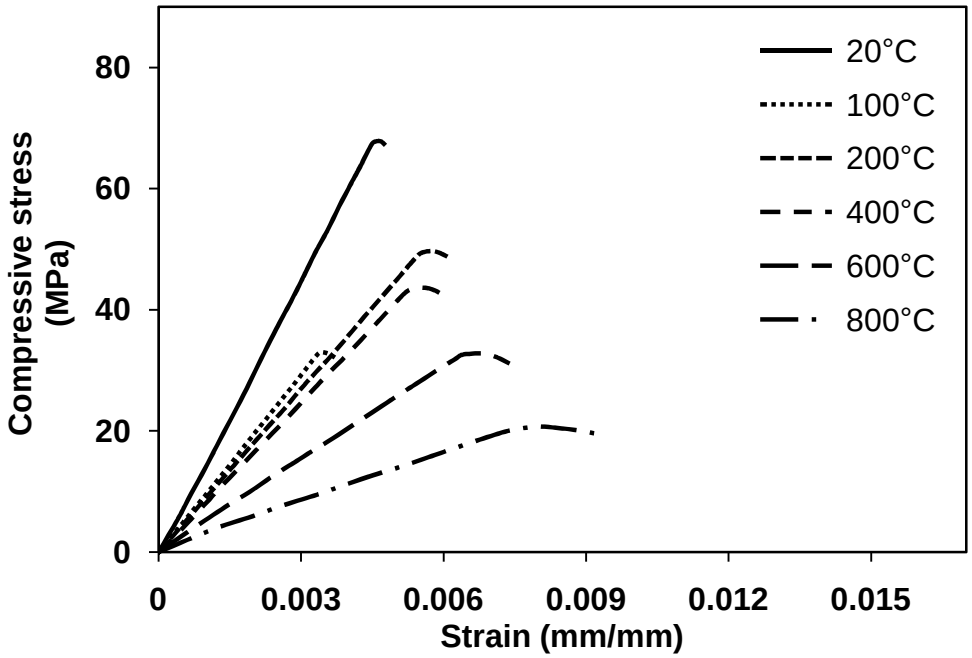

Figure 4.34 - High temperature stress-strain curves for SCC-P

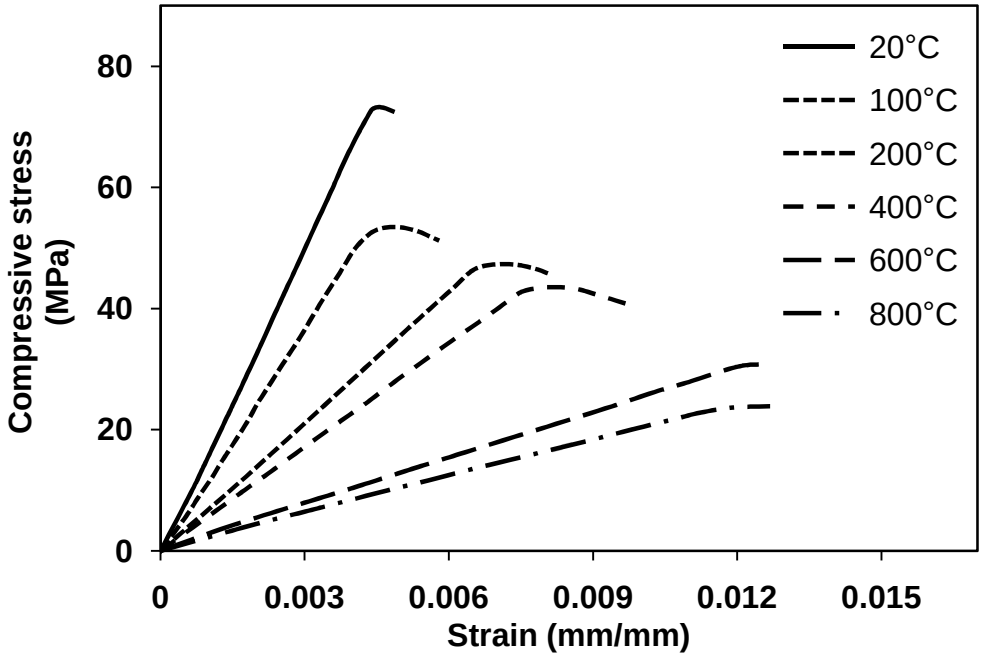

Figure 4.35 - High temperature stress-strain curves for SCC-H

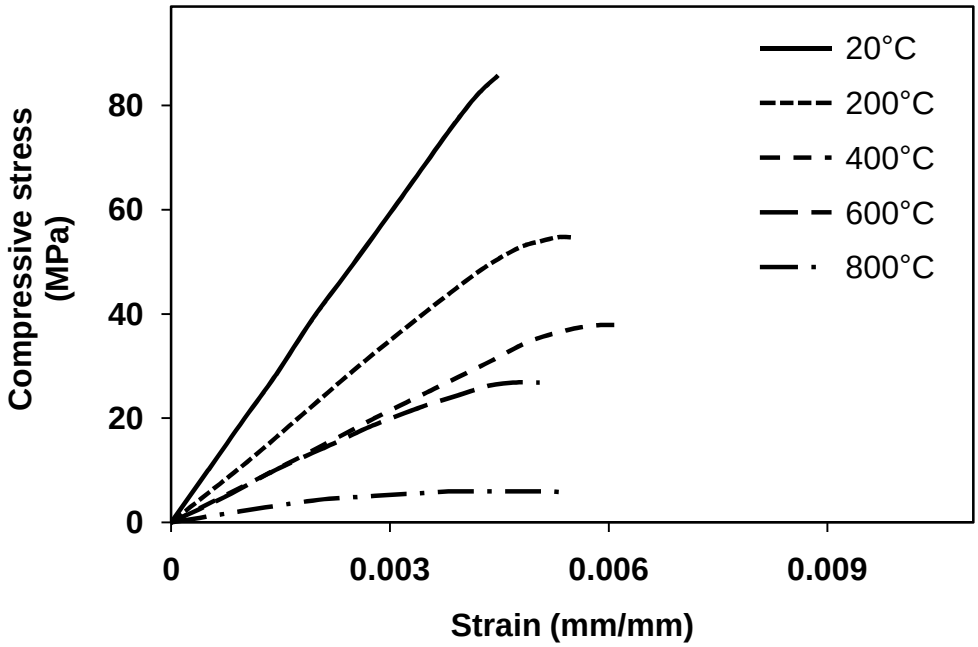

Figure 4.36 - High temperature stress-strain curves for FAC

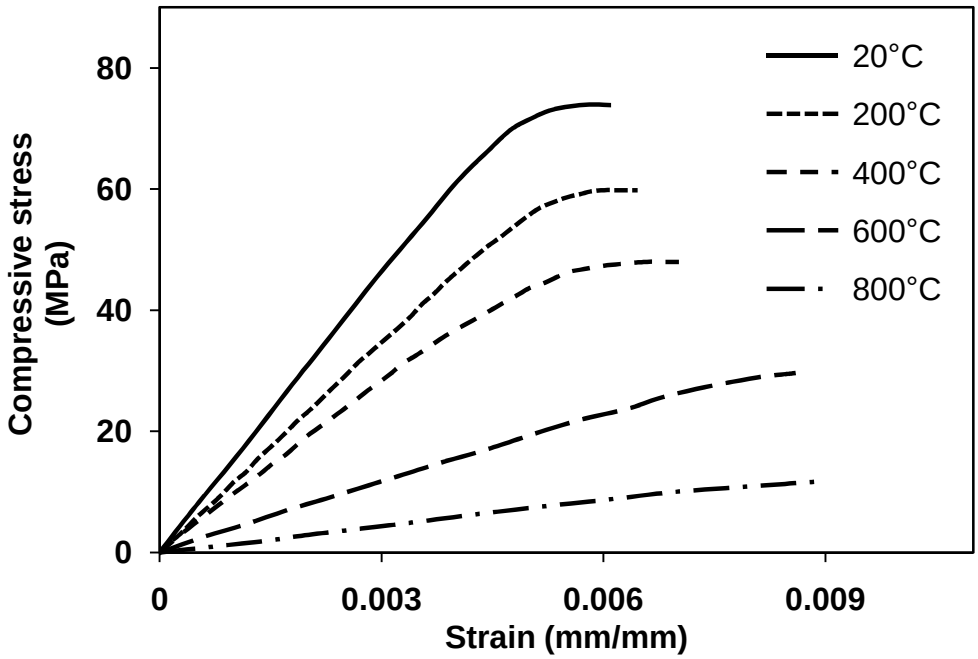

Figure 4.37 - High temperature stress-strain curves for FAC-P

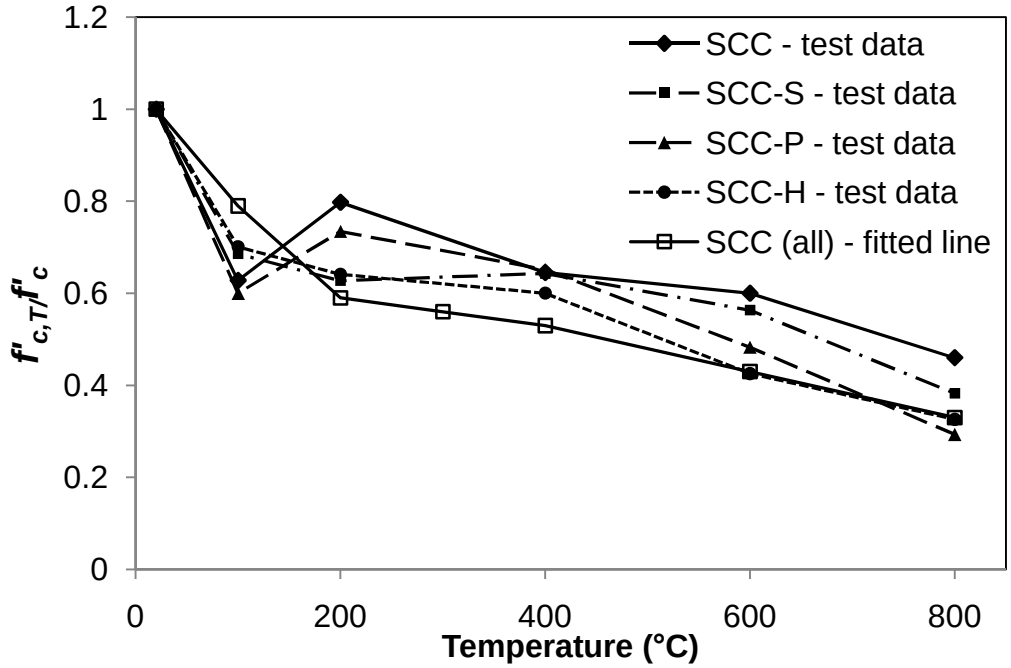

Figure 4.38 - Compressive strength test data of SCC with and without fibers compared with regression based fitted line

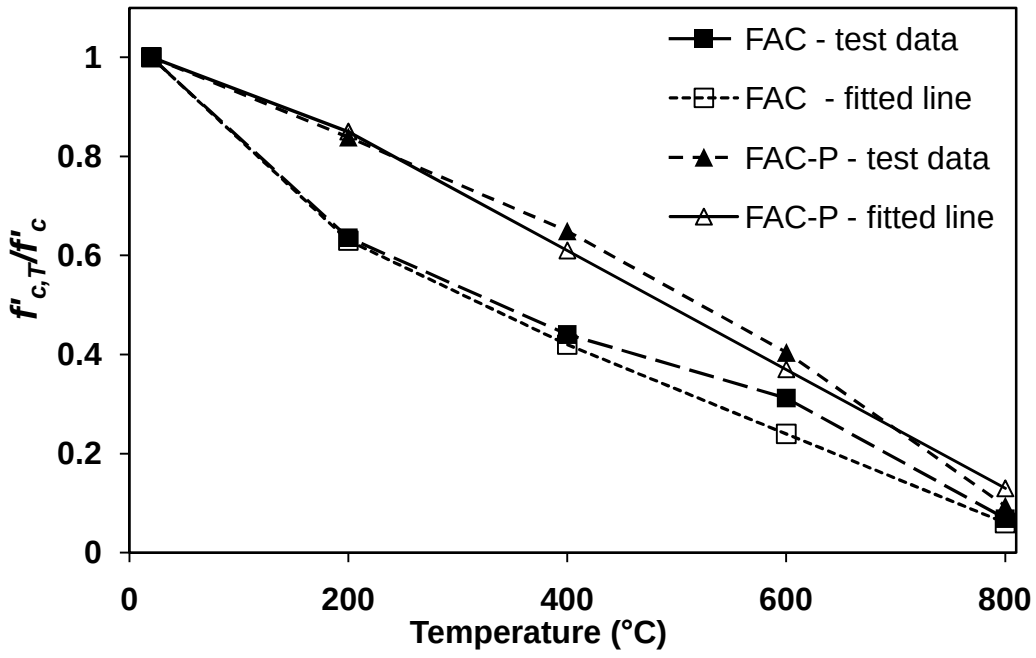

Figure 4.39 - Compressive strength test data of FAC and FAC-P compared with regression based fitted line

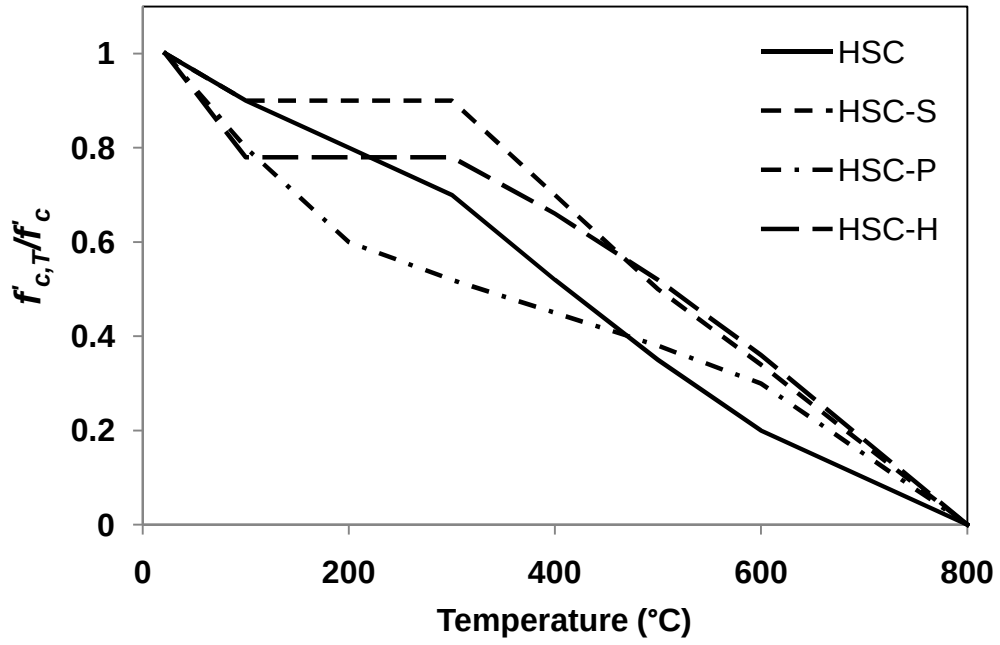

Figure 4.40 - Compressive strength relations for plain HSC and fiber reinforced HSC

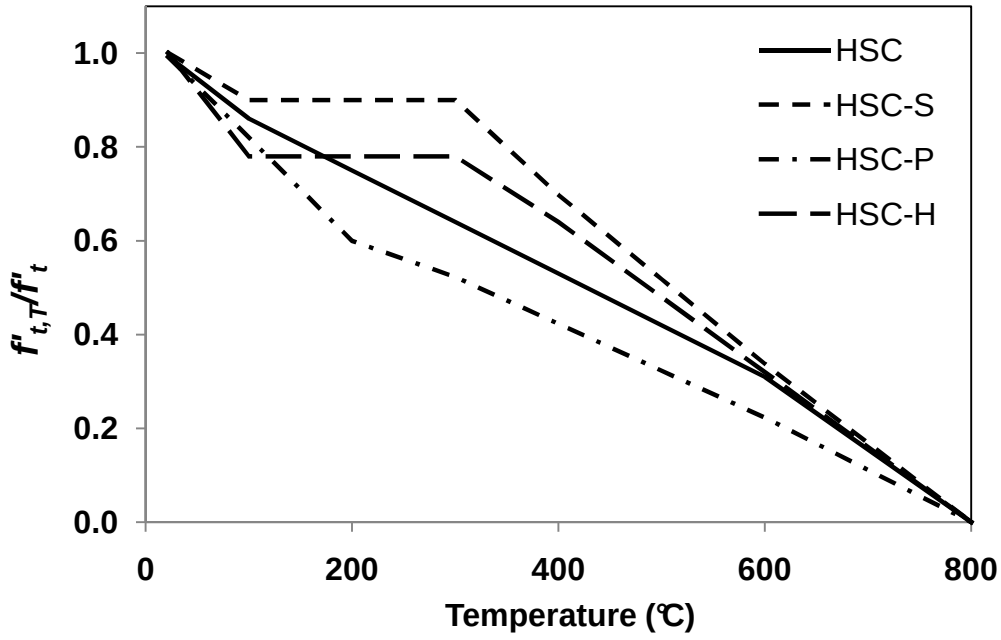

Figure 4.41 - Splitting tensile strength relations for plain HSC and fiber reinforced HSC

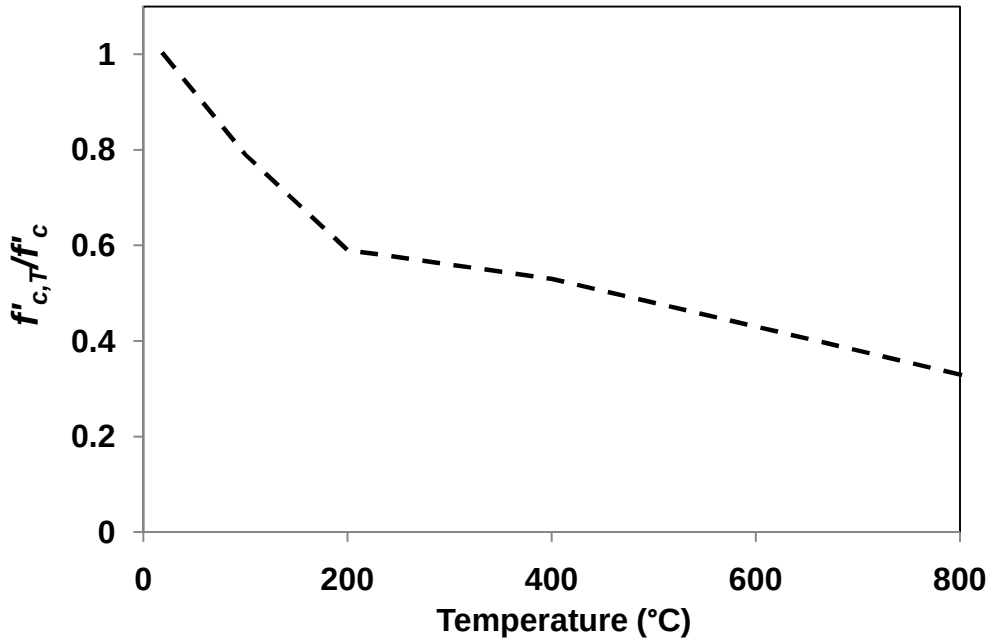

Figure 4.42 - Compressive strength relations for plain SCC and fiber reinforced SCC

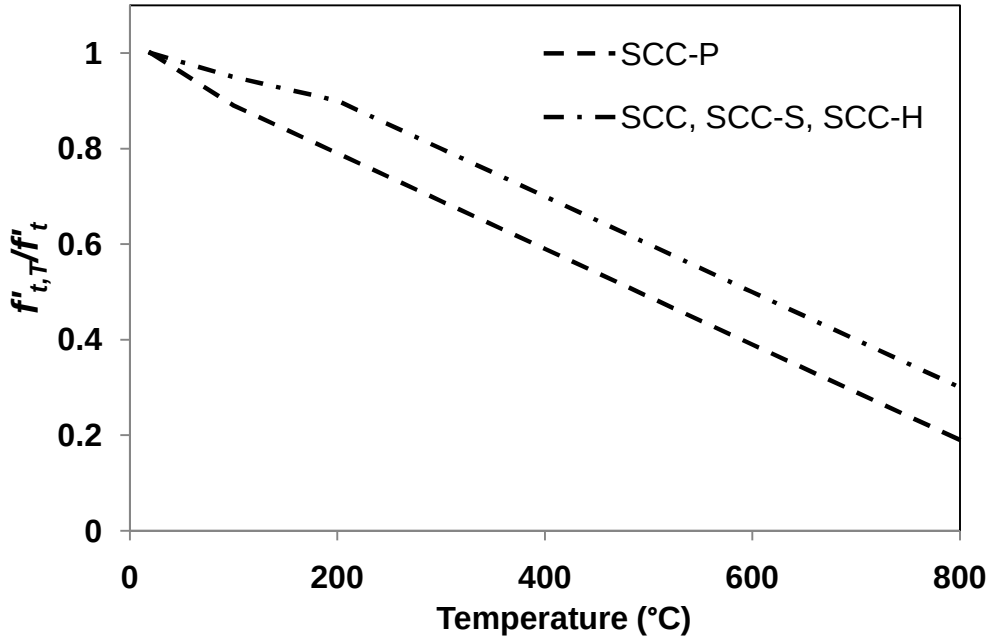

Figure 4.43 - Splitting tensile strength relations for plain SCC and fiber reinforced SCC

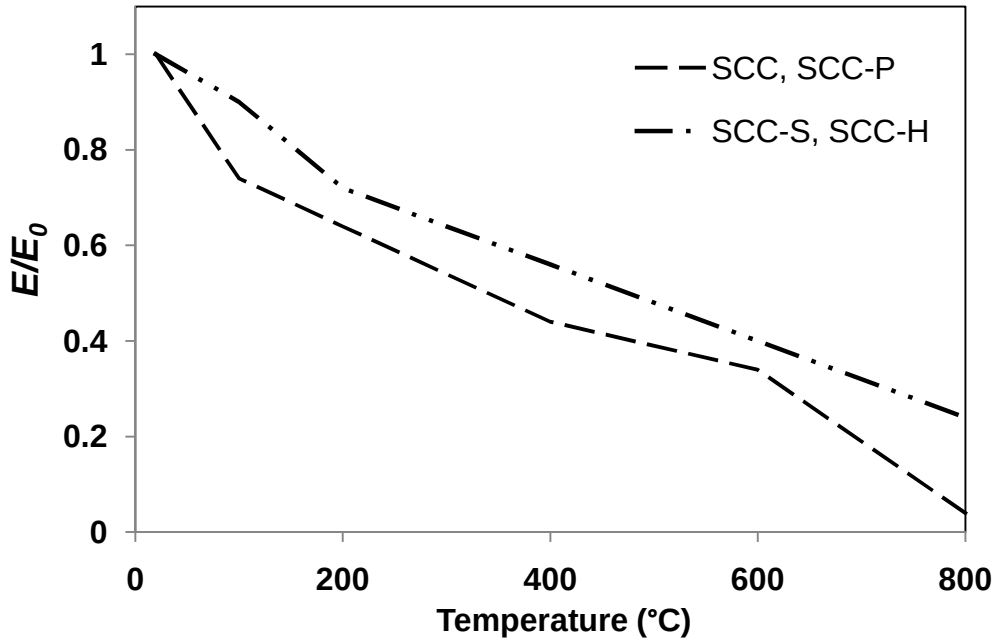

Figure 4.44 - Elastic modulus relations for plain SCC and fiber reinforced SCC

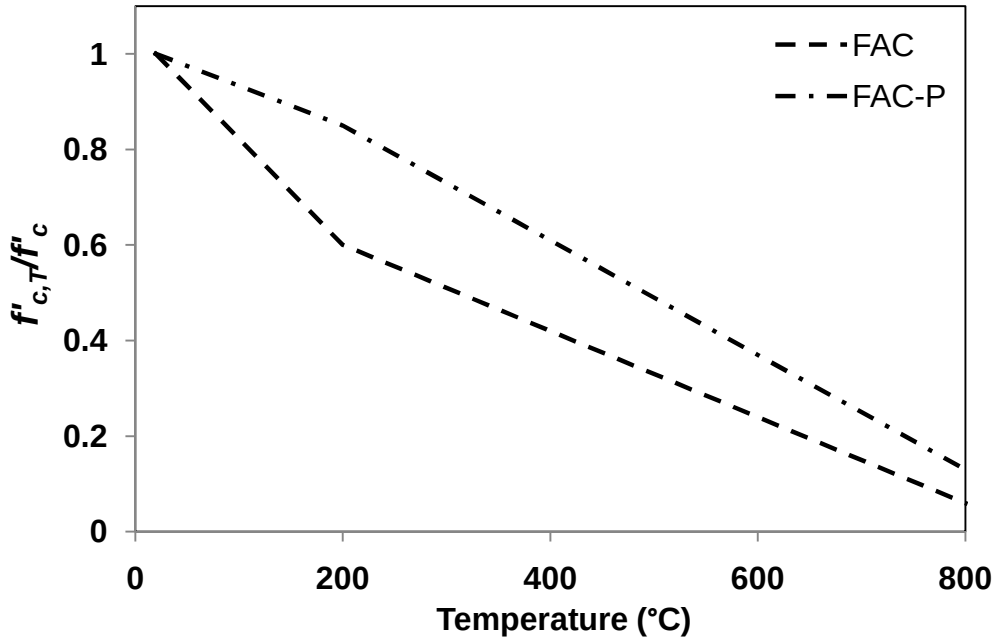

Figure 4.45 - Compressive strength relations for FAC and FAC-P

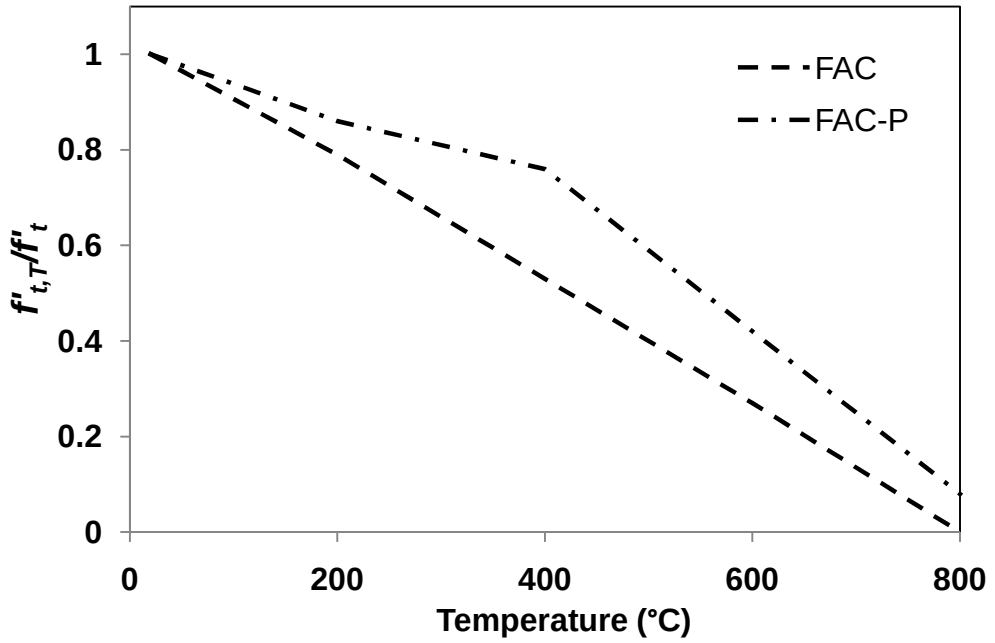

Figure 4.46 - Splitting tensile strength relations for FAC and FAC-P

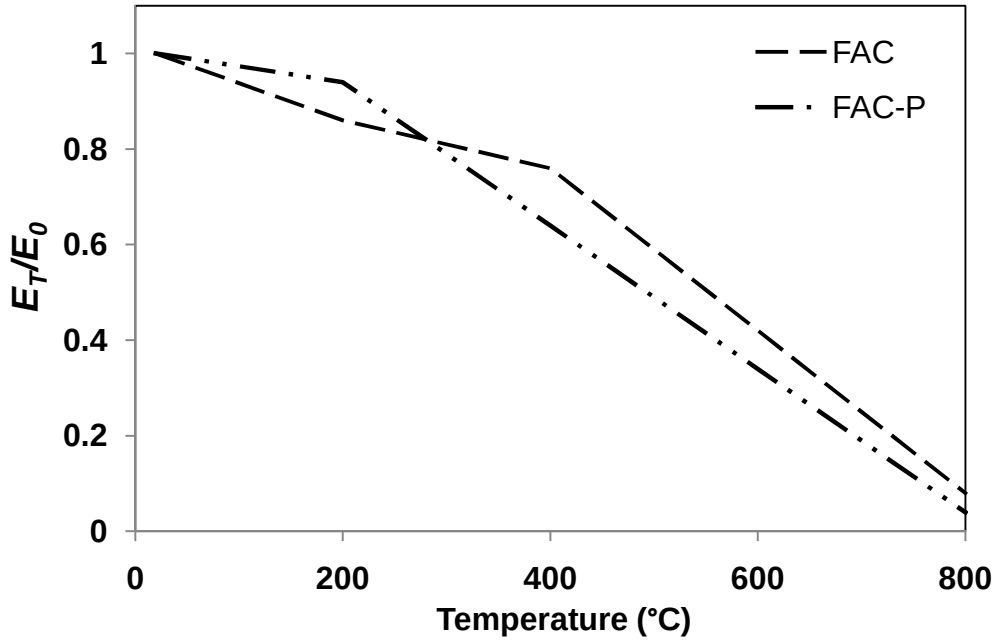

Figure 4.47 - Elastic modulus relations for FAC and FAC-P

CHAPTER 5

5 EXPERIMENTAL STUDIES

Part of this chapter is mainly based on the following journal papers:

- Kodur, V., and Khaliq, W. (2011). “Behavior of High Strength Fly Ash Concrete Columns under Fire Conditions." ASCE Journal of Structural Engineering, Submitted.
- Kodur, V. Mao, X. Raut, N. and Khaliq, W. (2011). “Simplified Approach for Evaluating Residual Strength of Fire-Exposed Reinforced Concrete Columns.” ASCE Structural Journal, submitted.
- Khaliq, W., and Kodur, V. (2012). "High temperature mechanical properties of high strength fly ash concrete with and without fibers." ACI Materials Journal, submitted and reviewed.

5.1 General

Literature review presented in Chapter 2 indicates that there is large amount of data on conventional NSC and HSC columns tested under standard fire scenarios. Also limited data is available on fire response of polypropylene fiber reinforced HSC columns. However, there is no data on fire performance of HPC columns fabricated with fly ash or with steel and hybrid fiber reinforcement. Moreover, for structural characterization of high temperature thermal and mechanical properties of HPC (as presented in Chapter 3 and Chapter 4), full scale fire tests are deemed essential. To overcome these shortcomings, an experimental program was designed to undertake four HPC columns. Since there is large amount of data on HSC columns, fire resistance tests were carried out on two FAC and two HSC columns (with different fiber combinations). This is to limit the number of experiments, due to high cost of fire tests. The

varied parameters included HPC type (FAC to HSC), addition of polypropylene fibers in FAC column and addition of steel and hybrid fibers in HSC columns.

To HPC columns (FAC, FAC-P, HSC-S and HSC-H) were designed, fabricated as per and ACI 318 (2008) and were tested under design fire scenario. These columns were well instrumented and collected a considerable amount of response data comprising cross-sectional temperatures, axial and lateral deformations and strains in rebars. This data from the fire tests helped to characterize the fire response of HPC columns and validate the numerical model. Discussion on results is presented based on fire response of columns comprising the thermal and structural response of these columns. Since columns were tested under design fires that present practical scenario during which the columns may not fail, three out of four tested columns survived the fire resistance tests. These three columns (FACP, HSC-S, HSC-H) were further subjected to post-fire strength tests to evaluate their residual strength capacity. Full details on residual strength tests are also presented in this Chapter.

5.2 Design and Fabrication of Specimens

The experimental program consisted of conducting fire resistance tests on four reinforced concrete columns, two of which were made of fly ash concrete and the other two made of fiber reinforced HSC. Of the two FAC columns, one was fabricated with plain FAC, while the other was fabricated with polypropylene fibers, referred to as FAC and FAC-P columns respectively. Of two HSC columns, one was steel fiber reinforced HSC and other with hybrid fiber (mix of polypropylene and steel fibers) reinforced HSC column, designated as HSC-S and HSC-H columns respectively. For comparison of results, the HSC columns were designed to have similar characteristics as that of FAC columns.

5.2.1 Design of Columns

The size of the test columns were dictated by the dimensions of furnace and loading equipment available for testing. The columns were designed as per ACI 318 (2008) and ACI 216.1 (2007) provisions as high strength slender columns having minimum of two hours fire resistance rating. As per ACI 216.1 Section 2.5.3, for two hours of fire resistance, 50 mm concrete cover is required, however, as per ACI 216.1 Table 2.3, minimum 250 mm columns dimension is required for same fire resistance. As column size could not be increased from 203 mm sides, therefore the actual fire resistance was estimated less than 2 hours base on both cover and size provisions. The design details are given in Appendix B where calculations for one column from each set of FAC and HSC columns is presented. The capacity of the columns was calculated using load-moment (P-M) interaction diagrams generated for these columns (Figures B.5 and B.7 Appendix B). The actual end conditions of these columns were partially-fixed, but for conservative P-M capacity calculations, pin-pin end conditions were considered which lead to a slenderness ratio of 55. Both FAC and FAC-P columns had higher load and moment capacities as compared to HSC-S and HSC-H columns. The overall load capacity of FAC and FAC-P columns was 2144 and 2020 kN respectively while for HSC-S and HSC-H columns it was 1612 and 1665 kN respectively. Similarly the moment capacity of FAC and FAC-P columns was 68 and 69 kN-m to that of 51 and 53 kN-m for HSC-S and HSC-H columns. These ultimate loads and moment capacities of columns are given in Table 5.2 as per Appendix B.

All four columns were 3300 mm long and were of square cross section of 203×203 mm. The columns had four 19 mm dia rebars as longitudinal reinforcement and 10 mm ties, at 200 mm spacing, as transverse reinforcement. The steel of main reinforcing rebars and ties had specified yield strength of 420 MPa. The details of column dimensions and provided reinforcement are

given in Figure 5.1. Generally, 135° bent ties are to be provided as lateral reinforcement for columns in seismic areas, however, recent studies have shown that fire resistance of columns also gets enhanced with the provision of 135° bent ties (Kodur and McGrath, 2003). Therefore the ties in the columns were bent at 135° and anchored in the concrete core to a length of 75 mm as shown in Figure 5.1. For minimum fire rating of two hours, 50 mm of concrete cover was provided as per ACI 216.1(2007).

5.2.2 Fabrication of Specimens

5.2.2.1 Mix Proportions

Four batches of concrete were used for fabricating these columns namely FAC, FAC-P, HSC-S and HSC-H. All four batches of concrete had ordinary Portland cement (Type I), carbonate coarse aggregate and natural source sand as fine aggregate. Fly ash (Type C) was used as replacement (25%) to cement in FAC and FAC-P mixes. To achieve desired high strength and workability, optimum amount of mineral admixtures, such as silica fume and slag (Grade 120), were added to batch mix. In FAC-P and HSC-H mixes, 2 kg/m^3 (0.22% by volume), MONOFILAMENT (multi-plus) type polypropylene fibers, were added. The 20 mm long polypropylene fibers were of nonabsorbent type and have a specific gravity of 0.91 and a melting point 162°C. In HSC-S and HSC-H mixes 42 kg/m^3 (0.54% by volume) NOVOCON XR type steel fibers were added. Steel fibers were 38 mm in length and 1.14 mm (0.045 in) equivalent diameter and had a specified tensile strength of 966 MPa. Mix proportions and attained compressive strengths at different ages for four batches of concrete (FAC and FAC-P, HSC-S and HSC-H) used for fabricating the columns are tabulated in Table 5.1. The compressive strength of different concrete mixes measured on 100×200 mm cylinders at 28 days ranged from

67-102 MPa. It can be seen from Table 5.1 that 28 days compressive strength of FAC and FAC-P concrete was significantly higher (102 and 100 MPa respectively) as compared to HSC-S and HSC-H (67 and 68 MPa respectively). Same is true for strength of these concretes at 90 days and on the test day. It should be noted that the quantity of silica fume was almost similar in batch mixes of both HSC and FAC columns (43 and 41 kg/m^3 respectively) therefore the additional improvement in strength properties of FAC and FAC-P concrete is attributed to fly ash in the mix. Strength in HSC-S and HSC-H was lower even with the addition of steel fibers. However, it should be noted that the real contribution of steel fibers in concrete is to increase the toughness of concrete as the fibers tend to increase the strain at peak load, and provide a higher energy absorption in post-peak portion of the load-deflection response (Mehta and Monteiro, 2006).

5.2.2.2 Fabrication of Columns

Horizontal wooden formwork was prepared to cast the columns. Longitudinal steel rebars were tied with lateral ties using binding wire to create the reinforcement cage. This reinforcement cage was placed inside the formwork as shown in Figure 5.2. At this stage, instrumentation consisting of strain gauges and thermocouples were attached to the steel rebars. All four concrete columns were cast and finished by placing the formwork in horizontal position. Fifteen 100x200 mm cylinders were also cast for strength measurements at different concrete age. In fabrication of columns, vibrators were used at moderate speed to ensure quality finish. The columns were then physically leveled and finished on the open side of the formwork as shown in Figure 5.3. After casting, the columns were initially moist cured in the forms for 7 days and then removed from the forms and stored at ambient conditions (more than six months) till tests were done. During storage, the conditions were maintained at about 22°C temperature and 40% relative humidity.

Three cylinders from each batch were tested to evaluate compressive strength at 7, 28, 90 days and on test day (about 8 months after casting of columns).

5.2.3 Instrumentation

The instrumentation in the columns included thermocouples (TCs) to record concrete and rebar temperatures, strain gauges (SGs) to record strain in steel rebars, and linear position transducers (LPTs) to measure axial and lateral deformations. Thirteen type-K (Chromel-alumel) thermocouples of 0.91 mm thickness were installed at three different cross-sections namely mid-height, top three-quarter, and bottom one-quarter cross-section in the fire exposed portion of the columns.

Figure 5.4 illustrates the position of three cross-sections and precise location of TCs at each cross-section. The arrangement for thermocouples was same for all four columns. At Section AA, TC 1 to TC 3 were attached to record rebars' temperatures, TC 4 and TC 5 for surface temperatures, TC 6 and TC 7 to record concrete temperatures at center and quarter depth of the cross-section. At section BB, TC 8 was attached to record rebar temperature, while TC 9 and TC 10 were installed to record temperatures of center the cross-section and ties. At Section CC, TC 11, TC 12, and TC 13 were attached to record rebar, concrete at quarter depth and tie temperatures respectively. Two high-temperature and one regular strain gauge namely HTSG 1, HTSG 2, and SG 3 were used at geometric mid-height (Section DD) of the columns and another three regular strain gauges namely SG 1, SG 2, and SG 3 were used at three-quarter-height (Section EE) of columns as shown in Figure 5.5. These strain gauges were attached to the steel rebars and the arrangement was similar in all four columns. Physical placement of thermocouples and strain gauges on to steel cage is shown in Figure 5.6.

The axial deformation of the columns was measured by placing two linear position transducers (LPTs) orthogonal to each other on top of each column attached to the top plate of the columns. The recording of axial deformation by two LPTs placed orthogonally helped to record data on two axes and compute actual axial deformation by comparing the two measurements. The columns were oriented in East-West and North-South directions of the furnace. The LPTs were placed North-East and North-West sides of the columns as shown in Figure 5.7.

Measurement of lateral deformations in a fire exposed column inside the furnace becomes very difficult due to harsher environment (very high temperatures). This difficulty was overcome through a specialized technique by using Chromel wires inside the furnace. Chromel wires that can resist high temperatures (up to 1350°C) were pulled out of Type-K (Chromel-alumel) thermocouples and were attached to columns by wrapping around and tying to columns. These wires were then extended outside of the furnace so as to attach to LPTs positioned outside of furnace for recording lateral deformations of the column. Figure 5.7 illustrates that these Chromel wires were attached to LPTs on two orthogonal faces of the column at mid height. The position of each axial and lateral LPT to measure axial and lateral deformation in all four columns is also illustrated in Figure 5.7. Two columns were tested at the same time in the furnace by placing them in east and west positions. Depending on the available openings, the lateral LPTs on east column were placed on north and east sides of the furnace, whereas for west column these LPTs were placed north and west sides of the furnace as shown in Figure 5.7

5.3 Fire Resistance Experiments

5.3.1 Test Equipment

The fire resistance tests were carried out by placing the columns in the structural fire test furnace at the Civil Infrastructure Laboratory (CIL) of Michigan State University (MSU). The test

furnace, integrated with a loading frame, has been specially designed to produce conditions, such as temperature, loads and heat transfer, to which a structural member might be exposed during a fire as shown in Figure 5.8(a). The furnace has the capacity to supply both heat and applied loads to the structural member that are present in a typical structural member exposed to fire.

The furnace consists of a steel loading frame (framework) supported by four steel columns, with a fire chamber that is 2440 mm wide, 3050 mm long, and 1775 mm high as shown in Figure 5.8(b). The maximum heat power the furnace can produce is 2.5 MW. Six natural gas burners located within the furnace provide thermal energy, while eight type-K thermocouples distributed throughout the test chamber as per ASTM E119 (2008), help monitor and control the furnace temperatures. Data from fire tests, which include temperatures, displacements, forces and strains, are collected using a "Darwin Data DA100/DP120-13" acquisition system. This system contains 70 thermocouple channels, 10 voltage channels for measuring displacements and forces, and 10 strain-gauge channels. These channels are connected to data acquisition system, which transfers the data at five second intervals throughout the fire test to a personal computer that stores it in a ".CSV" file using the "DAQ 32" computer program.

During the fire test, temperatures recorded in the furnace are used to manually adjust fuel supply and air intake, to maintain a temperature course consistent with the pre-determined standard or design fire scenarios (Kodur and Fike, 2009). In this way, the furnace temperature can be maintained along a desired time-temperature curve. Two small view ports on either side of the furnace wall are provided for visual monitoring of the fire-exposed columns during a test. The furnace accommodates two columns at a time and different load levels can be applied on each column.

5.3.2 Preparation of Columns for Fire Tests

The columns after curing for about 6 months (or more) were prepared for safe and secure testing. The columns were placed in furnace in a predetermined arrangement to fit precisely under vertical actuators and also to attach to bottom steel plate of size 406×406×60 mm that is fixed to the floor. A steel plate of size 406×406×25 mm was also attached to the top of the column where actuator loading head makes a contact with the column. These steel plates were bolted at each end of the column using four steel angles of 100×100×12 mm which helped to fix the column in position and for facilitating load transfer from the actuator. These end plate and angle attachments are illustrated in Figure 5.7. With these end conditions at the top and bottom, the column can be assumed to be partially restrained against rotation. The actuator sits on top of the fixed plate and provides a rotational stiffness of 250 kN.m/μrad. Figure 5.9 illustrates attached parts and the end restraint conditions at the top and bottom of the columns before testing.

On the test day, just prior to undertaking the fire tests, the room temperature moisture conditions (relative humidity) of the columns and compressive strength of concrete were measured. The relative humidity of concrete columns was measured at two different locations on the columns using a “Sensirion” relative humidity sensor (probe). For placing the probe, 8 mm holes were drilled at two different locations in each column and then the probe was placed in the hole and the hole was sealed for about 5 minutes until equilibrium of relative humidity and temperature was achieved. Once the equilibrium conditions were reached, the relative humidity at that position was recorded. The average of two relative humidity measurements for each column at the time of testing was between 90 and 91% as shown in Table 5.2. Higher relative humidity readings in the tested high columns, as compared to typical normal strength concrete columns

(Raut and Kodur, 2011), can be attributed to dense microstructure and compactness of high performance concrete mixes which minimizes evaporation of moisture.

Test day cylinder compressive strength of all four concretes was not much different from 90 days compressive strength, but it was significantly higher (ranging 5-19%) than 28 days compressive strength as shown in Table 5.1. Both fly ash and silica fume enhance concrete strength over time as the pozzolans react with calcium hydroxide continuously during the hydration process (Mehta and Monteiro, 2006; Mindess et al., 2003; Neville, 2004) and contribute to enhanced strength. The improvement in strength in all four concretes (FAC, FAC-P, HSC-S and HSC-H) is therefore attributed to the age of the specimens and continuous hydration process in presence of pozzolans.

The test day compressive strength was used to calculate the capacity of the columns and to evaluate the test load that was to be applied on columns during fire tests. As per ACI 318 (2008) design guidelines, a column is said to be slender when the slenderness ratio of columns is greater than 40, therefore these four columns, with slenderness ratio of 55, were designed as slender columns and the capacity was evaluated based on axial load-moment (P-M) interaction diagrams. The detailed capacity calculations and resulting P-M interaction diagrams of these columns are given in Appendix B. The calculated capacities for all the columns are also tabulated in Table 5.2.

5.3.3 Test Procedure

The fire resistance tests were carried out by placing two columns in the furnace and exposing them to selected design fire scenario. The columns were exposed to fire from all sides. First test was carried out on FAC and FAC-P columns, while second test was carried out on HSC-S and HSC-H columns. During the fire test, middle 1775 mm of the 3300 mm height of the columns

was exposed to fire. The columns were tested under a parametric (design) fire exposure which comprised of a growth phase as per ASTM E119 (2008) standard fire exposure and followed by a decay phase as shown in Figure 5.10. In test-I decay phase of 4.16°C/min was based on Eurocode design fire (Eurocode 1, 2002), whereas in test-II a faster decay rate of 11°C/min was selected to depict early extinguishing of fire.

As fire resistance of RC columns is significantly enhanced with use of fibers and also with 135° bent ties, a fire exposure of 3 hours was selected to see the failure of the columns against estimated fire resistance of 2 hours (or under) as per ACI 216.1. However, the decay (cooling) phase was 4 hours for test with cooling phase based on Eurocode design fire and 1.5 hours for second test with faster cooling rate. Total fire exposure duration for FAC and FAC-P columns in first test was 7 hours, and for HSC-S and HSC-H columns was 4.5 hours. The well-defined decay (cooling) phase was achieved by controlling temperatures (cooling) in the furnace (by blowing air through the vents in the furnace) so as the fire to decay at a predetermined cooling rate representing typical fire in a building.

All four columns were tested under a concentric axial load representing a load ratio of 0.4 for FAC and FAC-P columns and a load ratio of 0.6 for HSC-S and HSC-H columns. The load ratio is the ratio of the applied (test) load to the column capacity computed according to ACI 318 (2008). Earlier studies (Raut and Kodur, 2011) have shown that HSC columns perform better under 0.4 load ratio, therefore a higher load ratio of 0.6 was selected for HSC columns in this study. Another reason for selecting higher load ratio of 0.6 was the expected better fire performance of steel and hybrid fiber reinforced HSC columns.

The loading was applied approximately 30 minutes prior to start of the fire resistance tests and was maintained either until the column failed under fire exposure or to the end of the test. During the fire resistance tests on columns, temperature was controlled in such a way that the average temperature in the furnace followed, as closely as possible, the parametric fire scenario (Design fire 1 and Design fire 2). At the end of the fire test, once the furnace temperatures were down to room temperature, the surviving columns were unloaded and allowed to cool while still inside the furnace. These survived columns were used for residual strength tests as discussed in Section 5.5. A summary of test parameters and results from fire resistance tests for four columns namely FAC, FAC-P, HSC-S, and HSC-H is given in Table 5.2.

5.3.4 Measured Data and Test Observations

The test data comprising of furnace temperatures, column temperatures, axial deformations, lateral deformations, rebar strains and loading were recorded at every 5 seconds interval through data acquisition system. Visual observations were made every 5 minutes through the view ports in the furnace to record any major changes in the columns such as fire induced spalling, visible crack propagation and excessive deformations. Also photographs of columns were taken at regular intervals during the test. After completion of fire resistance tests, post-test observations were made to record failure pattern, extent of physical deterioration due to heat (fire) and spalling, concrete discoloration and condition of reinforcement. Volumetric measurements were done on fire exposed columns to quantify the extent of spalling resulting from fire exposure. The exposed length of each column was divided into a number of segments and the volume of each segment is computed by taking measurements with respect to a reference axes system. The total volume of a damaged column was then computed as the sum of the volumes of all the segments, and used to compute overall spalling. FAC column was the only column that failed during the

fire test as hydraulic jack could no longer maintain the load, whereas other three columns in this test program did not fail under the given fire exposure time.

5.4 Response of HPC Columns during Fire Exposure

Data generated from the above fire tests was utilized to compare the fire behavior of FAC, FAC-P, HSC-S, and HSC-H columns under different conditions. The test variables included concrete strength, effect of type of concrete, and effect of different fibers. A summary of results of fire resistance tests on the columns are tabulated in Table 5.2. The fire performance of these columns is evaluated in the form of thermal response, structural response, spalling behavior as well as fire resistance time.

5.4.1 Thermal Response

During fire tests, the temperature progression was recorded through thirteen thermocouples located at three cross-sections (sections AA, BB and CC) as shown in Figure 5.4. The thermal response of all four columns (FAC, FAC-P, HSC-S, and HSC-H) is shown in Figures 5.11 to 5.22 by plotting measured temperature profiles in rebars, and concrete as a function of fire exposure time. In all columns, an initial plateau can be seen in rebar and concrete temperatures around 100°C and this can be attributed to heat from fire being utilized for evaporation of free water in concrete. After this initial plateau, the temperatures in concrete and rebars increase with fire exposure time. It can be noted that, in all four columns, the progression of temperatures in concrete (at mid-depth) is lower than that in rebars. This can be attributed to lower thermal conductivity and higher specific heat of concrete which delays temperature rise to inner layers of concrete.

The temperatures profiles at sections AA and BB show inconsistent trend and this can be attributed to displacement (or damage) of TC's (TC3, TC4, TC5 at Section AA and TC8, TC9, TC10 at Section BB) at these locations resulting from fire induced spalling and direct exposure of rebars to fire temperatures. This disturbance in temperature profiles was not observed in FAC-P, HSC-S and HSC-H at all three cross-sections since there was no fire induced spalling. These temperature profiles show that addition of fibers (both steel and polypropylene) is quite beneficial in mitigating the fire induced spalling and retaining cross-sectional integrity of HPC columns.

A comparison of temperature rise in FAC and FAC-P columns indicates that temperatures in FAC column are slightly higher than that in FAC-P column throughout the fire exposure time (see Figure 5.23). The higher temperatures in FAC column can be attributed to two factors, occurrence of fire induced spalling leading to loss of concrete cross-section, and higher thermal conductivity of FAC (Kodur and Khaliq, 2011). The peak rebar temperatures attained in FAC column was 681°C at 270 minutes into the fire exposure, as compared to 645°C in FAC-P column. This lower temperature in FAC-P column can also be attributed to reduced thermal conductivity of FAC-P resulting from increased permeability (due to melting of polypropylene fibers).

To compare the performance of different types of HPC under fire conditions, fire resistance of the two types of concrete columns (FAC and HSC) tested in this program is also compared. The thermal response of FAC and FAC-P columns is compared with measured temperatures of HSC-S and HSC-H columns (see Figure 5.24). It can be seen that the temperature progression in both FAC and FAC-P columns follow similar trends to that of HSC-S and HSC-H columns, however both FAC and FAC-P columns had slightly higher temperature profiles. This can be attributed to

slightly higher thermal conductivity and specific heat of FAC (as compared to HSC) (Kodur and Khaliq, 2011).

5.4.2 Structural Response

Structural response of column is generally assessed by measuring axial and lateral deformations in column, and also strain in rebars under fire exposure. Both axial and lateral deformations were recorded in four columns and strain data was measured in steel rebars in the fire resistance tests is presented here. To gauge the relative performance of two types of HPC (FAC and HSC) the comparison of structural response for all four columns is presented.

5.4.2.1 Axial Deformations

The structural response of four columns is evaluated by comparing measured axial deformations as a function of fire exposure time, which is shown in Figure 5.25. An RC column, when exposed to fire, expands initially due to thermal expansion occurring both in steel rebars and in concrete. With increasing fire exposure time, temperatures in rebars rise and the steel (reinforcement) yields at about 600°C, a temperature that is critical for steel since it loses 50% of its yield strength (Lie, 1992). After steel yields, concrete core in the column progressively carries higher percentage of applied load. With increasing temperatures, strength and stiffness properties also deteriorate in concrete (Kodur and McGrath, 2003) leading to increased load induced mechanical strains which in turn results in contraction of the columns. With increasing fire exposure time, the strength of the concrete also decreases due to deteriorating properties of concrete, and ultimately, when the column can no longer support the load, failure of column occurs.

Results plotted in Figure 5.25 indicate that all four columns underwent expansion in the initial stages of fire exposure. Higher initial expansion in the case of FAC column can be attributed to

higher thermal strains. Further fire induced spalling that occurred in FAC column led to loss of cross section which resulted in loss of strength and contraction (100 minutes) much earlier than that in FAC-P column which led to failure of FAC column in 165 minutes. At this failure time, the rebars temperature in FAC column reached 630°C and mid-depth (concrete) temperature reached 560°C (as opposed to 570 and 470°C respectively in FAC-P column). This indicates that steel rebars had also lost strength entirely in FAC column due to fire exposure. Previous fire resistance studies have shown that the large deformation prior to failure results from high mechanical strains (due to significant loss of strength and stiffness of the columns) and also from significant levels of high temperature creep (Lie, 1992). Significant increase in the deformations in column FAC-P towards later stages of fire exposure can be attributed to effect of high temperature creep, which can be quite high when steel and concrete temperatures exceed 600°C.

The effect of fire on structural response of both HSC-S and HSC-H columns can also be gauged by reviewing the progression of axial deformation with time (Figure 5.25). These columns were exposed to similar fire scenario as that of FAC columns. Both these columns exhibit expansion phase followed by contraction similar to FAC columns. However, the axial expansion in both HSC-S and HSC-H columns is lesser than that in FAC column. It should be noted that HSC columns were subjected to higher load ratio (0.6) as compared to FAC columns (0.4). Therefore the lower axial expansion in case of HSC columns was due to influence of higher applied load. Both HSC-S and HSC-H columns expanded smoothly up to three hours before they started contracting. Also no spalling or major cracking was observed in HSC-S and HSC-H columns, this in turn led to their better fire performance than that of FAC column.

The axial deformation-time plot in Figure 5.25 illustrates that higher initial axial deformation and early contraction occurred in FAC column. Since FAC column had lost its cross-section in initial

30 minutes of fire exposure, it resulted in direct fire exposure of rebars leading to higher expansion of FAC column. Loss of cross-section in FAC column also compromised the structural integrity due to higher degradation in stiffness; this resulted in early contraction under load and led to failure. FAC-P column on the other hand sustained lesser axial deformation and contraction in initial stages for fire than that in FAC column. Moreover, as a result of spalling mitigation, due to melting of polypropylene fibers, the column cross-section in FAC-P column remained unchanged, thus lower degradation to stiffness occurred. As a result FAC-P column exhibited better fire resistance than FAC column.

Comparison of results from the tests on FAC and FAC-P columns with those of HSC-S and HSC-H columns in Figure 5.25 illustrates that axial deformations in FAC-P, HSC-S, and HSC-H columns follow almost similar trends in early stages of fire test. The gradual increase in expansion and contraction in HSC-S and HSC-H columns can be attributed to higher applied load (60% of ultimate load capacity) and enhanced ductility facilitated by presence of steel fibers. Even under higher axial loads, both HSC-S and HSC-H columns survived the entire fire test up to 4.5 hours. Fly ash concrete column had better strength properties as compared to HSC-S and HSC-H resulting from fly ash in the mix (as described in Section 5.2), however, the steel fibers improved the toughness and tensile strength properties in HSC-S and HSC-H concrete that resulted in higher fire resistance in HSC-S and HSC-H columns.

5.4.2.2 Lateral Deformations

The lateral deformation measured at mid-height is plotted as a function of fire exposure time for all four columns in Figure 5.26. All four columns had similar end (restraint) conditions with bottom end completely fixed and the top end partially fixed (as shown in Figure 5.9). All these columns exhibited lateral deformation in the expansion phase (in the initial stages of fire) and the

deformation reached 25 mm at 100 minutes in to fire exposure (see axial deformation plot in Figure 5.25). However, in FAC column, the lateral deformation significantly increased to 121 mm, at the time of failure, when the column moved in to contraction phase. Two factors that contributed to this excessive lateral deformation in FAC column are; reduced cross-section due to fire induced spalling and temperature induced stiffness degradation. This excessive lateral deformation led to failure of FAC column in 165 minutes through global buckling. Lateral deformation in FAC-P column increased to 45 mm at 180 minutes and then stabilized and slightly reversed in the cooling phase of fire. This onset of reversal and stabilization of lateral deformation in FAC-P column coincides with start of its axial contraction after undergoing initial expansion (as can be seen in Figure 5.25). The enhanced performance of FAC-P column can be attributed to its sustained integrity (without any loss of cross-section) due to mitigation of spalling facilitated by the melting of polypropylene fibers.

As shown in Figure 5.26, lateral deformation in HSC-S and HSC-H columns increased to about 30 mm at 150 minutes and then almost remained steady. This steadiness in lateral deformation in HSC-S and HSC-H columns, in comparison to FAC columns, can be attributed to slower degradation of stiffness in these columns resulting from presence of steel fibers. The other factor that enhanced the fire performance of HSC-S and HSC-H columns was sustained cross-sectional integrity of these columns facilitated by spalling mitigation.

5.4.2.3 Strain in Steel Reinforcement

The strains in the longitudinal reinforcement in the columns were monitored during the fire tests through high temperature and regular (room temperature) strain gages as explained in Section 5.2.3 and illustrated in Figure 5.5. The high temperature strain gauges can give reliable strain measurements in steel rebars for temperatures up to 300°C, whereas regular strain gauges are

reliable only up to 100°C. Due to limit of workable temperature range, functionality of these strain gauges is limited as data collected by them may be unstable and unreliable in high test temperatures up to 600-800°C. During the fire test, few of these strain gages (mostly regular) malfunctioned during fire tests, these strain gauges either got disconnected or simply broken due to fire exposure (temperature limitation). The measured strain from strain gauges attached to the longitudinal reinforcement at two sections of the tested columns is plotted as a function of fire exposure time in Figures 5.27-5.34. It can be seen from these figures that the strain data from tested columns appeared to be reliable only up to 20 minutes or less in to fire exposure. Moreover not all data gave good results and some of these results were irrational due to significant variation. The malfunctioning and bad results in strain gauges can be attributed to the cracking of concrete near the strain gauge, or intermittent de-bonding of the strain gauge from the reinforcing steel due to the sudden rise (thermal shocks) in rebar temperature due to fire exposure.

Results from two of the survived high temperature strain gauges (HTSG 1 and HTSG 2) in FAC column at Section DD (mid-height of column as shown in Figure 5.27) show that they recorded thermal expansion in steel rebars between 6 and 10 minutes. The recorded thermal strain was between 100-300 micrometer/m range. This is in good agreement to the load-axial deformation trends in FAC column as shown in Figure 5.25 where the FAC column is seen expanding in initial stages of the fire test. However, after 10 minutes in to fire exposure the strain data collected by both strain gauges became irrational either due to malfunctioning or deboning from steel rebars. On the other hand only one regular strain gauge (SG 2) survived at Section EE (three-quarter-height of column as shown in Figure 5.28). This strain gauge recorded thermal expansion in steel rebar up to 13 minutes and the maximum recorded stain was 500

micrometer/m before it stopped recording data. The small disturbance in the measurement recording at about 5 minutes into the fire test might have resulted from cracking and spalling that was in progress in FAC column at that time. The thermal strain in steel rebar is again rational and in good agreement to load-deformation of FAC column.

In the case of FAC-P column, all three stain gauges survived at Section DD (mid-height of column as shown in Figure 5.29) and recorded strain data correctly up to about 140 minutes with very little disturbance. The recorded thermal strain remained constant under 100 micrometer/m up to 120 minutes and increased up to 1500 micrometer/m before malfunctioning. The stain in steel rebars also depicts correctly the lower load-axial deformation in FAC-P column (Figure 5.25) up to 140-150 minutes before it started to contract. Only one stain gauge (SG 3) survived at Section EE (three-quarter-height of column as shown in Figure 5.29) and recorded strain data correctly up to about 25 minutes but with some disturbance. The maximum recorded strain was 800 micrometer/m at about 11 minutes of the fire exposure but then it shows contraction in steel rebar. This is not in line (agreement) with the load-deformation response of FAC-P in which expansion continued till 150 minutes. This result may have occurred due to some local disturbance concrete-steel rebar interaction and therefore deemed unreliable.

For HSC-S column, two high temperature strain gauges (HTSG 1 and HTSG 2) at Section DD and two regular strain gauges (SG 1 and SG 2) at Section EE survived and recorded strain data up to about 30 minutes as shown in Figures 5.31 and 5.32 respectively. The strain recorded by HTSG1 and HTSG2 at Section DD show expansion with a maximum thermal strain of 1500 micrometer/m before both the strain gauges malfunctioned. However data recorded till about 20 minutes is in good agreement with the load-deformation plot of column HSC-H (see Figure 5.25). The strain recorded by SG1 and SG2 at Section EE show irrational response data as these

show expansion and contraction at the same time at this section within 30 minutes. In the case of HSC-H, all three strain gauges survived at both cross-sections DD and EE and recorded thermal strains in steel rebars up to 20 and 40 minutes respectively as shown in Figures 5.33 and 5.34 respectively. At Section DD the two high temperature strain gauges recorded strains up to 1000 micrometer/m in 7-10 minutes. However, the strain recorded by SG3 at this section seems irrational as it might have gone bad under high temperature. At Section EE all three regular strain gauges show different strain progression and therefore measurements seem irrational. The SG1 shows increase in thermal strain up to 40 minutes in steel rebars that correlates with the actual load-deformation behavior of HSC-H column. However, SG2 shows no change in thermal strain and SG3 shows increase in thermal strain after about 30 minutes, therefore data recorded by both of these strain gauges is unreliable.

It should be noted that both regular and high temperature strain gages have temperature limitations for reliable operation (100 and 300°C respectively), therefore these are less reliable due to harsher temperature environments and complex physical and chemical processes that occur in structural members at elevated temperatures (Dwaikat, 2009). It should also be noted that the fire temperatures in fire test can reach up to 1000°C and steel rebar temperature can go as high as 800°C and therefore strain gauges cannot stably operate at these high temperatures. The problem associated with the reliability of high temperature strain gages was also encountered by other researchers (Dwaikat, 2009; Raut, 2011; Williams, 2004). Some previous researchers attributed the problem in strain gages to the electrical interference from the operation of the high voltage ignition and the control systems (Williams, 2004) associated with fire tests. One other reason for this problem could be that the strain gages are designed for low heating rate. Whereas in actual very high heating rate is encountered (about 10°C per minute for rebars),

and also these strain gauges could be directly exposed to fire when spalling occurs in the vicinity of the strain gauges. Due to the lack of consistency in strain gages, the strain data recorded by them should be cautiously used to infer any strain trends in the tested columns.

5.4.3 Spalling Progression

The progression and extent of spalling in columns was recorded qualitatively through visual observations made through the observation windows of the furnace during the fire test. Also, after the fire test, the quantity of spalling was evaluated by measuring the volumetric loss of concrete in fire exposed columns. The quantity of spalled concrete was evaluated by subtracting the remaining concrete section from the original volume of column and this is tabulated in Table 5.2.

In the case of FAC column, spalling due to high temperature started at about 12 minutes in to the test and continued till about 25 minutes. After its initial occurrence, spalling gradually subsided in FAC column and did not further penetrate into the concrete core inside steel cage. Figure 5.35 illustrates the columns status under fire conditions observed through view ports of furnace at 60 minutes into the fire test. The figure shows that out of four tested columns only plain FAC column suffered spalling. The extent of spalling in FAC column was moderate as compared to typical HSC column, which can be attributed to superior microstructure in FAC column.

In contrast, FAC-P, HSC-S, and HSC-H columns experienced no spalling throughout the fire exposure. The absence of fire induced spalling in FAC-P, and HSC-H columns can be attributed to enhanced permeability in concrete due to melting of polypropylene fibers at around 160°C. The increased permeability facilitated dissipation of steam and thus helped to limit pore pressure build-up so as not to exceed the tensile strength of concrete. The absence of spalling in HSC-S column columns can mainly be attributed to increased tensile strength at higher temperature

facilitated by the presence of steel fibers. In the case of HSC-H column, both mechanisms increased tensile strength through steel fibers and increased permeability through melting of polypropylene fibers prevented occurrence of spalling in concrete.

It has been shown in Chapter 4 that the presence of steel fibers decelerates the degradation of tensile strength in HPC. The improved high temperature tensile strength in HSC-S and HSC-H columns also helps to mitigate fire induced spalling. This beneficial effect in HSC-S and HSC-H can be seen Figure 5.36 which illustrates the state of the post fire conditions of columns after completion of fire tests as spalling was not encountered in these columns.

Post fire test volumetric measurements indicated the spalled concrete in FAC column was about 17% of its exposed volume, whereas this was about 40% in case of a typical HSC column (Raut and Kodur, 2011). These volumetric calculations indicate that spalling was less severe in FAC column compared to that of plain HSC columns (Raut and Kodur, 2011). This can be partly attributed to higher tensile strength of fly ash concrete which is about 20% higher than that of conventional high strength concrete as reported by Khaliq and Kodur (2012).

5.4.4 Failure Modes and Fire Resistance

The fire response of FAC and FAC-P columns was quite different from each other. Fire induced spalling in FAC column led to loss of cross-section in early stages of test. The reduced cross-section in FAC column suffered increased degradation in strength and stiffness due to high temperatures and led to failure of FAC column in 165 minutes. In the case of FAC-P column, melting of polypropylene fibers mitigated the fire induced spalling by dissipation of pore pressure. Melting of polypropylene fibers creates micro channels that help diffuse pore pressure build-up (Bilodeau et al., 2004) and its detrimental effects. Due to spalling mitigation and

survival of cross-sectional integrity, FAC-P column displayed better fire resistance than FAC column and survived the burnout conditions during the test.

In the case of HSC-S and HSC-H columns, fire induced spalling was also not encountered. The steel and hybrid fibers in HSC-S, and HSC-H columns decreased degradation of tensile strength, mitigated spalling and also increased toughness of concrete under fire conditions. The better fire resistance of HSC-S and HSC-H columns can therefore be attributed to presence of steel and hybrid fibers. A comparison of fire resistance of all four columns is tabulated in Table 5.2. With similar degradation in strength and stiffness to FAC and FAC-P columns, but with higher applied load, HSC columns exhibited better fire resistance than FAC and FAC-P columns.

Out of four tested columns, three columns (FAC-P, HSC-S, and HSC-H) survived the fire exposure conditions; this is typically a case once buildings are exposed to fire. However, significant strength and stiffness reduction is anticipated in fire exposed columns after the test. To characterize the post-fire capacity of the fire exposed columns and to establish their serviceability, residual strength tests were performed on survived (FAC-P, HSC-S, and HSC-H) columns.

5.4.5 Summary

Results from the fire resistance tests show that plain FAC column exhibits lower fire resistance performance compared to steel and hybrid fiber reinforce HSC columns. The fire resistance in FAC column was significantly affected by loss of cross-section due fire induced spalling. The fire response of FAC-P column was almost similar to HSC-S and HSC-H columns. However, HSC-S and HSC-H columns displayed lesser axial deformations than FAC and FAC-P columns. The fire resistance of FAC-P column was also enhanced due to spalling mitigation facilitated by burning of polypropylene fibers. Similarly presence of steel and hybrid fibers in HSC-S and

HSC-H columns also slowed the degradation of tensile strength and mitigated spalling, thus significantly enhanced the fire resistance of these columns.

5.5 Response after Fire Exposure

In many practical situations RC columns survive in burn-out fire scenarios. In such situations, repair of fire exposed RC structures is often more economical both in terms of cost and time, than to demolish and rebuild the structure. One of the major challenges therefore is to determine the extent of damage to fire exposed columns. To assess such damage and the capacity of structure for feasibility of repair, determination of residual strength in fire exposed RC columns an important factor.

The extent of strength loss in RC columns due to fire exposure is dependent on a number of factors, including type of fire exposure, temperatures in the concrete and steel, concrete and steel properties (including strength) and load level. Due to high thermal capacity and low thermal conductivity of concrete, RC columns may retain much of their initial strength under most realistic fires, particularly if the columns do not experience significant fire-induced spalling. In order to develop data on residual capacity of HPC columns, additional strength tests were carried out on the survived RC columns tested for fire resistance.

5.5.1 Tested Columns

Since FAC-P, HSC-S, and HSC-H columns did not fail during the fire resistance tests, residual strength tests were conducted on these three columns to determine the capacity of these columns after exposure to fire. These columns survived the fire exposure which lasted from 4 to 7 hours. After the fire tests, these columns were unloaded and left to cool down in the furnace for 24 hours before conducting residual strength tests at room temperature.

5.5.2 Equipment and Test Procedure

The residual strength tests were carried out using the same loading frame as used for fire resistance tests, but with the furnace lids removed. In the residual strength tests, the columns were gradually loaded with vertical actuators at a prescribed rate and axial deformations were recorded through LPTs attached to the top of the columns assembly. Each column was tested to failure under axial load with semi fixed support conditions as shown in Figure 5.9. The load was increased gradually at a rate of about 10 kN per minute and displacement was recorded as a function of load till failure of the columns. Due to severe fire exposure, these columns had already signs of cracks and surface scaling had occurred during the fire tests. During the loading for residual strength tests, significant cracking and spalling was observed in the columns due to the crushing of concrete under increasing load and this is illustrated in Figure 5.37.

5.5.3 Residual Strength Results

The results of axial load carrying capacity and post-fire residual strength of FAC-P, HSC-S, and HSC-H columns is tabulated in Table 5.2. It can be seen that all three columns (FAC-P, HSC-S, and HSC-H) displayed significant residual load-carrying capacity after exposure to fire. FAC-P column retained lowest residual capacity of 697 kN that is about 34.5% of its ultimate strength capacity while in HSC-S and HSC-H columns, higher residual strength capacity was retained as 839 and 741 kN, which is about 44.5 and 52% of their ultimate strength capacity respectively. This is despite the fact that severe fire-induced degradation in strength and stiffness is encountered in RC members during fire resistance tests. The higher residual capacity in FAC-P, HSC-S, and HSC-H columns can be attributed to the partial regain of strength by concrete and steel upon cooling, and strain hardening of the steel reinforcement.

The measured load deformation response for the three columns during the residual strength tests is captured in Figure 5.38. It can be seen that the axial deformation is higher in HSC-S and HSC-H columns as compared to that in FAC-P column. This higher load-deformation capacity in HSC-S and HSC-H can be attributed to presence steel fibers in the mix which induced toughness and ductility of these columns. This improvement is in agreement with the fact that after exposure to high temperatures, fiber reinforced HSC shows a higher overall residual compressive and flexural strength and a higher elastic modulus (Lau and Anson, 2006) as compared to plain HSC. After fire exposure FAC-P column acted more like plain HSC showing less load-deformation capacity as compare to both HSC-S and HSC-H columns. Overall, hybrid fiber reinforced HSC column displayed better post-fire performance facilitated by beneficial effects from both polypropylene and steel fibers.

5.6 Summary

Results from fire resistance tests show plain and fiber reinforced FAC columns exhibit lower fire resistance than fiber reinforced HSC columns. The use of fibers enhances the fire resistance of both FAC and HSC columns through spalling mitigation and enhanced mechanical properties. The three columns tested for residual strength retained significant load carrying capacity that ranged from 34.5 to 52% of ultimate strength capacity. As indicated by test results, this serviceability of columns is helpful for their rehabilitation and restoration. Results from the fire tests provide a better understanding of the response of plain and fiber reinforced HPC columns under realistic fire, and load conditions. These tests provide valuable data for validating computer models for tracing the fire response of HPC columns. The HPC columns can retain much of their load carrying capacity after exposure to fire, particularly once different fibers are used in the HPC mix.

Table 5.1 - Mix proportions for four batches of concrete.

Components	FAC	FAC-P	HSC-S	HSC-H
Cement (Type I), kg/m^3	416	416	513	513
Fine aggregate, kg/m^3	705	705	684	684
Course aggregate (max size 10mm), kg/m^3	1041	1041	1078	1078
Silica fume, kg/m^3	41	41	43	43
Fly ash - Class C (25% replacement of cement), kg/m^3	141	141	-	-
Slag - Grade 120), kg/m^3	76	76	-	-
Water, kg/m^3	135	135	130	130
Water cement ratio (w/c)	0.33	0.33	0.25	0.25
Retarding admixture – Type D, kg/m^3	3.8	3.8	-	-
High range water reducer/Superplasticizer – Type F, kg/m^3	9.12	9.12	15	15
Slump, mm	150	100	100	90
Polypropylene fibers, kg/m^3 (0.22% by volume)	-	2	-	2
Steel fibers, kg/m^3 (0.54% by volume)	-	-	42	42
Unit weight of concrete, kg/m^3	2564	2530	2490	2464
Compressive strength (MPa)				
7 days	76	72	66	68
28 days	102	81	67	68
90 days	107	100	72	75
Test day	107	100	77	80

Table 5.2 - Summary of test parameters for fire resistance test on columns.

Column designation	Fire exposure (ASTM E119 – decay)	Total test time (minutes)	Concrete strength (MPa)		Column strength (kN)	Load ratio (%)	Applied load (kN)	Relative humidity (%)	Failure times (minutes)	Extent of spalling	Residual strength kN (% of ultimate load capacity)
			28 Days	Test day							
FAC	LF- decay @4.16°C/min	435	102	107	2144	40	858	90	Failed (165)	Severe	-
FAC-P	LF- decay @4.16°C/min	435	81	100	2020	40	808	90.25	No Failure (435)	Nil	697 (34.5%)
HSC-S	SF- decay @11°C/min	270	72	77	1612	60	967	91.25	No Failure (270)	Nil	839 (52%)
HSC-H	SF- decay @11°C/min	270	75	80	1665	60	999	89.65	No Failure (270)	Nil	741 (44.5%)

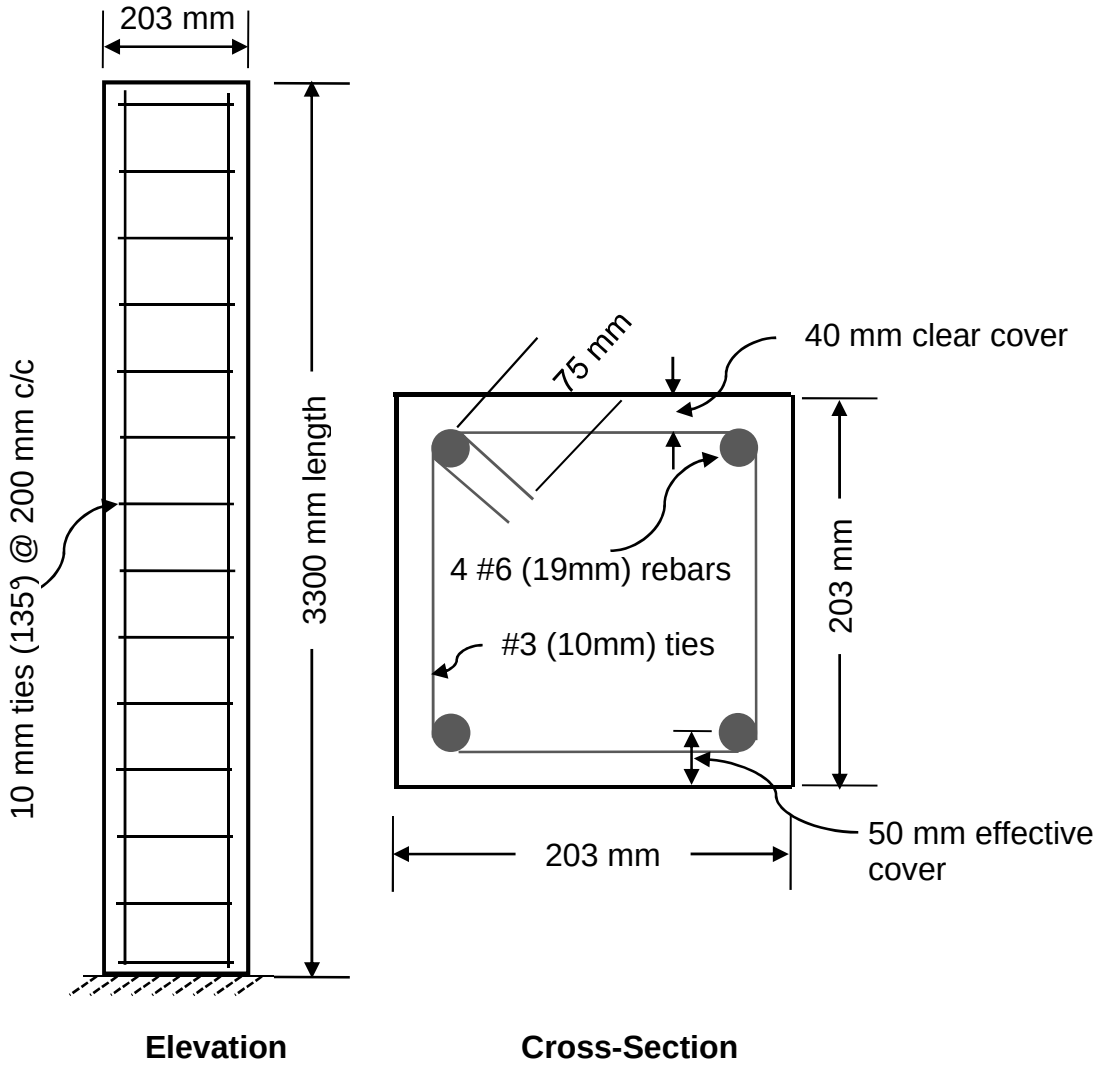

Figure 5.1- Column elevation and cross-section showing design details

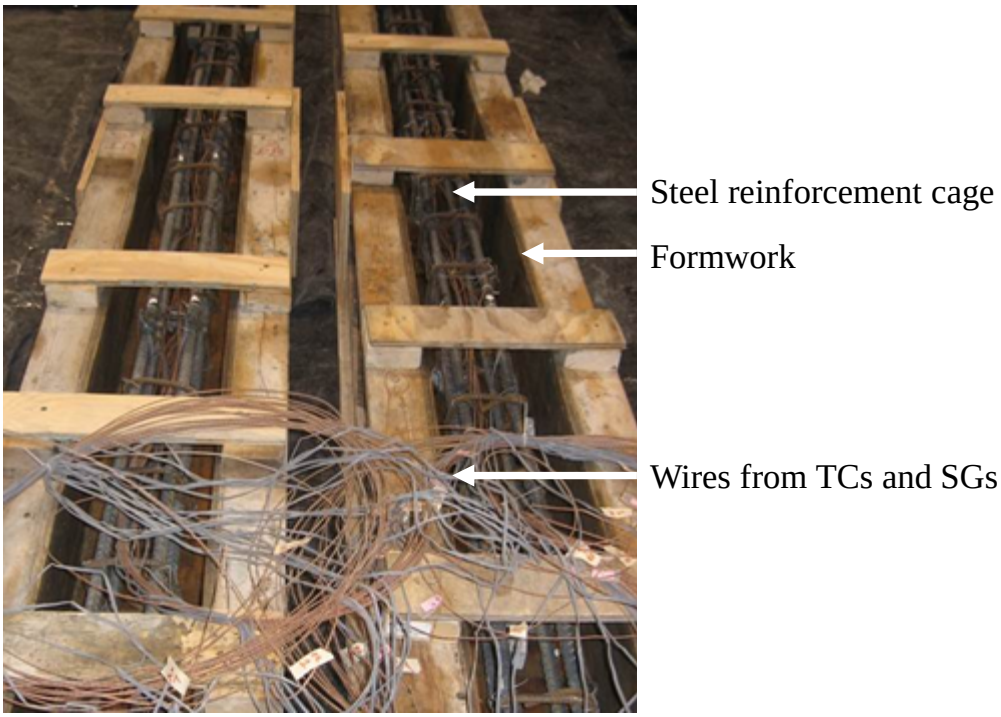

Figure 5.2 - Steel cages inside column formwork with instruments wiring

Figure 5.3 - Casting and finishing of columns

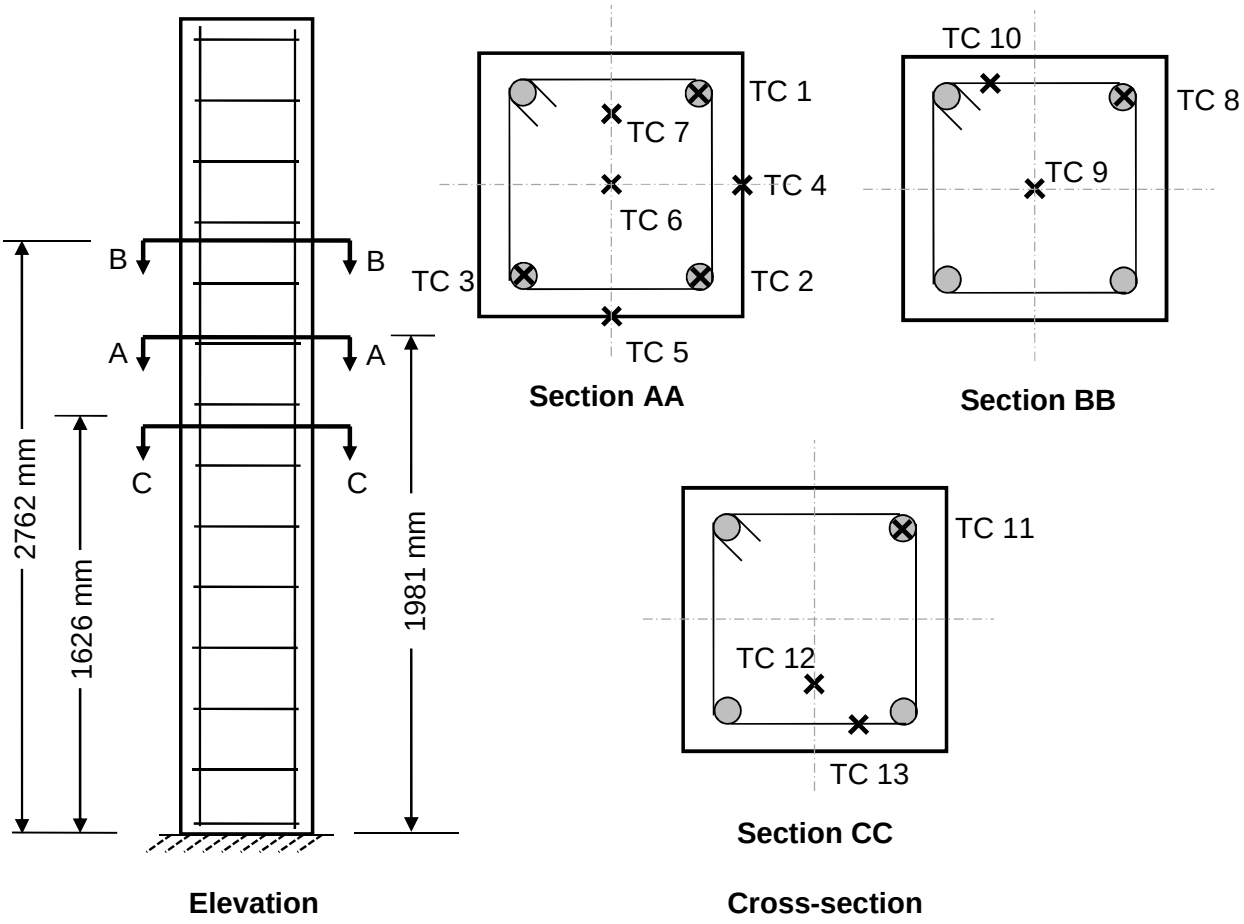

Figure 5.4 - Column cross-section showing location of thermocouples (TCs)

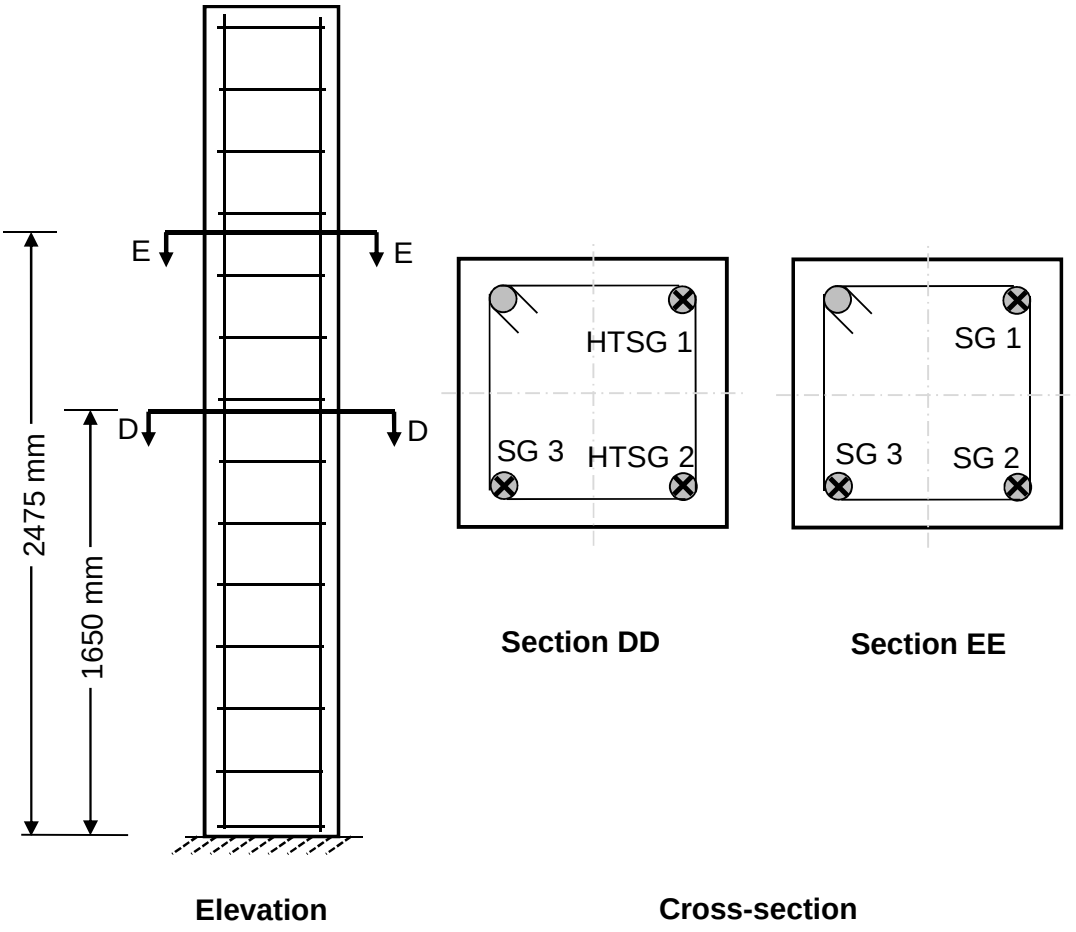

Figure 5.5 - Column cross-section showing location of strain gauges (SGs)

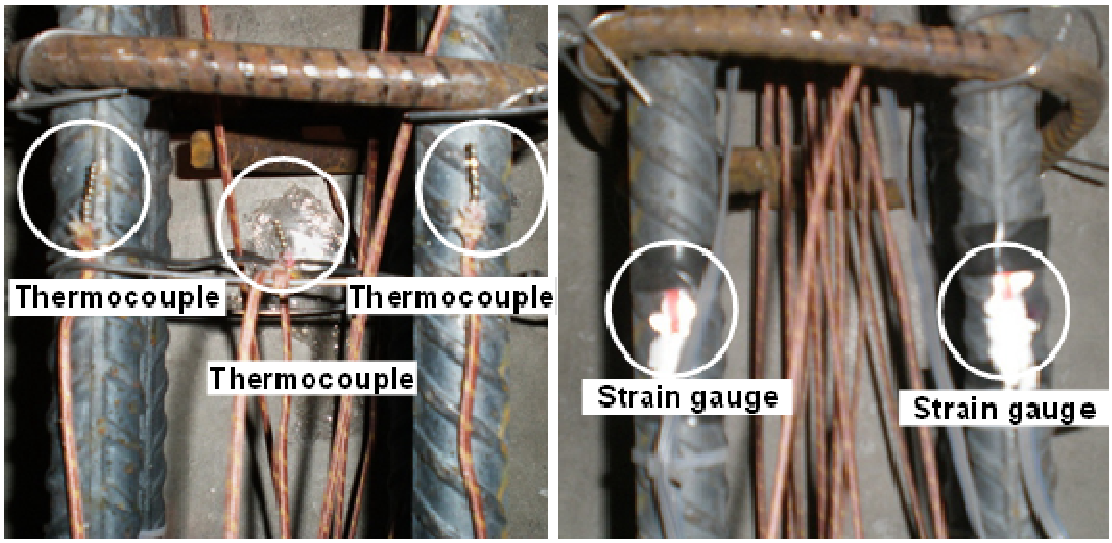

Figure 5.6 - View of thermocouples in cross-section and strain gauges attached to steel rebars

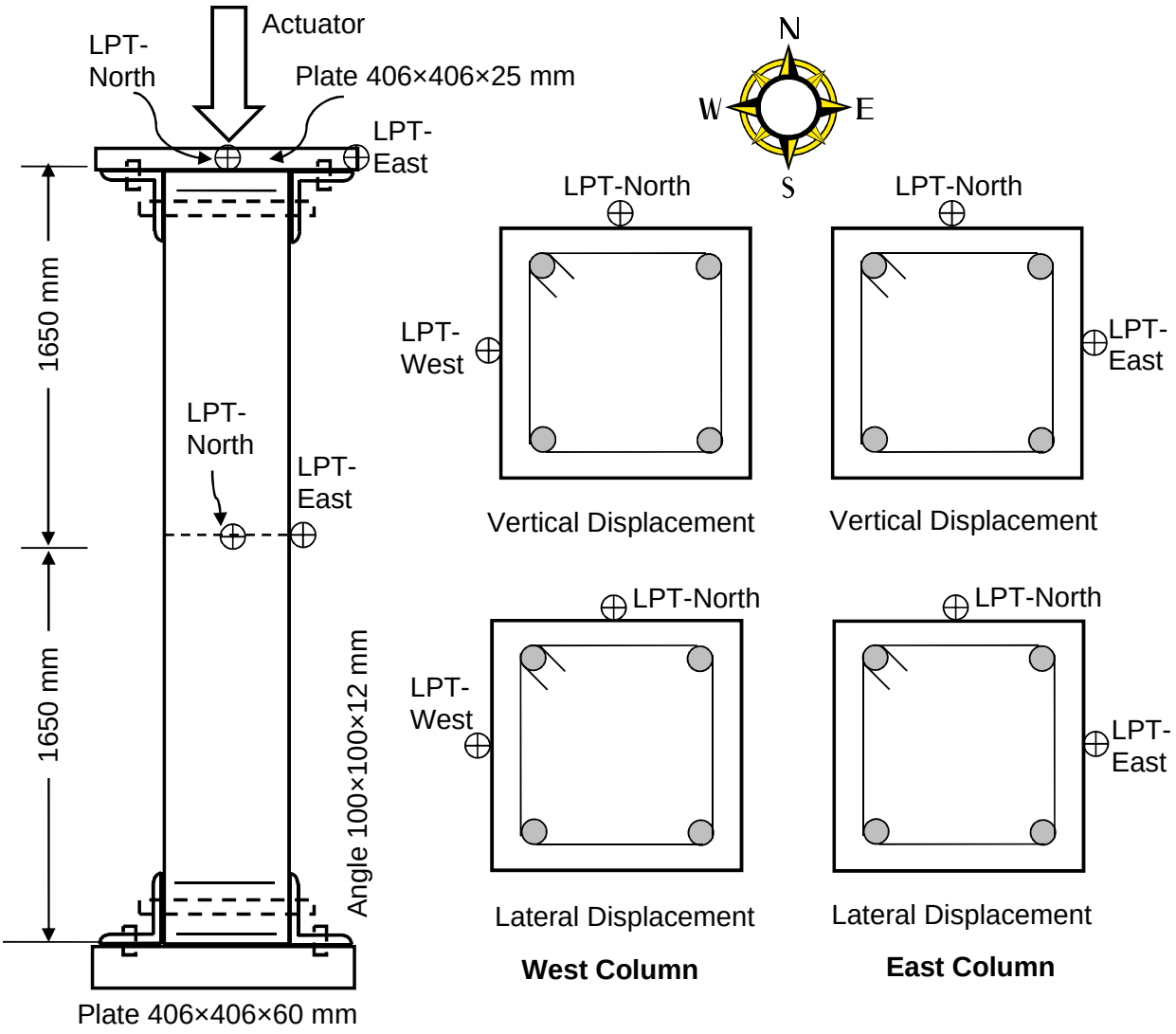

Figure 5.7 - Column cross-section showing location of linear position transducers (LPTs)

(a) Picture of furnace and loading frame

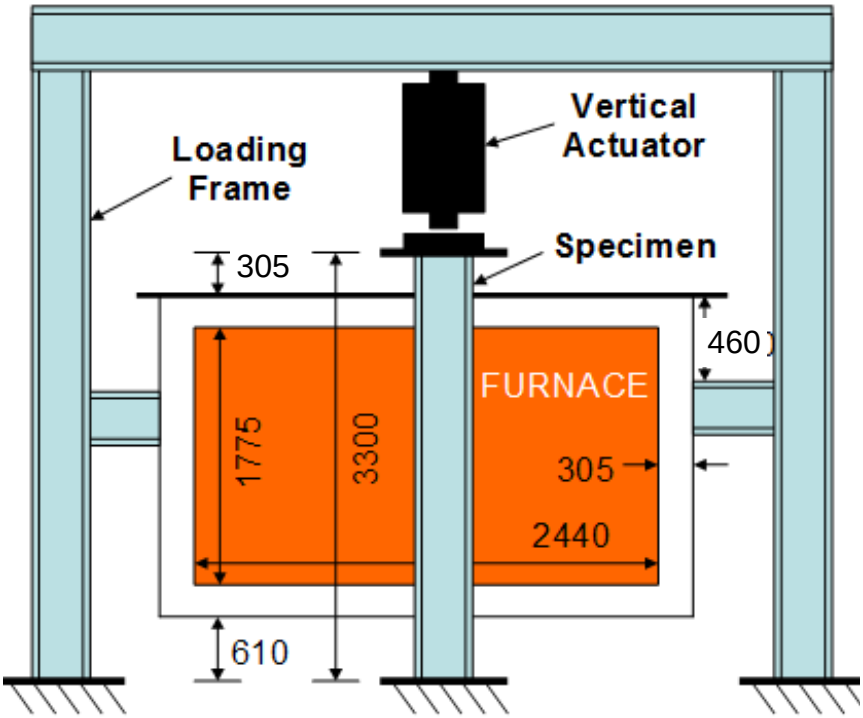

(b) Schematic for column position relative to furnace

Figure 5.8 - Structural fire testing facility at MSU's Civil Infrastructure Laboratory

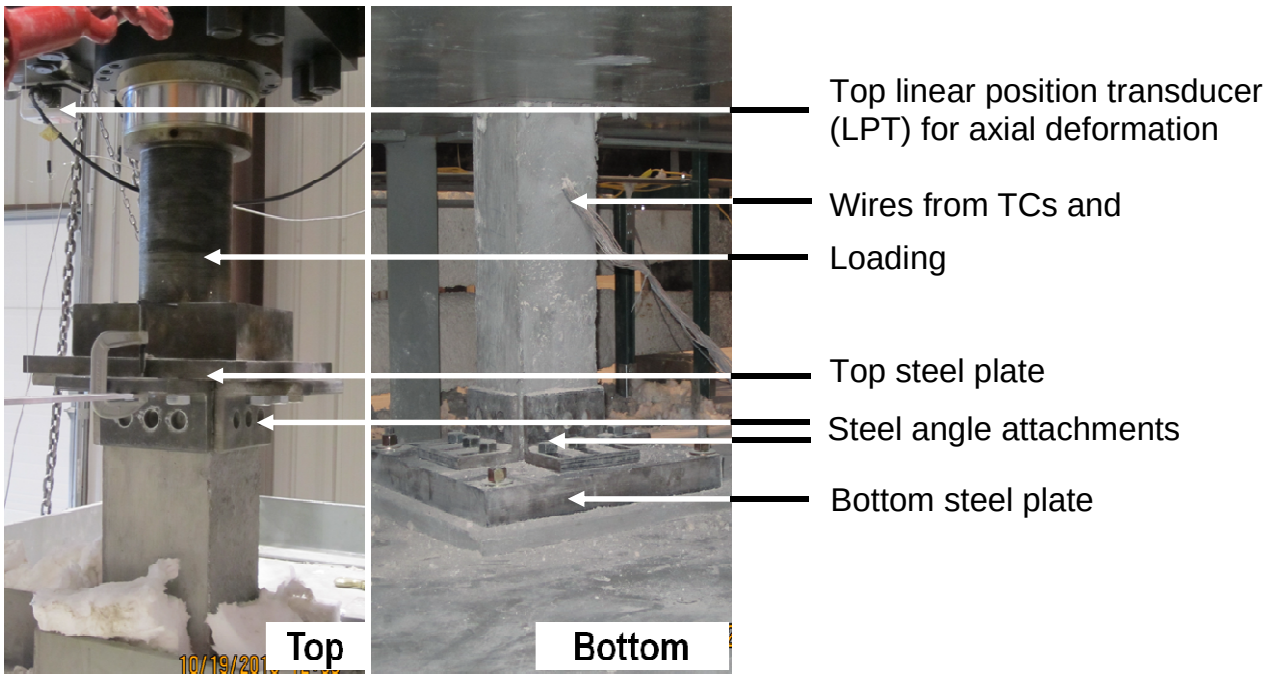

Figure 5.9 - End conditions for the columns before fire tests

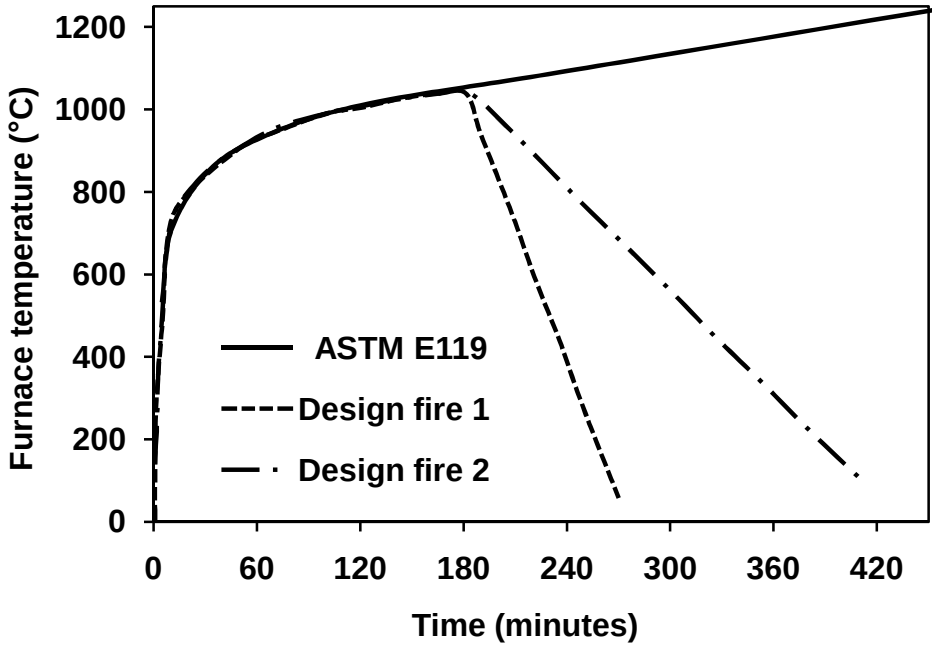

Figure 5.10 - Time temperature curve for fire scenario

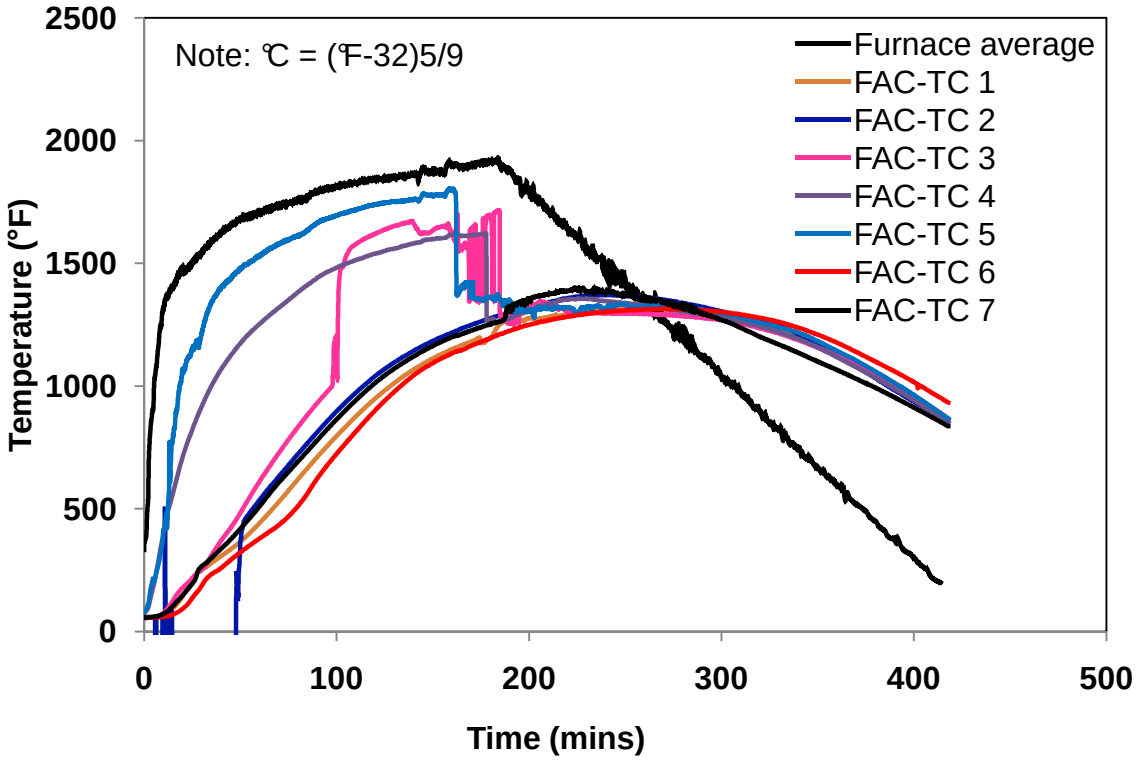

Figure 5.11 - Measured rebars and concrete temperatures for FAC column at Section AA

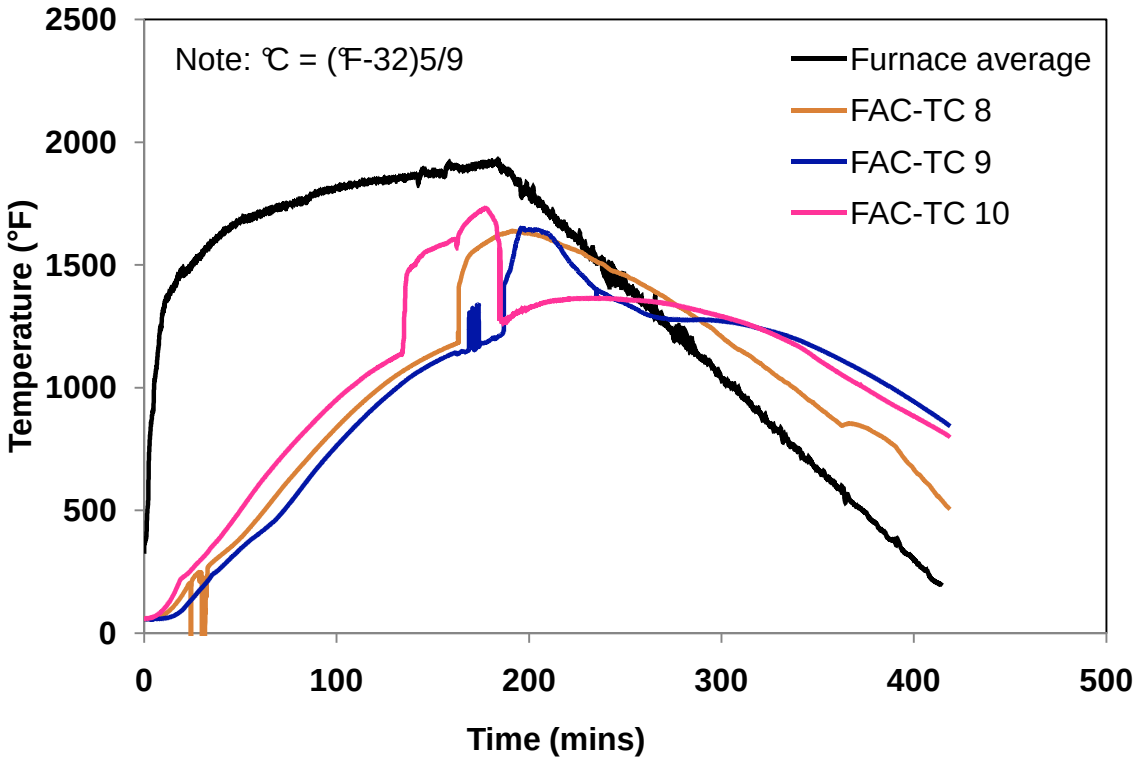

Figure 5.12 - Measured rebars and concrete temperatures for FAC column at Section BB

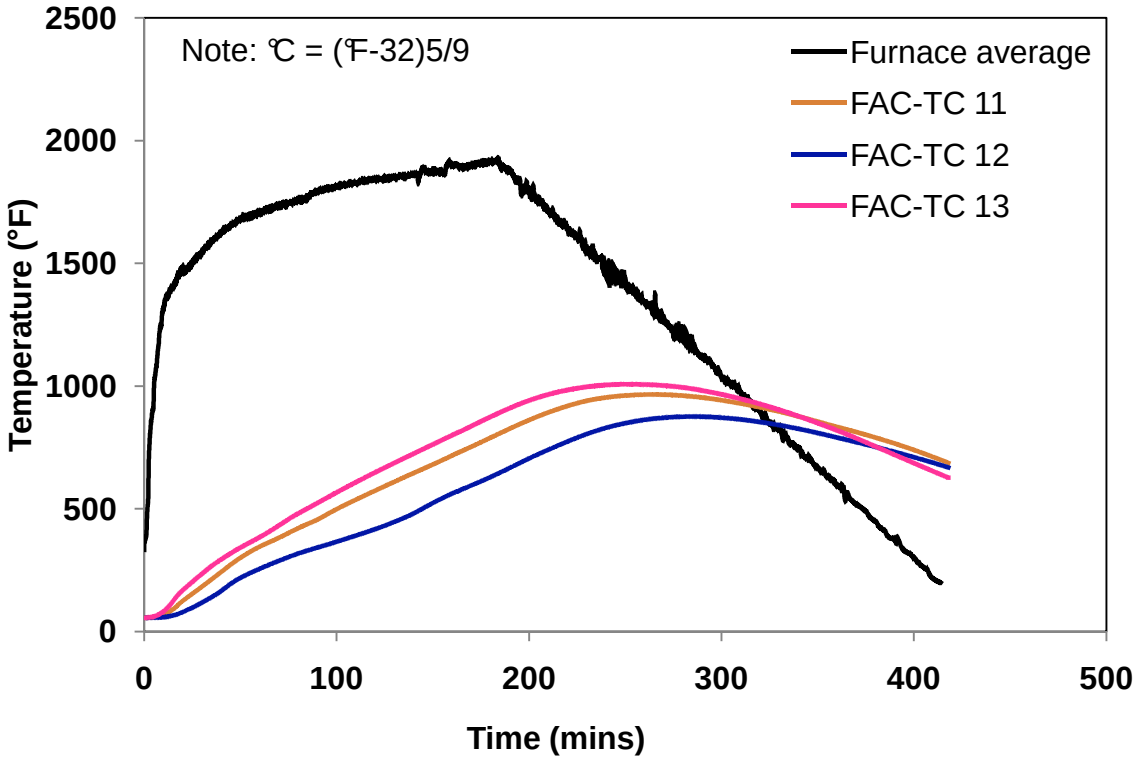

Figure 5.13 - Measured rebars and concrete temperatures for FAC column at Section CC

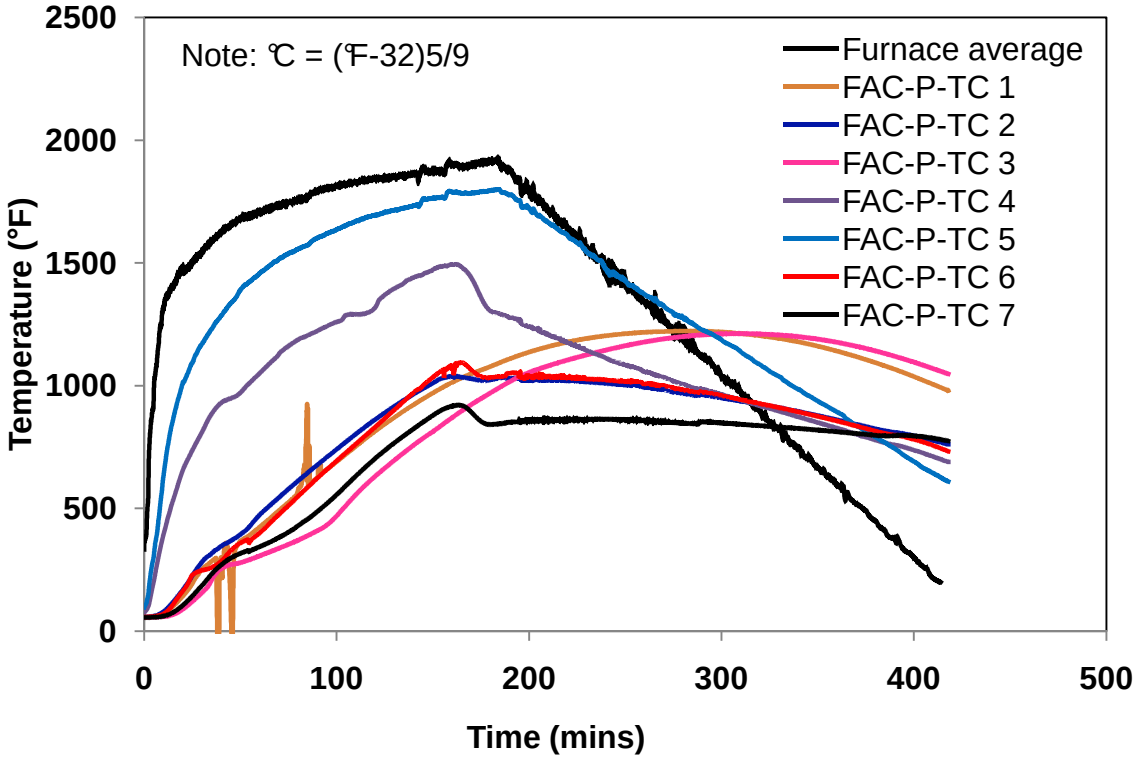

Figure 5.14 - Measured rebars and concrete temperatures for FAC-P column at Section AA

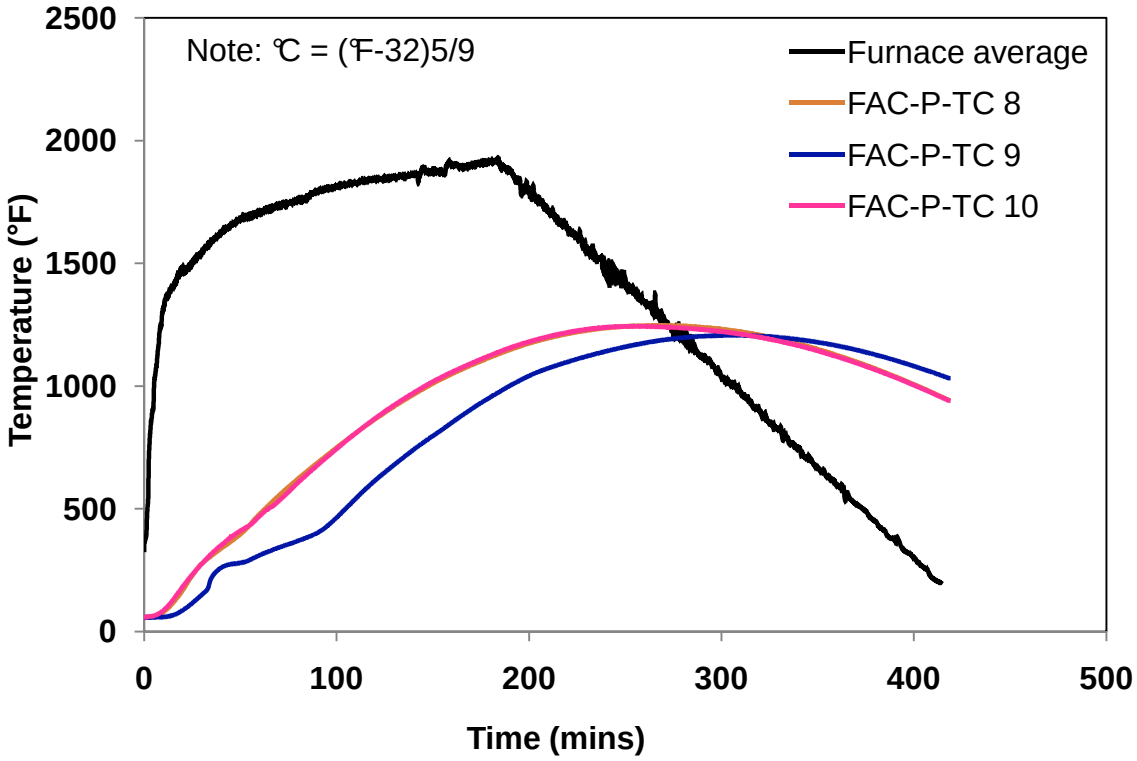

Figure 5.15 - Measured rebars and concrete temperatures for FAC-P column at Section BB

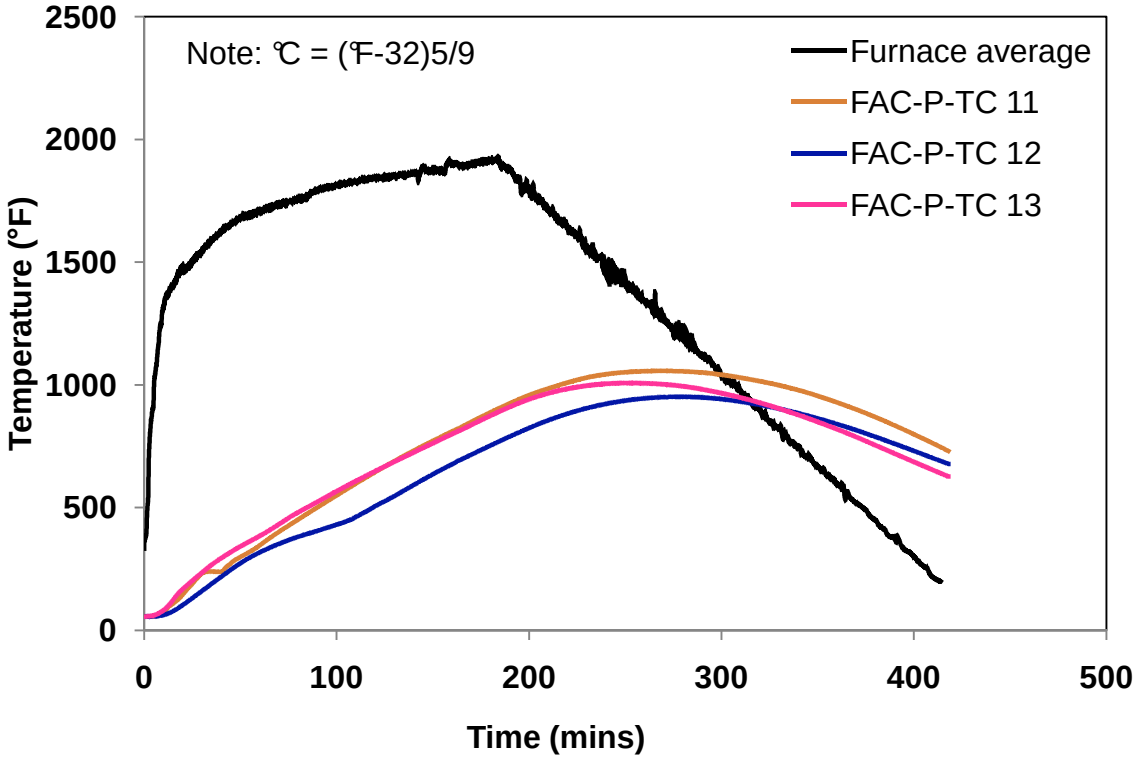

Figure 5.16 - Measured rebars and concrete temperatures for FAC-P column at Section CC

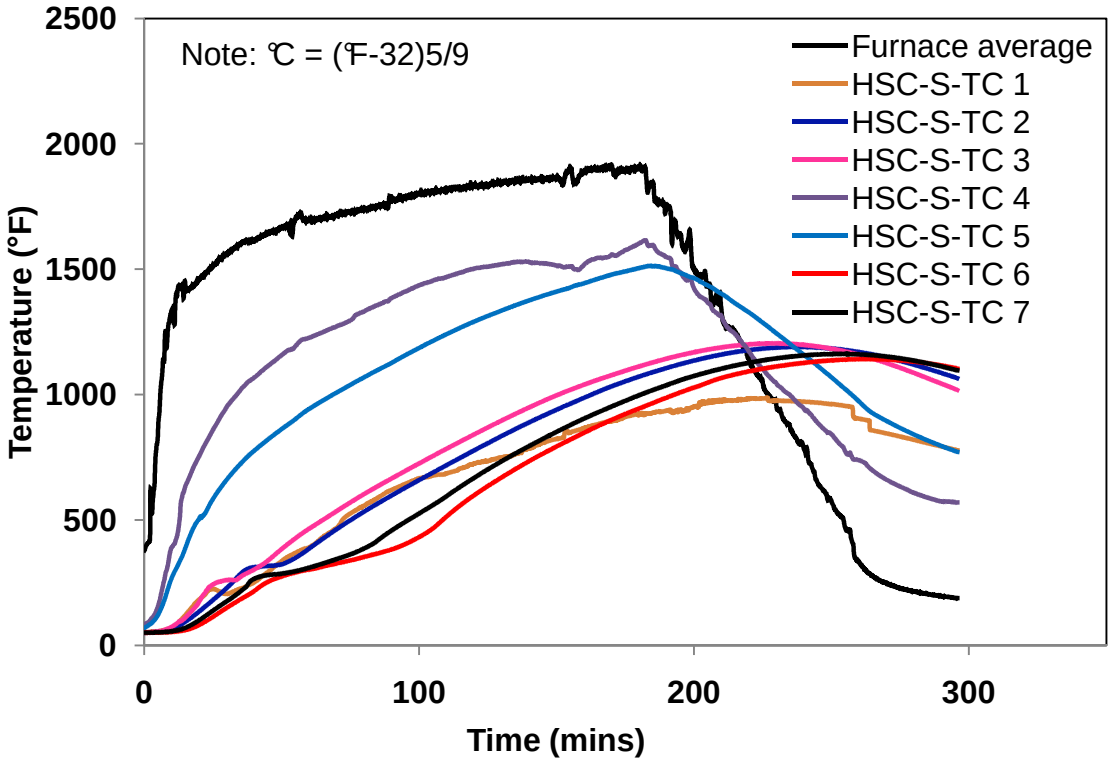

Figure 5.17 - Measured rebars and concrete temperatures for HSC-S column at Section AA

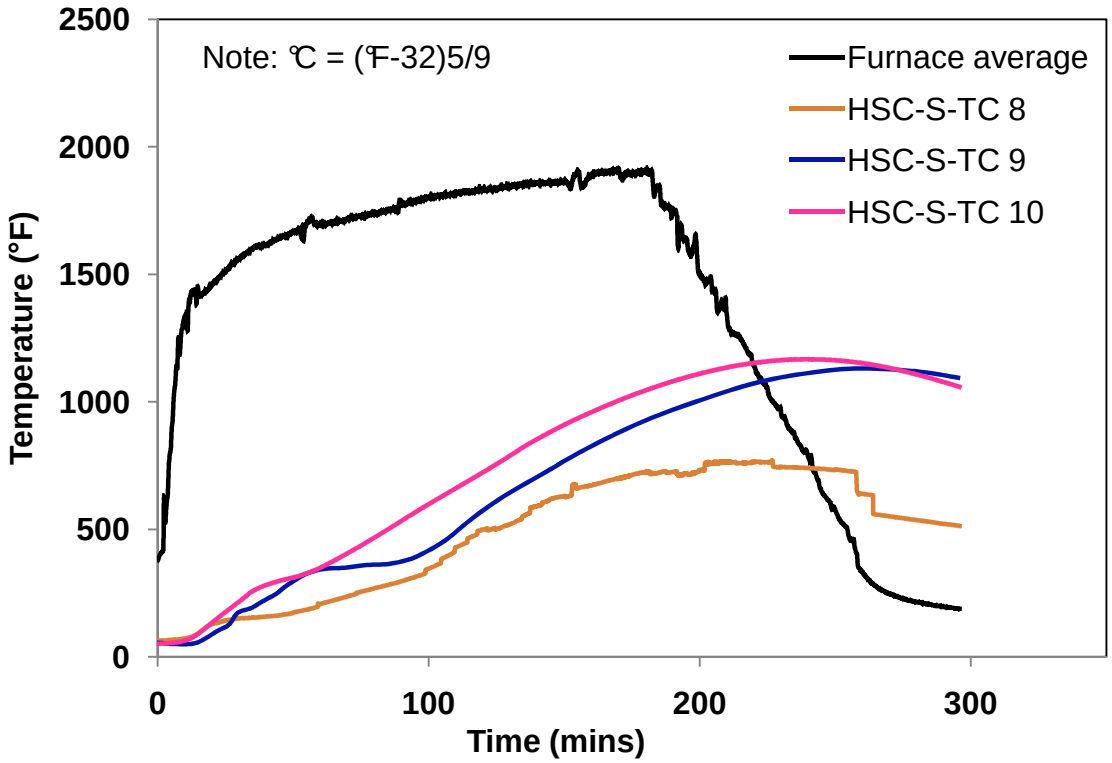

Figure 5.18 - Measured rebars and concrete temperatures for HSC-S column at Section BB

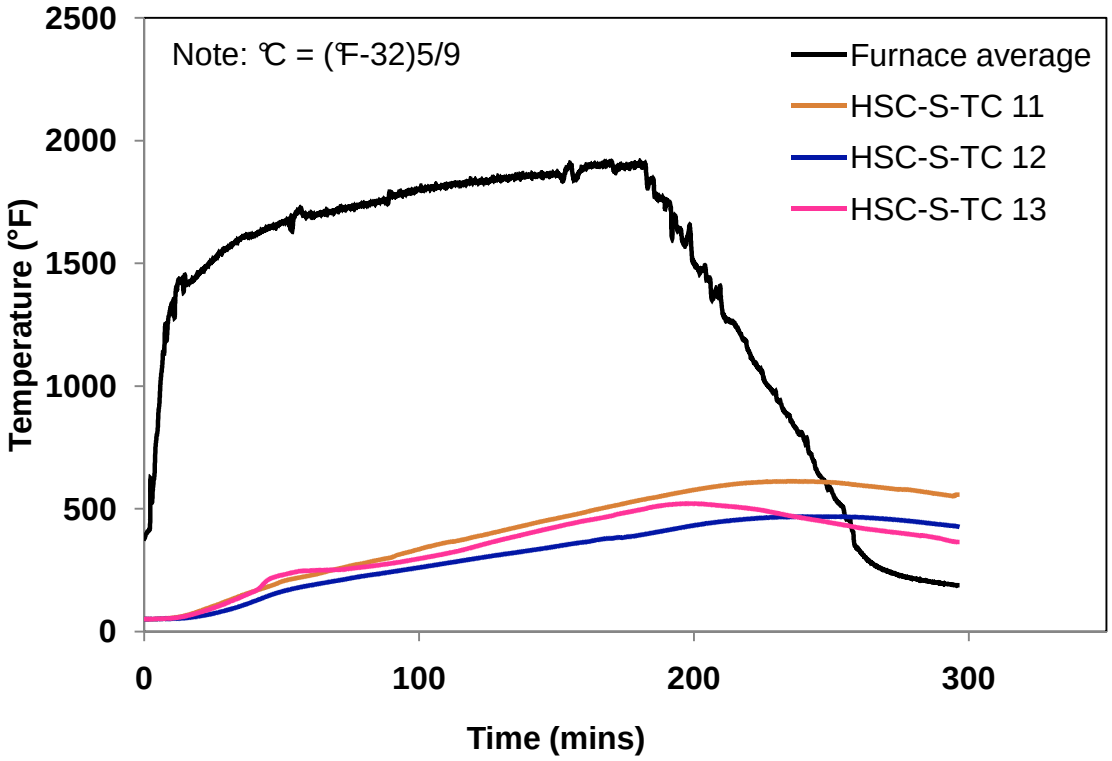

Figure 5.19 - Measured rebars and concrete temperatures for HSC-S column at Section CC

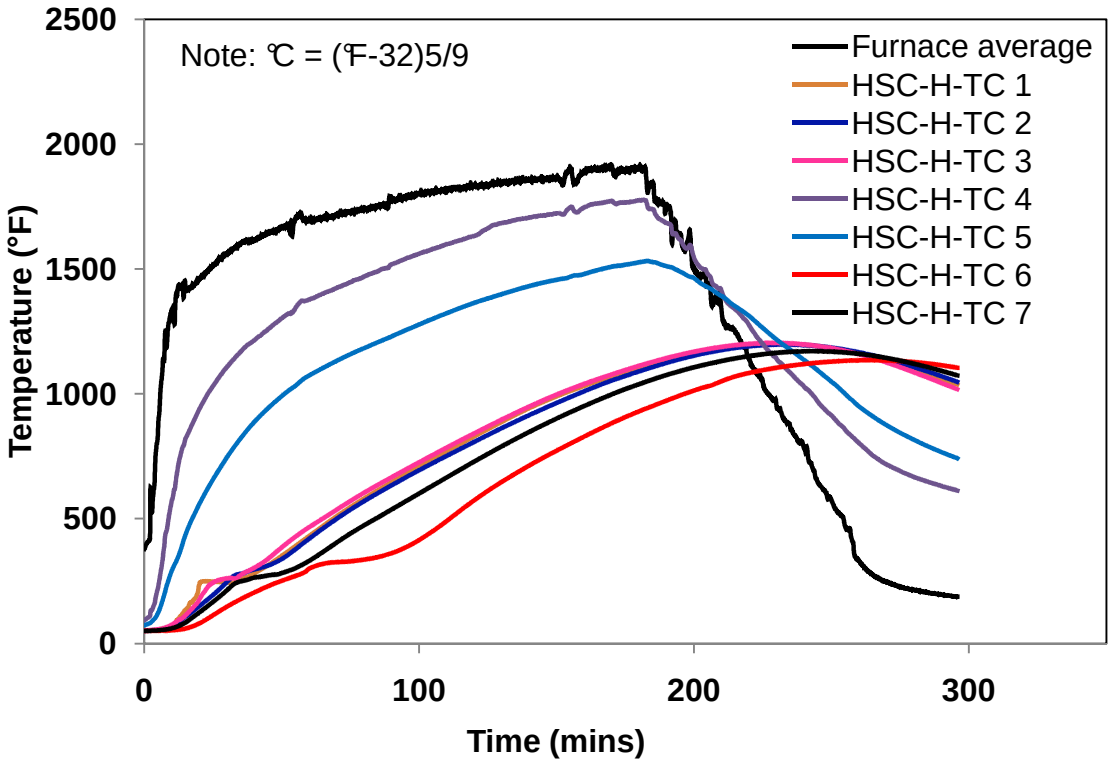

Figure 5.20 - Measured rebars and concrete temperatures for HSC-H column at Section AA

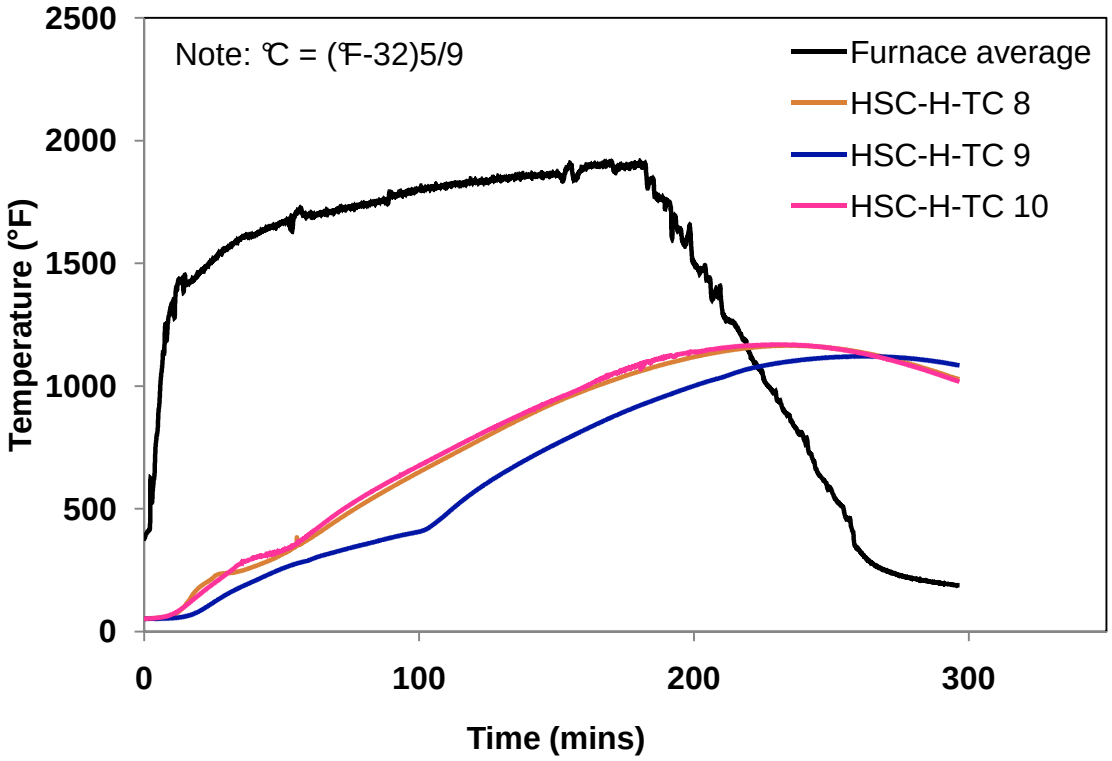

Figure 5.21 - Measured rebars and concrete temperatures for HSC-H column at Section BB

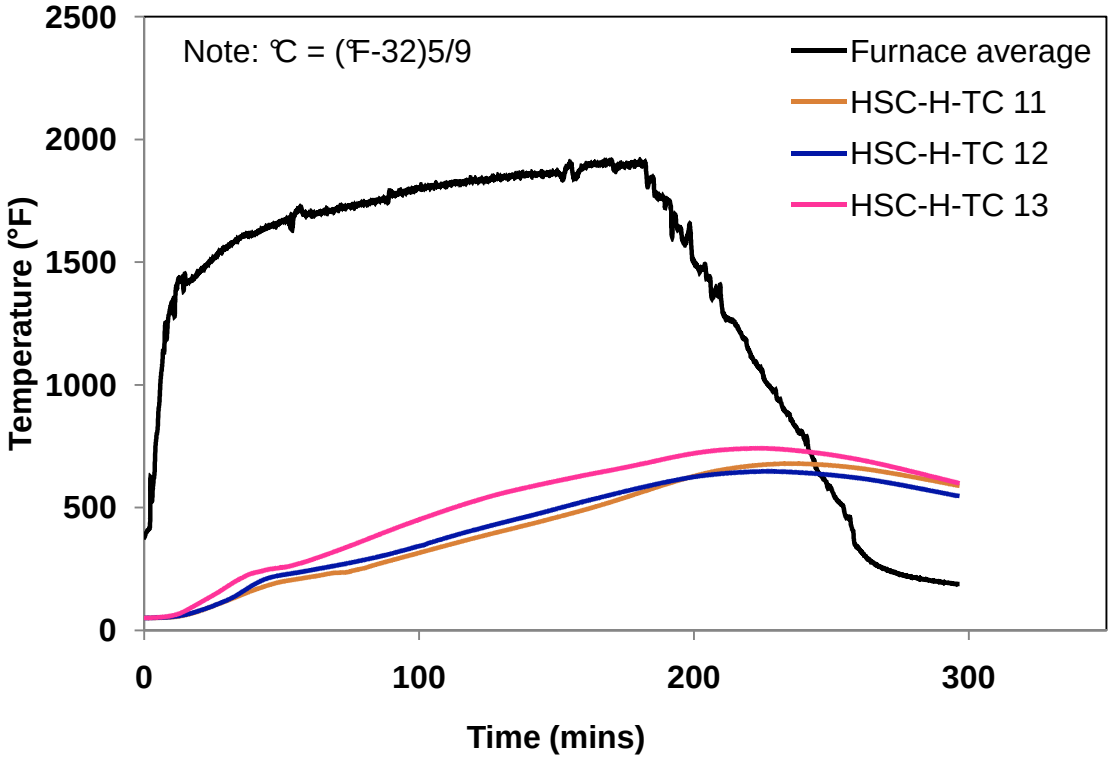

Figure 5.22 - Measured rebars and concrete temperatures for HSC-H column at section CC

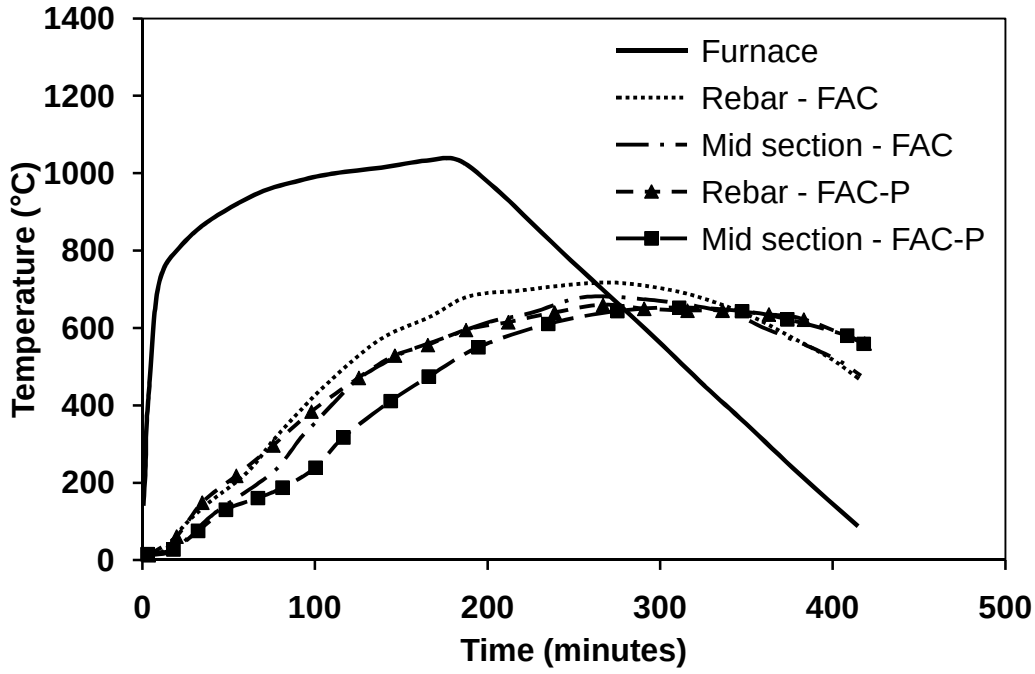

Figure 5.23 - Comparison of measured temperature distribution for FAC and FACP columns

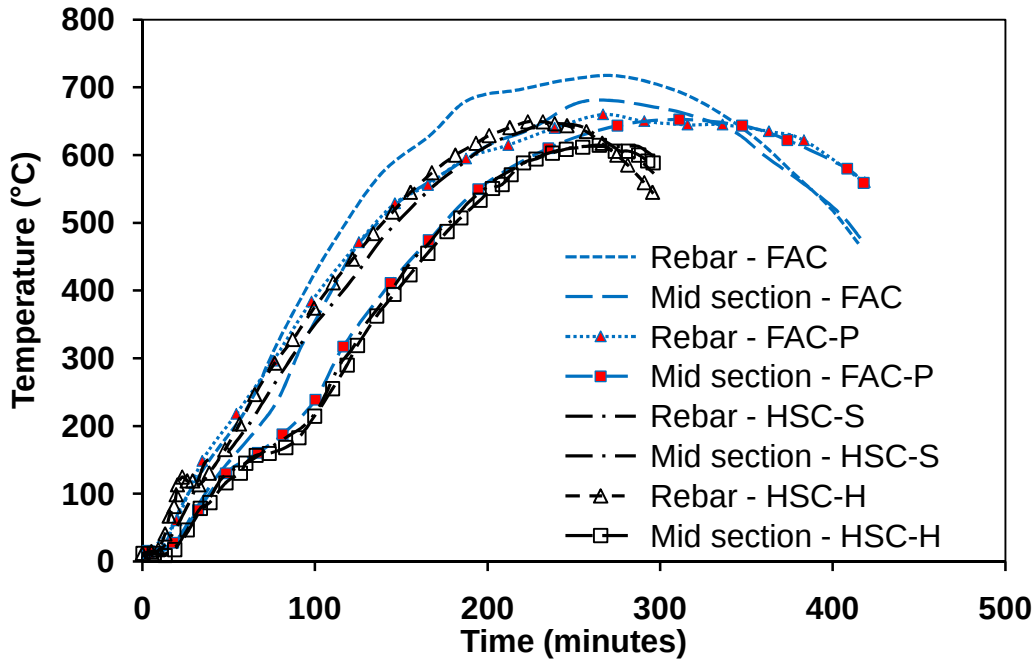

Figure 5.24 - Comparison of temperature distribution for FAC and HSC columns

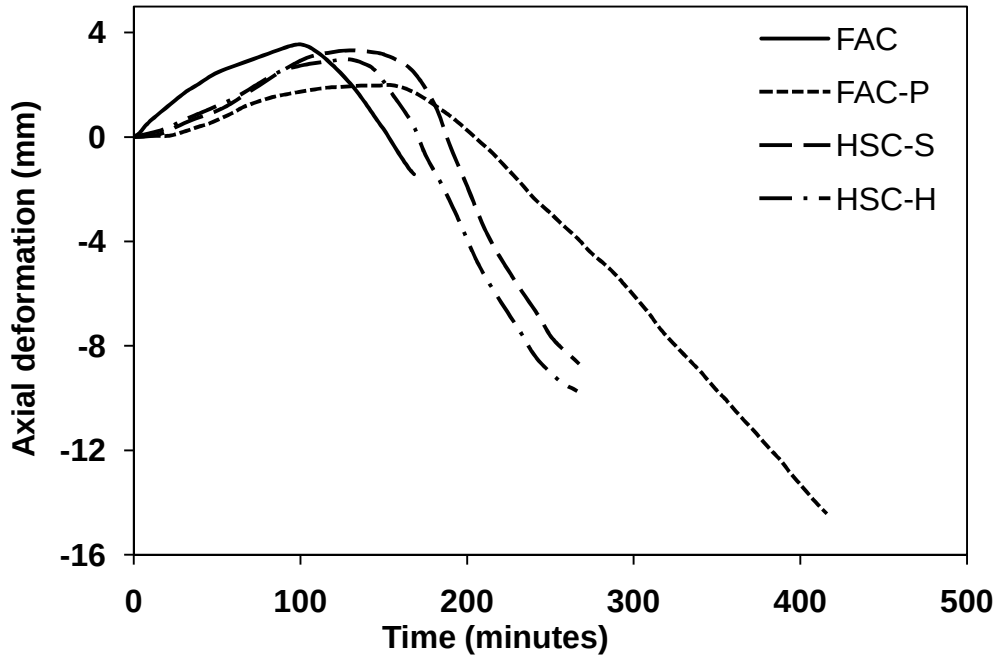

Figure 5.25 - Measured axial deformations as a function of fire exposure time

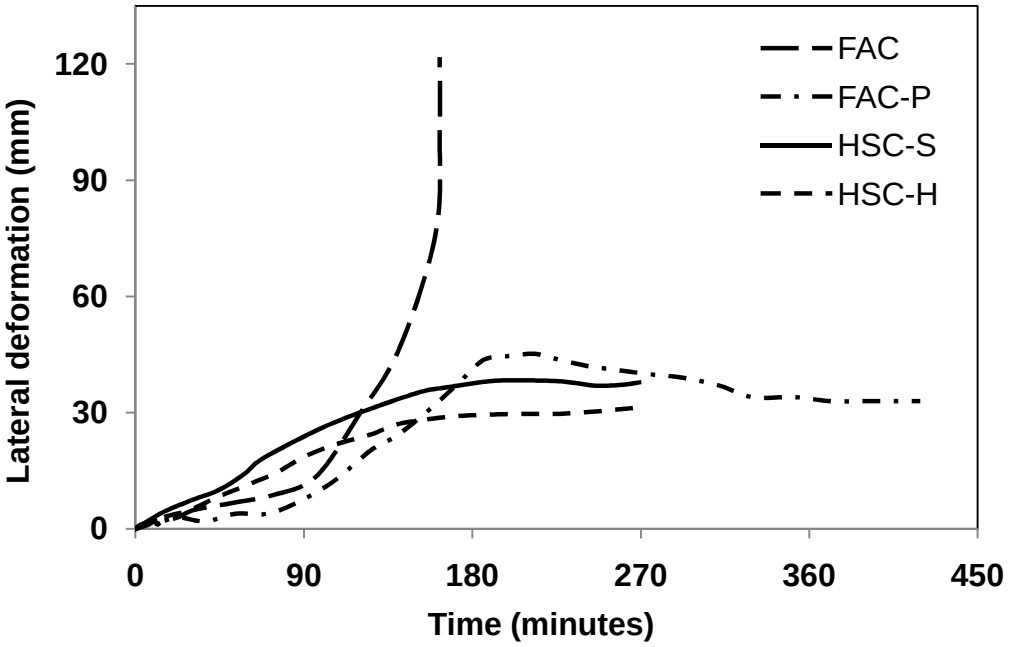

Figure 5.26 - Measured lateral deformations as a function of fire exposure time in tested columns

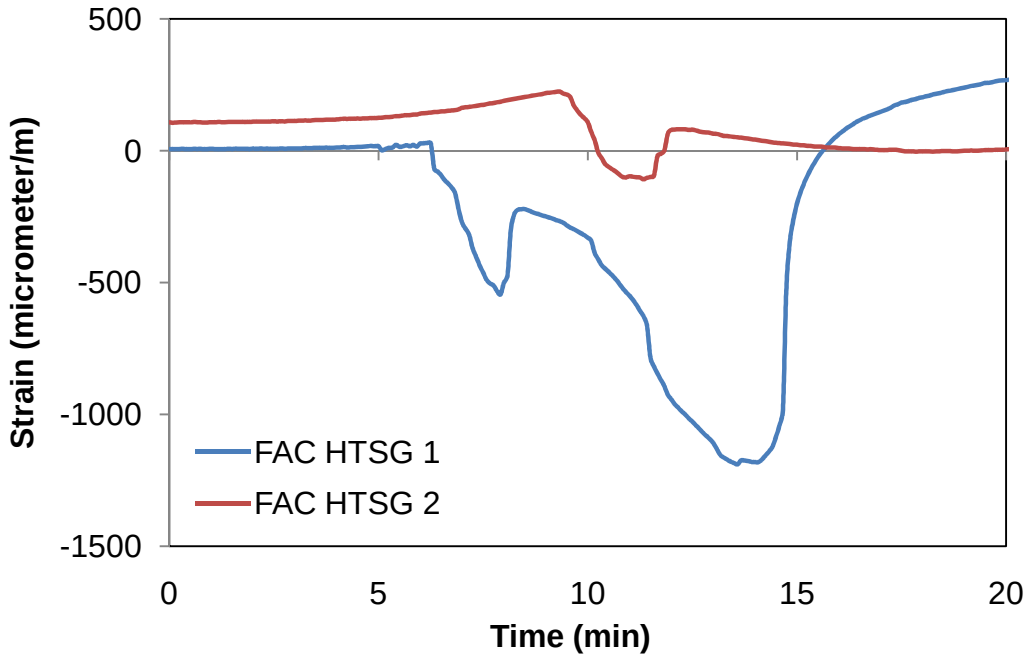

Figure 5.27 - Measured axial strains as a function of fire exposure time for FAC column at Section DD

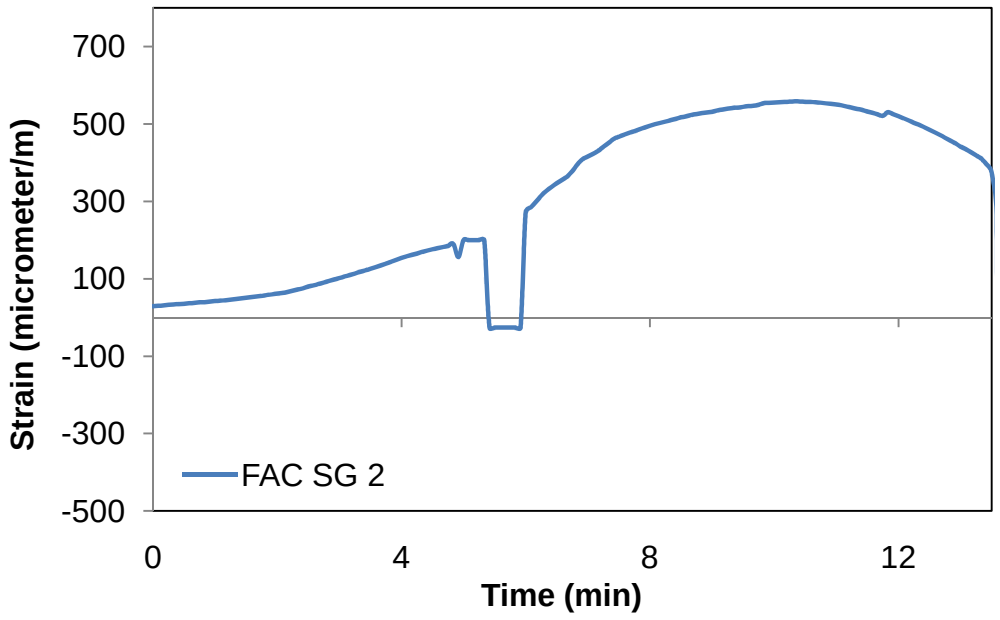

Figure 5.28 - Measured axial strains as a function of fire exposure time for FAC column at Section EE

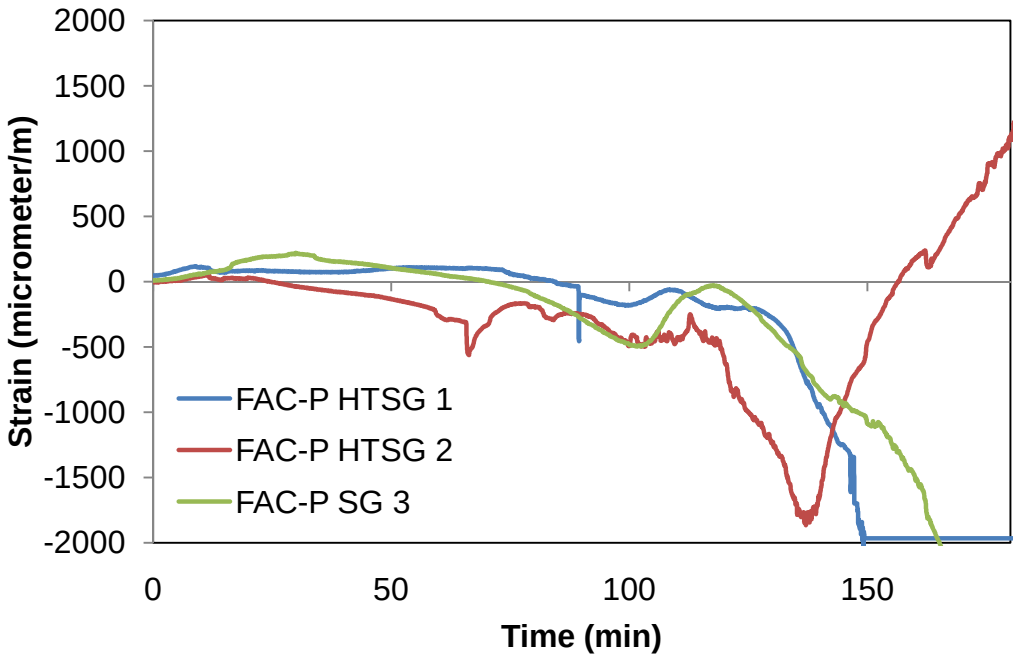

Figure 5.29 - Measured axial strains as a function of fire exposure time for FAC-P column at Section DD

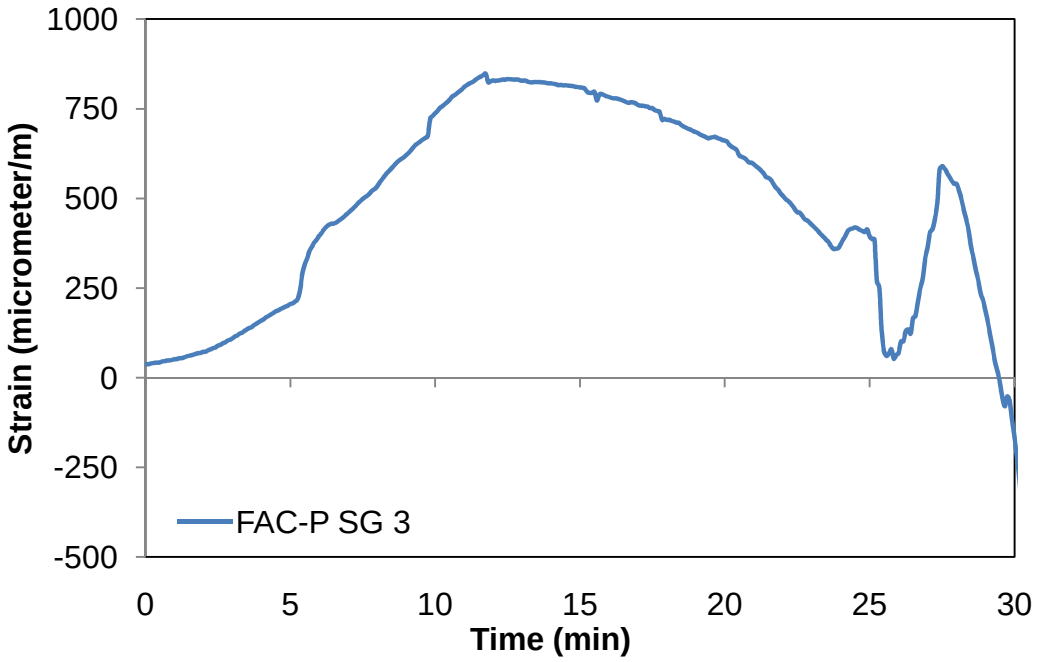

Figure 5.30 - Measured axial strains as a function of fire exposure time for FAC-P column at Section EE

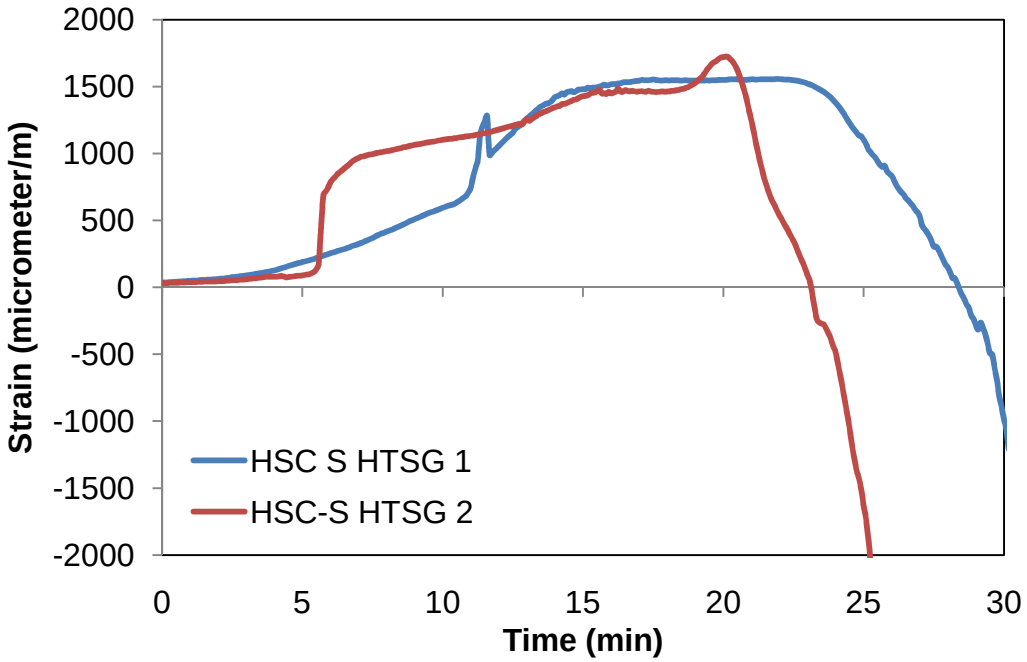

Figure 5.31 - Measured axial strains as a function of fire exposure time for HSC-S column at Section DD

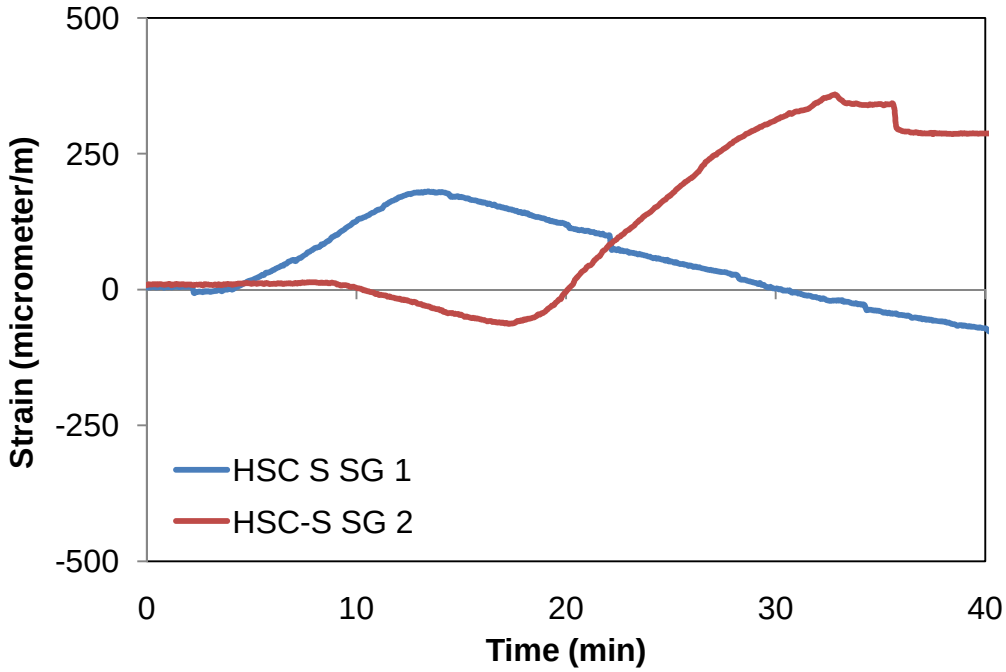

Figure 5.32 - Measured axial strains as a function of fire exposure time for HSC-S column at Section EE

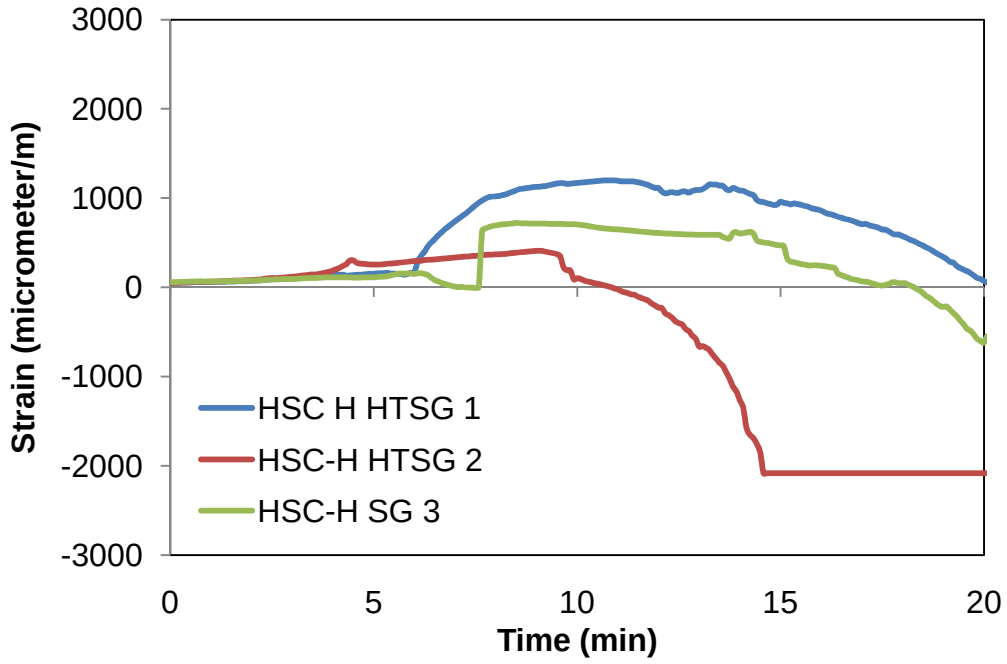

Figure 5.33 - Measured axial strains as a function of fire exposure time for HSC-H column at Section DD

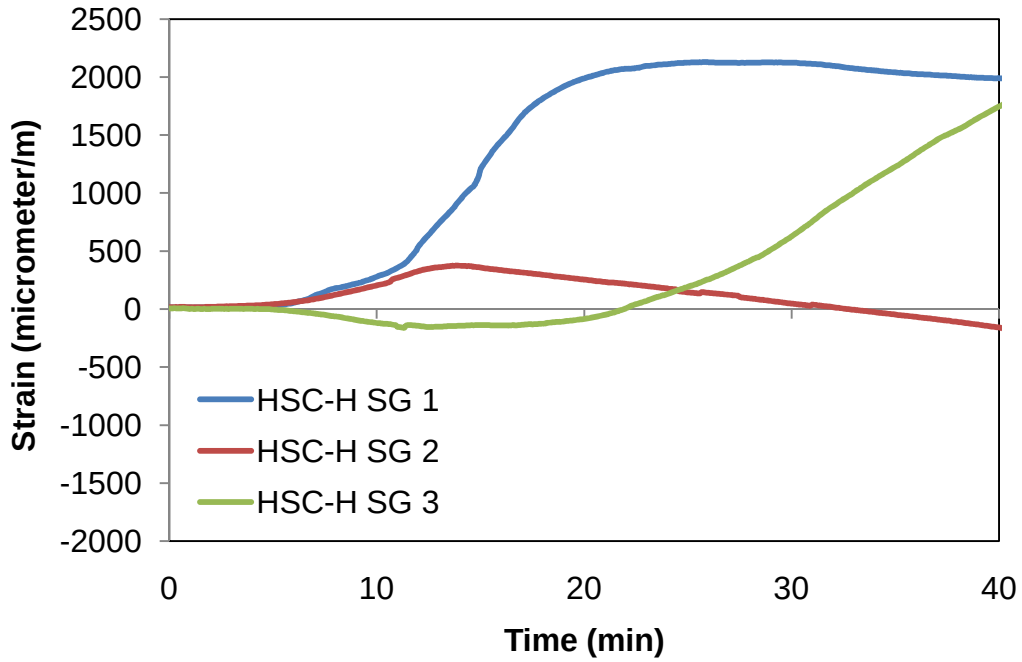

Figure 5.34 - Measured axial strains as a function of fire exposure time for HSC-H column at Section EE

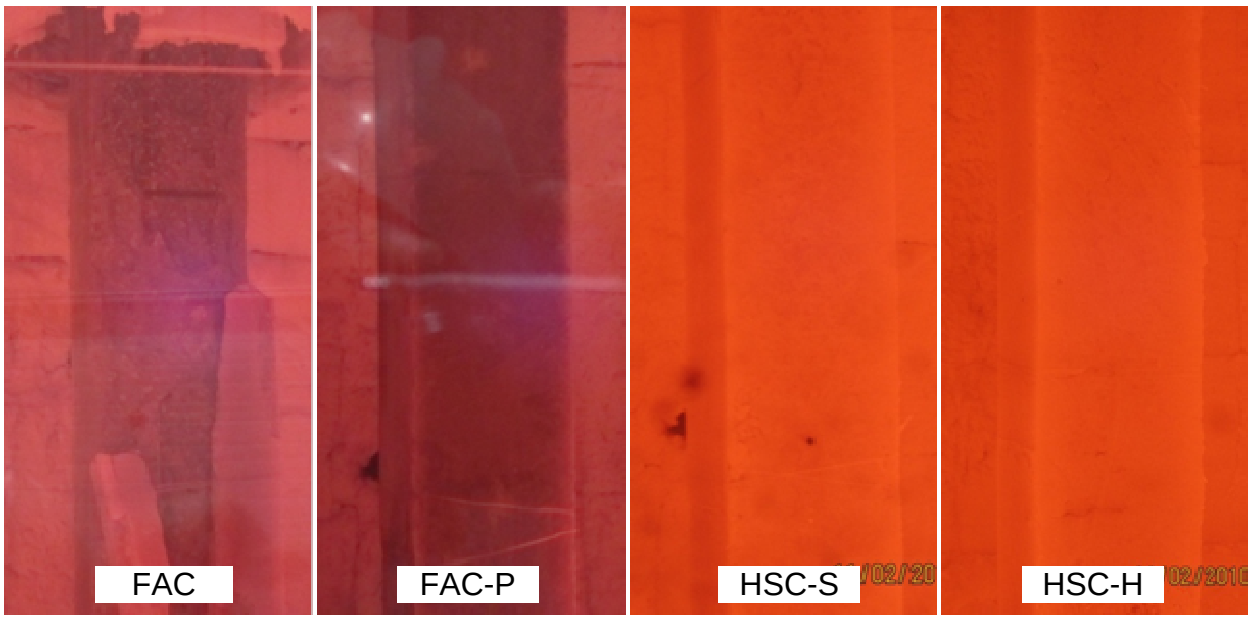

Figure 5.35 – State of columns during fire test at 60 minutes into the test

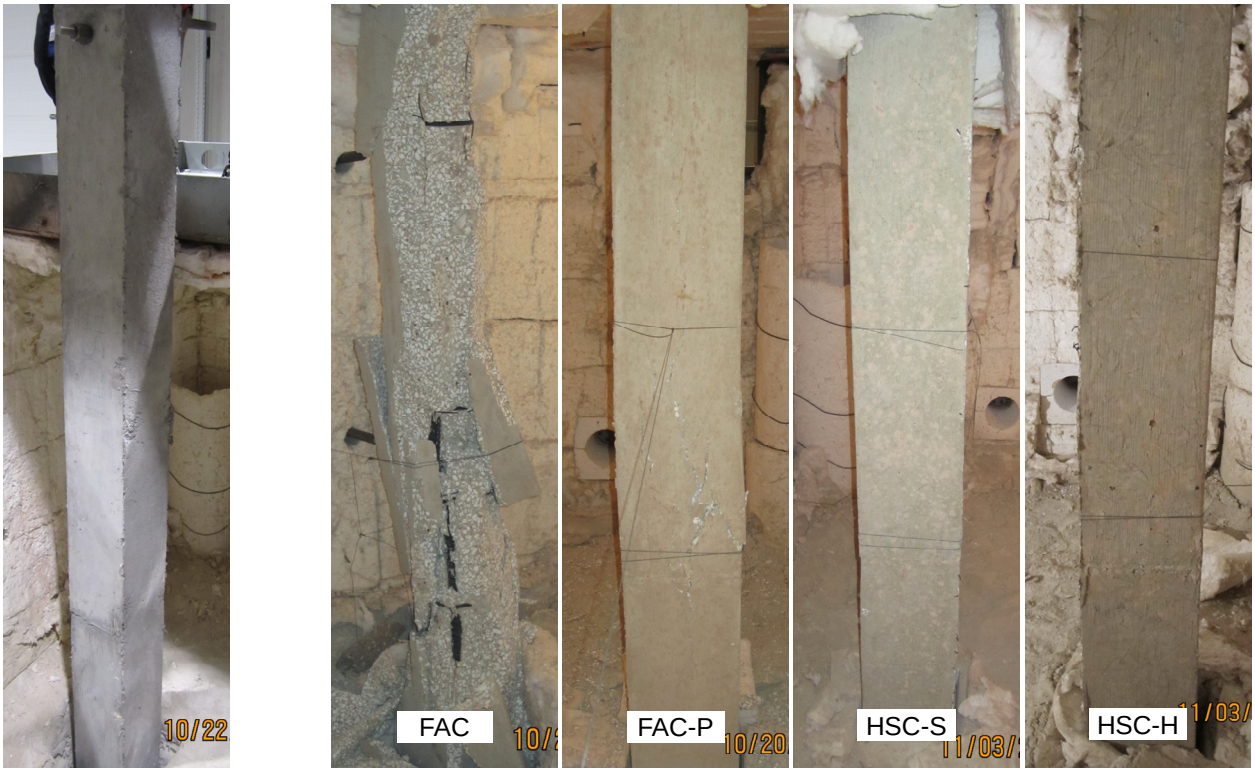

(a) Typical column before test (b) Columns after fire test

Figure 5.36 - State of columns before and after the fire resistance tests

Figure 5.37 - Columns after residual strength tests

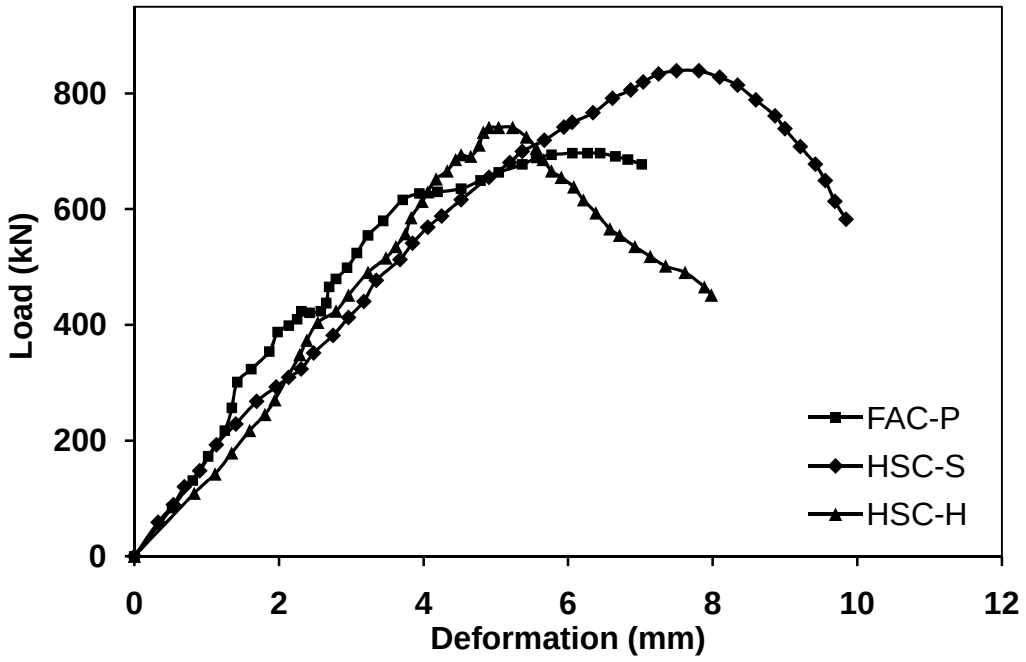

Figure 5.38 - Load-deformation response of fire exposed columns during residual strength tests

CHAPTER 6

6 NUMERICAL MODEL

This chapter is mainly based on the following conference presentation and paper:

- Khaliq, W., Raut, N. K., and Kodur, V. K. R. (2011). "Effect of tie configuration on fire performance of high strength concrete columns." Proc., Conference presentation, ACI Fall 2011Conference.
- Khaliq, W. and Kodur, V. K. R. (2012). "Effect of tie configuration on fire performance of high strength concrete columns." SiF 2012 Conference at Zurich, Switzerland.

6.1 General

Fire response of concrete structures can be evaluated by applying heat transfer, thermodynamics, and structural mechanics principles. For reliable fire response predictions, all influencing factors including fire scenario, high temperature material properties, size of member, load, spalling, and tie configuration have to be properly accounted for in fire resistance analysis. Developing a numerical model for evaluating fire resistance is quite complex due to interdependency of many of these significant parameters, as well as fire induced phenomenon such as cracking, spalling, de-bonding and moisture migration that occurs in concrete structures. Currently available commercial softwares are capable of accounting for complex structural geometry, but they are not capable of fully accounting for microstructural phenomenon such as moisture migration, pore pressure and spalling that occurs within a RC member under fire conditions.

Recently a macroscopic finite element (MFE) computer model was developed by Kodur et al. (2009) and this model can account for most of the above mentioned factors and can capture the fire response of RC beams and columns. However, this model does not account for high temperature material properties of HPC (with and without fibers) and pore pressure induced tie opening up in reinforced concrete columns. To enhance the capability two sub-models are developed as part of current study. The first sub-model is to incorporate high temperature properties of HPC and the second sub-model is to account the effect of tie configuration on fire response of reinforced concrete columns.

6.2 Macroscopic Finite Element Model for Fire Resistance Analysis

6.2.1 General

The macroscopic finite element (MFE) based numerical model, developed by Kodur et al. (2009), uses moment-curvature (M–κ) relations to trace the response of an RC structural member (column or beam) in the entire range of loading up to failure under fire. In this model, the RC structural member is divided into a number of segments along its length and the mid-section of the segment is assumed to represent the behavior of the whole segment (Kodur et al., 2009). The cross section, representing mid-section of each segment, is subdivided into elements forming a two dimensional mesh. The fire resistance analysis is carried out by incrementing time in intervals. The flowchart involving the various steps of analysis is shown in Figure 6.1.

At each time interval, the analysis is performed through three main steps namely, (1) establishing temperatures due to fire, (2) carrying out heat transfer analysis to determine temperature distribution in cross-section and (3) performing strength and deflection analysis. As part of step three fire induced axial restraint force in RC structural member is calculated and then M–κ

relationship is generated based on axial and lateral forces computed in previous sub-step for each segment and finally structural analysis of the member is performed to compute axial deformations and internal forces.

Full details of the model, including derivation of equations and validation of the model are comprehensively presented by Kodur et al. (2009) and Raut (2011). However, for the sake of completeness, overall procedure used in the model and some of the main drawbacks in existing model are presented here.

6.2.2 Fire Temperatures

First step in fire resistance analysis is calculation of fire temperatures. The fire temperature is assumed to follow a standard fire curve such as ASTM E119 (ASTM E119-08b, 2008) or ISO 834 standard fire or any other design fire scenario. The time-temperature relationship for the ASTM E119 and ISO 834 standard fire can be approximated by the following equations:

$$T_f = T_0 + 750\left(1 - \exp\left(-3.79553\sqrt{t_h}\right)\right) + 170.41\sqrt{t_h} \quad (6.1)$$

$$T_f = 20 + 345\log(8t + 1) \quad (6.2)$$

where t_h = time (hours), T_0 = initial temperature (°C), and T_f = fire temperature (°C).

Any other design fire, standard hydrocarbon fire and user defined fire can be used in the model based on the known time temperature relations.

6.2.3 Thermal Analysis

6.2.3.1 Cross-sectional Temperatures

The temperatures within the cross-section of each segment are computed using the finite element approach. The fire exposure to columns can be from 1-, 2-, 3-, or all 4-sides and the fire

temperature established in Section 6.2.2 forms the input to thermal analysis. The cross-sectional area of each segment (mid-section) is subdivided into a number of elements and temperature rise in a column segment is derived by establishing a heat balance for each element. The temperature is assumed to be uniform along the length of the segment and thus the calculations are performed for a unit length of each segment. Steel reinforcement is not specifically considered in the thermal analysis because it does not significantly influence the temperature distribution in the column cross-section (Lie and Irwin, 1993). However, in the model, the location of the steel reinforcement is accounted for while discretizing the column cross-section in to elements for thermal analysis such that more accurate temperature distribution is obtained.

Based on the conservation of energy, the following equation can be obtained for one dimensional heat transfer problems (Cook et al., 2007):

$$\rho c \frac{dT}{dt} = -\frac{dq}{dx} + Q \qquad (6.3)$$

Applying Fourier's law, which relates the heat flux to the temperature gradients as $q = -k\frac{dT}{dx}$, Eq. (6.3) can be written as

$$\rho c \frac{dT}{dt} = \frac{d\left(k\frac{dT}{dx}\right)}{dx} + Q \qquad (6.4)$$

Thus, the governing heat transfer equation within a rectangular column cross-section, that represents a two dimensional problem, can be written as:

$$\rho c \frac{dT}{dt} = \nabla k \nabla T + Q \qquad (6.5)$$

where k = thermal conductivity, ρc = heat capacity, T = fire temperature, t = time, Q = heat source, and q = heat flux.

At the fire-column interface, the mechanism for heat transfer is through radiation and convection. The heat flux on the boundary due to convection and radiation can be given by the following two equations which relate the heat flux due to convection and radiation to the temperature of fire (or ambient temperature for faces not exposed to fire):

$$q_{rad} = h_{rad}\left(T - T_E\right) \tag{6.6}$$

$$q_{con} = h_{con}\left(T - T_E\right) \tag{6.7}$$

where

q_{rad} and q_{con} are radiative and convective heat fluxes,

h_{rad} and h_{con} are radiative and convective heat transfer coefficient,

$$h_{rad} = 4\sigma\varepsilon\left(T^2 + T_E^2\right)\left(T + T_E\right), \tag{6.8}$$

T_E = temperature of the environment surrounding the boundary,

σ = Stefan-Boltzmann constant taken as 5.67×10^{-8} (W/m^2.°K^4), and

ε = emissivity factor.

Therefore, the total heat flux on the column boundaries (q_b) can be given by the equation:

$$q_b = \left(h_{con} + h_{rad}\right)\left(T - T_E\right) \tag{6.9}$$

Using Fourier's Law, the governing heat transfer equation on the boundary of the column can be written as:

$$k\left(\frac{\partial T}{\partial y}n_y + \frac{\partial T}{\partial z}n_z\right) = -h\left(T - T_f\right) \tag{6.10}$$

where

n_y and n_z = components of the vector normal to the boundary in the plane of the cross-section, and

$h = h_{rad} + h_{con}$

Since the column may be exposed to fire from any of the four sides, two types of boundary equations are to be considered for thermal analysis, namely:

- Fire exposed boundaries where the heat flux is governed by the following equation:

$$k\left(\frac{\partial T}{\partial y}n_y + \frac{\partial T}{\partial z}n_z\right) = -h_f\left(T - T_f\right) \qquad (6.11)$$

- Unexposed boundary where the heat flux equation is given by:

$$k\left(\frac{\partial T}{\partial y}n_y + \frac{\partial T}{\partial z}n_z\right) = -h_c\left(T - T_0\right) \qquad (6.12)$$

where

h_f and h_c are heat transfer coefficient of the fire side and the cold side, respectively, and

T_f and T_0 are fire and cold side temperature, respectively.

6.2.3.2 Pore Pressure Calculations

The cross-sectional temperatures generated above are utilized to evaluate pore pressure in each segment at each time step (Dwaikat, 2009; Dwaikat and Kodur, 2009; Raut, 2011). The pore pressure calculations are quite complex in concrete medium and a number of assumptions are made to deal the complications involved with moisture migration under elevated temperatures. Some of the key assumptions are:

- Concrete is a continuum medium. The solid skeleton (concrete structure) is assumed to be undeformable. This is because the mechanical and thermal deformation of the solid phase is small when compared to the volume changes due to other processes such as evaporation.
- Water vapor is an ideal gas, which is valid for most engineering applications (Harmathy, 1969; Harmathy, 1971; Huang, 1979).
- Mobility of liquid water is ignored. This assumption is valid because Darcy's coefficient (permeability) for liquid water in concrete is much smaller than that for water vapor (Harmathy, 1969; Sahota and Pagni, 1979).
- The effect of air is ignored in the analysis. This assumption is considered to be valid because the mass of air in concrete is much smaller than the mass of water.
- Water is incompressible liquid. This assumption is valid because the volumetric deformation of liquid water due to pressure is much smaller than the volumetric changes due to other processes such as evaporation.
- The effect of latent heat and heat of dehydration is not accounted for in the analysis. Accounting for latent heat and heat of dehydration will slightly reduce the predicted temperatures. Thus, latent heat and heat of dehydration can be conservatively ignored in the analysis.

The governing equations for the calculation of vapor pressure in concrete are derived using four main principles; namely:

- Conservation of mass for liquid water,
- Ideal gas law,
- Total volume of all different components in a unit volume of concrete equals unity, and

- Conservation of mass for water vapor.

The basic equations that govern the conservation of mass for liquid water is given by:

$$E = m_{LW0} - m_L + m_D \tag{6.13}$$

where E = mass of evaporated water, m_{LW0} = mass of liquid water at time t = 0 (initial mass of liquid water), m_L = mass of liquid water at any time, t, and m_D = mass of liquid water formed due to dehydration.

The ideal gas law is used to relate the pressure, the volume, the mass, and the temperature for water vapor. Equations are derived based on the conservation of mass of water vapor using Darcy's Law, which relates the mass flux to the pressure gradients. Mathematically solving constitutive equations, a simplified equation is obtained for pore pressure calculations by introducing three parameters, *A*, *B*, and *C* as follows:

$$A\frac{dP_V}{dt} = \nabla B \nabla P_V + C \tag{6.14}$$

where

$$A = \left[\left(1 - \frac{m_V}{V_V \rho_L}\right)\frac{dm_L}{dP_V} + \frac{V_V M}{RT}\right]$$

$$B = m_V \frac{k_T}{\mu_V}$$

$$C = \left[\left(1 - \frac{m_V}{V_V \rho_L}\right)\left(-\frac{dm_L}{dT} + \frac{dm_D}{dT}\right) + \frac{m_V}{T} + \frac{m_V}{V_V \rho_L^2}\frac{d\rho_L}{dT}\left(m_D - m_L\right)\right]\frac{dT}{dt}$$

Finite difference analysis in space and time domains is utilized to solve Eq. 6.14 to compute the pore pressure P_V. The parameters A, B, C are based on a particular temperature and resultant

pore pressure is computed at target temperature. In equation 6.14 P_V =pore pressure, m_V = mass of water vapor, R = gas constant, M = molar mass of water, V_V = volume fraction of water vapor, and T = temperature (°K) V_L = volume fraction of liquid water, V_D = volume fraction of dehydrated liquid water, and ρ_L = density of liquid water, k_T = intrinsic permeability of concrete at temperature, T, and μ_V = dynamic viscosity of water vapor.

6.2.3.3 Initial Boundary Conditions

The initial boundary conditions for pore pressure calculations are assumed as follows:

- Initial pore pressure (P_{V0}) can be computed as:

$$P_{V0} = RH \cdot P_{S0} \tag{6.15}$$

  where RH = initial relative humidity in the concrete, and P_{S0} = initial saturation pressure which can be computed based on the initial temperature of concrete.

- On the boundaries (surface) of the column the water vapor is assumed to be transferred through diffusion. Thus, the governing mass transfer equation of water vapor at the column boundaries can be written as:

$$\lambda\left(\frac{\partial P_V}{\partial y}n_y + \frac{\partial P_V}{\partial z}n_z\right) = -D_0\left(\rho_V - \rho_{V\infty}\right) \tag{6.16}$$

  where D_0 = diffusion coefficient of water vapor at the boundaries of the column, ρ_V = density of water vapor in the concrete boundaries, and $\rho_{V\infty}$ = density of water vapor in the surrounding environment. By assuming $\rho_{V\infty}$ to be constant during fire exposure (due to the

lack of information on the changes that take place in the surrounding environment of the column), Eq. (6.15) can be written as:

$$\lambda\left(\frac{\partial P_V}{\partial y}n_y+\frac{\partial P_V}{\partial z}n_z\right)=-\frac{D_0 M}{RT}\left(P_V-\frac{RT\rho_{V\infty}}{M}\right) \tag{6.17}$$

6.2.3.4 Finite Element Solution

Galerkin finite element formulation is applied to solve the heat transfer equation Eq. (6.5) and the differential equation for pore pressure development Eq. (6.14). Both equations can be written in the following form:

$$A_1\frac{du}{dt}=\nabla B_1\nabla u+C_1 \tag{6.18}$$

The governing equation at the column boundaries for both heat and mass transfer can be written as:

$$A_{11}\left(\frac{\partial u}{\partial y}n_y+\frac{\partial u}{\partial z}n_z\right)=-B_{11}\left(u-C_{11}\right) \tag{6.19}$$

The cross-section of an RC column is divided into elements as shown in Figure 6.2. According to the finite element formulation, the material property matrices and the equivalent nodal heat or mass flux (stiffness matrix K_e, mass matrix M_e, and nodal heat or mass flux F_e) are generated for each element. These matrices are given by the following equations (Williams, 2004)

$$K_e=\int_A\left[B_1\frac{\partial N}{\partial x}\frac{\partial N^T}{\partial x}+B_1\frac{\partial N}{\partial y}\frac{\partial N^T}{\partial y}\right]dA+\int_\Gamma NB_{11}N^T\,ds \tag{6.20}$$

$$M_e=\int_A A_1NN^T\,dA \tag{6.21}$$

$$F_e = \int_A NC_1 dA + \int_\Gamma NB_{11}C_{11} ds \qquad (6.21)$$

where N = vector of the shape functions, A_1, B_1, C_1, A_{11}, B_{11} and C_{11} = parameters computed by comparing equations (6.5), (6.11), (6.12), (6.14) and (6.17) with equations (6.18) and (6.19) for heat and mass transfer, Γ = boundary of the column, and s = distance along the boundary Γ.

6.2.3.5 Spalling Calculations

Once the pore pressure in various concrete elements is calculated, a simplified approach is applied to determine spalling. The computed pore pressure is compared against the temperature dependent tensile strength of concrete as shown in Figure 2.18. When the effective pore pressure exceeds the temperature dependent tensile strength at that time step, spalling is assumed to occur in that concrete element; i.e.:

$$nP_V > f_{tT} \qquad (6.23)$$

where: n is porosity of concrete and is equal to $V_V + V_L$, f_{tT} = tensile strength of concrete for temperature, T, V_V is volume fraction of water vapor, V_L is volume fraction of liquid water.

Once stress due to pore pressure exceeds the tensile strength, spalling occurs, the concrete element is assumed to be lost (removed from the section) and the reduced concrete section and new boundary surface is considered in the subsequent hydro-thermal and strength analyses. In this way, the coupling between spalling and hydro-thermal analysis will be accounted for in the model.

6.2.4 Strength Analysis

6.2.4.1 General Analysis

The third step in the numerical model is the strength analysis at the mid-section of each segment. The cross-sectional temperature distribution generated from hydro-thermal analysis is used as input to the strength analysis. For the strength analysis, the following assumptions are made:

- Plane sections before bending remain plane after bending.
- There is no bond-slip between steel reinforcement and concrete.

At each time step, the strength analysis is performed in three sub-steps; namely, estimating the axial force in each segment of the restrained column, generating the M-κ relationship for each segment, and carrying out nonlinear stiffness analysis to trace the response of the column under fire conditions.

The strength calculations are carried out using the same mesh used for thermal analysis as shown in Figure 6.2(d). The temperatures, deformations and stresses in each element are represented by those at the center of the element. The temperature in each element is obtained by averaging the nodal temperatures of rectangular elements. For steel rebars the temperature is assumed to be that at the center of the rebar.

The total strain in a concrete element, at any fire exposure time, is taken as the sum of the thermal expansion, the mechanical strain, the creep strain, and the transient strain:

$$\varepsilon_t = \varepsilon_{th} + \varepsilon_{me} + \varepsilon_{cr} + \varepsilon_{tr} \qquad (6.24)$$

where ε_t = total strain, ε_{th} = thermal strain, ε_{me} = mechanical strain, ε_{cr} = creep strain, and ε_{tr} = transient strain in concrete.

Thermal strain (ε_{th}) is directly dependent on the temperature in the element and can be obtained by knowing the temperature and thermal expansion of the concrete. Creep strain is assumed to be function of time, temperature, and stress level, and is computed based on Harmathy's (1993) approach using the following expression:

$$\varepsilon_{cr} = \beta_1 \frac{\sigma}{f_{c,T}} \sqrt{t}\, e^{d(T-293)} \qquad (6.25)$$

where β_1 = 6.28×10^{-6} $s^{-0.5}$, d is a constant taken as 2.658×10^{-3} K^{-1}, T = concrete temperature (°K) at time t (s), $f_{c,T}$ = concrete compressive strength at temperature T, and σ = stress in the concrete at the current temperature.

The transient strain (ε_{tr}), which is specific for concrete under fire conditions, is computed based on the relationship proposed by Anderberg and Thelandersson (Anderberg and Thelandersson, 1976). The transient strain is related to thermal strain as follows:

$$\Delta\varepsilon_{tr} = k_2 \frac{\sigma}{f_{c,20}} \Delta\varepsilon_{th} \qquad (6.26)$$

where k_2 = a constant ranges between 1.8 and 2.35 (a value of 2 will be used in the analysis), $\Delta\varepsilon_{th}$ = change in thermal strain, $\Delta\varepsilon_{tr}$ = change in transient strain, and $f_{c,20}$ = concrete strength at room temperature.

For steel reinforcement, the total strain, at any fire exposure time, is calculated as the sum of three components, as given by the following equation:

$$\varepsilon_{ts} = \varepsilon_{ths} + \varepsilon_{mes} + \varepsilon_{crs} \qquad (6.27)$$

where ε_{ts}, ε_{ths}, ε_{mes} and ε_{crs} are total strain, thermal strain, mechanical strain, and creep strain in the steel reinforcement, respectively.

Similar to concrete, thermal strain (ε_{th}) in steel can be directly calculated from the knowledge of rebar temperature and the thermal expansion coefficient of the reinforcing steel. Creep strain (ε_{cr}) in steel reinforcement is computed based on Dorn's theory and the model proposed by Harmathy (Harmathy, 1967) with some modifications made to account for different values of yield strength of steel. According to Harmathy's model, creep strain in steel is given by the following expression:

$$\varepsilon_{crs} = \left(3Z\varepsilon_{t0}^{2}\right)^{1/3}\theta^{1/3} + Z\theta \qquad (6.28)$$

where

$$Z = \begin{Bmatrix} 6.755\times10^{19}\left(\dfrac{\sigma}{f_y}\right)^{4.7} & \dfrac{\sigma}{f_y} \le \dfrac{5}{12} \\ 1.23\times10^{16}\left(e^{10.8\left(\sigma/f_y\right)}\right) & \dfrac{\sigma}{f_y} > \dfrac{5}{12} \end{Bmatrix},$$

$\theta = \int e^{-\Delta H/RT}dt$, $\dfrac{\Delta H}{R} =$ 38900°K, t = time (hours), $\varepsilon_{t0} = 0.016\left(\dfrac{\sigma}{f_y}\right)^{1.75}$, σ = stress in steel, and f_y = yield strength of steel.

Figure 6.3 shows the distributions of total strain, stress, and internal forces for the column cross-section at any fire exposure time. The total strain in any element (concrete or rebar) can be related to the curvature of the column by the following expression:

$$\varepsilon_t = \varepsilon_0 + \kappa y \qquad (6.29)$$

where: ε_0 = total strain at the geometrical centroid of the column cross-section, κ = curvature, and y = the distance from the geometrical centroid of the column cross-section.

In the model, Eq. (6.24) to Eq. (6.29) can be used to carry out strain computation of a segment at any given fire exposure time. At any time step, and for an assumed value of ε_0 and κ, the total strain in each element (concrete or rebar) can be determined using Eq. (6.29). Then the thermal, transient (for concrete only), and creep strains in the concrete and rebars are evaluated using known temperatures and corresponding equations derived above. Using the knowledge of total, thermal, transient, and creep strains, the mechanical strain in concrete or steel element can be evaluated by rearranging Eqs. (6.24) to Eq. (6.27):

$$\varepsilon_{me} = \varepsilon_t - \varepsilon_{th} - \varepsilon_{cr} - \varepsilon_{tr} \qquad \text{for concrete} \qquad (6.30)$$

$$\varepsilon_{mes} = \varepsilon_{ts} - \varepsilon_{ths} - \varepsilon_{crs} \qquad \text{for steel} \qquad (6.31)$$

Then for the estimated mechanical strain, the stress in the element can be established using the temperature dependent stress-strain relations of steel and concrete. Detailed procedure for evaluating thermal, mechanical, creep and transient strains in concrete and reinforcing steel is given by Dwaikat (2009).

6.2.4.2 Calculation of Fire Induced Axial Force

RC columns can develop significant restraint forces under fire exposure. The degree of restraint is dependent on the support conditions and will determine the behavior and fire resistance of an RC column. Generally, the axial restraint force in an RC column is compressive during the expansion phase of the column and tensile when the column starts contracting. Thus the axial restraint force is computed as:

$$P_r = k_r \Delta \quad (6.32)$$

where: P_r = axial restraint force, k_r = axial restraint stiffness provided by adjoined beams supported by the column, Δ = axial deformation of the column.

For an assumed value of axial restraint force P_r, an iterative procedure is used to solve for change in segment length in order to compute the axial strain in each segment. The constitutive equations for calculating the total axial strain and axial strain in each segment and also the governing compatibility equations are given by Dwaikat (2009). These equations are solved to ensure the compatibility requirements with Δ being calculated using Eq. (6.32). The value of P_r is modified until compatibility conditions are satisfied within a pre-determined tolerance. The error involved in the estimation of total axial strain and stain in segment becomes smaller if shorter time steps are used.

6.2.4.3 Generation of Moment-Curvature Relationships

Once the axial restraint force in the column is computed, the moment-curvature (M-κ) relationships for each segment of the beam or column are generated through an approach analogous to the method used for the analysis of prestressed concrete beams. In this approach, M-κ relationships are established by iterating the central total strain (ε_0) and the curvature (κ).

At each time step, analysis starts with an assumed value of curvature and central total strain (in concrete) are assumed. Then, the total strain in each of the rebars and concrete elements is computed from the assumed strain and curvature. The stresses in the rebars and the concrete elements are determined utilizing the constitutive laws for concrete and reinforcing steel. The temperature in rebars is assumed to be equal to the temperature at the location of the center of the

rebar. Once the stresses are known, the forces are computed in the concrete and the rebars. The curvature is then iterated until equilibrium of forces is satisfied (internal force equal to the fire induced axial restraint force). Once the equilibrium is satisfied, the moment and the corresponding curvature are calculated. Thus, the values of moment and curvature are stored to represent a point on the M-κ curve. The value of the central total strain is incremented to generate subsequent points on the moment curvature curve. This procedure is repeated for each time step of fire exposure and the values of the M-κ curves are stored as a point on moment curvature curve at various time steps. The generated M-κ curves are used for tracing the behavior of the column through nonlinear structural analysis. The generation of M-κ relationships is an important part of the numerical model since these relationships form the basis for the fire resistance analysis of the RC column.

6.2.4.4 Column Analysis

The M-κ relationships and the axial restraint force generated for various segments are utilized to trace the response of the whole column exposed to fire. At each time step the deformations in the column are evaluated through a stiffness approach. The secant stiffness for each segment is determined from the M-κ relationships, based on the moment level reached in that particular segment.

Each node in the idealized column is assumed to have five degrees of freedom (namely; two rotations and three displacements) in the case of rectangular columns and three degrees of freedom (namely; rotation and two displacements) in the case of circular columns. The deformation of the column is computed using an iterative procedure described by Campbell and Kodur (1990). Accordingly, an iterative column analysis is carried out at each time step first, a

linear analysis is carried out using the initial rigidity of the column (EI_0) to determine the moment distribution along the span of the column. The segment having the maximum bending moment is selected to be the critical segment.

The second step is to increment the curvature in the critical segment and the curvature and moment distributions along the span of the column (in each segment) are computed for each increment of the curvature. An iterative procedure is employed to obtain the solution at each increment of curvature such that equilibrium, compatibility, and convergence conditions are satisfied, and the procedure is illustrated in Figure 6.4.

For each increment, a target curvature is selected for the critical segment. The column is analyzed under a unit load and the bending moment and the curvature in each segment are computed. The curvature in each segment is multiplied by a scaling factor that is computed through dividing the target curvature in the critical element by the computed curvature in the same element. The new secant rigidity for the next iteration can be computed from the generated M-κ relationship. The iterative procedure continues until convergence is achieved where the rigidity in each segment is approximately maintained within a certain tolerance.

In the iterative procedure described above, the stiffness matrix and the loading vector are computed for each longitudinal segment. Then these matrices are assembled in the form of nonlinear global stiffness equation, which can be written as:

$$K_g \delta = P_f + P_S \tag{6.332}$$

where: K_g = global stiffness matrix, δ = nodal displacements, P_f = equivalent nodal load vector due to applied loading, and P_s = equivalent nodal load vector due to P-δ effect.

The effect of the second order moments, developed due to the axial restraint force, is calculated using the following equation:

$$P_S = -K_{geo}\delta \qquad (6.34)$$

where: K_{geo} = geometric stiffness matrix, δ = nodal displacements, and P_S = equivalent nodal load vector due to P-δ effect.

The second order moments are then added to the external loads in the stiffness analysis as given by equation (6.33). Thus, for any given time step, the temperatures (in concrete and steel), moment capacity and curvatures, as well as deformations in the column are known for a given fire exposure. These output parameters are used to evaluate failure of the column either at local (in each segment) or at global (whole column) levels.

6.2.4.5 Failure Limit State

The model generates various critical output parameters, such as temperatures, stresses, strains, internal forces, and deformations at various fire exposure times. These output parameters are used to check against predefined failure criteria. At every time step, each segment of the structural member is checked against thermal, strength and deflection failure criteria. The analysis is continued until strength failure of the structural member is reached. The different failure limits incorporated into the model are:

- The temperature in steel rebars exceeds the critical temperature which is 593°C for reinforcing steel.
- The applied load exceeds the load carrying capacity of the column.
- Resultant axial deflections exceed the limiting deflection and rate of deflection.

The user has the option to specify any (or all) of the failure limit states mentioned above to define failure.

6.3 Limitations of Existing Numerical Model

The model generates various critical output parameters, such as temperatures, stresses, strains, axial restraint force, axial deformation, lateral deformation, and axial load and moment capacities at various fire exposure times. The temperatures, capacity and deflections generated in each time step are used to evaluate failure of the column at that time step. However, this numerical model does not take in to account two important factors that influence the fire resistance of HPC columns. These factors are (1) specific high temperature material properties of HPC such as FAC and SCC (plain and with different fiber combinations) and (2) effect of modified (135°) tie configuration on fire response of HPC columns. The two tie configurations that are used for RC columns are show in Figure 6.5(a). It can be seen from Figure 6.5 that modifying the tie configuration to 135° significantly reduces the spalling progression and thus enhances fire performance of RC columns. Both of these factors are critical for accurate and realistic fire resistance predictions for HPC columns.

6.4 Extension to Macroscopic Finite Element Model

The above presented MFE model is extended for fire resistance analysis of HPC columns by incorporating two factors namely high temperature material properties of HPC, and the effect of tie configuration on fire performance of columns. As part of this extension, two subroutines are developed, one to capture the pertinent high temperature properties to HPC and second one for accounting for the effect of tie configuration.

6.4.1 High Temperature Properties

As discussed in Chapter 2, columns made of HPC have lower fire resistance than conventional concretes and it is due to different thermal and mechanical properties of HPC as compared to conventional concrete. It is therefore imperative to incorporate specific HPC properties in the numerical model to evaluate the fire resistance of RC columns made from that particular HPC. For HPC namely HSC, FAC, SCC and FRC, various empirical property relations which have been developed as part of characterization of high temperature material property tests presented in Chapter 3 and 4 are incorporated into the model. These relations are thermal conductivity, specific heat and thermal expansion, and compressive strength, splitting tensile strength, elastic modulus and stress-strain curves. These high temperature material property relations are incorporated as new subroutines in the MFE model that define high temperature material properties in fire resistance calculations.

The thermal properties of HPC (HSC, FAC, SCC and fiber reinforced concrete) are added to thermal part (thermal solver) of MFE model and given a material number at appropriate place. Compressive and tensile strength of concrete are also incorporated in thermal solver of the MFE model. Tensile strength relations are incorporated into thermal solver of the model for different types of HPC so that spalling could be accurately predicted for specific concrete type. As shown in Figure 6.1 the spalling is checked after thermal analysis and pore pressure calculations. At this step the tensile strength of HPC (with and without fibers) is used against effective pore pressure, if pore pressure overcomes the tensile strength of concrete it is assumed that spalling has occurred and geometry of the cross-section of columns is updated for further calculations. The mechanical properties comprising of compressive strength, tensile strength and elastic modulus are also incorporated into structural part (structural solver) of the MFE model and given a

material number. The NSC and HPC columns are assumed to have a permeability of the order 10^{-16} and 10^{-18} m^2 respectively. The melting of polypropylene fibers in concrete is taken into account by varying the permeability of HPC from 10^{-18} to 10^{-17} m^2 at 160°C when polypropylene fibers melt away and enhance the permeability of HPC. With this addition, model is able to predict realistic fire response of HPC columns by inputting unique high temperature material properties of HSC, SCC, and FAC with and without fibers.

6.4.2 Approach to Model Tie Configuration

The beneficial effect of lateral confinement in concrete columns, both tie configuration (135°) and closer spacing of ties, has been well recognized in seismic design of columns (Bayrak and Sheikh, 2001; Pantazopoulou, 1998; Richart et al., 1929). This design philosophy is based on the principle that the compressive strength of the confined concrete core of a column after stress induced spalling should be equal to the strength of the gross section of the column before the occurrence of spalling (Richart et al., 1929). The ties in column, when bent at 135°, achieve sufficient lateral confinement and enhance ductility of column under seismic loading (Bayrak and Sheikh, 2001; Berry and Eberhard, 2005; Pantazopoulou, 1998).

Similar approach, as that developed for seismic loading, can be applied to model the effect of tie configuration on fire resistance of reinforced concrete columns. However, in the case of fire conditions, additional stresses due to temperature induced vapor pressure and thermal strains are to be considered along with mechanical stresses due to loading on the column. Also, bond strength that develops at the tie-concrete interface deteriorates with temperature and also due to occurrence of fire induced spalling. The force acting on the ties from pore pressure, mechanical

loading and thermal effects should be checked against this bond strength so as to ensure that the ties have sufficient resistance and do not open-up through yielding.

When RC columns are exposed to fire, temperatures in concrete, steel reinforcement and ties gradually increase. The increasing temperatures in concrete lead to build-up of pore pressure which cannot be dissipated due to low permeability of concrete (characteristic of HSC). When this pore pressure exceeds tensile strength of concrete, spalling occurs. The fire induced spalling in concrete usually occurs in high strength concrete (HSC) structural members because of low permeability associated with HSC. Such spalling not only leads to loss of cross-section in the column, but also alters the bond resistance of the ties.

When exposed to fire, significant level of internal stresses are generated on ties and these stresses result from load induced mechanical strains, temperature induced thermal expansion, and fire induced vapor pressure as a result of water becoming vapor. The effective stress that is the sum of three stresses (pore pressure, mechanical loading and thermal effects) acts as hoop stress on ties. The resistance provided by ties against the effective stress is through the bond (strength) action between tie and concrete interface, which also degrades with increasing temperatures. When the force resulting from effective stress exceeds the bond strength of ties, the ties will open-up (fail) through yielding of the ties.

The equations for confinement damage model under fire conditions can be derived based on approach adopted in seismic analysis of concrete columns. Under axial load, concrete core expands laterally and pushes against longitudinal rebars resulting in traverse loads. From longitudinal rebars, these traverse loads are transferred to ties. At the tie level, where lateral restraints are present, the lateral force is higher, whereas at the level between the two ties this force will be smaller as the longitudinal rebars can deform outward and concrete core and

expand without restraint. The pressure exerted by the expanding concrete core in the form of hoop stress on ties and the resultant confinement provided by ties to longitudinal rebars can be used to model the tie behavior.

Free body diagram of various components of an RC column and forces acting on rebar and ties is illustrated in Figure 6.6. The longitudinal rebar between the two ties is subjected to a force which varies as sinusoidal wave function (Bayrak and Sheikh, 2001). At the level of ties a lateral restraint is provided by tie corners, and the resulting force on longitudinal rebar is higher (Figure 6.6(a)). At the mid-level between the two ties, the force is the lowest as the concrete core can expand relatively easily and thus exert force on longitudinal rebars. This force varies along the longitudinal rebar and its variation can be taken as:

$$F_{(x)} = F_0 + F_V \times cos\left(\frac{2\pi x}{s}\right) \geq 0 \qquad (6.35)$$

where *F(x)* is the force function acting along longitudinal rebar, F_0 is the average force acting on longitudinal rebar; *Fv* is the magnitude of variable part of force; (*x)* is the coordinate (distance) along the length of rebar and (*s*) is tie spacing as shown in Figure 6.6(b) and (c). The unknowns in Eq (6.35), F_0 and F_v, at a given distance (*x*) can be determined by applying force equilibrium and geometric boundary conditions. These two unknowns F_0 and F_v, can be related to tie spacing (*s*) and critical tie spacing (s_{cr}). Critical tie spacing, taken from the analogy used in seismic design, is at the mid-height between two ties where effective confined concrete area is assumed to be zero (Bayrak and Sheikh, 2001).

This implies that if $s = s_{cr}$ at $x = s_{cr}/2$, the force exerted by ties on longitudinal rebars ($F_{(x)}$) becomes zero, leading to variable part of the force F_v as:

$$F_v = F_0\left(\frac{s}{s_{cr}}\right)^2 \tag{6.36}$$

By substituting the value of F_v back to Eq. (6.35) the force acting on longitudinal bars can be calculated as:

$$F_{(x)} = F_0\left[1+\left(\frac{s}{s_{cr}}\right)^2 \times \cos\left(\frac{2\pi x}{s}\right)\right] \tag{6.37}$$

The force developed in the ties can be obtained by integrating the force on longitudinal rebar and applying relevant boundary conditions:

$$F_{tie} = 2\int_0^{s/2} F_{(x)}dx \tag{6.38}$$

Solving Eq (6.38) gives the total tie force acting on the corner of the longitudinal rebar which translates to:

$$F_{tie} = 2A_{tie}\sin\left(\frac{\pi}{4}\right)\sigma_{core} \tag{6.39}$$

where A_{tie} is cross sectional area of tie, σ_{core} is stress resultant which is the sum of load induced stress, thermal stress and pore pressure coming from concrete core.

Knowing the applied load on the column during fire exposure, load induced (mechanical) stress can be evaluated at any given fire exposure time. It should be noted that this stress significantly increases with increasing temperature due to degradation of strength properties of concrete and steel. Further, if there is any fire induced spalling, the cross-section of column reduces and this

leads to higher mechanical stresses in column. The second component of the stress acting on the ties is the fire induced thermal stress which can be evaluated knowing the temperatures in the column. The thermal stress is evaluated by utilizing thermal expansion multiplied by the elastic modulus of concrete both of which vary as a function of temperature.

The third component of the stress that is acting on the ties is the pore pressure in concrete which can be evaluated through an hydrothermal model (Kodur et al., 2009). This model uses the principles of mechanics and thermodynamics including the conservation of mass of liquid water and water vapor to predict the pore pressure in the concrete exposed to fire (Dwaikat and Kodur, 2009). In the hydrothermal model, the mass transfer equation for water vapor inside heated concrete can be written as:

$$A\left(\frac{dP_V}{dt}\right) = \nabla B \nabla \sigma P_V + C \qquad (6.40)$$

where: σP_V = pore pressure, t = time, A, B and C = parameters that depend on pore pressure, temperature, rate of increase in temperature, permeability of concrete, initial moisture content, and the isotherms used in the analysis. Isotherms are used to predict the liquid water inside concrete as a function of pore pressure for a constant temperature.

Finite element analysis is used to solve Eq (6.40) and compute the pore pressure (σP_V) distribution within the elements of each segment along the length of the structural member. With combination of the three stresses resulting from pore pressure (σP_V), thermal expansion ($\sigma_{thermal}$), and mechanical loading ($\sigma_{mechanical}$) resultant effective stress on tie is calculated. The equation governing this condition at time T is given by:

$$\sigma_{core,T} = \sigma_{P_V} + \sigma_{thermal} + \sigma_{mechanical} \quad (6.41)$$

where σP_V is stress due to pore pressure, $\sigma_{thermal}$ is stress coming from thermal expansion of concrete core and $\sigma_{mechanical}$ is stress resulting from axial load on column. With the effective stress ($\sigma_{core,T}$) at temperature T known in the tie, the force acting on ties (F_{tie}) is computed as:

$$F_{tie,T} = 2A_{tie}\sin\left(\frac{\pi}{4}\right)\sigma_{core,T} \quad (6.42)$$

The resisting force provided by the tie is the force developed between the tie and concrete interface. This tie-concrete interface force is dependent on the length of the tie leg, the bar diameter and the yield strength of the steel rebar used as ties. The bond strength therefore can be related by taking into account the yield strength of the multiplied by the tie-concrete interaction area which is given by the relation for room temperature calculations:

$$F_{bond} = (2\pi r l_d) f_y \quad (6.43)$$

where f_y is the yield strength of steel at room temperature, l_d is the development length of the leg of the tie, and (r) is the radius of steel rebar used as tie. However, as steel strength also degrades with temperature, the resulting resisting bond strength of the ties also decreases with temperature and is given by the relation:

$$F_{bond} = (2\pi r l_d) f_{s,T} \quad (6.44)$$

where $f_{s,T}$ is the stress in steel at temperature T.

Knowing the force acting on ties and bond strength that develops in ties, the state of tie can be checked and failure (opening up of ties) is said to occur when.

$$F_{tie} > F_{bond} \quad (6.45)$$

It can be seen that the resistance of tie (F_{bond}) is dependent on temperature as well as the bond between tie-concrete interfaces; therefore it is highly dependent on cross-sectional integrity of RC column. In case of fire induced spalling, the outer cover of cross-section spalls away leaving the outer side of 90° tie exposed to fire and the tie-concrete interaction lost which leaves the bond strength reduced to half. However, in the case of 135° tie, the legs of the tie are bent inside concrete core and even in the case of fire induced spalling; the tie-concrete interaction is not lost which is an advantage compared to 90° ties.

6.5 Computer Implementation

The macroscopic finite element (MFE) computer program described in Section 6.2 is extended by incorporating new subroutines based on “high temperature material properties” and “tie sub-model”. Figure 6.7 illustrates the flowchart showing schematic of main program and the additional subroutines that are added. The high temperature thermal and mechanical properties of HPC presented in Chapter 3 and 4 respectively, are incorporated into both thermal and structural solvers of the MFE model (depicted by gray diamond boxes in main program in Figure 6.7). These new material properties are utilized for carrying out thermal analysis, pore pressure and spalling calculations, and strength analysis base on moment-curvature (M-κ) relationships. The “tie sub-model” subroutine is incorporated in structural solver of the MFE model and is utilized to further carry out calculation of tie forces (effective force on tie and bond strength) at each time step. Upon calculating the M-κ response and after meeting the equilibrium and compatibility conditions, the program carries out structural analysis at each time step based on failure limit state (including tie failure). The iterative procedure continues till fire resistance is obtained based

failure time either due to failure of ties, or strength failure limit state. If any failure limit is not attained the analysis continues to the end of investigation run-time.

For necessary computations to execute the program, the macroscopic finite element computer model is developed in FORTRAN language. The details on idealization of structural member, cross-sectional discretization, segment length, time domain, fire scenario, and exposure conditions are explained in details by Raut (Raut, 2011) and Kodur et al. (Kodur et al., 2009).

6.5.1 Input Data

The basic input for the program consists of geometric properties, cross-sectional properties (including tie configuration), material properties (including HPC), and general data such as the number of time increments. The sequential order of the input data must be followed in the input file. Consistent SI units must be used throughout input and analysis.

6.5.2 Output Results

The output from the program includes the results from thermal and structural analyses. At each incremental time step, the temperature at each elemental node is computed by hydro-thermal analysis. The output results include the fire resistance times based on failure or non-failure of member, the M-κ curves, axial deformation, and rate of deflection, F_{tie} and F_{bond} at each time step.

6.6 Validation of Numerical Model

6.6.1 General

The previous version of the model has been earlier validated for NSC and HSC columns (Raut, 2011). However, further validations are required with the incorporation of high temperature

material properties for HPC. Six fire tested columns namely FAC, FAC-P, HSC2, HSC3, HSC5, and HSC6 were analyzed for validation studies as part of current study. Two columns FAC and FAC-P are selected from the experimental study presented in Chapter 5 and four columns HSC2, HSC3, HSC5, and HSC6 were selected from fire test data reported by Kodur and McGrath (2003) for validations of effect of tie configuration. Critical response parameters, such as cross-sectional temperatures, axial deformation, failure times including tie failure, and effect of tie configuration on fire response are compared with test data measured in fire resistance tests on RC columns.

6.6.2 Validation Studies

The proposed model is being validated for RC columns by comparing predictions from the model with measured data from fire tests. Recently characterized thermal and mechanical properties for HPC (Chapter 3 and 4) are used in the analysis, whereas properties of reinforcing steel used in the analysis are as per ASCE manual (1992). The validity of the macroscopic finite element model for RC columns is established by comparing the predictions from the analysis with the fire test data reported in Chapter 5 for columns FAC and FAC-P and test data published earlier by Kodur and McGrath (2003) for columns HSC2, HSC3, HSC5 and HSC6. This selected study is one of the few available in literature in which effect of tie configuration on fire response of RC columns was experimentally investigated.

The geometric properties consisting of elevation and cross-section of FAC and FAC-P columns are illustrated in Figure 6.8 and that of columns HSC2, HSC3, HSC5 and HSC6 are illustrated in Figure 6.9. The columns are analyzed by exposing columns to the ASTM E119 (2008) standard time-temperature curve. The fire resistance of the columns was evaluated based on both strength failure and tie failure (yielding/opening) criteria. Predicted results from the analysis are

compared to the measured values from the fire tests in Figures 6.10 to 6.16 and also tabulated in Table 1.

6.6.2.1 Temperature and Structural Response Predictions

Details on six columns including test parameters selected for predicting fire response of HPC columns are given in Table 6.1. The table also shows the actual experimental test parameters such as, column size, fire scenario, tie configuration, concrete strength, column strength and applied load. Validation study on these columns is presented here:

For the analysis, the RC column was divided into 40 equal length segments along its length and the mid-plane of each segment was assumed to represent the segmental behavior. The cross-section of each segment was divided with a 30x30 mesh of equal elemental size of with square network of lines. This mesh can be coarsened or refined based on the accuracy of results desired and availability of analysis time. For analyses of these columns the empirical relations on thermal properties comprising of thermal conductivity, specific heat, thermal expansion, and mechanical properties including compressive strength, splitting tensile strength and elastic modulus presented used in Chapter 3 and 4 were used. The time domain was divided into increments of one minute and the transient analysis was carried out at each time step. The validity of the model is established by comparing predictions from the model with measured temperatures, deflections and fire resistance times. Failure time was recorded when the column was no longer capable of supporting the applied load or failure of tie occurs as per prescribed criteria.

Two tested HPC columns (FAC and FAC-P) from current study reported in Chapter 5 were analyzed using the macroscopic finite element model. Each column is analyzed under the fire

scenarios they were exposed to in tests which are given in Table 6.1. Figure 6.8 illustrates the cross-sectional dimensions and layout of thermocouples for FAC and FAC-P columns. For validation of temperatures three thermocouple positions at three places namely rebar, quarter depth and mid depth of column cross-section were selected out of seven used in actual fire tests as shown in Figure 6.8. Figures 6.10 and 6.11 illustrate the predicted and measured temperatures as a function of fire exposure time for FAC and FAC-P columns. As FAC column suffered spalling during the fire test therefore the rebar temperature went quite erratic during the fire test, however the temperature predicted by the model in the rebar was quite high without showing any noise in it. This stability in predicted temperature can be attributed to mathematical calculations that can show higher temperatures but do not capture the extreme fluctuation in temperatures in case of ongoing spalling in cross-section. These high temperature predictions however generally lead to conservative fire resistance calculations. A slight difference can be observed between measured and predicted temperatures of FAC-P column as shown in Figure 6.11. This is attributed to the way the model handles the permeability parameters which could be different form the actual permeability conditions in column on melting of polypropylene fibers.

Figure 6.12 illustrates the measured and predicted axial deformations of FAC and FAC-P columns. The figure shows that there is a good agreement between the measured and the predicted axial deformations for these columns. For FAC, FAC-P columns, the model predicted about similar axial deformation with little conservative values for FAC-P. The comparison of axial deformation for these columns illustrates that the numerical model handled material properties for the new types of concrete very well and reasonably predicted the behavior of RC columns made of new types of concrete.

The fire resistance predicted by model is compared to the measured fire resistance values for FAC, FAC-P in Table 6.1. The model predicted the fire resistance of FAC and FAC-P columns quite acceptable limits. The fire resistance time predicted by model for FAC column was 156 minutes as compared to 165 minutes measured time that was based on strength criteria and no tie failure was predicted in this column. This can be attributed to the high cross-sectional temperature profiles captured for FAC columns that resulted from spalling leading to this conservative fire resistance prediction. FAC-P column did not fail in the fire tests and the model prediction was also confirming the survival in the 270 minute analysis.

Though detailed comparisons are presented only for two columns, the predicted temperatures, deformations, and fire resistance also compared well with test data for the other four columns tested. Good comparison was observed between predicted and measured response parameters.

6.6.2.2 Tie Configuration

Four columns namely HSC2, HSC3, HSC5, and HSC6 were analyzed in the validation study on effect of tie configuration on RC columns from fire test data reported by Kodur and McGrath (2003). For validation purpose, similar parameters were used for analysis as were used for experiments. As shown in Table 6.1, columns HSC2 and HSC3 had conventional 90° bent ties at 406 mm spacing, whereas HSC5 and HSC6 columns had 135° bent ties at 76 mm spacing. In the case of columns HSC5 and HSC6 additional confinement was provided by adding middle tie leg as shown in Figure 6.9. However, in the analysis it was neglected and analysis was run only for main ties being critical. Columns HSC2 and HSC5 were axially loaded to 40% of their capacity, while columns HSC3 and HSC6 were loaded to 60% of their room capacity. Concrete compressive strength for these columns ranged from 86-120 MPa as shown in Table 6.1. Specified yield strength of steel rebars was 420 MPa.

The thermal analysis is carried out by calculating cross-sectional temperatures and pore pressure. In the analysis, when the pore pressure in an element exceeds temperature dependent tensile strength of concrete, that element is removed from the cross-section for further analysis. Extent of actual spalling data was not available for these columns from the test data; therefore for purpose of calculations the outer concrete cover outside steel cage is assumed to have spalled in first 60 minutes. Next, the strength and stiffness analysis is carried out by using high temperature concrete and steel mechanical properties. The output parameters namely temperatures at various locations (ties), mechanical stress, thermal stress and pore pressure are generated from the model. Using these parameters effective stress is evaluated and the force acting on the tie is computed using Eq 6.42. Also with increasing temperatures in ties and loss of concrete cover bond strength degrades with fire exposure time. The force acting on the tie is then checked against bond strength to evaluate failure of the ties. This procedure is repeated for each time step till the failure of column occurs through reaching one of the failure limit states (Dwaikat and Kodur, 2009).

Figure 6.13 illustrates the predicted development of pore pressure in the columns as a function of fire exposure time. The pore pressure increases with fire exposure time, reaches a peak value and then drops with time. The increase in pore pressure can be attributed to build-up of moisture clog resulting from moisture movement inside concrete matrix. As the temperature in concrete increases beyond 100°C, water present in concrete evaporates, leading to build-up of pore pressure that increases with depth. This pore pressure build-up drives part of water vapor to move away from heated surface deep into the inner layers of concrete member. This migrated water vapor condensates and results in saturation of concrete microstructure. This phenomenon

is referred to as moisture clog and depending on concrete permeability (strength) this can result in to significant variation in pore pressure during fire exposure (Dwaikat and Kodur, 2009).

Figure 6.13 shows that a peak pore pressure of 4.5 MPa gets developed in plain HSC concrete column. In HSC columns, the lower permeability (Mindess et al., 2003; Noumowé et al., 2009) does not facilitate the escape of water vapor and resultantly, higher pore pressure gets developed in these columns. In addition to pore pressure development, another phenomenon that occurs with increase in cross-sectional temperatures is the degradation of bond between reinforcement (ties) and concrete. The degradation of bond strength for different tie configurations (10 mm ties) is illustrated in Figure 6.14. The bond strength is dependent on the temperature in ties and any loss of cross section due to fire induced spalling.

The significant drop in bond strength in 90° bent ties, at about 60 minutes, results from loss of cover concrete from fire induced spalling. As a result of spalling, theh concrete cover outside ties is lost, which results in significant reduction in bond strength in 90° bent ties (dropping to half of the bond strength at that particular time) as interaction between tie legs and cover concrete is lost. Such loss in bond strength is not encountered in 135° bent ties as the legs of the ties are bent inward and embedded in to the concrete core. The drop in bond strength in HSC2 and HSC3 columns at 60 minutes into the fire exposure therefore occurs due to loss of concrete cover from fire induced spalling.

The effective force (computed by Eq 6.42) that is acting on the ties results from a combination of stresses generated from pore pressure, mechanical strain (loading) and thermal strain in fire exposed columns. Figure 6.15 illustrates the development in effective force acting on ties with fire exposure time plotted against the bond strength for columns HSC2 and HSC3, with 90° bent ties. The predicted effective force acting on ties in column HSC3 is higher than that in column

HSC2 and this is due to higher loading ratio (0.6). As a result of higher loading ratio, the effective force acting on ties in column HSC3 is higher than that in column HSC2. The analysis shows that the ties (bent at 90°) failed due to opening-up (yielding) in column HSC3 at 120 minutes into the fire exposure time and this contributed to failure of this column. On the other hand, ties did not fail in column HSC2, which can be attributed to lower mechanical stress induced from loading in column HSC2.

Figure 6.16 illustrates the effective force on ties and resisting bond strength in 135° bent ties for columns HSC5 and HSC6. Both of these columns had 135° bent ties and therefore exhibited similar bond strength degradation in ties. However, as column HSC6 was subjected to higher load ratio (0.6), the predicted effective tie force induced in column HSC6 was higher than that in column HSC5. Although fire induced spalling was assumed in HSC5 and HSC6 columns at 60 minutes into the fire exposure, the predicted bond strength in ties was not lost as that in 90° bent ties, this shows clear advantage of bending ties at 135° into concrete core over conventional 90° bent ties. As a result of higher bond strength in 135° bent ties, the fire resistance of columns HSC5 and HSC6 was significantly increased.

The results from fire resistance analysis show that the model predictions, based on high temperature material properties and tie configuration sub-model, are in good agreement with experimentally measured fire resistance values for the six HPC columns. Similar to the observations in the tests, no failure was predicted in ties for column FAC-P. For the remaining five columns (FAC, HSC2, HSC3, HSC5, HSC6) the predicted fire resistance values compared well with the measured ones as shown in Table 6.1.

6.7 Summary

A macroscopic finite element model was extended to take in to account high temperature properties for HPC (plain and with different fiber combinations) and effect of tie configuration on fire response of RC columns. For this purpose a tie configuration sub-model was developed based on principles used in seismic design. The effective stress resulting from fire induced pore pressure, mechanical loading and thermal effects is evaluated and the effective force acting on tie is computed and compared against the developed tie-concrete interface bond strength with fire exposure time. The extended model is validated against fire test data on HPC columns, and it shows that predictions from the model are in good agreement with test data from experiments. Based on these validation studies, it is concluded that the capability of macroscopic finite element model is enhanced for predicting the fire response of RC columns with incorporation of “high temperature properties of HPC” and “tie-sub model” subroutines.

Table 6.1 - Parameters and results for RC columns tested at MSU used in the temperature and structural response validation study

S No	Column designation	Size (mm)	Fire scenario	Tie configuration	Concrete strength Test day (MPa)	Column strength (kN)	Load ratio (%)	Applied load (kN)	Relative humidity (%)	Fire resistance measured	Fire resistance predicted	Ties failure
1	**FAC**	203	ASTM E119 & EC decay @4.16°C/ min	135°@h	107	2144	0.4	858	90	165	156	No
2	**FAC-P**	203	ASTM E119 & EC decay @4.16°C/ min	135°@h	100	2020	0.4	808	90.25	NF*	270	No
3	**HSC2**	406	ASTM E119	90°@h	86	5900	0.4	2406	86	224	213	No
4	**HSC3**	406	ASTM E119	90°@h	96	7400	0.6	4450	57	104	120	Yes
5	**HSC5**	305	ASTM E119	135°@h/4	120	3145	0.4	1250	68	290	282	No
6	**HSC6**	305	ASTM E119	135°@h/4	120	3145	0.6	1890	64	266	254	No

*No failure

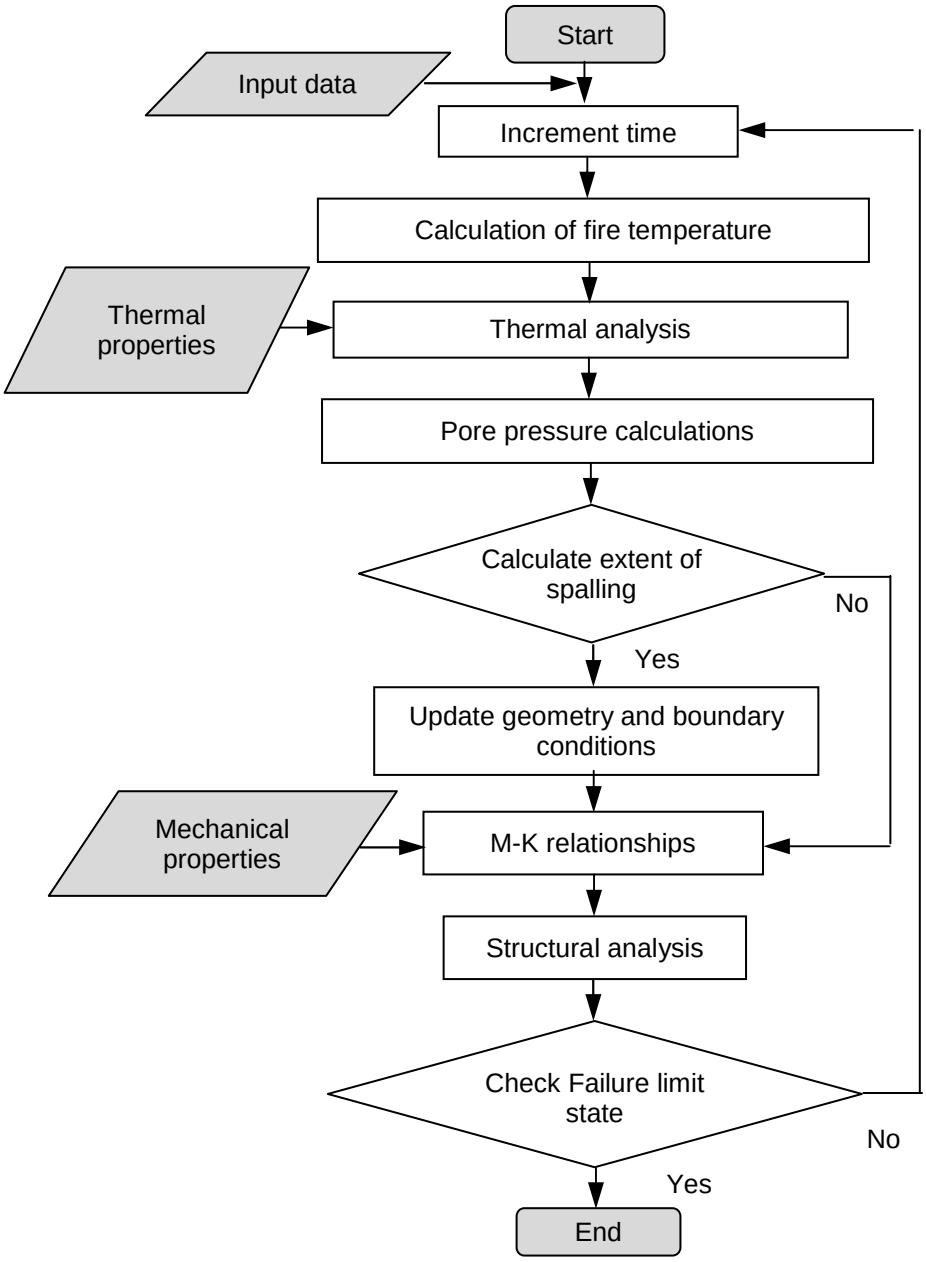

Figure 6.1 - Flowchart showing the steps associated with analysis of fire exposed RC column

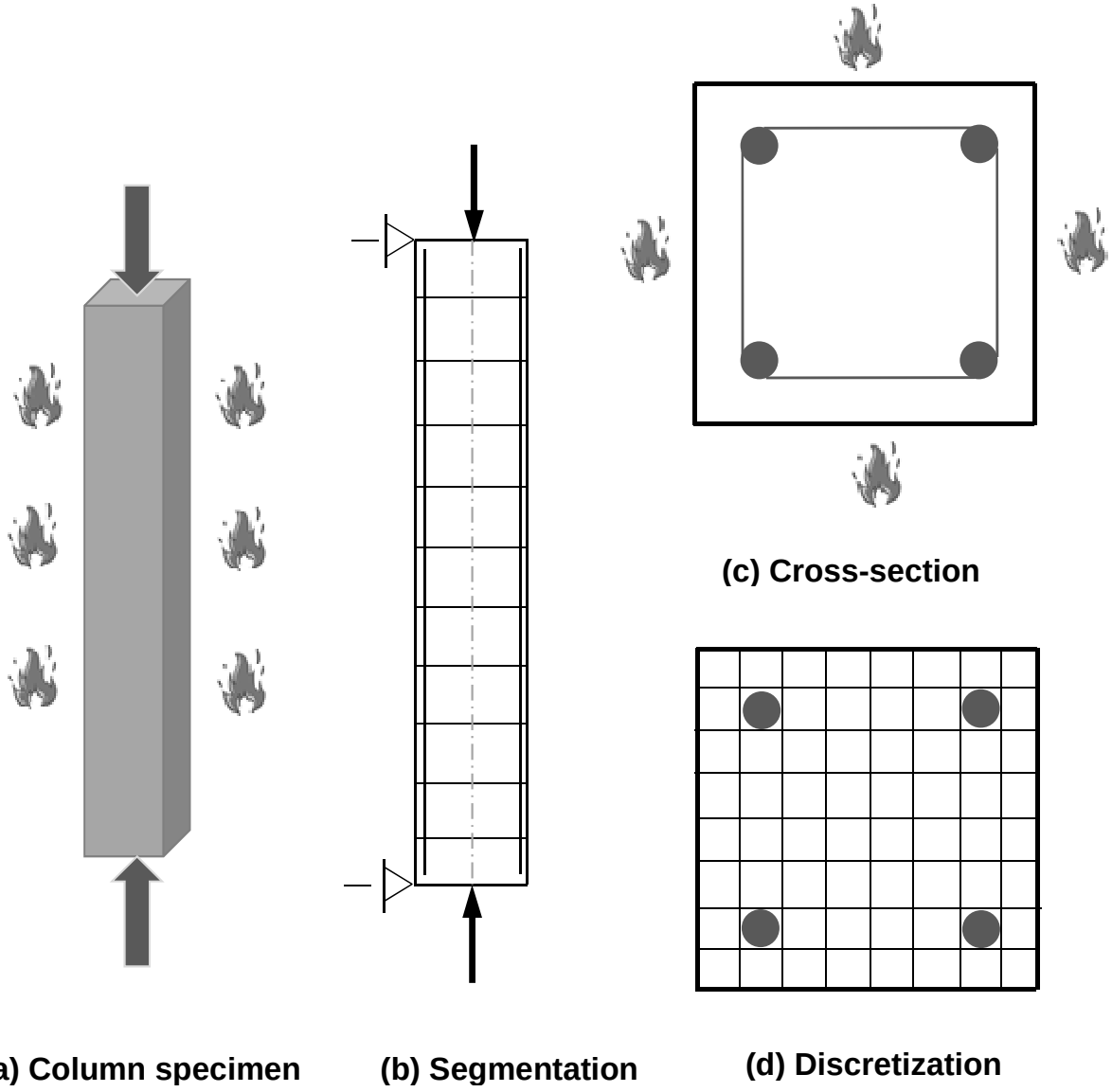

Figure 6.2 - Layout of idealized RC column and discretization of its cross-section for fire resistance analysis

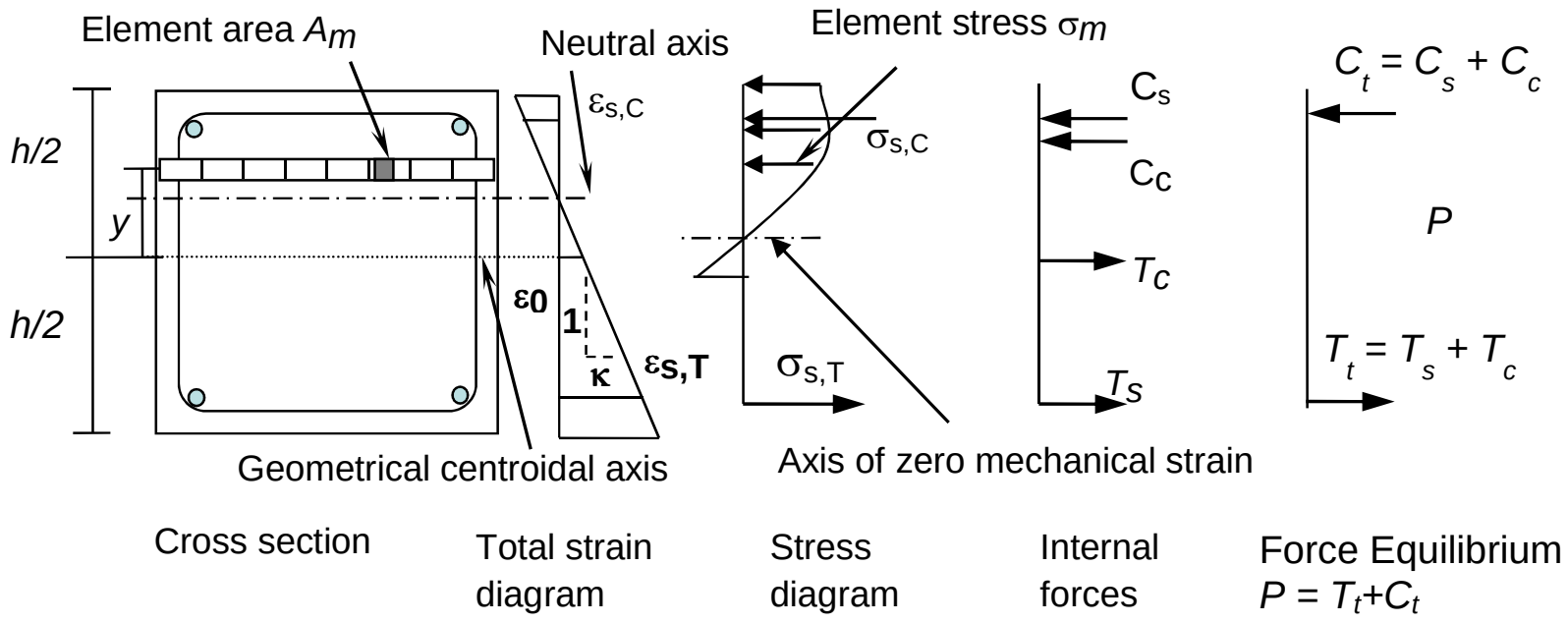

Figure 6.3 - Variation of strain, stress and internal forces in a cross-section of fire exposed RC column

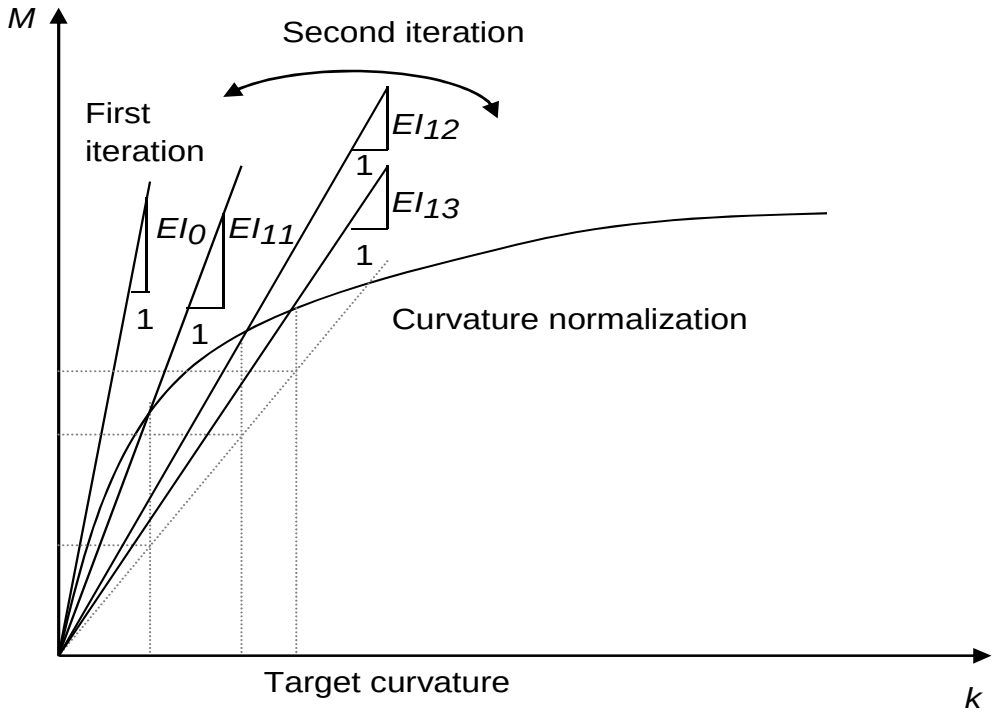

(a) Moment curvature curve for a column segment

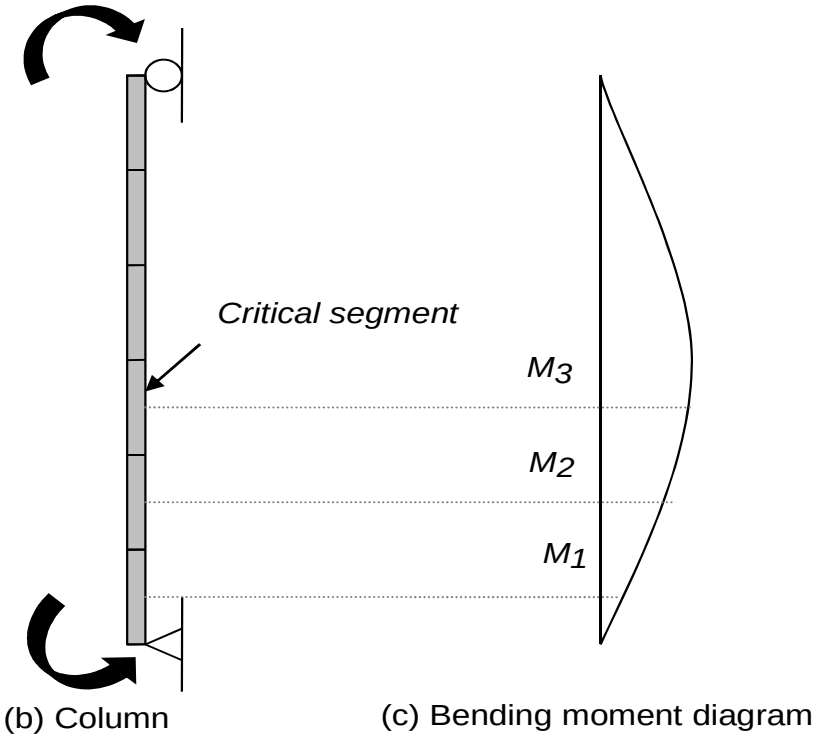

(b) Column (c) Bending moment diagram

Figure 6.4 - Illustration of Curvature Controlled Iterative Procedure used for Structural Analysis

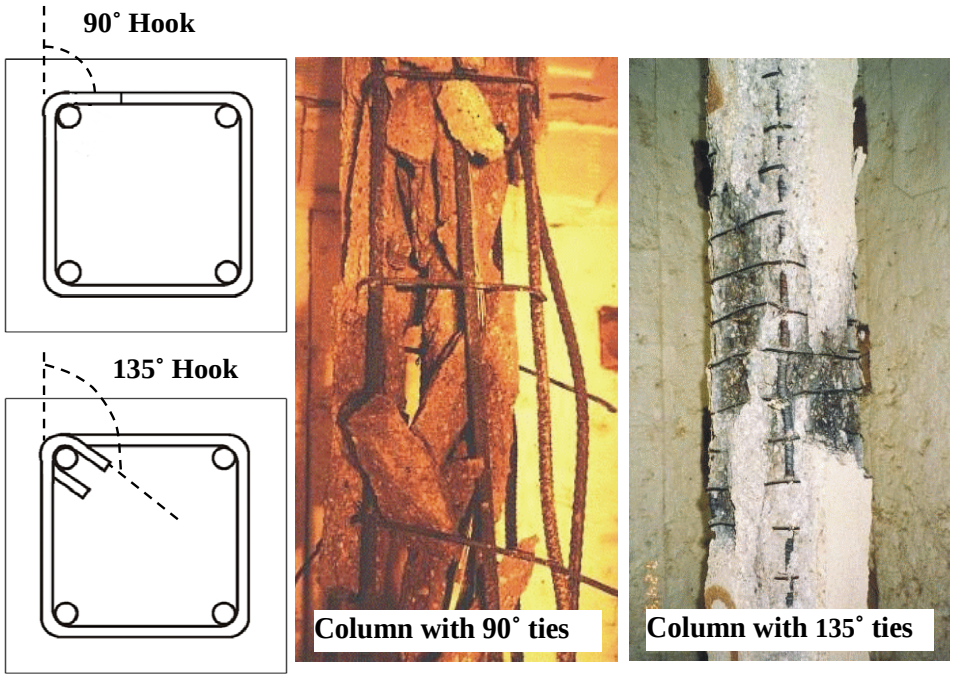

(a) Tie configuration (b) HSC columns after fire tests

Figure 6.5 - Comparison of fire performance of RC columns with conventional 90° ties and modified 135° ties

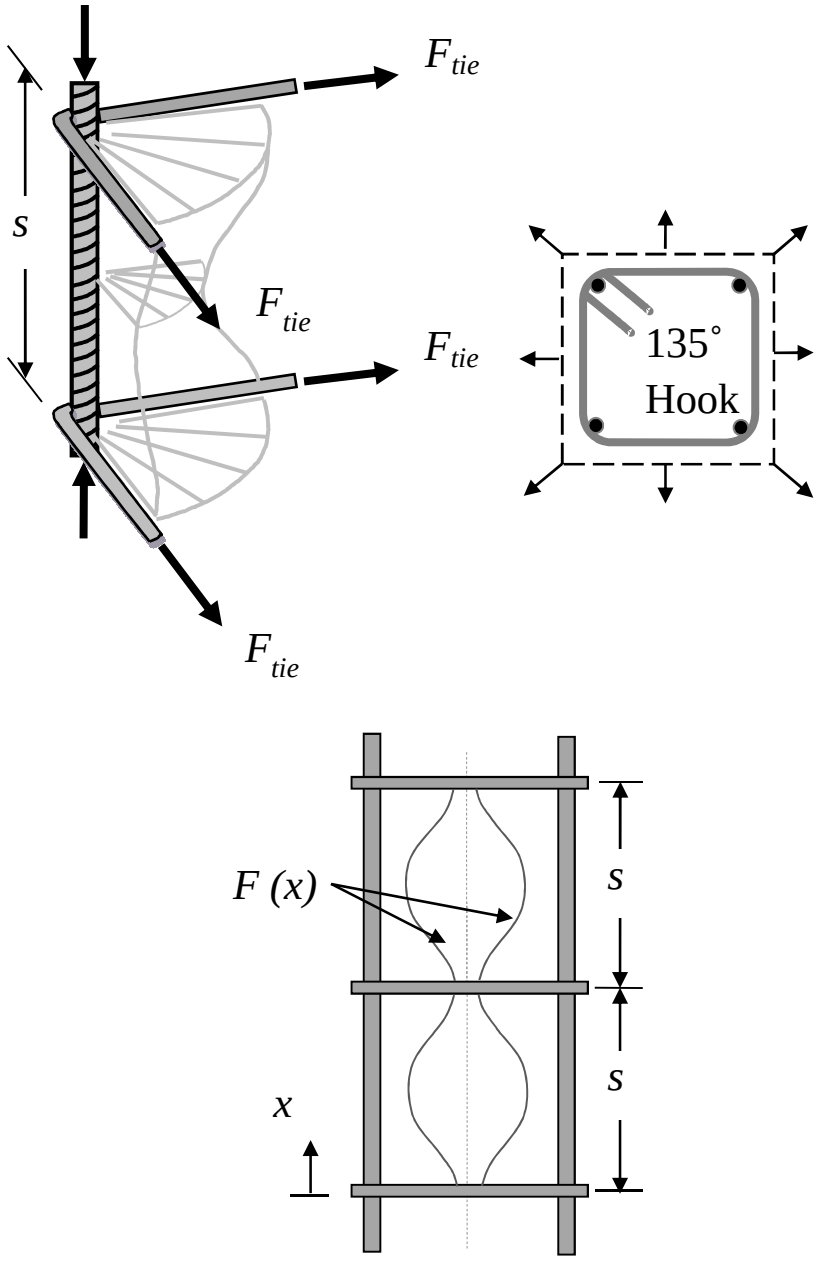

(a) Free body diagram of lateral and longitudinal reinforcement in an RC column

Figure 6.6 - Longitudinal rebar and transverse tie model and assumed forces

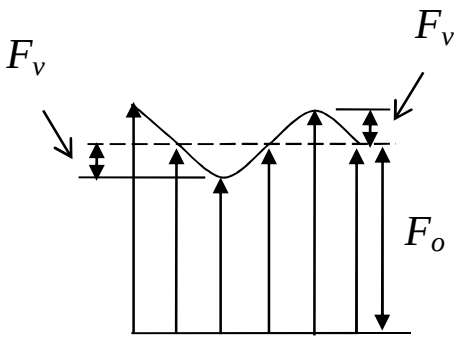

(b) Assumed force distribution in ties and longitudinal bars

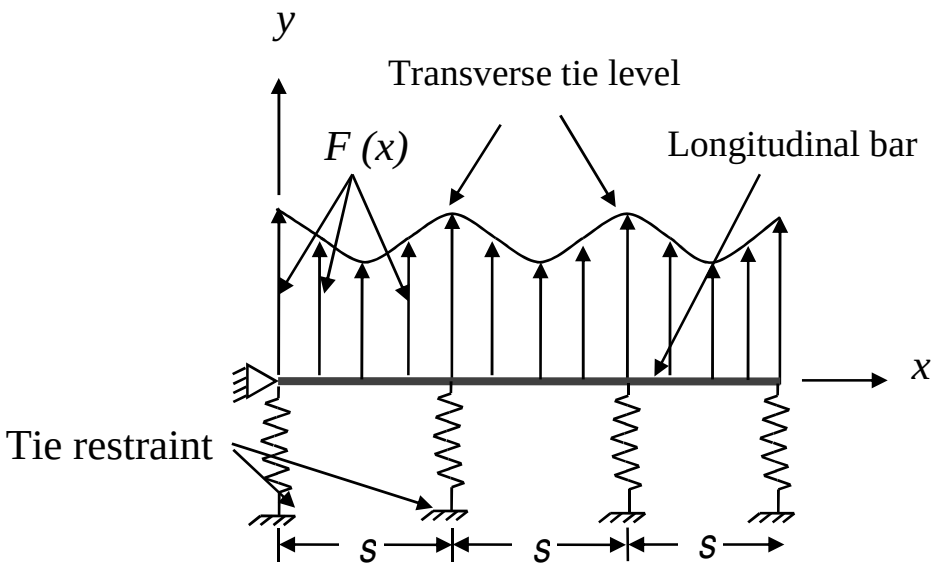

(c) The model for ties and longitudinal bar

Figure 6.6 - (cont'd) Longitudinal rebar and transverse tie model and assumed forces

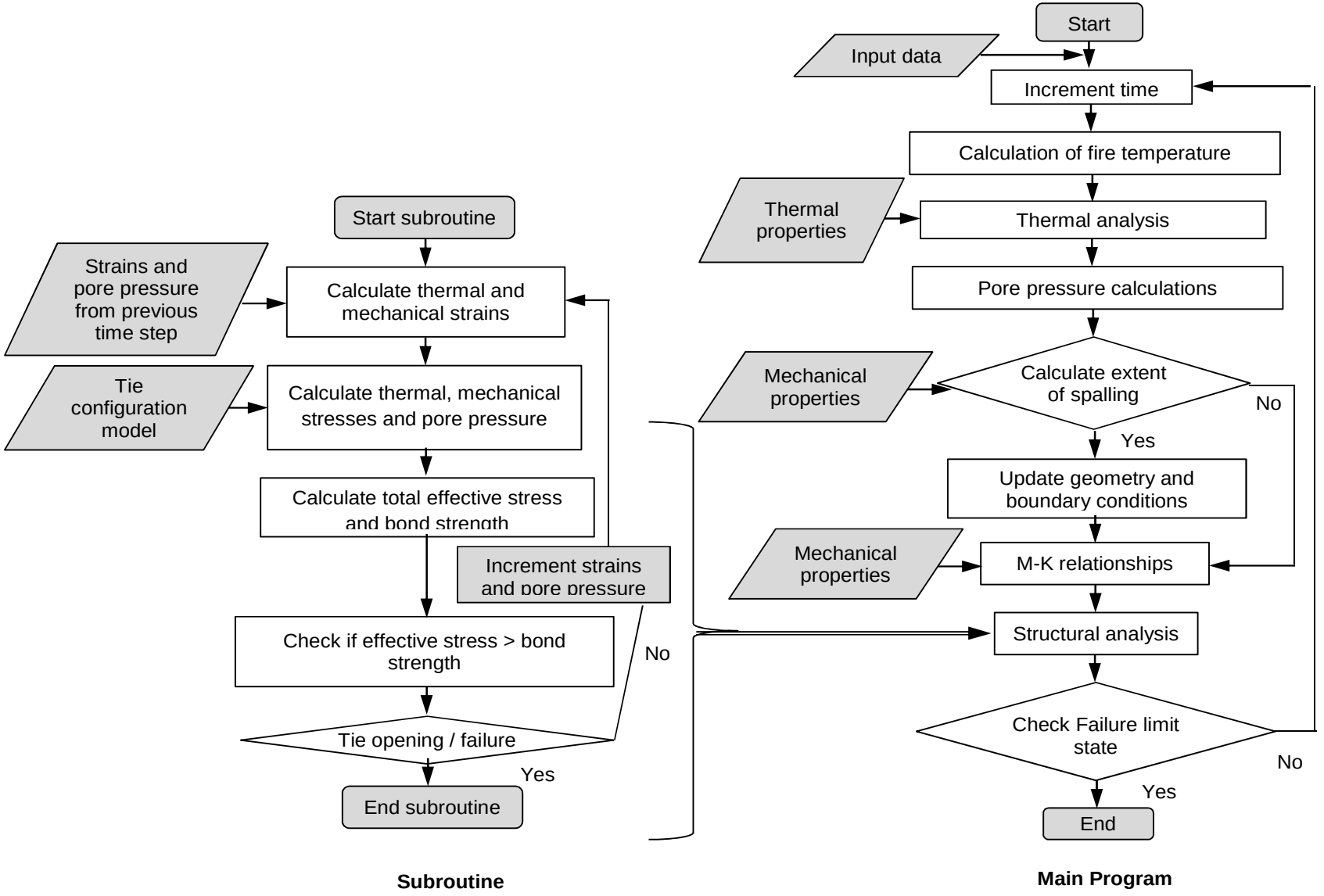

Figure 6.7 - Flowchart showing steps to calculate forces in tie configuration subroutine

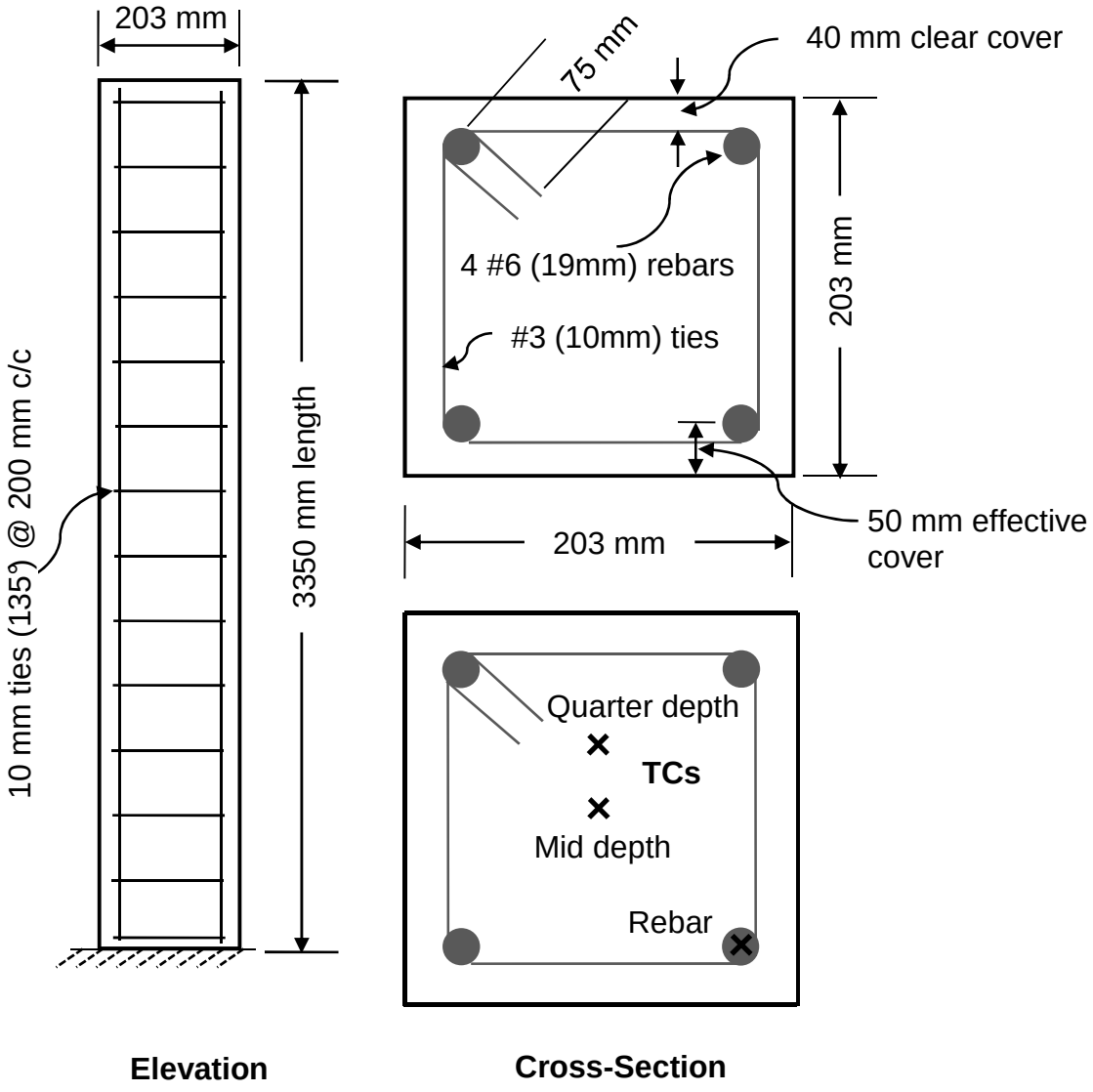

Figure 6.8 - Physical details and location of thermocouples for columns FAC and FAC-P

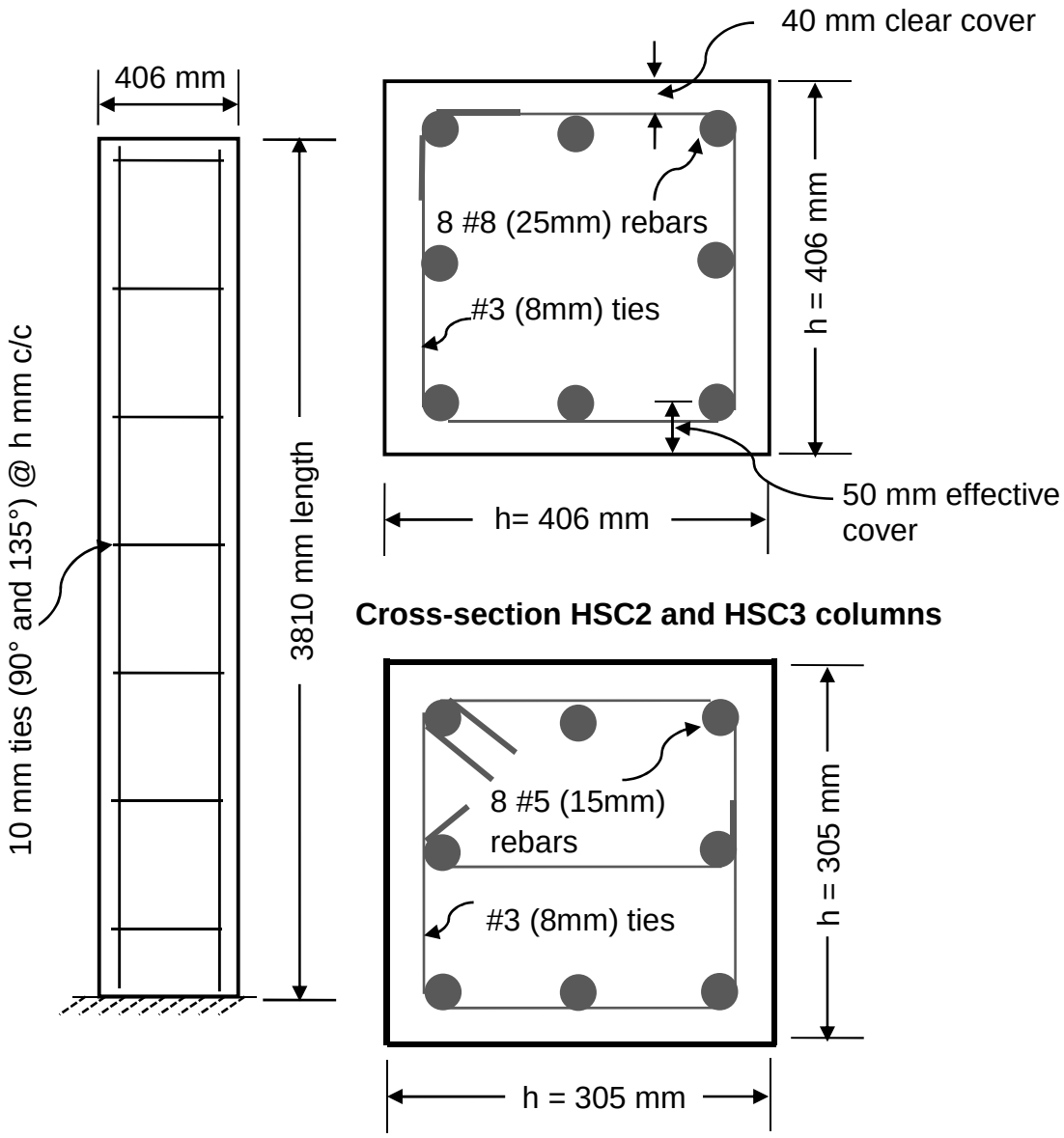

Figure 6.9 - Physical details and location of thermocouples for columns HSC2, HSC3, HSC5 and HSC6

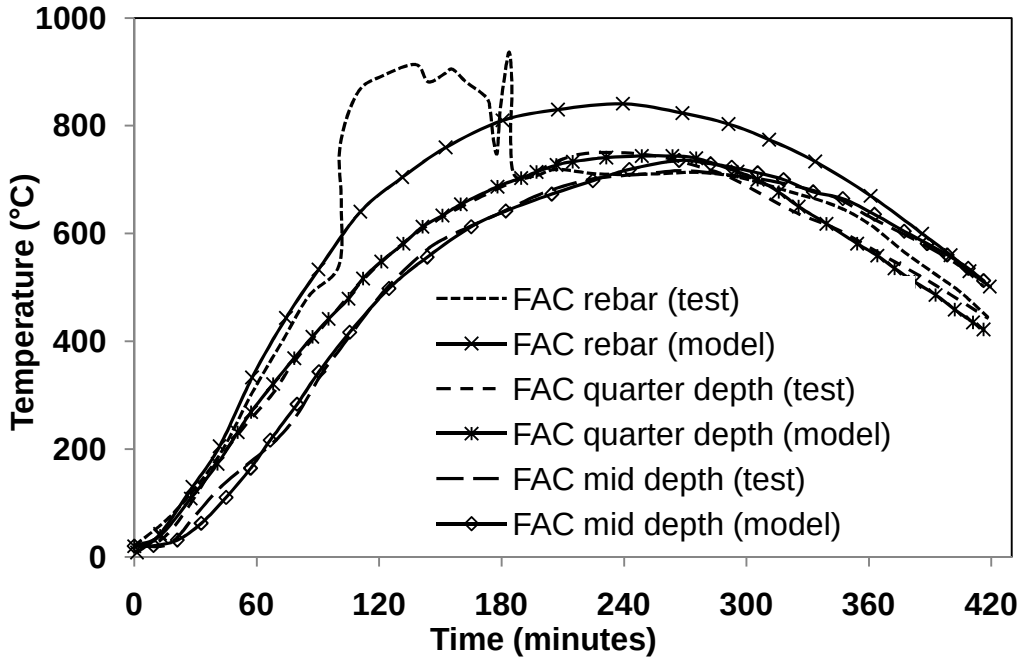

Figure 6.10 - Comparison of measured and predicted temperatures in FAC column

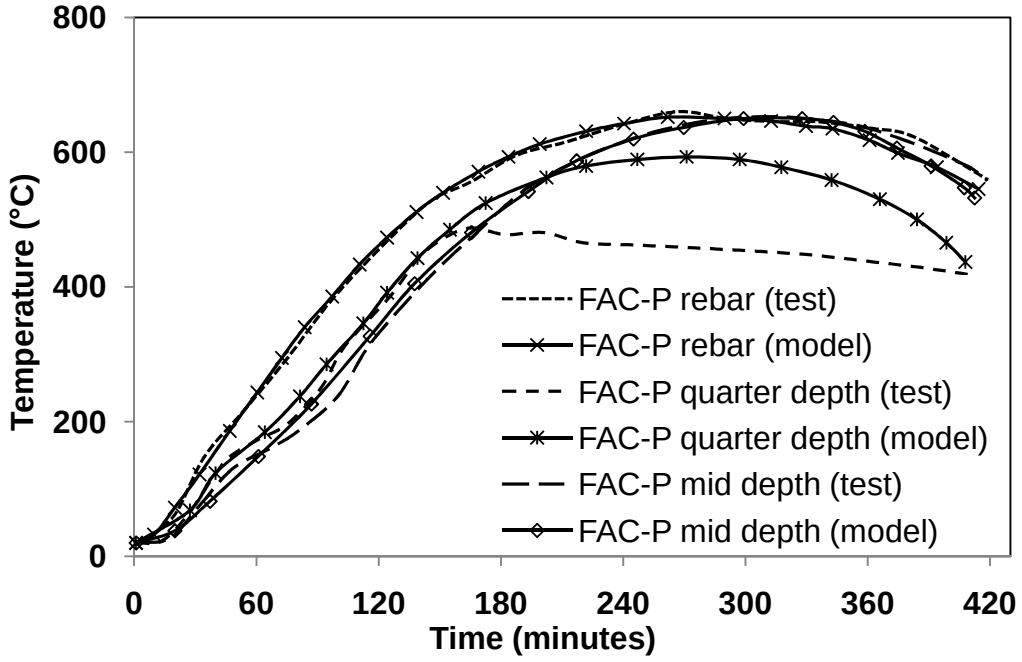

Figure 6.11 - Comparison of measured and predicted temperatures in FAC-P column

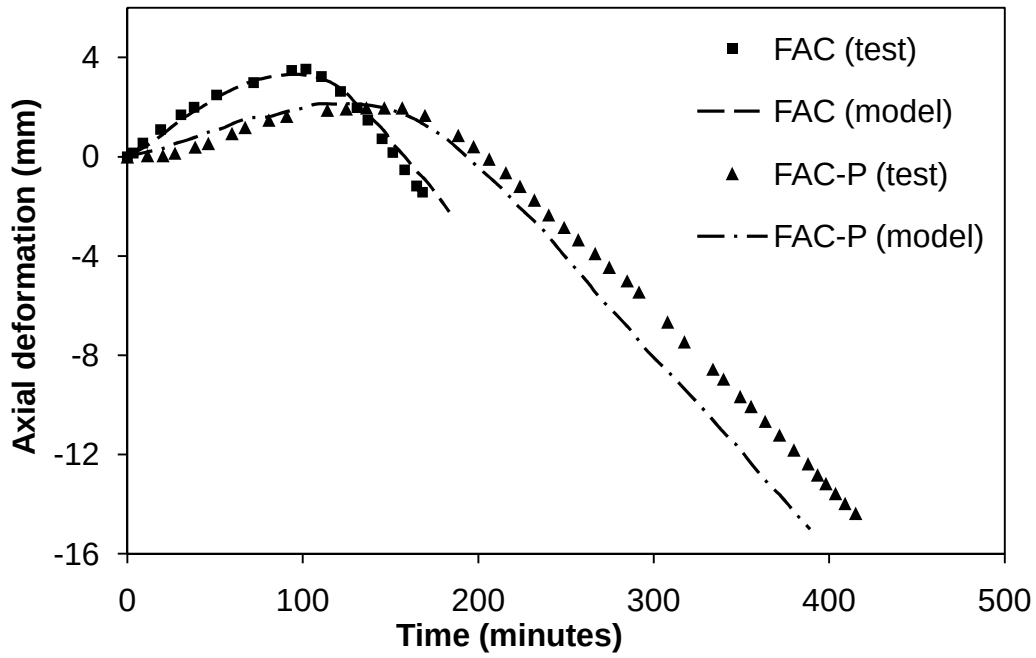

Figure 6.12 - Comparison of measured and predicted axial deformations in FAC, FAC-P columns

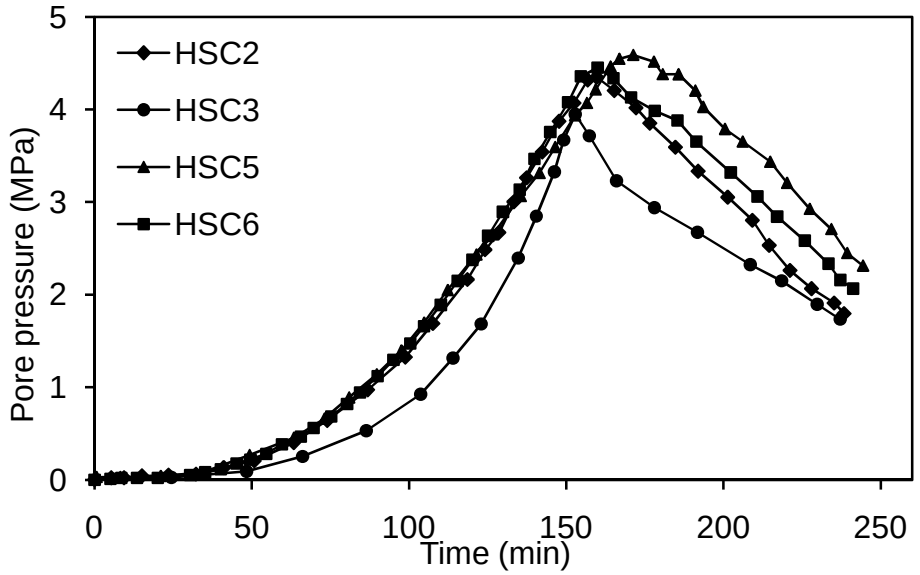

Figure 6.13 - Predicted pore pressure at cover depth HSC2, HSC3, HSC5, and HSC6 columns

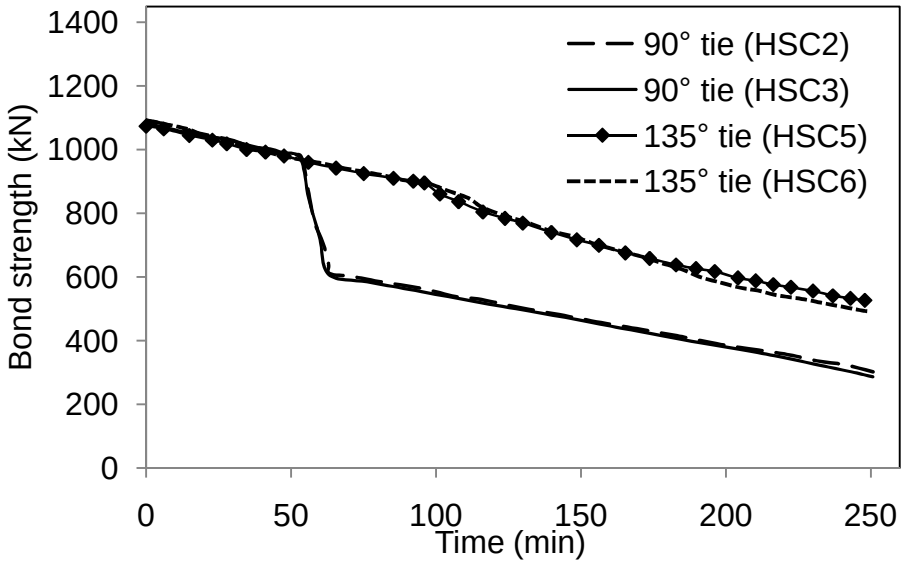

Figure 6.14 - Predicted bond strength offered by various ties in selected columns

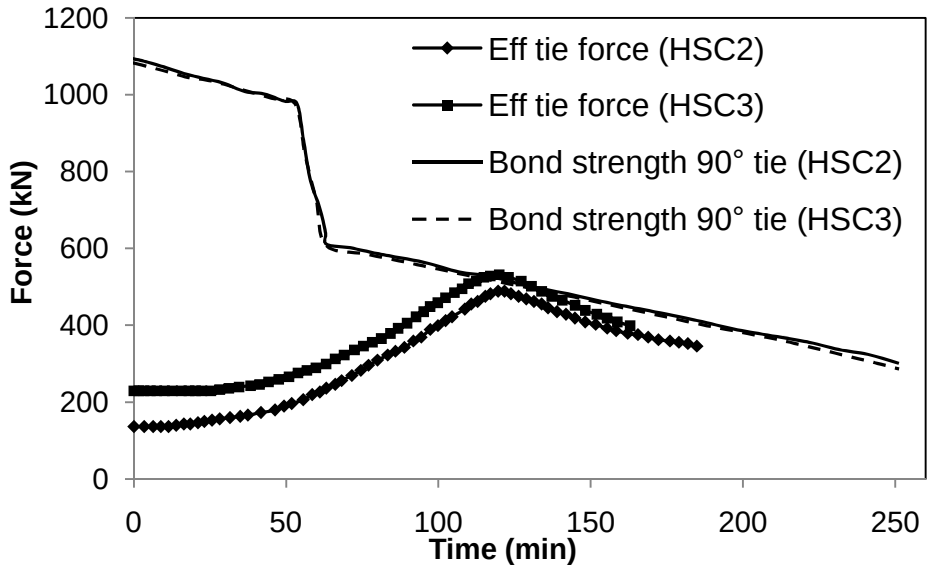

Figure 6.15 - Predicted effective tie force compared to bond strength in 90° tie in NSC, HSC1 and HSC2 columns

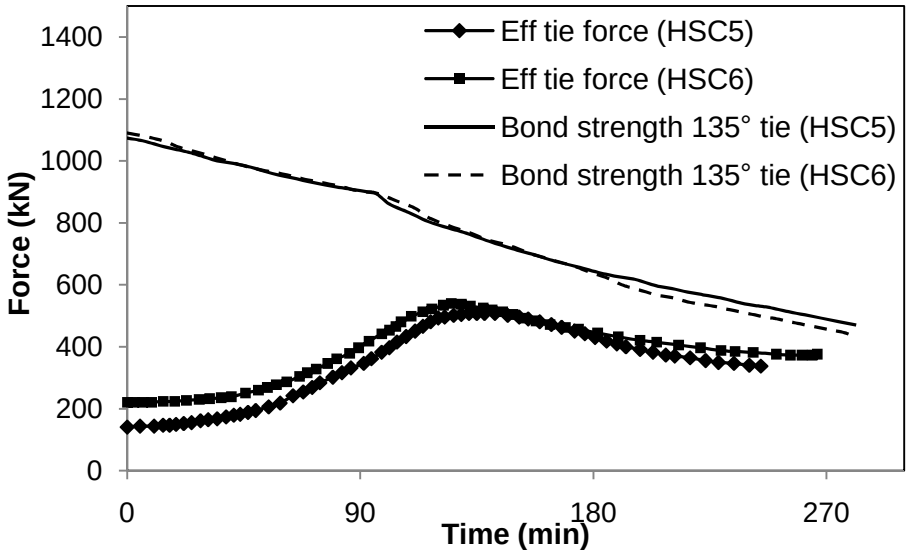

Figure 6.16 - Predicted effective tie force compared to bond strength in 135° tie in HSC3 and HSC4

CHAPTER 7

7 PARAMETRIC STUDIES

This chapter is mainly based on the following conference presentation and paper:

- Khaliq, W., Raut, N. K., and Kodur, V. K. R. (2011). "Effect of tie configuration on fire performance of high strength concrete columns." Proc., Conference presentation, ACI Fall 2011Conference.
- Khaliq, W. and Kodur, V. K. R. (2012). "Effect of tie configuration on fire performance of high strength concrete columns." SiF 2012 Conference at Zurich, Switzerland.

7.1 General

Fire response of reinforced concrete columns, as discussed in Chapter 2, is influenced by numerous of factors. Many of these influencing factors are interdependent and this makes fire resistance predictions of RC columns quite complex. The effects of many of these factors on fire response of RC columns are quantified in previous studies. However, the effect of tie configuration on fire performance of HPC columns is not quantified. Further there is no information on the extent of influence of specific high temperature properties of HPC on fire resistance of HPC columns. To evaluate the effect of tie configuration and specific properties of HPC on fire resistance of HPC columns, parametric studies are carried out in this chapter. The fire resistance analysis is carried out utilizing the numerical model presented in Chapter 6. Also the usefulness of numerical model in evaluating fire response of RC columns with different types of HPC and tie configurations is demonstrated in this Chapter.

7.2 Factors influencing Fire Resistance

There are several factors that influence the fire response of RC columns. These factors have been well studied through qualitative parametric studies (Ali et al., 2001; Kodur, 2003; Lie and Woolerton, 1988; Raut, 2011). The main factors that have been quantified consist of:

- Fire scenario
- Size (cross-section) of column
- Concrete cover thickness
- Aggregate type
- Load ratio
- Reinforcement ratio
- Load eccentricity (uniaxial and biaxial)
- Fire exposure scenarios (1-, 2-, 3-, or 4-sides)
- Concrete strength (or permeability)

However, the factors that influence the fire response of HPC columns and that have not been studied include:

- Effect of specific concrete type (HPC)
- Effect of tie configuration (90° and 135° bent ties)

The effect of tie configuration (90° of 135°) on fire performance of RC columns is studied previously through limited fire tests. However, there is no numerical approach to explain the effect of tie configuration through principles of mechanics. Similarly, for fire resistance predictions of the RC columns made of HPC, high temperature thermal and mechanical properties specific to concrete type are to be incorporated in numerical models. The effect of

these factors on fire response of RC columns has been investigated as part of parametric studies described below.

7.3 Parametric Studies

To generate data on the effect of tie configuration and high temperature material properties of HPC (with and without fibers), fire resistance analyses are carried out by varying these parameters in the practical range. Results from parametric studies are utilized to quantify the effect of permeability (strength), effect of load ratio, use of fibers, and columns size on fire response of RC columns based on different tie configurations.

7.3.1 Selection of RC Columns

For the fire resistance analysis, RC columns with square cross-section were selected and the strength (permeability), high temperature properties of concrete, tie configuration, load ratio, and type of fibers were varied within a pre-defined range. The elevation and cross-sectional details of the selected columns are shown in Figure 7.1. The columns were designed as per ACI 318 (2008) specifications with regards to size, reinforcement ratio, and cover thickness. For each column, two tie configurations of 90° and 135° were assumed. For the analysis, the columns were assumed to be fixed at both ends. High temperature property relations comprising of thermal properties (thermal conductivity, specific heat, thermal expansion and mass loss) as proposed in Chapter 3 and mechanical properties (compressive strength, splitting tensile strength, and elastic modulus) as proposed in Chapter 4 were used specific to HPC type. High temperature properties for reinforcing steel followed the relations given in ASCE manual (1992).

7.3.2 Range of Parameters

The ranges of parameters varied for analysis include:

- Three permeability values based on NSC and HPC (plain and with polypropylene fibers) by changing three permeability coefficients 10^{-16}, 10^{-17} and 10^{-18}.
- Two types of tie configuration (90° and 135°) with two tie sizes (#3 (10 mm) and #4 (13 mm))
- Five load ratios (30%, 40%, 50%, 60%, 70%)
- Three types of fibers (steel, polypropylene, and hybrid)
- Three column sizes (305mm, 406 mm and 610 mm)

7.3.3 Analysis Procedure

The fire resistance analyses of RC columns were carried out using the extended MFE model at one minute time increments. For the analysis, the column was divided into 40 equal segments along its length. As the curvature variation along the length of the column depends on the length and number of the segments, it was reported by Raut (2011) that 40 segments along column length gave optimized results. Each column segment (represented by central section) was then discretized into quadrilateral elements of 10 mm size for the analysis. The discretization and analysis procedure is similar to that adopted in the validation of the model, which is presented in detail in Chapter 6. The columns were exposed to ASTM E119 standard fire scenario (ASTM E119-08b, 2008). Based on spalling information from literature on HSC (Dwaikat and Kodur, 2010; Yu et al., 2011), concrete cover of the columns was assumed to be lost due to occurrence of fire induced spalling up to 60 minutes in to the fire exposure in plain HPC columns (HSC, SCC, and FAC). The cross-sectional temperatures, pore pressure, mechanical stress due to loading, thermal stress due to thermal effects, effective force on ties, and bond strength were evaluated at every time step in fire resistance calculations. The fire resistance of the columns was evaluated based on the failure of ties and strength failure limit state.

7.4 Results from Parametric Studies

Results from fire resistance analyses are presented in Tables 7.1 to 7.3 and in Figures 7.2 to 7.9. The main factors that are studied are the effect of tie configuration (90° and 135°) and the effect of high temperature properties of HPC on fire response of HPC columns. Other factors that influence the effective force acting on ties, such as concrete strength (permeability), load ratio, and use of fibers are also included in the parametric studies. The effect of various parameters on fire response of RC columns is discussed below.

7.4.1 Effect of Permeability (Strength)

The strength in HPC is achieved through application of mineral and chemical admixtures that consume the calcium hydroxide ($CaOH_2$) which is produced in concrete matrix through process of hydration. $CaOH_2$ is a weak link in concrete and with addition of mineral admixtures such as silica fume, flay ash and slag (silicates in nature), these react with $CaOH_2$ over time to convert it to primary binding cement gel, calcium silicate hydrate (C-S-H). In the process, the porosity gets reduced and, very dense and impermeable microstructure of concrete develops, which imparts higher strength and durability in concrete. Therefore strength in concrete can directly be related to permeability, as higher the strength of concrete, lower is its permeability. Once exposed to higher temperatures, this impermeability in concrete hinders dissipation of fire induced pore pressure. This results in damage to dense microstructure, resulting in loss of strength and stiffness of HPC. Thus impermeability which is beneficial for durability of HPC becomes a disadvantage for HPC structural members under fire conditions.

There are generally two types of permeability associated with concrete: liquid permeability and gas permeability (Boel et al., 2008; Mindess et al., 2003; Noumowé et al., 2009). Generally, gas

permeability is mostly used as representative property for concrete due to difficulties associated for measuring liquid permeability in different HPC. Gas permeability is typically in the range of $2.4x10^{-12}$ to $6.8x10^{-16}$ for NSC and $1.5x10^{-17}$ to $2.1x10^{-18}$ for HSC (Boel et al., 2008; Dwaikat and Kodur, 2009; Kalifa et al., 2001; Noumowé et al., 2009). In parametric studies, pore pressure predictions were carried out for two initial (room temperature) permeability values of concrete: high permeability of $2x10^{-16}$ m^2 (representing NSC) and low permeability of $2x10^{-18}$ m^2 (representing HPC). These permeability values for NSC and HSC are kept constant (no variation with temperature) throughout the fire resistance analysis. However, for polypropylene fiber reinforced HPC, the initial permeability which is taken as $2x10^{-18}$ m^2 (that represents the permeability range for HPC), was increased to $2x10^{-17}$ m^2 once polypropylene fibers melted at 170°C during.

Figure 7.2 illustrates that the accumulated pore pressure is highly dependent on permeability of concrete. Results from the analysis shows that pore pressure increases with fire exposure time until it reaches a peak value and then it decreases. The increase in pore pressure can be attributed to build-up of moisture clog resulting from moisture movement inside concrete matrix. This build-up of moisture clog can lead to significantly high pore pressure during fire exposure. It can be seen from Figure 7.2 that a peak pore pressure of 4.5 MPa gets developed in HPC columns with low permeability of $2x10^{-18}$ m^2, whereas in the case of higher permeability of $2x10^{-16}$ m^2 such as for NSC, the pore pressure can be as low as 2 MPa.

High permeability of concrete in the NSC column facilitates dissipation of water vapor and thus there is lower build-up of pore pressure, whereas low permeability of concrete in HSC column, does not facilitate the escape of water vapor and resultantly, higher pore pressure gets developed

in HSC columns (Mindess et al., 2003; Noumowé et al., 2009). With medium level of permeability ($2x10^{-17}$ m^2) assumed in polypropylene fiber reinforced column HSC1, resulting from melting of polypropylene fibers around 170°C under fire conditions, it can be seen that considerable reduction in pore pressure occurs. This reduction in pore pressure is beneficial in mitigating fire induced spalling and also resulting in lower fire induced forces acting on ties.

As pore pressure is one of the primary contributors to total effective force that develops on ties, therefore higher pore pressure will result in higher effective force acting on ties in the case of columns made of HPC. This implies that a 90° bent tie with lower bond strength will have high susceptibility to failure as compared to a 135° bent tie. On the other hand lower pore pressure results in lower effective force acting on ties; therefore failure of 90° ties is not encountered in NSC and polypropylene fibers reinforced HPC columns.

7.4.2 Effect of Tie Configuration

The degradation of bond strength for two types of tie configuration (90° and 135°) for tie sizes of (#3 (10 mm) and #4 (13 mm)) is illustrated in Figure 7.3. With rise in cross-sectional temperatures, bond between tie and concrete interface degrades. Two factors that contribute to loss of bond strength are; (1) degradation in strength of ties (steel) with rise in temperature of steel (ties) and (2) occurrence of fire induced spalling in concrete surrounding the ties. To account for occurrence of fire induced spalling in plain HPC column, it is assumed that outer concrete cover is lost and there is no tie-concrete interface at outer side of tie legs. In such a scenario, the loss of concrete cover significantly affects the bond at tie-concrete interface and thus bond strength is reduced.

Results shown in Figure 7.3 illustrate degradation of bond strength (at steel-concrete interface) in RC columns with 90° and 135° bent ties as a function of fire exposure time. It can be seen that a

significant drop in bond strength occurs in 90° bent ties, at about 60 minutes, which results from high temperatures developing in ties due to direct heating from fire (due to spalling off of concrete cover) and loss of tie-concrete interface. As a result the bond strength reduces to half of its original value. Such loss in bond strength is not encountered in 135° bent ties as the legs of the ties are bent inward and embedded in to the concrete core and spalling outside the core do not affect the bond between tie ends and concrete. This also helps in keeping the fire induced spalling to outside of steel cage (concrete core) and mitigates further loss of cross-section (concrete) in HPC columns. Increasing the size of the tie from #3 to #4 enhances the bond strength of ties throughout fire exposure time; however, the variation in the loss of bond strength with fire exposure time is similar to that in #3 ties. Even in the case of #4 ties, higher loss of bond strength is encountered in 90° bent ties as compared to 135° bent ties.

Figure 7.4 illustrates the development of effective force acting on ties in an HSC column as a function of fire exposure time. Also plotted in this graph is the degrading bond strength as a function of time for 90° and 135° bent ties. It can be seen that the force acting on the ties increases with fire exposure time and this is due to increase in resulting pore pressure. On the other hand, strength and stiffness properties of HSC column also degrade with temperature, which result in higher stresses due to applied loading. All the three fire induced stresses (pore pressure, applied loading, and thermal effects) combined together act as effective stress (σ_{core}) on ties. From this stress (σ_{core}), effective force acting on tie is evaluated using Eq 6.42. It can be seen in Figure 7.4 that effective fore in tie increases from 230 kN at the start of the run to about 532 kN in 120 minutes thus taking over degrading bond strength of 90° ties at 120 minutes. This leads to failure of 90° ties, whereas bond strength in 135° ties remains much higher than the effective force on the tie and thus no failure occurs in 135° ties.

Figure 7.5 illustrates the development of effective force in 90° and 135° bent ties in NSC column as a function of temperature. Because of continuous dissipation of pore pressure in NSC column, the effective force acting on tie remains much lower and the bond strength that is degrading in the case of 90° ties does not fall below the effective tie force. Therefore no failure of ties occurs in NSC column even with provision of 90° bent ties. This leads to the conclusion that provision of 90° and 135° bent ties will not make any difference in NSC columns under fire conditions.

7.4.3 Effect of Load Ratio (Level)

The effective force that is acting on ties of an RC column arises from a combination of three stresses namely fire induced pore pressure, applied loading and temperature induced thermal strain (from thermal effects). Depending on the load level, the mechanical stress from loading can be significant component of effective stress acting on the ties. These stresses tend to increase tremendously under fire conditions due to degradation of mechanical (strength) properties of HPC column and this leads to significant increase in the effective force acting on ties. Figure 7.6 illustrates the development of effective force on ties as a function of fire exposure time in 305 mm size HPC columns (HSC1 to HSC5) under different load ratios of 0.3 to 0.7.

For comparison purpose, bond strength developed in columns with 90° and 135° bent ties is also plotted as a function of fire exposure time in Figure 7.6. For 10% rise in load ratio, there is 15-25% increase in peak effective force acting on ties. This shows stress from loading is a major contributor to effective force on ties (next only to that from pore pressure). It can be seen from the Figure 7.6 that, even at lower load ratio of 0.4 (in column HSC2), failure of ties can result in columns with 90° ties. Conversely, in column (HSC3) with 135° bent ties no failure of ties occurs for load levels up to 0.5 (load ratio), however, in the case of columns with 135° bent ties, the ties fail by yielding/opening up under higher applied load ratios of 0.6 (column HSC4) and

0.7 (column HSC5). The predictions show that with each 10% increase in load ratio, the fire resistance of HPC columns is reduced by an average of 25 minutes for columns provided with 135° ties.

Fire resistance of HPC columns (HSC1 to HSC5) under five load ratios (load levels) are tabulated in Table 7.1. It can be seen that HSC columns with 90° bent ties can fail under lower load ratio of 0.4. However, HSC columns provided with 135° bent ties can survive without failure of ties till load ratio reaches 0.5. It can be seen that at 0.6 load ratio (60% load level) in column HSC4, the fire resistance is 90 minutes and 126 minutes with 90° and 135° bend ties respectively. It shows that in plain HPC columns, an improvement of about 35 minutes in fire resistance can be achieved just by bending ties at 135°.

7.4.4 Effect of fibers

The presence of fibers can influence both thermal and structural response of HPC columns under fire conditions. To illustrate this influence, ten HPC columns (with and without fibers) were analyzed and the results of analysis are tabulated in Table 7.2. For illustrating thermal response, cross-sectional temperatures at two locations (quarter depth and mid depth) are plotted in Figures 7.7 and 7.8 for HSC and FAC columns (plain and with different fiber combinations). Further to illustrate the influence of fibers on pore pressure development in HSC and FAC columns (plain and with different fiber combinations), pore pressure is plotted in Figure 7.9. Table 7.2 shows the fire resistance predictions for these ten HPC columns made of three HPC types (HSC, SCC and FAC) with different fiber combinations.

It can be seen from figures 7.7 and 7.8 that type of fibers has an effect on the resulting temperature profiles in the column cross-section. The predicted temperatures are lower for fiber reinforced concrete as compared to plain form of that specific concrete (HSC, SCC, or FAC).

This can be attributed to the thermal conductivity and specific heat properties of different HPC types (plain and with fibers). The temperatures in the case of polypropylene and hybrid fibers reinforced HPC are about 25-40°C lower than those in plain HPC columns throughout the fire exposure time. This lowering of temperatures decreases pore pressure built up in the columns. The lower temperature development leads to lower effective force acting on ties, thus an enhancement of about 30 minutes is attained in fiber reinforced HPC columns.

It can be seen from Table 7.2 that the fire resistance of fiber reinforced HSC-P and HSC-H columns increased to 218 and 230 minutes respectively as compared to 192 minutes for plain HSC column. Similar improvement of about 30 minutes in fiber reinforced FAC and SCC columns is observed in Table 7.2. Addition of steel fibers in the concrete mix also increase the fire resistance of HPC columns to an average of 20 minutes which can be attributed to slower degradation of tensile strength with temperature in steel fiber reinforced HPC.

Figure 7.9 illustrates development of pore pressure in fiber reinforced HPC columns (steel, polypropylene, or hybrid fibers) as a function of fire exposure time. Significant reduction in pore pressure occurs in polypropylene fiber reinforced HSC and FAC columns due to melting of polypropylene fibers. The pore pressure drops from 5 MPs to about 3MPa in polypropylene and hybrid fiber reinforced HSC and FAC columns. Pore pressure development in steel fiber reinforced HSC column is similar to plain HPC column. However, slower degradation of tensile strength in steel and hybrid fiber reinforced columns (HSC-S, HSC-H, SCC-S and SCC-H), leads to higher fire resistance as shown in Table 7.2.

7.4.5 Effect of Column Size

To study the effect of pore pressure and effective tie force development in different column sizes, three square columns namely HSC1, HSC2 and HSC3 (size 305 mm, 406 mm, and 610

mm) were analyzed. The elevation and cross-section details (properties of the section) of these columns are given in Figure 7.1. The columns were analyzed under 90° and 135° tie configuration and fire resistance analysis was carried out by exposing these columns to ASTM E119 standard fire and subjecting them to axial load equivalent to 40% and 60% of their ultimate capacity. Table 7.3 shows the design parameters and predicted fire resistance of the three different size columns.

From Table 7.3 it can be seen that column HSC3 with 610 mm size and 0.4 load ratio, has the highest fire resistance of 297 minutes among three columns based on strength failure criteria as no tie failure occurred in these columns. On the other hand, columns HSC2 (406 mm sides) and column HSC1 (305 mm sides) under 0.4 load ratio exhibited a fire resistance of 231 and 192minutes respectively. These results indicate fire resistance increases with increase in cross-sectional size of the column. Further no tie failure occurred when the load ratio was 0.4. This is as expected since larger mass of concrete acts as a heat sink and thus the overall temperature rise within the column is lower in large size columns. However, when the above three columns (HSC1, HSC2, and HSC3) were analyzed under higher load ratio of 0.6, failure of columns HSC1 and HSC2 occurs through the failure of 90° ties at 159 and 188 minutes. However, in the case of HSC3 column (610 mm sides) under 0.6 load ratio, no failure of ties (90° bent ties) occurs and this column exhibits fire resistance of 270 minutes. This trend of increasing fire resistance with increasing column size is well established in literature (Raut, 2011).

Figure 7.10 illustrates the development of pore pressure at 40 mm concrete depth in columns HSC1, HSC2, and HSC3. It can be seen that there is no substantial difference in pore pressure built-up in all three HPC columns with different cross-sectional sizes (305 mm, 406 mm, and

610 mm). As the model predicts the pore pressure at a predetermined concrete depth in column; the build-up of pore pressure remains independent of column size.

7.5 Summary

Results of fire resistance analyses is presented to discuss the effect of tie configuration (90° and 135°) on the fire response of HPC columns. Based on the trends, it is evident that concrete permeability has significant influence on pore pressure development under fire conditions, as lower permeability (as in HPC columns) leads higher pore pressure development. A higher pore pressure results in increased effective force on ties. Bond strength of ties (tie-concrete interface) is not lost in 135° bent ties on occurrence of fire induced spalling. Load ratio also has significant effect on failure/yielding of ties, since higher load ratio leads to higher effective force acting on ties. Presence of steel, polypropylene, or hybrid fibers enhances fire resistance of HPC columns in two ways; by mitigation of fire induced spalling and by slower degradation of tensile strength in HPC. Increase in column size leads to increased fire resistance of HPC columns with no influence on pore pressure development in HPC columns.

Table 7.1 - Results for HPC columns with different load ratios

Column designation	Concrete type	Size (mm)	Column strength (kN)	Load ratio (%)	Applied load (kN)	Fire resistance predicted		Failure of ties	
						90°	135°	90°	135°
HSC1	HSC	305	1636	0.3	490	NF	NF*	No	No
HSC2	HSC	305	1636	0.4	655	117	NF*	Yes	No
HSC3	HSC	305	1636	0.5	818	101	NF*	Yes	No
HSC4	HSC	305	1636	0.6	980	90	126	Yes	Yes
HSC5	HSC	305	1636	0.7	1145	80	111	Yes	Yes

NF* - no failure

Table 7.2 - Results for HPC columns with different fiber combinations

Column designation	Concrete type	Size (mm)	Concrete strength (MPa)	Column capacity (kN)	Load ratio (%)	Applied load (kN)	Fire resistance predicted
HSC	HSC	305	81	1636	0.4	655	192
HSC-S	HSC	305	89	1798	0.4	719	205
HSC-P	HSC	305	71	1434	0.4	754	218
HSC-H	HSC	305	67	1354	0.4	542	230
SCC	SCC	305	61	1232	0.4	493	185
SCC-S	SCC	305	57	1152	0.4	461	196
SCC-P	SCC	305	56	1132	0.4	453	210
SCC-H	SCC	305	57	1152	0.4	461	224
FAC	FAC	305	72	1455	0.4	582	190
FAC-P	FAC	305	74	1495	0.4	598	215

Table 7.3 - Results for HPC columns with different column sizes

Column designation	Concrete type	Size (mm)	Column capacity (kN)	Load ratio (%)	Applied load (kN)	Fire resistance predicted	Tie/Strength failure
HSC1	HSC	305	1636	0.4	655	192	Strength
HSC2	HSC	406	2350	0.4	940	231	Strength
HSC3	HSC	610	5316	0.4	2130	297	Strength
HSC1	HSC	305	1636	0.6	982	159	Tie (90°)
HSC2	HSC	406	2350	0.6	1410	188	Tie (90°)
HSC3	HSC	610	5316	0.6	3190	265	Strength

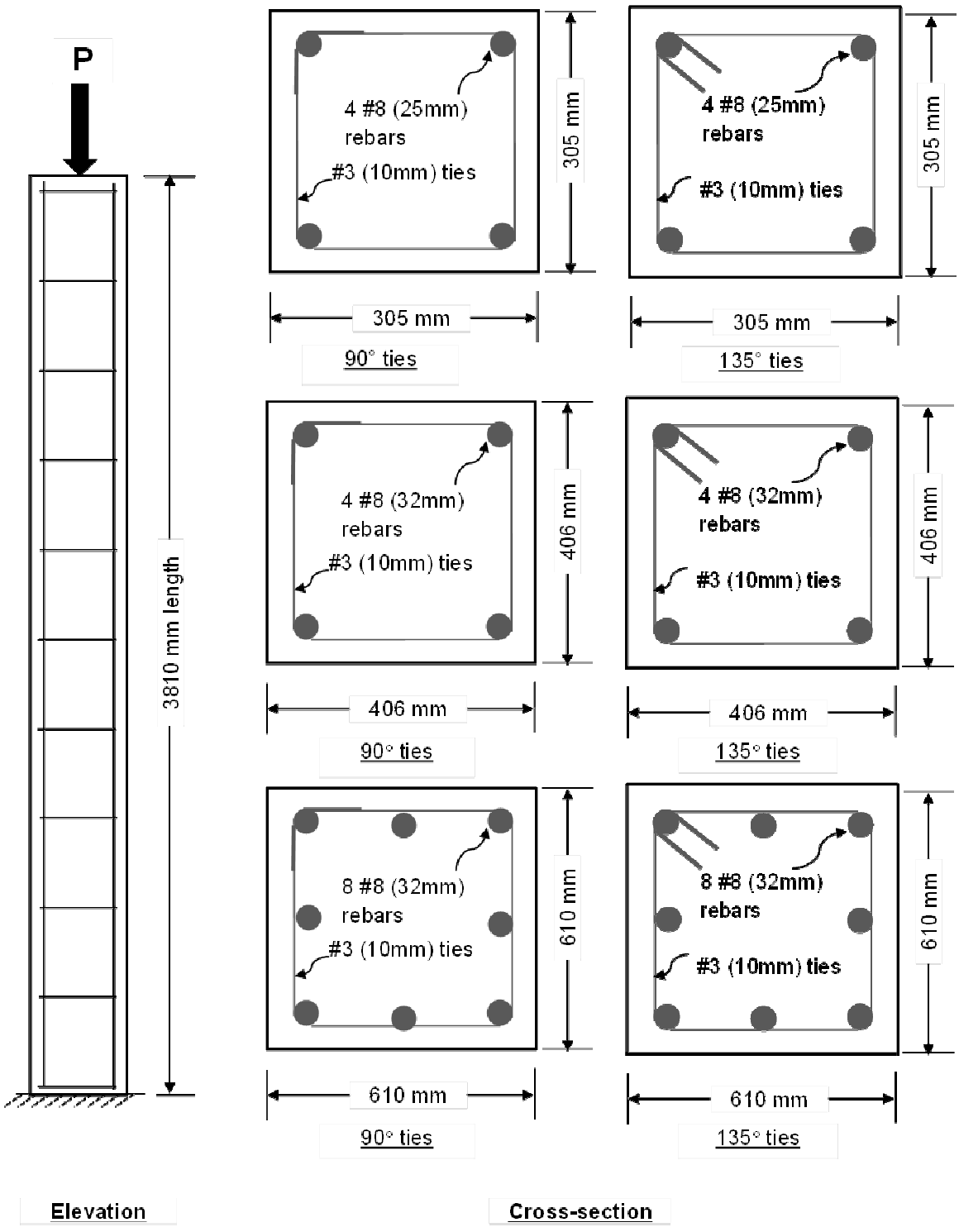

Figure 7.1 - Elevation and cross-sections of RC columns used in parametric study

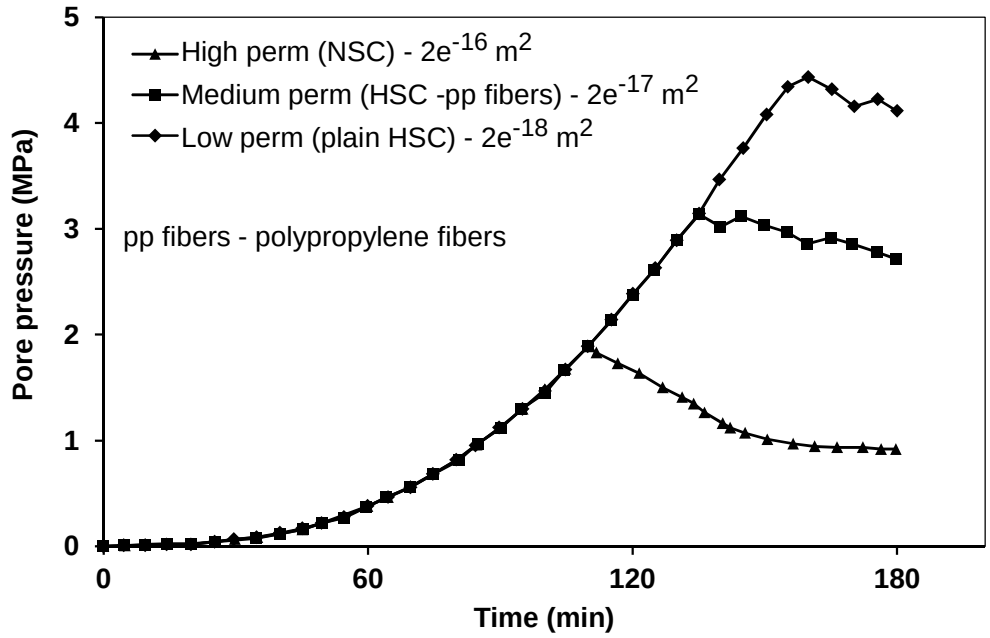

Figure 7.2 – Effect of permeability on pore pressure development in RC columns

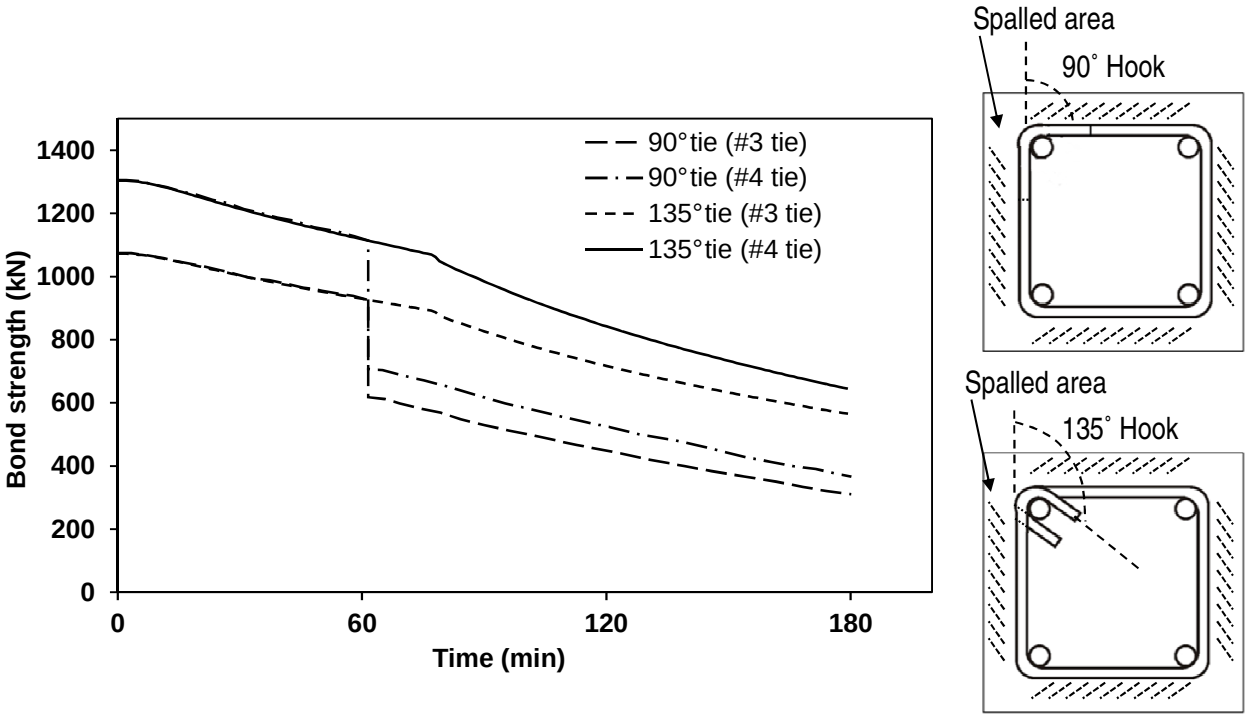

Figure 7.3 - Effect of tie size on bond strength in RC columns with 90° and 135° ties

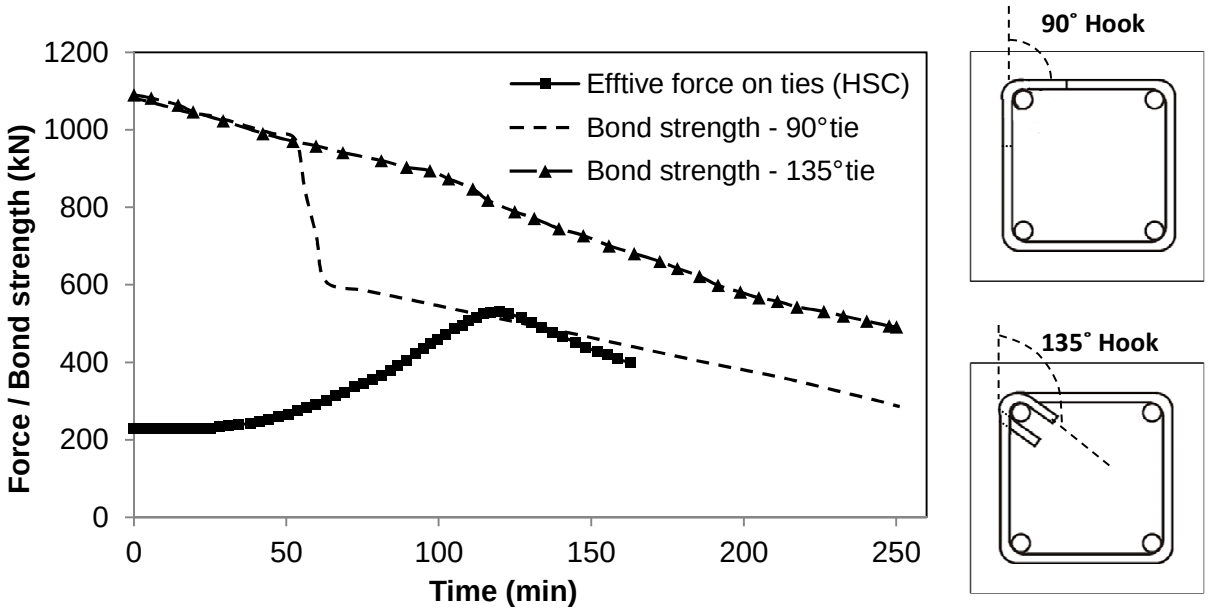

Figure 7.4 - Comparison of force acting on ties against bond strength in HSC column with 90° and 135° ties

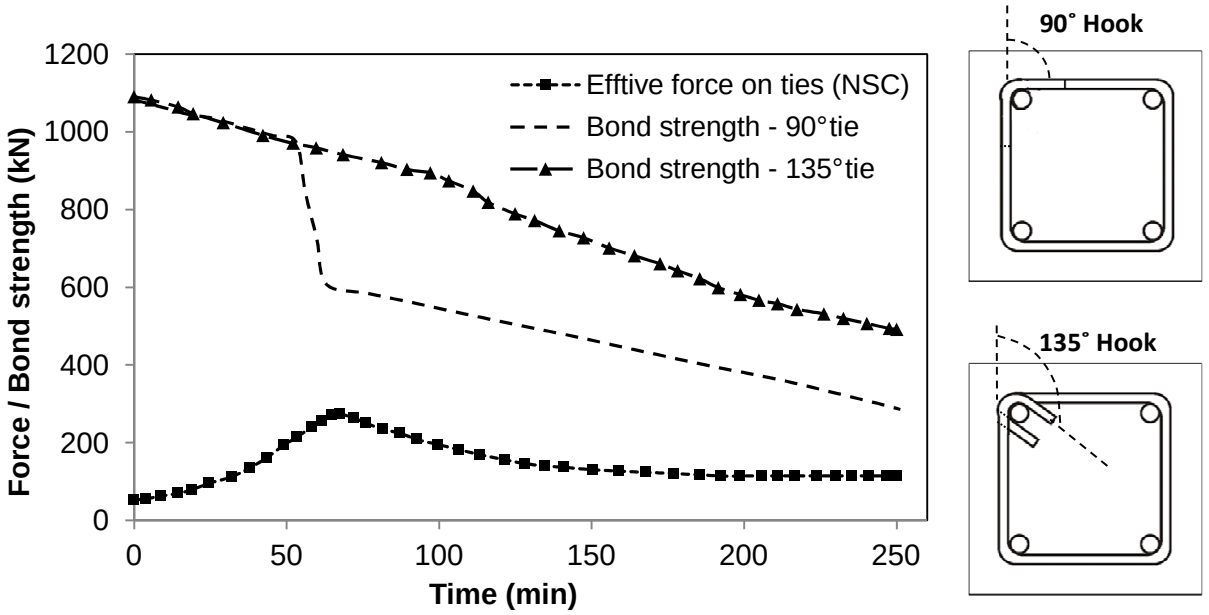

Figure 7.5 - Comparison of force acting on ties against bond strength in NSC column with 90° and 135° ties

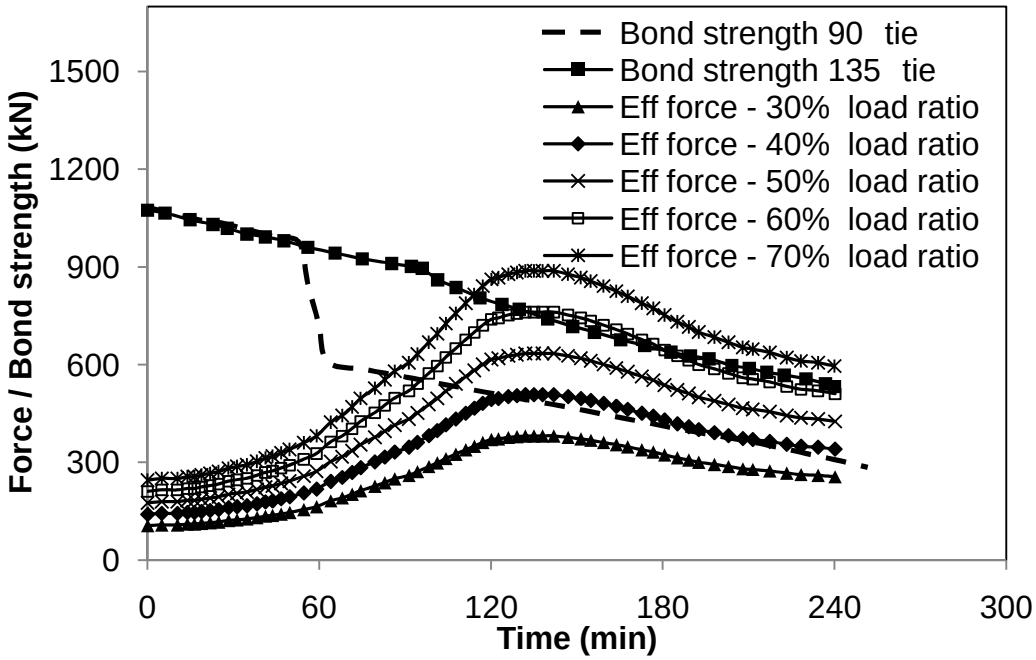

Figure 7.6 - Effect of load level on the effective force acting on ties in RC columns

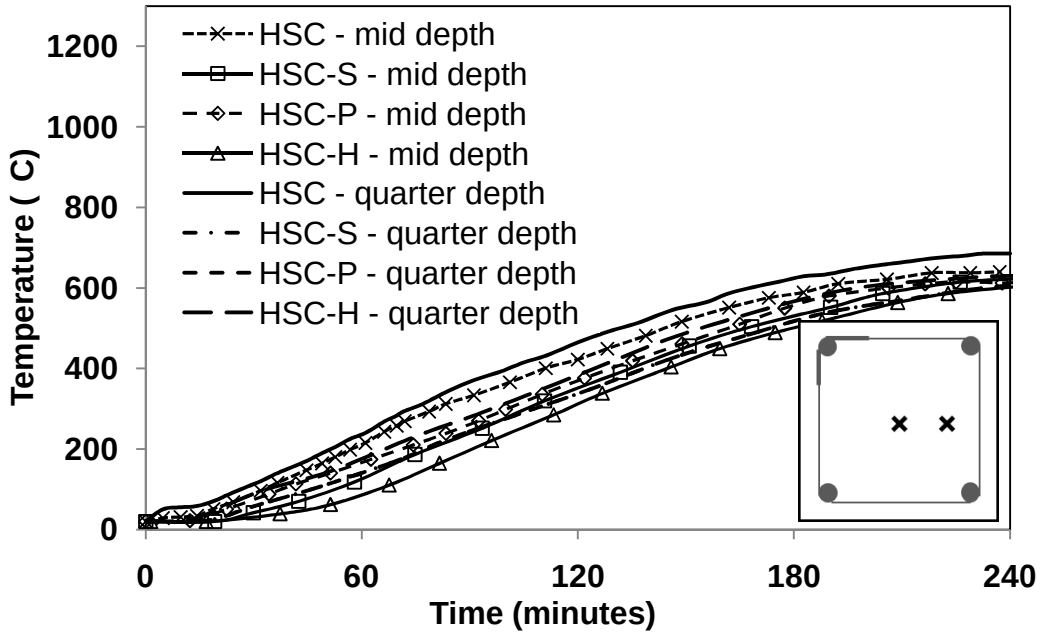

Figure 7.7 - Temperature response HSC column with different fiber combinations

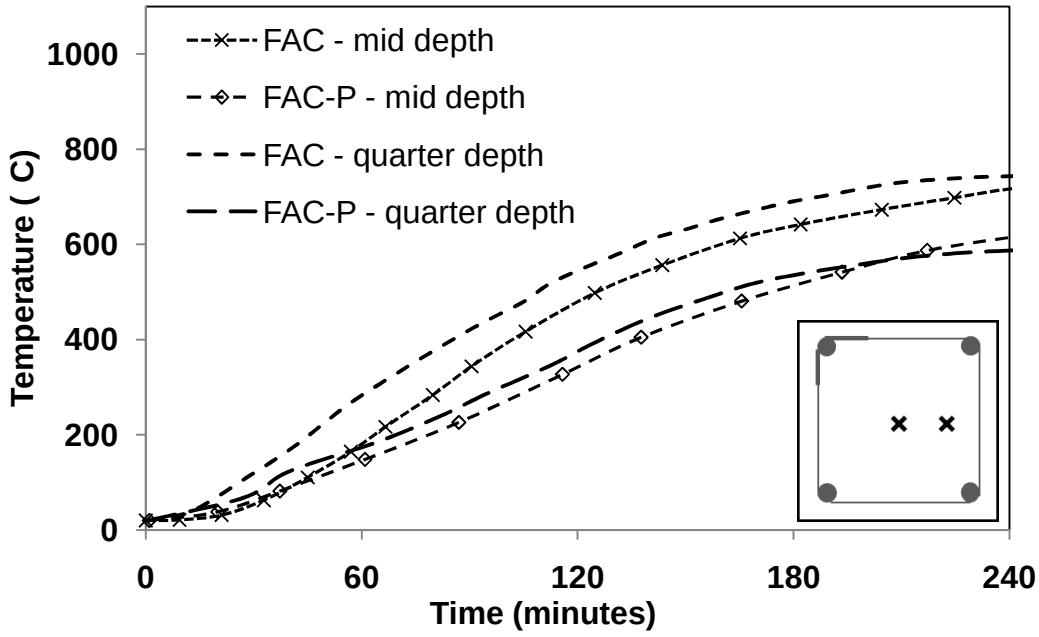

Figure 7.8 - Temperature response of FAC column with different fiber combinations

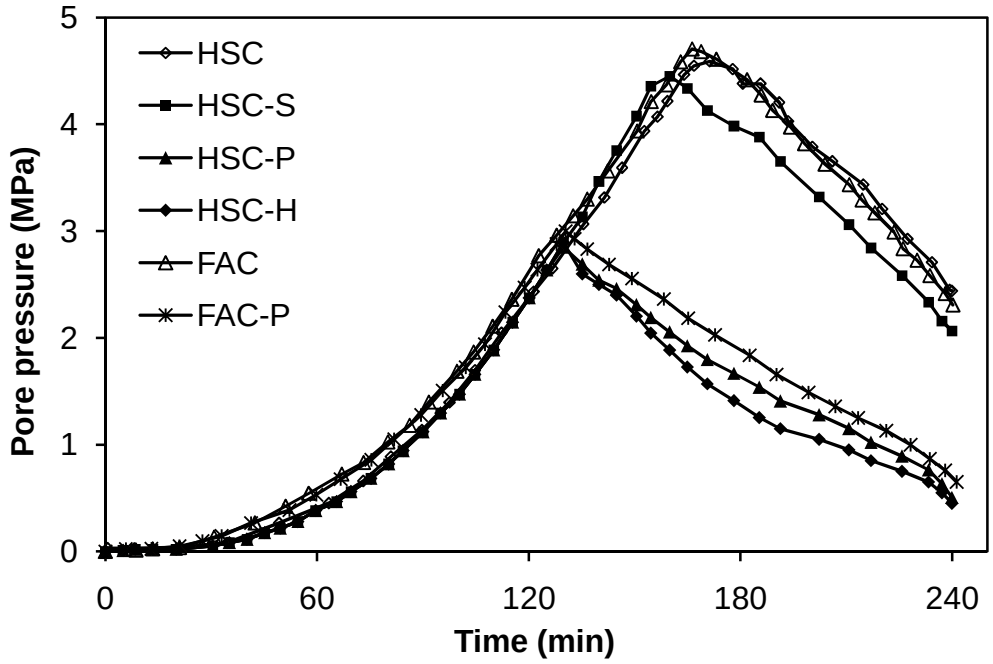

Figure 7.9 - Pore pressure development in RC columns with different fiber combinations

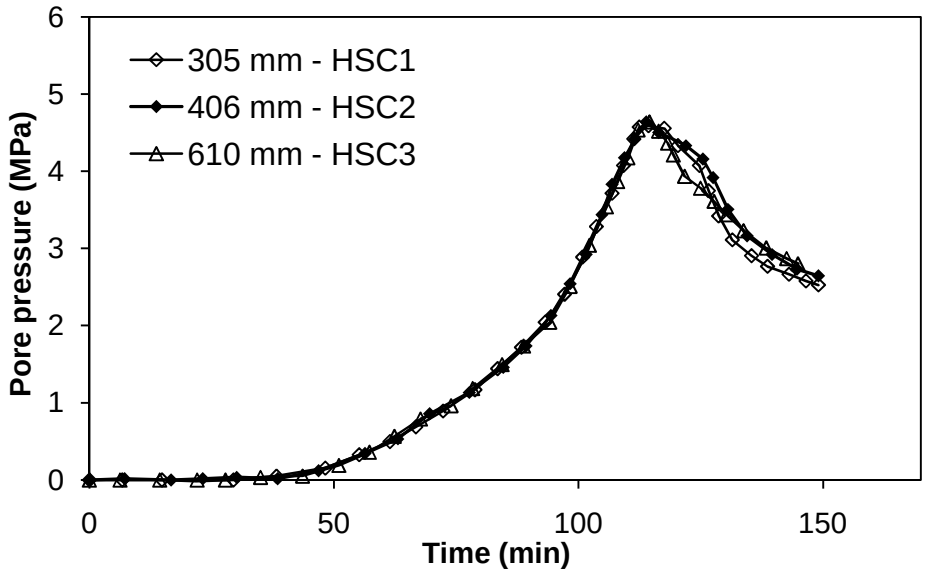

Figure 7.10 - Effect of column size on development of pore pressure at 40 mm depth

CHAPTER 8

8 CONCLUSIONS AND RECOMMENDATIONS

8.1 General

The experimental and numerical studies presented in this thesis provide data and high temperature property relations for evaluating the fire performance of RC columns made of high performance concrete. The thermal properties consisting of thermal conductivity, specific heat, thermal expansion, and mass loss and mechanical properties consisting of compressive strength, splitting tensile strength, elastic modulus, and stress-strain curves were generated in 20-800°C for different types of HPC. Simple empirical relations, obtained through regression analysis on measured test data, are proposed for high temperature properties of HPC (with and without fibers). Also, a numerical approach is developed to account for the effect of tie configuration on fire resistance predictions of RC columns and the sub-model is built into an existing macroscopic finite element (MFE) model for fire resistance analysis of RC columns. The extended model was validated against data generated from fire resistance tests on HPC columns. The validated MFE model was then utilized to undertake parametric studies to quantify the effect of strength (permeability), tie configuration, load ratio, fibers, and column sizes on fire resistance of HPC columns.

8.2 Key Findings

Based on the information presented in this study, the following are the key conclusions:

- Data generated from high temperature thermal property tests on HPC indicate that:

- Temperature has significant influence on thermal conductivity and specific heat of HSC, FAC, and SCC and these properties decrease with temperature in a similar fashion as that of conventional NSC. Specific heat of all these three concretes (HSC, SCC, and FAC) remains almost constant up to about 400°C, and there after increases up to about 650°C before following a constant trend in 650-800°C range.
- Thermal expansion increases with temperature for HSC, SCC, and FAC in entire 20-800°C. Thermal expansion is about 25% higher in case SCC as compared to HSC in 400-800°C temperature range.
- No significant mass loss occurs in HSC, SCC, and FAC up to 600°C. The mass loss increases beyond 600°C, and at 800°C, mass loss reaches to about 90% of initial mass for FAC and SCC and to about 80% of initial mass in the case of HSC.
- The addition of steel, polypropylene, or hybrid fibers to HSC, SCC, and FAC batch mixes does not significantly alter the thermal conductivity in 20-800°C temperature range. The addition of these fibers to HSC, SCC, and FAC also does not alter the specific heat in 20-400°C; however, the presence of fibers do increase the specific heat of these concretes in 400-800°C temperature range.
- Presence of fibers (steel, polypropylene or hybrid) in SCC increases thermal expansion in 200-800°C, however in the case of HSC and FAC the presence of fibers decreases the thermal expansion of concretes throughout 200-800°C range.
- The presence of steel, polypropylene or hybrid fibers does not influence the mass loss of HSC, SCC and FAC in the entire 20-800°C temperature range.

- Data generated from high temperature mechanical property tests on HPC indicate that:

- Compressive strength, tensile strength and elastic modulus of HSC, SCC, and FAC degrade with temperature at a faster rate as compared to conventional NSC. Among high performance concretes, SCC (plain and with fibers) retains higher compressive strength as compared to FAC and HSC (plain and with fibers) throughout 20-800°C temperature range. At 800°C, SCC retains of 40-45% of its initial room temperature compressive strength while HSC and FAC retain only 10-20% of initial strength.
- Splitting tensile strength of HSC, SCC and FAC degrade with temperature, and the loss in tensile strength is lower in case of SCC than that in HSC and FAC in 20-800°C temperature range. SCC retains about 90% of its initial splitting tensile strength at 400°C, and 20% of its initial splitting tensile strength at 800°C. Conversely, HSC and FAC retain only 50% of initial splitting tensile strength at 400°C and this degradation reaches to 10% in HSC and zero in FAC at 800°C.
- Elastic modulus of SCC and FAC does not degrade significantly up to 200°C; however rapid deterioration of elastic modulus occurs in 200-800°C, and reaches to zero at 800°C.
- Both plain SCC and plain FAC exhibit stiff stress-strain response throughout 20-800°C range with higher peak stress developing at lower (peak) strains. Addition of steel, polypropylene or hybrid fibers to HPC transforms the stiffer stress-strain response to a ductile mode.
- Addition of steel, polypropylene, or hybrid fibers to HPC mixes does not have much influence on high temperature compressive strength of HSC, SCC, and FAC. However, presence of steel and hybrid fibers in HPC mixes slows down degradation in tensile strength of HSC and SCC up to 400°C, beyond which there is little influence of fibers.

- Presence of polypropylene fibers in HPC mixes does not have much effect on high temperature stress-strain response of SCC-P; however, ductility of SCC-S and SCC-H at high temperature increases in the presence of steel fibers in the concrete. Presence of fibers in FAC-P also leads to attainment of higher peak strains in 200-800°C.

- Results from fire resistance tests on FAC and HSC columns indicate that:
  - Plain FAC column experiences significant fire induced spalling and thus fire resistance of FAC column decreases to about 60% as that of polypropylene fiber reinforced FAC-P column.
  - The presence of fibers (steel, polypropylene or hybrid fibers) enhances fire resistance of HPC columns and the addition of any of these fiber types are equally effective in mitigating fire induced spalling in HPC columns.
  - Steel, polypropylene or hybrid fiber reinforced HPC columns can retain significant residual strength capacity after fire damage (exposure). HPC columns with steel, polypropylene, or hybrid fibers can have residual strength capacity that is in the range of 34 to 52% of original capacity, even after exposure to severe fire scenarios (similar to that used in the fire tests).
- The proposed tie sub-model, based on mechanics principles, accounts for significant fire induced forces resulting from pore pressure, mechanical loading and thermal strains.
- Results from parametric studies indicate that the factors such as concrete strength (permeability), tie configuration, and load ratio, have significant influence on effective force acting on ties in fire exposed HPC columns. Specifically:
  - Increased impermeability (concrete strength) leads to higher pore pressure in HPC columns. The pore pressure in typical high strength concrete columns can reach about 5

MPa, while that in conventional normal strength concrete columns can reach about 1 MPa.

- The effective stress acting on ties increases with load level and when the load level reaches 40%, failure of ties can occur in plain HPC columns with 90° bent ties. The fire resistance can decrease by about 15 minutes with each 10% increase in load level.
- The size (cross-sectional size) of columns does not have much effect on pore pressure development in HPC columns. However, with increased column size, fire resistance gets higher since the area farthest away from fire in the central concrete core of large size columns is less exposed to detrimental effects (temperature) of fire.
- Presence of polypropylene fibers in HPC columns reduces pore pressure accumulation thus leading to lower effective force on ties, which in turn enhances the fire resistance.

8.3 Recommendations for Future Research

While this research has advanced the state-of-the-art with respect to fire response of HPC both at material and at structural levels, further studies are required to fully characterize the complex material behavior and structural members of HPC. The following are some of the key recommendations for further research in this area:

- The material properties of HPC can be further refined by taking into account the significant factors such as change in permeability (pore structure), and moisture content as a function of temperature. Effect of cooling phase of fire on the properties should also be established so that model predictions can be enhanced for accuracy under design fire scenarios.
- There is lack of test data in the literature on the fire performance of fiber reinforced fly ash and self-consolidating concrete columns. Further fire resistance tests should be carried out on fiber reinforced fly ash and self-consolidating concrete columns.

- Strain gauge measurements in fire resistance tests can be highly useful in validating computer models under combined effects of applied load and fire. The high temperature strain gages used in the current study did not provide reliable measurements under fire exposure due limitations of these gauges at high temperatures (above 300°C). Thus there is a need for developing reliable procedure to obtain high temperature strains in rebars.

8.4 Research Impact

The information developed as part of this research will have significant impact on use of high performance concrete in building applications. HPC offer excellent strength and durability characteristics, but are much more susceptible to faster degradation of strength properties and fire induced spalling and thus have lower fire resistance. This aspect can be overcome either through the addition of fibers or by reconfiguring the ties through bending the ends of ties at 135° into the concrete core. Since mixing and placing the fiber reinforced concrete in a job site can be labor intensive, bending the ties at 135° can offer a practical and economical solution in many situations.

The proposed extensions to macroscopic finite element model take into account the high temperature thermal and mechanical properties of different HPC (plain and with different combination of fibers), and the effect of tie configuration in fire resistance evaluation of HPC columns. These enhancements will help to recognize the inherent fire resistance in HPC columns. Overall, this research will lead to wider application and use of HPC in building applications.

APPENDIX A

APPENDIX A

Equipment Techniques for Measurement of Thermal Properties

A.1 Hot Disk Technique

This appendix gives a brief theoretical description of the Hot Disk Thermal Constants Analyzer used to measure the thermal conductivity and specific heat of different HPC in this study. Hot Disk is relatively new equipment and it combines the measurements of three heat transfer properties (thermal conductivity, thermal diffusivity, and specific heat) in a single test unlike existing test techniques of separately evaluating these properties. The use of Hot Disk equipment is also simple with major effort in sample preparation and high temperature equipment installation. The high temperature mica sensors need more care as these are fragile and brittle due to mica coating and these sensors get burned and consumes in a single high temperature measurement of 20-800°C. Extra care is needed for proper installation of mica sensors with specified resistance between 5 to 10 ohms. The input parameters first need to be evaluated at room temperature for establishing room temperature thermal properties and then these parameters are used as input for high temperature properties evaluation.

Based on the theory of the Transient Plane Source (TPS) technique, recognized in ISO 22007-2 (2008), the Hot Disk Thermal Constants Analyzer utilizes a sensor element in the shape of a double spiral. This Hot Disk sensor acts both as a heat source for increasing the temperature of the sample and a ”resistance thermometer” for recording the time dependent temperature increase. In most cases the sensor element is made of a 10 μm thick Nickel-metal double spiral, with precisely designed dimensions (width, number of windings and their radii). This spiral is supported by a material to protect its particular shape, to give it mechanical strength and keep it

electrically insulated. The polyimide “Kapton” is such a material, which can be used throughout the temperature range from 10 K to 500 K. A “Mica” material is also available as supporting/insulating material and in that case the upper limit of the temperature range is extended to 1000 K.

The encapsulated Ni-spiral sensor is then sandwiched between two halves of the sample (solid samples). During a pre-set time, 200 resistance recordings are taken, and from these the relation between temperature and time is established. A few parameters, like the Heating power to increase the temperature of the spiral, the measurement time for recording 200 point and the size of the sensor are used to optimize the settings for the experiment so that thermal conductivities from 0.005 W/mK to 500 W/mK can be measured. Measurements on standard materials ranging from Polystyrene to Aluminum metal show that the accuracy over the whole range of Thermal Conductivities is within +/- 5% and the reproducibility is within +/- 2%.

The Hot Disk sensor is clamped between two pieces of the sample, with two flat sides facing the sensor. They are clamped together, completely covering the sensor. The mounting pressure or surface roughness is not important, but the thermal contact between the sample and the sensor should be fair for hard samples, in particular for moderately- and high-conducting materials.

The sensor and sample are initially allowed to settle at isothermal conditions. Then, a constant electrical power is applied to the Hot Disk heating element. The heat that is generated in the heating elements will then dissipate into the surrounding sample. Simultaneously, the temperature increase in the sensor is recorded as a function of time. This temperature increase data is then used to estimate the bulk thermal transport properties of the material.

The heating power applied causes an initial temperature increase. Several important factors – not related to the bulk properties of the sample – influence the recorded temperature increase. They

are: the sensor insulation, the interfacial thermal contact resistance between sensor and sample surface (influenced by surface roughness, mounting pressure, etc.) as well as possible thin surface layers on the sample surface (*e.g.* thin oxidation layers). All these factors have a considerable impact on the recorded temperature increase.

If we assume that the thermal transport properties are constant in the radial direction with respect to the plane of the sensor, but different from the thermal transport properties in the axial direction, one can derive the following model to be used for the analysis and curve-fitting procedure.

$$\Delta T_i = \left(\frac{P_0}{\lambda_r \cdot \lambda_a \cdot \pi^{3/2} \cdot r} \right) \cdot D_0 \cdot (\tau_i) \qquad \text{(A.1)}$$

where $\tau_i = \sqrt{\frac{t_i - t_{corr}}{\theta}}$ is a dimensionless "time"

and $\theta = \frac{r^2}{a_r}$ is the characteristic time of the experiment.

Index *i* denotes the data points, which range from 1 to 200, and the indices *a* and *r* refer to axial and radial thermal transport properties, respectively. Parameter *A* incorporates the imperfect thermal contact conditions in a measurement, while the remainder of Eq (A.1) is in accordance with the ideal theory assuming perfect thermal contact conditions, and zero specific heat capacity of the sensor itself. This remainder of Eq (A.1) is referred to as the ideal model.

Figure A.1 displays a typical average temperature increase as a function of $D_0(\tau)$. The model fitted to experimental data results in a straight-line fitting – where the intercept at time zero

represents the steady-state temperature difference across the interfacial layers and interfacial thermal resistances between the heating elements and the bulk surface of the sample, including the thermal contact resistance. Also, low conducting surface layers, such as thin oxidation layers, are compensated for in parameter *A.* The sensor insulation requires typically a settling time of the order $d_{sensor}^{2}/a_{sensor}$, where d_{sensor} represents the thickness and a_{sensor} the thermal diffusivity of the sensor insulation. However, the establishment of a constant heating power is not instantaneous. Both these phenomena are treated with the use of a time correction, and initial points deviating from the model fitting should be omitted in the analysis.

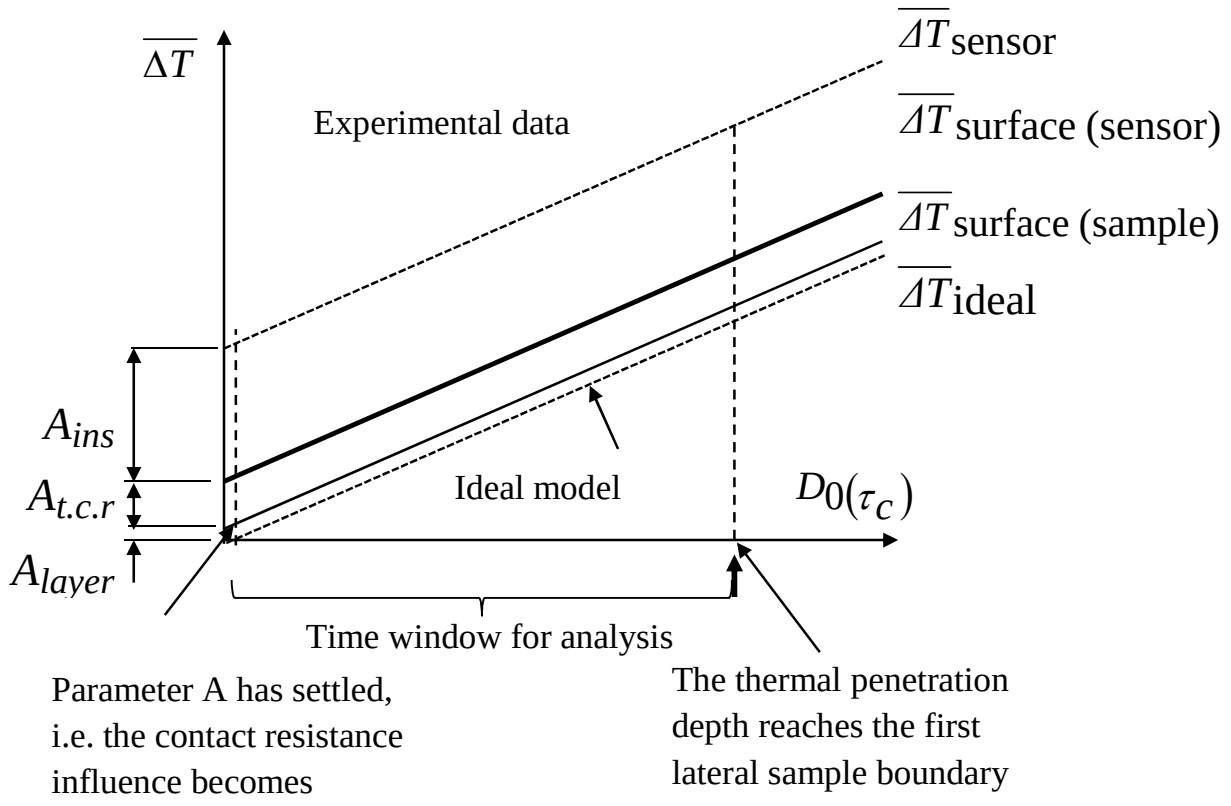

Figure A.1 - The average temperature response as a function of $D_0(\tau)$

Eq A.1, gives a straight-line curve fitting, where parameter *A* is modeled as a sum of different constant contributions to the total thermal resistance between the sensor heating element and the bulk surface.

It should be noted that the recorded temperature increase is often appreciably higher than the maximum temperature increase of the sample surface itself, particularly for high-conducting samples. Now, as all these interfacial influences may be summed up in the constant *A*, and thus be separated from the properties inside the bulk of the sample, we see that the bulk thermal conductivity may be found in the slope of the straight-line fit, and the thermal diffusivity in the best-model fitting of the $D_0(\tau)$ function. For isotropic samples, $\lambda=(\lambda_r.\lambda_a)^{1/2}$ and $a = a_r$, and the volumetric specific heat may be obtained as $\rho c_p = \lambda/a$.

The model, Eq (A.1), represents the experimental data very well. For instance, with a temperature increase of about 1 degree K, a standard deviation for all curve-fitted points of the order 10^{-5} K is commonly obtained, if the sample is homogeneous. This result in standard deviations of the order of (or better than) 0.1% for the bulk thermal conductivity $(\lambda_r\lambda_a)^{1/2}$ even if the sample is dismounted and remounted with different mounting pressures (which results in rather scattered values of *A* from measurement to measurement), or the sensor insulation may creep between measurements. So far it is obvious that the sensitivity is limited by the performance of the electronics used in the measuring system.

Non-ideal experimental conditions like sensor heat capacity, heat losses through sensor leads and variation in output of power during the transient, all of these influences normally within 1% of the total output of heating power and are compensated for accurately in the Hot Disk software.

Other non-ideal conditions may appear when the insulating layer of the sensor is comparatively large, say 100 μm or larger. However, these geometry deviations are small for sensors of larger diameter, and at present, a calibration approach (against a well-known, homogeneous reference material with known anisotropy and heat capacity) makes it possible to calibrate different sensors to obtain full consistency in all estimated properties within 0.1-0.4%, independent of the sensor used. Uncalibrated sensors of various kinds reproduce thermal conductivity results within typically 1% between different types of sensors, and thermal diffusivity within typically 3-4%.

A.2 Thermomechanical Analysis (TMA) Technique

In the TMA technique thermal expansion properties of the sample are monitored against time or temperature under a specified programmed atmosphere an follows ASTM test procedure (ASTM E831, 2006). TMA measures deformation of the sample under non-oscillating load. The applied load is kept very low to measure the dimension change of the sample also called thermo dilatometry. Usually a small load of 2kN is sufficient to keep the probe in place over sample. A typical system of TMA is shown in Figure 3.5a. The sample is placed on the inert surface pedestal and probe is allowed to rest upon it exerting load controlled be the force controller as shown in Figure 3.5c. The movement of the probe resulting from specimen changes is measure by a linear variable differential transducer (LVDT) which produces electrical signal related to position of the probe. The programmed controller controls the rate of heating and temperatures are measured by thermocouples in furnace and at pedestal. Data from LVDT and the thermocouples are stored and processed in real time by computer.

TMA basically uses the modulated temperature techniques to carry thermal analysis. In modulated temperature thermal analysis, a sinusoidal temperature “forcing function” is added to the traditional linear (or isothermal) underlying heating rate. This forcing function induces in the

sample a sinusoidal response that may be de-convoluted to yield reversing and non-reversing information.

When applied to thermo-mechanical analysis (TMA), the temperature modulation produces a sinusoidal change in test specimen length. Figure A.2, for example, shows the modulated temperature at the figure bottom and the length change at the top both as their first derivatives. Discrete Fourier transformation is applied in real time to continuously determine the average value and the amplitude value for each signal (Price, 1998).

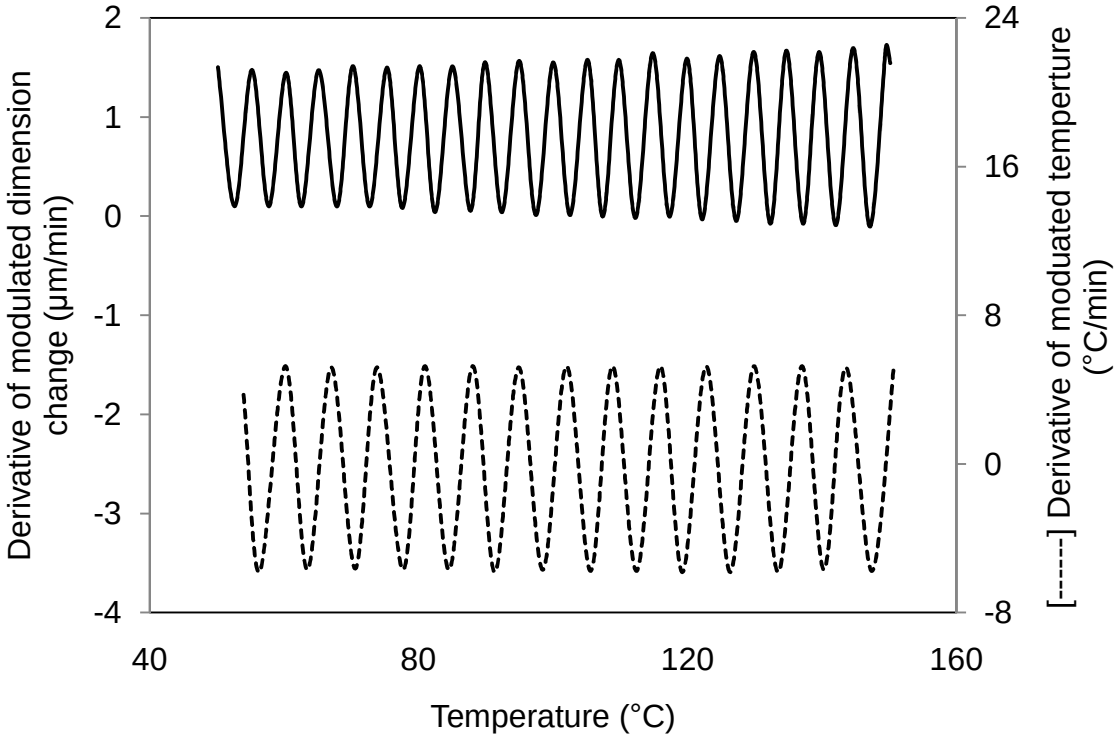

Figure A.2 - Modulated temperature (bottom) and the length change (top) both as their first derivatives.

The governing equation for modulated TMA is given by

$$dL/dt = A\, dT/dt + f(t, T) \qquad \text{A.2}$$

where L is length, T is temperature, t is time, A is expansivity, and f(x) is “function of time and Temperature”. The left hand term of equation 1, known as the total length change rate, is shown

on the right to be composed of two parts; a reversing contribution proportional to the time rate of change of the independent parameter (temperature) and a non-reversing contribution from the absolute value of that independent parameter.

Of course in TMA, the dependent parameter measured is length (not the time rate of change of length) so the governing equation takes on the form of:

$$L_{total} = L_{reversing} + L_{nonreversing} \quad \text{A.3}$$

where *Ltotal* is the average length from the Fourier de-convolution, *Lreversing* is the (length amplitude / temperature amplitude) $\int dT/dt\ K$. The "average length", "length amplitude" and "temperature amplitude" are the signals derived from the Fourier transformation process. $\int$ dT/dt is the underlying heating rate averaged over a single period while K is a calibration constant close to unity. The non-reversing length is obtained from the difference between the total and reversing contributions.

$$L_{nonreversing} = L_{total} - L_{reversing} \quad \text{A.4}$$

There is always a "lag" between the applications of the forcing function and the resultant response. The use of sinusoidal forcing functions provides for the easy measurement and interpretation of the magnitude of this lag through the use of a Lissajous plot. Evaluation of the midpoint and extrema values of the Lissajous plot yields the phase lag. In modulated TMA, this lag is rather large compared to other modulated temperature techniques, about 28 s, due to the large thermal mass and low thermal conductivity of the quartz sample stage and measuring probe. A practical rule-of-thumb is that the period of the applied forcing function should be about ten times the time constant. So for modulated TMA, a period of about 300 seconds (5mins) is used. The applied temperature amplitude is selected based upon the value of the expansivity

value A in equation A.2, but is typically ± 5°C. And as with all modulated temperature approaches, at least 5 cycles is required across a transition in order to have reliable Fourier de-convolution. This results in the typical underlying heating rate of 2°C/min or less. The value of the calibration coefficient is determined, as is the length change calibration of the TMA, from the use of a reference material with a known coefficient of thermal expansion (CTE) value (Blaine and Hahn, 1998).

APPENDIX B

APPENDIX B

Design of Column Specimens

B.1 Column Capacity Calculations

This appendix summarizes the design calculations using ACI 318 (2008) and ACI 216.1 (2007) provisions for FAC, FAC-P, HSC-S, and HSC-H columns. Dimensions for design of columns are mainly dictated by fire test furnace in with these columns were to be tested. Table B.1 gives the dimensions and properties of the steel used in calculations. Calculations for one column each from set of FAC and HSC columns is presented here and ultimate strength and factored design capacity is summarized for all columns in Table B.2 and B.5 for FAC and HSC columns respectively.

Table B.1 - Design parameters used for the columns

Design parameter	Notation	Value
Gross area (Cross-section = 203x203 mm)	Ag	41209 mm^2
Steel yield strength	f_y	420 MPa
Steel area (4 # 6 bars)	A_{st}	$4 \times 285 = 1140$ mm^2
Length of column	l	3300 mm
Concrete cover to main rebars for minimum 2 hours fire resistance	-	50 mm (ACI 216.1 2.5.3)
Column end conditions	-	Pin-pin

Note: Maximum usable strain at extreme concrete compressive fiber shall be assumed equal to 0.003. (ACI 10.2.3)

Notations:

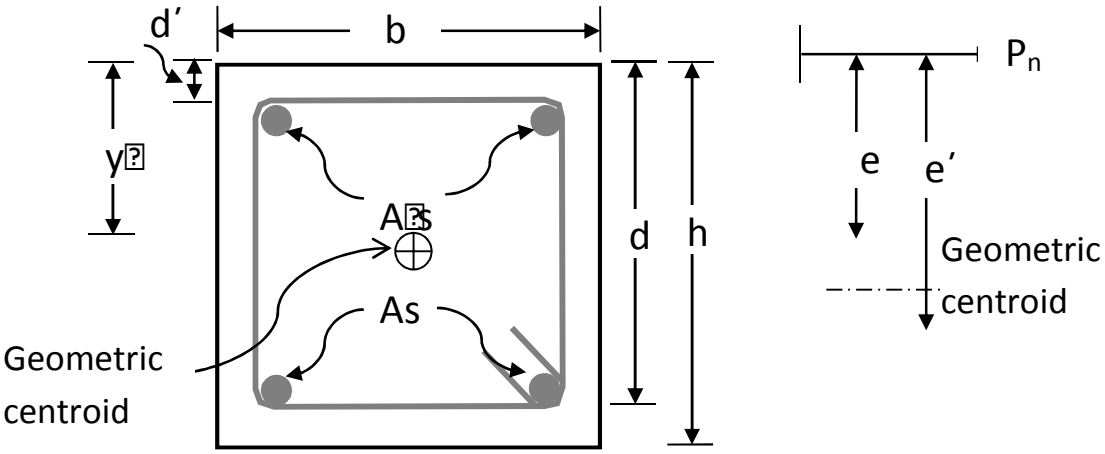

c = distance to neutral axis

$\bar{y}$ = distance to geometric centroid

ε_s = steel strain in tension side

ε'_s = steel strain in compression side

e = eccentricity of load to geometric centroid

e' = eccentricity of load to tension steel

d' = effective cover of compression steel

Figure B.1 - Notations used in calculations

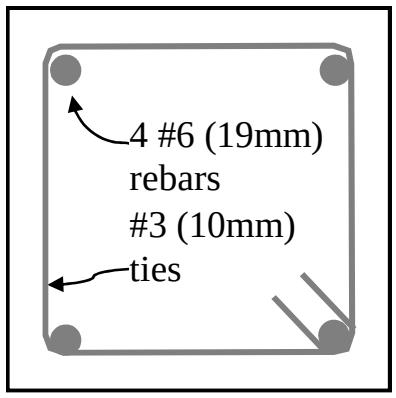

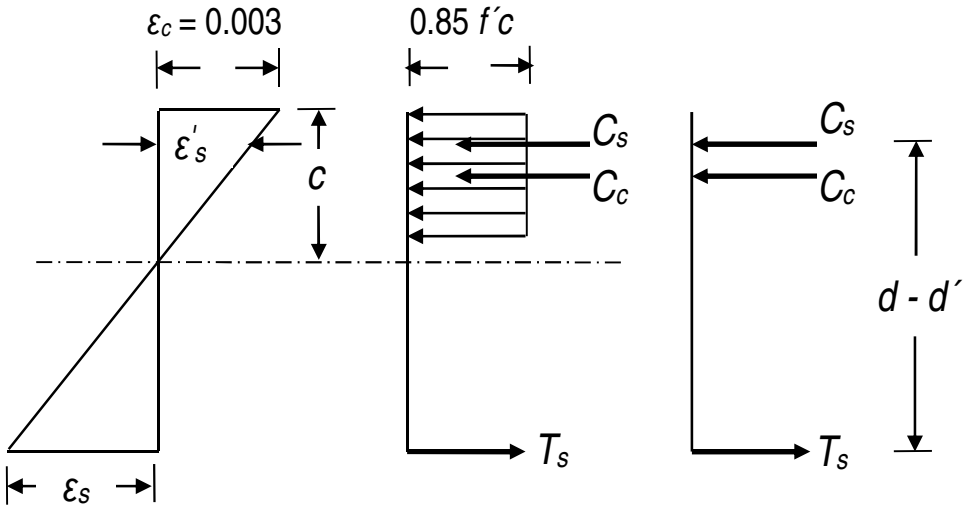

Strains

$$\varepsilon_S = 0.003\frac{d-c}{c}$$

$$\varepsilon'_S = 0.003\frac{c-d'}{c}$$

Stresses

$$f_S = E_S\varepsilon_S \le f_y$$

$$f'_S = E_S\varepsilon'_S \le f_y$$

Internal forces

$$C_C = 0.85\,f'_c\,ba$$

$$C_S = A'_S\,f'_S$$

$$C_t = A_S\,f_S$$

Figure B.2 - Stress-strains and forces in columns

B.2 P-M interaction Diagram for FAC column

Table B.2 - Calculated factored capacities of FAC and FAC-P columns

Column	Factored strength property	Value
FAC		
	Compressive strength (f'_c)	107 MPa
	Ultimate load (P_u)	2144 kN
	Ultimate moment (M_u)	68.12 kN.m
FAC-P		
	Compressive strength (f'_c)	100 MPa
	Ultimate load (P_u)	2020 kN
	Ultimate moment	68.65 kN.m

Point 1 - (depth of neutral axis > d)

c = infinity

$Pn = 0.8(A_{net} \times 0.85\, f'_c + Ast\ fy)$

$= 0.8 \times (40069 \times 0.85 \times 107 + 1140 \times 420)/1000 = 3298$ kN

$\varphi Pn = 0.65 \times = 2144$ kN

Mn = 0

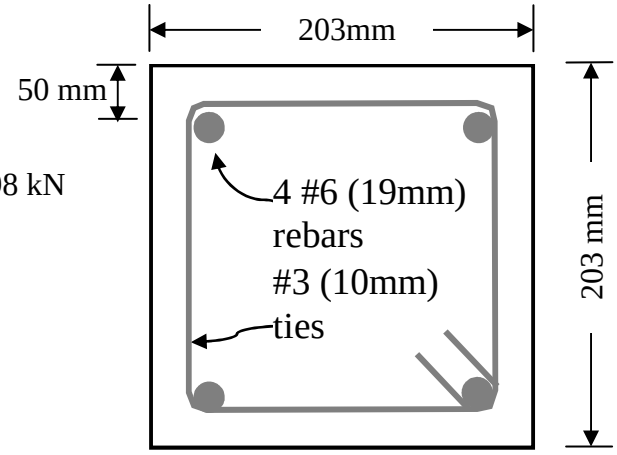

Figure B.3 - Cross-section of RC column

Point 2 - (depth of neutral axis at d)

at c = d = 153 mm

$$f's = Es \times \varepsilon's = 200000\ \frac{0.003(c - d')}{c} \leq fy$$

$$f's = Es \times \varepsilon's = 200000\ \frac{0.003(153 - 50)}{153}$$

$= 403\ MPa < 420\ MPa$

$Cs = A's \times\ f's = 570 \times \frac{403}{1000} = 230\ kN$

$fs = Es\ \times\ fs = 200000\ (0.003(d - c))/c$

$fs = Es\ \times\ fs = 200000\ (0.003(d - c))/c = 0$

$Ts = 0$

$Cc = 0.85\ \times f'c\ \times \beta \times a\ \times b$

$= 0.85\ \times 107 \times 203\ \times 0.85 \times \frac{153}{1000} = 2401.09\ kN$

$Pn = Cc + Cs - Ts = 2401.09 + 230\ - 0 = 2631.33\ kN$

φPn = 0.65 × 2631.33 = 1710.36 kN

$Mn = Cc\left(\bar{y} - \frac{a}{2}\right) + Cs(\bar{y} - d') + Ts\ (d - \bar{y})$

Mn = 99.43 kN.m

φMn = 0.65 × 99.43 = 64.63 kN.m (ACI 9.3.2)

Point 3 - (depth of neutral axis < d)

at c = d = 122.4 mm

$f's = Es\ \times\ \varepsilon's$

$= 200000\ \frac{0.003(c - d')}{c} \leq fy$ (ACI 10.2.4)

$$f's = Es \times \varepsilon's = 200000 \frac{0.003(122.4 - 50)}{122.4}$$

$$= 354.90 < 420\ MPa$$

$$Cs = A's \times f's = 570 \times \frac{354.90}{1000}$$

$$= 202.29\ kN \qquad \text{(ACI 10.2.4)}$$

$$fs = Es \times fs = 200000\ (0.003(d - c))/c$$

$$fs = Es \times fs = 200000 \frac{0.003(153-122.4)}{122.4} = 354.93 \text{ MPa} < 420 \text{ MPa}$$

$$Ts = As \times fs = 570 \times \frac{354.93}{1000} = 85.5\ kN$$

$$Cc = 0.85 \times f'c \times \beta \times c \times b$$

$$= 0.85 \times 107 \times 0.85 \times 122.4 \times 203/1000 = 1920.87\ kN$$

$$Pn = Cc + Cs - Ts = 1920.87 + 202.29 - 85.5$$

$$= 2037.7\ kN \qquad \text{(ACI 10.3.6)}$$

φPn = 0.65 × 2037.7 = 1324.5 kN (ACI 9.3.2)

$$Mn = Cc\left(\bar{y} - \frac{a}{2}\right) + Cs(\bar{y} - d') + Ts\ (d - \bar{y})$$

Mn = 109.87 kN.m

φMn = 0.65 × 109.87 = 71.41 kN.m (ACI 9.3.2)

Obtain more points for P-M diagram at given in Table B.3

Table B.3 - Calculation of nominal load and moment for P-M diagram for FAC column

Point #	c (mm)	Pn (kN)	φPn (kN)	Mn (kN.m)	φMn (kN.m)
1	inf	3298.46	2144.00	0.00	0.00
2	153.00	2631.33	1710.36	99.44	64.63
3	122.40	2037.67	1324.48	109.87	71.41
4	91.80	1368.38	889.45	109.78	71.36
5	61.20	783.63	509.36	88.06	57.24
6	30.60	24.00	15.60	43.66	28.38
7	0.01	-478.64	-311.12	0.02	0.01

From all these points we get the load-moment (P-M) interaction diagram for FAC column as plotted in Figure B.4.

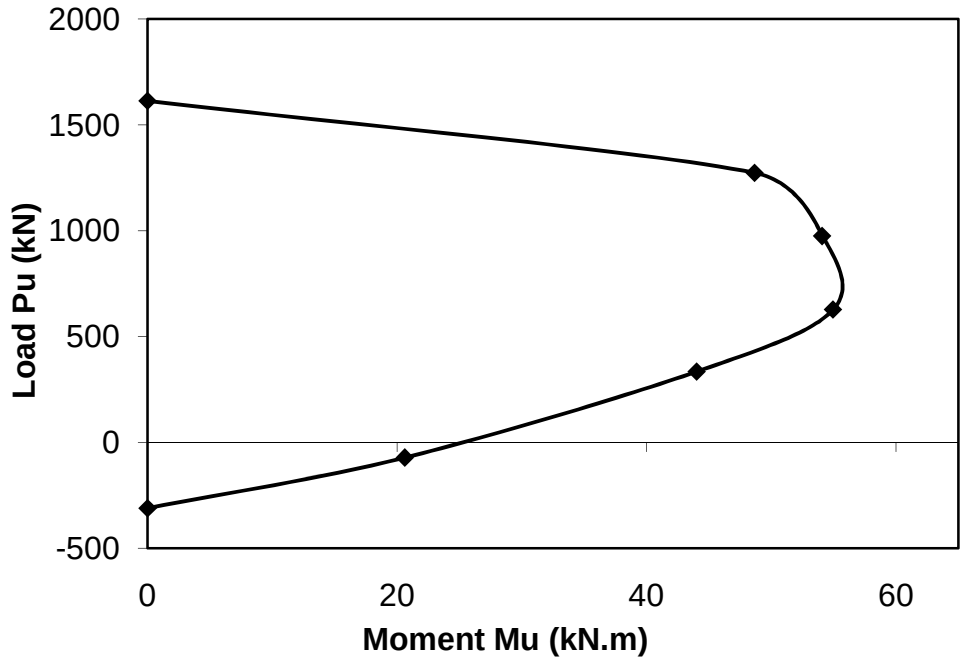

Figure B.4 - Load-moment interaction diagram for FAC column

Calculate the critical buckling load of the column

Pin ended (k = 1)

Check slenderness

Radius of gyration $r = 0.3 \times h$

Where h = dimension of column

h = 203 mm

r = 0.3 × 203 = 60.9

l_u = 3350 mm = 3.35 m

k_{lu} = 1*3350 = 3350 mm

$$\frac{kl_u}{r} \leq 40 \qquad \text{(ACI 10.10)}$$

Slenderness ratio = 3350/60.9 = 55 >40

Hence the column is slender and moment magnification method should be used.

Calculate buckling load – concentrically loaded slender column

$$E_{FAC} = 3.32\sqrt{f'c} + 6895(w_c/2320)^{1.5}$$

$E_{FAC} = 3.32\sqrt{107}/1000 + 6895(2564/2320)^{1.5}$ = 42352 MPa

$$I_g = \frac{bd^3}{12} = 141515140.1\ mm^4$$

Flexural rigidity = EI (ACI 10.15)

$$EI = \frac{0.4EcI_g}{1+\beta_d}$$

$$EI_{FAC} = \frac{0.4 \times 42352 \times 141515140.1}{(1+0.5)1000} = 1.62e^{12}\ MPa$$

Euler buckling Load P_c (ACI 10.13)

$$P_c = \frac{\pi^2 EI}{(kl_u)^2}$$

$$P_{c\,FAC} = 1408.89\ kN$$

Calculate the load and moment capacity of the column, the moment calculated by moment magnification factor will be checked against P-M diagram. Capacity is calculated by using iterations by assuming different Pu and then calculation of δ_{ns} as tabulated in Table B.4:

$$\delta_{ns} = Cm/(1 - \frac{Pu}{0.75Pc})$$

Table B.4 - Load and moment capacity calculated by moment magnification method.

Mu (kN.m)	**Pu (kN)**	$\boldsymbol{\delta_{ns}}$	**e (mm)**
0.00	0.00	1.00	0.00
5.63	222.40	1.20	25.65
14.04	444.80	1.49	31.75
27.95	667.20	1.98	42.16
55.35	889.60	2.94	62.74
56.17	894.05	2.97	63.50
57.01	898.50	3.00	64.01
68.54	951.87	3.40	72.64

Superimposing the calculated Pu and Mu against P-M diagram of the column gives the capacity of the column.

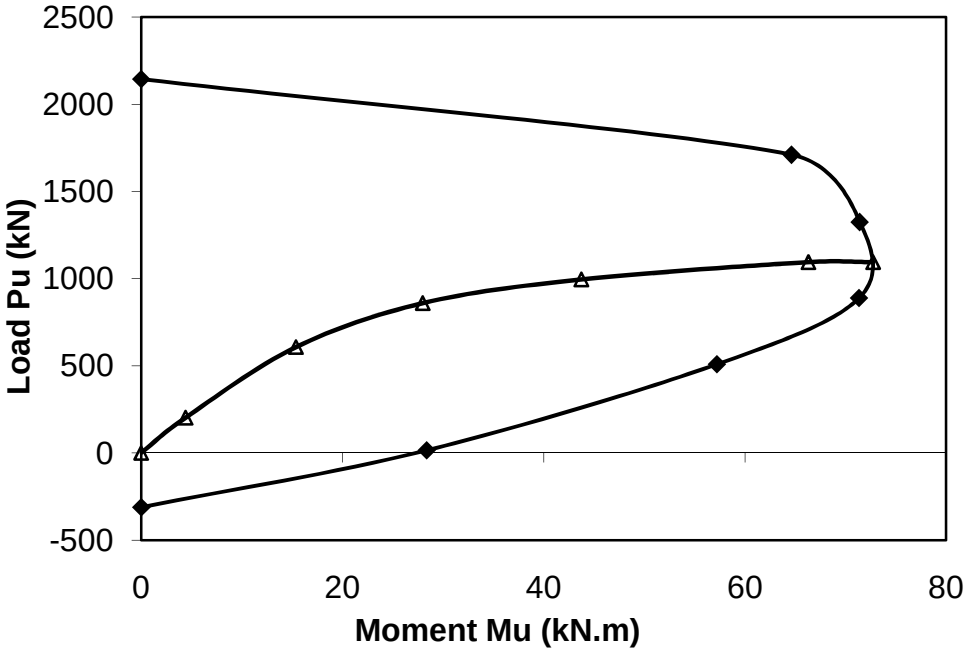

Figure B.5 - Calculation of ultimate load from load-moment interaction diagram for FAC column

B.3 P-M interaction Diagram for HSC-S and HSC-H column

Design parameters for HSC-S and HSC-H are same as given in table B.1.

Table B.5 - Calculated factored capacities of HSC-S and HSC-H columns

HAC-S		
	Compressive strength (f'_c)	77 MPa
	Ultimate load (P_u)	1612 kN
	Ultimate moment (M_u)	50.84 kN.m
HAC-H		
	Compressive strength (f'_c)	80 MPa
	Ultimate load (P_u)	1665 kN
	Ultimate moment (M_u)	53.45 kN.m

Point 1 - (depth of neutral axis > d)

c = infinity

Pn = 0.8(A_{net} × 0.85 f´$_c$ + Ast fy)

= 0.8 × (40069×0.85×77+1140×420)/1000 = 2481.05 kN

φPn = 0.65 × = 1612 kN

Mn = 0

Point 2 - (depth of neutral axis at d)

at c = d = 153 mm

$$f's = Es \times \varepsilon's = 200000 \frac{0.003(c - d')}{c} \leq fy$$

$$f's = Es \times \varepsilon's = 200000 \frac{0.003(153 - 50)}{153} = 403\ MPa < 420\ MPa$$

$$Cs = A's \times f's = 570 \times \frac{403}{1000} = 230\ kN$$

$$fs = Es \times fs = 200000\ (0.003(d - c))/c$$

$$fs = Es \times fs = 200000\ (0.003(d - c))/c = 0$$

$$Ts = 0$$

$$Cc = 0.85 \times f'c \times \beta \times a \times b$$

$$= 0.85 \times 77 \times 203 \times 0.85 \times \frac{153}{1000} = 1727.89\ kN$$

$$Pn = Cc + Cs - Ts = 1727.89 + 230 - 0 = 1958.13\ kN$$

φPn = 0.65 × 1958.13 = 1272.78 kN

$$Mn = Cc\left(\bar{y} - \frac{a}{2}\right) + Cs(\bar{y} - d') + Ts\ (d - \bar{y})$$

Mn = 74.88 kN.m

φMn = 0.65 × 74.88 = 48.67 kN.m (ACI 9.3.2)

Point 3 - (depth of neutral axis < d)

at c = d = 122.4 mm

$$f's = Es \times \varepsilon's = 200000 \frac{0.003(c-d')}{c} \leq fy \quad \text{(ACI 10.2.4)}$$

$$f's = Es \times \varepsilon's = 200000 \frac{0.003(122.4-50)}{122.4} = 354.90 < 420\ MPa$$

$$Cs = A's \times f's = 570 \times \frac{354.90}{1000}$$

$$= 202.29\ kN \quad \text{(ACI 10.2.4)}$$

$$fs = Es \times fs = 200000\ (0.003(d-c))/c$$

$$fs = Es \times fs = 200000 \frac{0.003(153-122.4)}{122.4} = 354.93 \text{ MPa} < 420 \text{ MPa}$$

$$Ts = As \times fs = 570 \times \frac{354.93}{1000} = 85.5\ kN$$

$$Cc = 0.85 \times f'c \times \beta \times c \times b$$

$$= 0.85 \times 77 \times 0.85 \times 122.4 \times 203/1000 = 1382.31\ kN$$

$$Pn = Cc + Cs - Ts = 1382.31 + 202.29 - 85.5 = 1499.11\ kN \quad \text{(ACI 10.3.6)}$$

φPn = 0.65 × 1499.11 = 974.41 kN (ACI 9.3.2)

$$Mn = Cc\left(\bar{y} - \frac{a}{2}\right) + Cs(\bar{y} - d') + Ts\ (d - \bar{y})$$

Mn = 83.22 kN.m

φMn = 0.65 × 83.22 = 54.10 kN.m (ACI 9.3.2)

Obtain more points for P-M diagram as given in Table B.6

Table B.6 - Calculation of nominal load and moment for P-M diagram for HSC-S column

Point #	c	Pn	φPn	Mn	φMn
1	infinity	2481.05	1612.68	0.00	0.00
2	153.00	1958.13	1272.78	74.88	48.67
3	122.40	1499.11	974.42	83.22	54.09
4	91.80	964.46	626.90	84.54	54.95
5	61.20	514.34	334.32	67.73	44.02
6	30.60	-110.65	-71.92	31.74	20.63
7	0.01	-478.69	-311.15	0.01	0.01

From all these points we get the P-M diagram

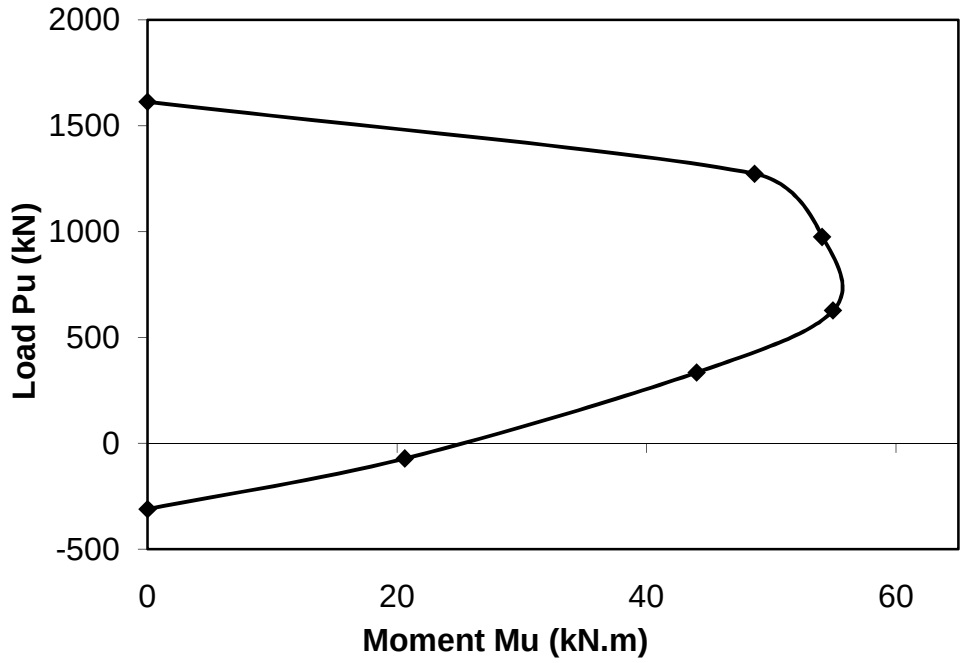

Figure B.6 - Load-moment interaction diagram for HSC-S column

Calculate buckling load – concentrically loaded slender column

$$E_{FAC} = 3.32\sqrt{f'c} + 6895(w_c/2320)^{1.5}$$

$$E_{FAC} = 3.32\sqrt{107}/1000 + 6895(2530/2320)^{1.5} = 37142.88 \text{ MPa}$$

$$I_g = \frac{bd^3}{12} = 141515140.1\ mm^4$$

Flexural rigidity = EI (ACI 10.15)

$$EI = \frac{0.4 E_c I_g}{1+\beta_d}$$

$$EI_{FAC} = \frac{0.4 \times 37142.88 \times 141515140.1}{(1+0.5)1000} = 1.40e^{12}\ MPa$$

Euler buckling Load P_c (ACI 10.13)

$$P_c = \frac{\pi^2 EI}{(kl_u)^2}$$

$$P_{c\ HSC-S} = 1232.7\ kN$$

Calculate the load and moment capacity of the column, the moment calculated by moment magnification factor will be checked against P-M diagram. Capacity is calculated by using iterations by assuming different Pu and then calculation of δ_{ns} as tabulated in Table B.7:

$$\delta_{ns} = Cm/(1 - \frac{Pu}{0.75Pc})$$

Table B.7 - Load and moment capacity calculated by moment magnification method.

Mu (kN.m)	Pu (kN)	δ_{ns}	e (mm)
0.00	0	1	0
5.64	222.4	1.2	25.4
14.11	444.8	1.5	33.02
28.22	667.2	2	43.18
56.45	889.6	3	63.5
65.86	934.08	3.3	71.12
68.00	942.976	3.4	73.66

Superimposing the calculated Pu and Mu against P-M diagram of the column gives the capacity of the column.

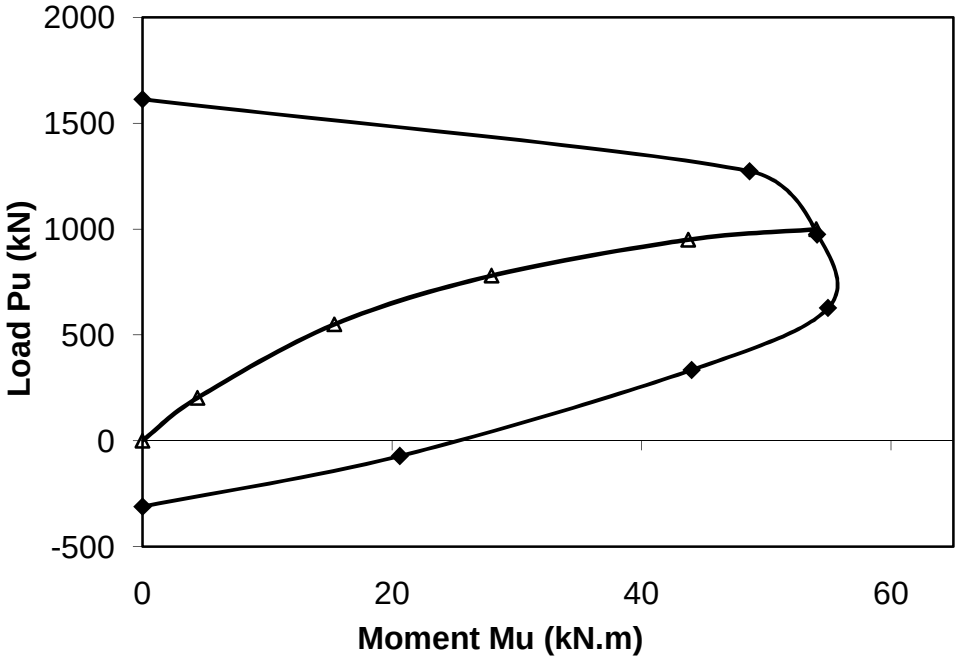

Figure B.7 - Calculation of ultimate load from load-moment interaction diagram for HSC-S column

REFERENCES

ACI-318 (2008). "Building Code Requirements for Reinforced Concrete and Commentary." American Concrete Institute, Farmington Hills, MI.

ACI 216.1 (2007). "Code requirements for determining fire resistance of concrete and masonry construction assemblies." *ACI 216.1-07 / TMS-0216-07*, American Concrete Institute, Farmington Hills, MI, 1-32.

Adl-Zarrabi, B., Boström, L., and Wickström, U. (2006). "Using the TPS method for determining the thermal properties of concrete and wood at elevated temperature." *Fire and Materials*, 30, 359-369.

Ali, F. (2002). "Is high strength concrete more susceptible to explosive spalling than normal strength concrete in fire?" *Fire and Materials*, 26, 127–130.

Ali, F., and Nadjai, A. (2008). "Fire resistance of concrete columns containing polypropylene & steel fibers." *ACI Special Publication, SP-255-9, American Concrete Institute, Farmington Hills, MI*, 255(9), 199-216.

Ali, F., Nadjai, A., Silcock, G., and Abu-Tair, A. (2004). "Outcomes of a major research on fire resistance of concrete columns." *Fire Safety Journal*, 39(6), 433-445.

Ali, F. A., O'Connor, D., and Abu-Tair, A. (2001). "Explosive spalling of high strength concrete columns in fire." *Magazine of Concrete Research* 53(3), 197-204.

Anagnostopoulos, N., Sideris, K. K., and Georgiadis, A. (2009). "Mechanical characteristics of self-compacting concretes with different filler materials exposed to elevated temperatures." *Materials and Structures*, 42(10), 1393-1405.

Anderberg, Y., and Thelandersson, S. (1976). *Stress and deformation characteristics of concrete at high temperatures, 2-Experimental investigation and material behaviour model*, Bulletin 54, Lund Institute of Technology, Lund, Sweden

ASCE (1992). "Structural fire protection." ASCE Committee on Fire Protection, Structural Division, American Society of Civil Engineers, New York.

ASTM C39 (2009). "Standard Test Method for Compressive Strength of Cylindrical Concrete Specimens." ASTM International, West Conshohocken, PA.

ASTM C78 (2009). "Standard Test Method for Flexural Strength of Concrete." ASTM International, West Conshohocken, PA.

ASTM C496 (2004). "Standard Test Method for Splitting Tensile Strength of Cylindrical Concrete Specimens." ASTM International, West Conshohocken, PA.

ASTM C496 (2011). "Standard Test Method for Splitting Tensile Strength of Cylindrical Concrete Specimens." ASTM International, West Conshohocken, PA.

ASTM C1113 (2009). "Standard Test Method for Thermal Conductivity of Refractories by Hot Wire (Platinum Resistance Thermometer Technique)." ASTM International, West Conshohocken, PA.

ASTM C1269 (2011). "Standard Test Method for Determining Specific Heat Capacity by Differential Scanning Calorimetry." ASTM International, West Conshohocken, PA.

ASTM C1583 (2004). "Standard Test Method for Tensile Strength of Concrete Surfaces and the Bond Strength or Tensile Strength of Concrete Repair and Overlay Materials by Direct Tension (Pull-off Method)." ASTM International, West Conshohocken, PA.

ASTM E119-08b (2008). "Standard test methods for fire tests of building construction and materials." ASTM International, West Conshohocken, PA.

ASTM E831 (2006). "Standard Test Method for Linear Thermal Expansion of Solid Materials by Thermomechanical Analysis." ASTM International, West Conshohocken, PA.

ASTM E1530 (2011). "Standard Test Method for Evaluating the Resistance to Thermal Transmission of Materials by the Guarded Heat Flow Meter Technique." ASTM International, West Conshohocken, PA.

ASTM E1868 (2010). "Standard Test Method for Loss-On-Drying by Thermogravimetry." ASTM International, West Conshohocken, PA.

ASTM Standard E119 (2007). "Standard test methods for fire tests of building construction and materials." ASTM International, West Conshohocken, PA.

Bamonte, P., and Gambarova, G. (2010). "High-temperature resistance of self-consolidating concrete." *Proc., ACI Spring Convention 2010.*

Bayrak, O., and Sheikh, S. A. (2001). "Plastic hinge analysis." *Journal of Structural Engineering, ASCE*, 127(9), 1092-1100.

Bazant, Z. P. (1997). "Analysis of pore pressure, thermal stress and fracture in rapidly heated concrete." *International Workshop on Fire Performance of High Strength Concrete*, NIST SP 919, Gaithersburg, MD, 155-164.

Bažant, Z. P., and Chern, J. (1987). "Stress-induced thermal and shrinkage strains in concrete." *Journal of Engineering Mechanics, ASCE*, 113(10), 1493-1511.

Bažant, Z. P., and Kaplan, M. F. (1996). *Concrete at high temperatures: material properties and mathematical models*, Longman Group Limited, Essex, England.

Behnood, A., and Ghandehari, M. (2009). "Comparison of compressive and splitting tensile strength of high-strength concrete with and without polypropylene fibers heated to high temperatures." *Fire Safety Journal*, 44(8), 1015-1022.

Bentz, D. P. (2000). "Fibers, percolation, and spalling of high-performance concrete." *ACI Materials Journal*, 97(3), 351-359.

Berry, M. P., and Eberhard, M. O. (2005). "Practical performance model for bar buckling." *Journal of Structural Engineering, ASCE*, 161(7), 1060-1070.

Bilodeau, A., Kodur, V. R., and Hoff, G. C. (2004). "Optimization of the type and amount of polypropylene fibers for preventing the spalling of lightweight concrete subjected to hydrocarbon fire." *Cement and Concrete Composites*, 26(2), 163-174.

Blaine, R. L., and Hahn, B. K. (1998). "Obtaining kinetic parameters by modulated thermogravimetry." *J Therm Anal Calorim*, 54(2), 695-704.

Boel, V., Audenaert, K., and Schutter, G. D. (2008). "Gas Permeability and Capillary Porosity of Self-compacting Concrete." *Journal of Materials and Structures*, 41(7), 1283-1290.

Buchanan, A. H. (2002). *Structural Design for Fire Safety*, John Wiley and Sons Ltd, Chichester, England.

Campbell, T. I., and Kodur, V. (1990). "Deformation controlled nonlinear analysis of prestressed cocnrete continuous beams." *PCI Journal*, PCI, 42-55.

Carette, G. G., Painter, K. E., and Malhotra, V. M. (1982). "Sustained high temperature effect on concretes made with normal portland cement, normal portland cement and slag, or normal portland cement and fly ash." *Concrete International*, 4(7), 41-51.

Castillo, C., and Durrani, A. J. (1990). "Effect of transient high temperature on high strength concrete." *ACI Materials Journal*, 87(1), 47-53.

Chan, Y. N., Peng, G. F., and Anson, M. (1999). "Residual strength and pore structure of high-strength concrete and normal strength concrete after exposure to high temperatures." *Cement and Concrete Composites*, 21(1), 23-27.

Chen, B., and Liu, J. (2004). "Residual strength of hybrid-fiber-reinforced high-strength concrete after exposure to high temperatures." *Cement and Concrete Research*, 34, 1065-1069.

Cheng, F. P., Kodur, V. K. R., and Wang, T. C. (2004). "Stress-strain curves for high strength concrete at elevated temperatures." *National Research Council of Canada, Report # NRCC-46973*, 1-30.

Cook, R. D., Malkus, D. S., Plesha, M. E., and Witt, R. J. (2007). *Concepts and applications of finite element*, John Wiley & Sons, Inc., NY, USA.

Dias, W. P. S., Khoury, G. A., and Sullivan, P. J. E. (1990). "Mechanical properties of hardened cement paste exposed to temperaures up to 700°C." *ACI Mateials Journal*, 87(2), 160-166.

Dwaikat, M. B. (2009). "Flexural response of reinforced concrete beams exposed to fire." Doctoral Thesis, Michigan State University, East Lansing, Michigan, USA.

Dwaikat, M. B., and Kodur, V. K. R. (2010). "Fire induced spalling in high strength concrete beams." *Fire Technology*, 46(1), 251-274.

Dwaikat, M. B., and Kodur, V. K. R. (2009). "Hydrothermal model for predicting fire induced spalling in concrete structural systems." *Fire Safety Journal*, 44(3), 425-434.

EC2-1-2 (2004). "Design of concrete structures – Part 1-2, General rules – Structural Fire design." CEN.

Eurocode 1 (2002). "EN 1991-1-2: Actions on structures. Part 1-2: General actions - Actions on structures exposed to fire." European Committee for Standardization, Brussels, Belgium.

Eurocode 2 (2004). "EN 1992-1-2: Design of concrete structures. Part 1-2: General rules - Structural fire design." European Committee for Standardization, Brussels, Belgium.

Fares, H., Remond, S., Noumuwe, A., and Cousture, A. (2010). "High temperature behaviour of self-consolidating concrete microstructure and physicochemical properties." *Cement and Concrete Research*, 40(3), 488-496.

Felicetti, R., and Gambarova, P. G. (1998). "Effects of high temperature on the residual compressive strength of high-strength siliceous concretes." *ACI Materials Journal*, 95(4), 395-406.

Felicetti, R., Gambarova, P. G., Rosati, G. P., Corsi, F., and Giannuzzi, G. (1996). "Residual mechanical properties of high-strength concretes subjected to high-temperature cycles." International Symposium of Utilization of High-Strength/High-Performance Concrete, Paris, France, 579-588.

FIB Bulletin 38 (2007). "Fire design of concrete structures - materials, structures and modelling." The International Federation for Structural Concrete (fib - fédération internationale du béton), Switzerland.

Flynn, D. R. (1999). "Response of high performance concrete to fire conditions: review of thermal property data and measurement techniques." National Institute of Standards and Technology, Millwood, US.

Fu, Y. F., Wong, Y. L., Poon, C. S., and Tang, C. A. (2005). "Stress-strain behavior of high-strength concrete at elevated temperatures." *Magazine of Concrete Research*, 57(9), 535-544.

Fu, Y. F., Wong, Y. L., Poon, C. S., Tang, C. A., and Lin, P. (2004). "Experimental study of micro/macro crack development and stress-strain relations of cement-based composite materials at elevated temperatures." *Cement and Concrete Research*, 34(5), 789-797.

Furumura, F., Abe, T., and Shinohara, Y. (1995). "Mechanical properties of high strength concrete at high temperatures." *High performance concrete; material properties and design; prodeedings of the Fourth Weimar Workshop on High Performance Concrete; Material Properties*, 237-254.

Ganguli, S., Roy, A. K., and Anderson, D. P. (2008). "Improved thermal conductivity for chemically functionalized exfoliated graphite/epoxy composites." *Carbon* 46(5), 806-817.

Harada, T., Takeda, J., Yamane, S., and Furumura, F. (1972). "Strength, elasticity and thermal properties of concrete subjected to elevated temperatures." *International Seminar on Concrete for Nuclear Reactor, ACI Special Publication, SP34-21*, 34(1), 377-406.

Harmathy, T. Z. (1970). "Thermal properties of concrete at elevated temperatures." *ASTM Journal of Materials*, 5(1), 47-74.

Harmathy, T. Z. (1969). "Simultaneous moisture and heat transfer in porous systems with particular reference to drying." *I & E C Fundamentals*, 8(1).

Harmathy, T. Z. (1971). "Moisture and heat transport with particular reference to concrete." *National Council of Canada, NRCC 12143*.

Harmathy, T. Z. (1967). "A comprehensive creep model." *Journal of Basic Engineering*, 89(3), 496-502.

Harmathy, T. Z. (1993). *Fire safety design and concrete*, John Wiley & Sons Inc., New York, NY.

Harmathy, T. Z., and Allen, L. W. (1973). "Thermal properties of selected masonry unit concretes." *ACI Journal, Proceedings*, 70(2), 132-142.

Hertz, K. D. (2003). "Limits of spalling of fire-exposed concrete." *Fire Safety Journal*, 38(2), 103-116.

Hu, X. F., Lie, T. T., Polomark, G. M., and MacLaurin, J. W. (1993). "Thermal properties of building materials at elevated temepratures." *Internal Report - 643 , Institute for Research in Construction, Natrional Research Council Canada*, 1-54.

Huang, C. L. (1979). "Multi-phase moisture transfer in porous media subject to temperature gradient." *International Journal of Heat and Mass Transfer*, 22, 1295-1307.

ISO/DIS22007-2:2008 (2008). "Determination of thermal conductivity and thermal diffusivity, Part 2: Transient plane heat source (hot disc) method." ISO, Geneva, Switzerland.

Kalifa, P., Chéné, G., and Gallé, C. (2001). "High-temperature behavior of HPC with polypropylene fibers from spalling to microstructure." *Cement and Concrete Research*, 31(10), 1487-1499.

Khaliq, W., and Kodur, V. (2012). "High temperature mechanical properties of high strength fly ash concrete with and without fibers." *ACI Materials Journal*, Submitted.

Khoury, G. A. (1992). "Compressive strength of concrete at high temperatures: a reassessment." *Magazine of Concrete Research*, 44(161), 291-309.

Khoury, G. A. (2008). "Concrete spalling assessment methodologies and polypropylene fibre toxicity analysis in tunnel fires." *Structural concrete*, 9(1), 11-18.

Khoury, G. A., Grainger, B. N., and Sullivan, P. J. E. (1985). "Strain of concrete during fire heating to 600 °C." *Magazine of Concrete Research*, 37(133), 195-215.

Kim, G. Y., Kim, Y. S., and Lee, T. G. (2009). "Mechanical properties of high-strength concrete subjected to high temperature by stressed test." *Transactions of Nonferrous Metals Society of China*, 19, 128-133.

Kodur, V., and Khaliq, W. (2011). "Effect of temperature on thermal properties of different types of high strength concrete." *Journal of Materials in Civil Engineering, ASCE*, 23(6), 793-801.

Kodur, V., and Raut, N. (2010). "Performance of concrete structures under fire hazard: emerging trends." *ICI Journal*, April - June 2010, 7-18.

Kodur, V. K. R. (2003). "Fiber Reinforcement for Minimizing Spalling in High Strength Concrete Structural Members Exposed to Fire." *ACI, Special Publication, Innovations in Fibre-Reinforced Concrete for Value*, 216-14, 221-236.

Kodur, V. K. R., and Fike, R. (2009). "Guidelines for improving the standard fire resistance test specifications." *Journal of ASTM International (JAI)*, 6(7), 16.

Kodur, V. R. (2003). "Fire resistance design guidelines for high strength concrete columns." National Research Council, Canada, 1-11.

Kodur, V. R. (2003). "Fire resistance design guidelines for high strength concrete columns." *National Research Council of Canada, Institute for research in Construction*, Internal Report No. 46116, 1-11.

Kodur, V. R. (1999). "Fire performance of high strength concrete structural members." *Construction Technology update No. 31*, Institute for Research in Construction, Canada.

Kodur, V. R. (1999). "Fiber reinforced concrete for enhancing structural fire resistance of columns." *American Concrete Institute*, SP 182-12(12), 215-234.

Kodur, V. R. (2000). "Spalling in high strength concrete exposed to fire - concerns, causes, critical parameters, and cures." *Proc., Proceedings of the ASCE Structures Congress*, 1-9.

Kodur, V. R., Dwaikat, M., and Raut, N. (2009). "Macroscopic FE model for tracing the fire response of reinforced concrete." *Engineering Structures*, 31(6), 2368-2379.

Kodur, V. R., Dwaikat, M. M. S., and Dwaikat, M. B. (2008). "High temperature properties of concrete for fire resistance modeling of structures." *ACI Materials Journal*, 105(5), 517-527.

Kodur, V. R., and Harmathy, T. Z. (2008). "Properties of building materials." *SFPE Handbook of Fire Protection Engineering*, P. J. DiNenno, ed., National Fire Protection Association, Quincy, MA, 1-167-161-195.

Kodur, V. R., and McGrath, R. (2003). "Fire endurance of high strength concrete columns." *Fire Technology*, 39(1), 73–87.

Kodur, V. R., and McGrath, R. (2006). "Effect of silica fume and lateral confinement on fire endurance of high strength concrete columns." *Can. J. Civ. Eng.*, 33, 93-102.

Kodur, V. R., and McGrath, R. (2003). "Fire endurance of high strength concrete columns." *NRCC-45141*, , National Research Council Canada, Ottawa, Canada, 1-13.

Kodur, V. R., and Sultan, M. A. (1998). "Structural behaviour of high strength concrete columns exposed to fire." *Proc., Proceedings, Int. Symposium on High Performance and Reactive Powder Concrete*, 217–232.

Kodur, V. R., and Sultan, M. A. (1998). "Thermal propeties of high strength concrete at elevated temperatures." *American Concrete Institute, Special Publication*, SP-179, 467-480.

Kodur, V. R., and Sultan, M. A. (2003). "Effect of temperature on thermal properties of high-strength concrete." *Journal of Materials in Civil Engineering*, 15(2), 101-107.

Kodur, V. R., Wang, T. C., Cheng, F. P., and Sultan, M. A. (2002). "A model for evaluating the fire resistance of high performance concrete columns." National Research Council Canada, Canada, 1-10.

Lau, A., and Anson, M. (2006). "Effect of high temperatures on high performance steel fibre reinforced concrete." *Cement and Concrete Research*, 36(9), 1698-1707.

Li, M., Qian, C., and Sun, W. (2004). "Mechanical properties of high-strength concrete after fire." *Cement and Concrete Research*, 34(6), 1001-1005.

Li, W., and Guo, Z. H. (1993). "Experimental investigation of strength and deformation of concrete at elevated temperature." *Journal of Building Structures*, 14(1), 8-16.(in Chinese).

Lie, T. T. (1992). "Structural fire protection." ASCE Committee on Fire Protection, Structural Division, American Society of Civil Engineers, New York, NY, 225-229.

Lie, T. T., and Irwin, R. J. (1993). "Method to calculate the fire resistance of reinforced concrete columns with rectangular cross section." *ACI structural Journal*, 90(1), 52-60.

Lie, T. T., and Kodur, V. R. (1996). "Thermal and mechanical properties of steel-fibre-reinforced concrete at elevated temperatures." *Canadian Journal of Civil Engineering*, 23(2), 511-517.

Lie, T. T., and Woolerton, J. L. (1988). "Fire Resistance of Reinforced Concrete Columns - Test Results." *National Research Council Canada, Report 569*.

Mehta, P. K., and Monteiro, P. J. M. (2006). *Concrete: Microstructure, Properties, and Materials*, The McGraw-Hill Companies, Inc., New York, USA.

Mendenhall, W., and Sincich, T. (2007). *Statistics for engineering and the sciences*, Prentice Hall, New Jersey, USA.

Mindess, S., Young, J. F., and Darwin, D. (2003). *Concrete*, Pearson Education, Inc., New Jersey, USA.

Nasser, K. W., and Marzouk, H. M. (1979). "Properties of mass concrete containing fly ash at high temperatures." *ACI Journal*, 76(4), 537-550.

Neville, A. M. (2004). *Properties of Concrete*, Pearson Education Limited, Essex, England.

Noumowé, A. (2005). "Mechanical properties and microstructure of high strength concrete containing polypropylene fibres exposed to temperatures up to 200°C." *Cement and Concrete Research*, 35, 2192-2198.

Noumowé, A., Siddique, R., and Debicki, G. (2009). "Permeability of high-performance concrete subjected to elevated temperature (600°C)." *Construction and Building Materials*, 23 (5), 1855-1861.

Pantazopoulou, S. J. (1998). "Detailing for reinforcement stability in RC members." *Journal of Structural Engineering, ASCE*, 124(6), 623-632.

Persson, B. (2004). "Fire resistance of self-compacting concrete, SCC." *Materials and Structures*, 37(9), 575-584.

Phan, L. T. (1996). "Fire performance of high-strength concrete: A report of the state-of-the-art." National Institute of Standards and Technology, Gaithersburg, Md, USA.

Phan, L. T. (2007). "Spalling and mechanical properties of high strength concrete at high temperature." *Concrete under Severe Conditions: Environment & Loading, CONSEC' 07 Tours*, CONSEC committee, France.

Poon, C. S., Azhar, S., Anson, M., and Wong, Y. L. (2001). "Comparison of the strength and durability performance of normal- and high-strength pozzolanic concretes at elevated temperatures." *Cement and Concrete Research*, 31(9), 1291-1300.

Popovics, S. (1998). *Strength and related properties of concrete, a quantitative approach*, John Wiley and Sons Publisher, New York.

Price, D. M. (1998). "Novel methods of modulated-temperature thermal analysis." *Thermochim Acta*, 315(1), 11-18.

Purkiss, J. A. (2007). *Fire safety engineering design of structures*, Butterworth-Heinemann - Elsevier, Oxoford, UK.

Raut, N. (2011). "Response of high strength concrete columns under fire-induced biaxial bending." Doctoral Thesis, Michigan State University, East Lansing, MI, USA.

Raut, N., and Kodur, V. K. R. (2011). "Response of high strength concrete columns under design fire exposure." *Journal of Structural Engineering, ASCE*, 137(1), 69-79.

Richart, F. E., Brandtzaeg, A., and Brown, R. L. (1929). "A study of the failure of concrete under combined compressive stresses." Engineering Experimental Station, Univ. of Illinois, Urbana IL.

RILEM TC 129-MHT (2000). "Test methods for mechanical properties of concrete at high temperatures, Part 4 - Tensile strength for service and accident conditions." *Materials and Structures*, 33, 219-223.

RILEM TC 129-MHT (1995). "Test methods for mechanical properties of concrete at high temperatures - Compressive strength for service and accident conditions." *Materials and Structures*, 28(3), 410-414.

Rossi, P. (1994). "Steel fiber reinforced concrete (SRC): An example of French research." *ACI Materials Journal*, 91(3), 273-279.

Sahota, M. S., and Pagni, P. G. (1979). "Heat and mass transfer in porous media subjecte to fire." *International Journal of Heat and Mass Transfer*(1069-1081), 22.

Schneider, U. (1988). "Concrete at high temperatures - A general review." *Fire Safety Journal*, 13, 55-68.

SFPE (2008). *Handbook of Fire Protection Engineering*, Society of Fire Protection Engineers and National Fire Protection Association.

Shah, S. P. (1991). "Do fibers increase the tensile strength of cement-based matrixes?" *ACI Materials Journal*, 88(6), 595-602.

Shehata, M. H., and Thomas, M. D. A. (2000). "The effect of fly ash composition on the expanison of concrete due to alkaki-sislica reaction." *Cement and Concrete Research*, 30(12), 1063-1072.

Shi, H., Xu, B., Shi, T., and Zhou, X. (2008). "Determination of gas permeability of high performance concrete containing fly ash." *Journal of Materials and Structures*, 42(6), 1051-1056.

Shin, K. Y., Kim, S., Kim, J., Chung, M., and Jung, P. (2002). "Thermo-physical properties and transient heat transfer of concrete at elevated temperatures." *Nuclear Engineering and Design*, 212(1-3), 233-241.

Sideris, K. K. (2007). "Mechanical characteristics of self-consolidating concrete exposed to elevated temeperatures." *Journal of Materials in Civil Engineering, ASCE*, 19(8), 648-654.

Tang, W. C., and Lo, T. Y. (2009). "Mechanical and fracture properties of normal- and high-strength concretes with fly ash after exposure to high temperatures." *Magazine of Concrete Research*, 61(5), 323-330.

VanGeem, M. G., Gajda, J. W., and Dombrowski, K. (1997). "Thermal properties of commercially available high-strength concretes." *Cement, Concrete, and Aggregates*, 19(1), 38-53.

Wackerly, D. D., Mandenhall III, W., and Scheaffer, R. L. (2008). *Mathematical statistics with applications*, Thomson Higher Education, Belmont, CA, USA.

Williams, B. K. (2004). "Fire performace of FRP-strengthened reinforced concrete flexural memebers." PhD Thesis, Queen's University, Kongston, Ontario, Canada.

Xiao, J., and König, G. (2004). "Study on concrete at high temperature in China—an overview." *Fire Safety Journal*, 39(1), 89-103.

Xu, Y. G., Wong, Y. L., and Anson, M. (2001). "Impact of high temperature on PFA concrete." *Cement and Concrete Research*, 31(7), 1065-1073.

Yu, X., Zha, X., and Huang, Z. (2011). "The influence of spalling on the fire resistance of RC structures." *Advanced Materials Research*, 255 - 260, 519-523.